RAPID CONSTRUCTION OF PET PROBES VIA TETRAZINE LIGATION

Mengzhe Wang

A dissertation submitted to the faculty at the University of North Carolina at Chapel Hill in partial fulfillment of the requirements for the degree of Doctor of Philosophy in the Joint Department of Biomedical Engineering in the University of North Carolina and North Carolina State University

Chapel Hill
2019

Approved by:

Zibo Li

Paul A. Dayton

Rihe Liu

David S. Lalush

Yen-Yu Ian Shih

ABSTRACT

Mengzhe Wang: Rapid Construction of PET Probes via Tetrazine Ligation
(Under the direction of Dr. Zibo Li)

Positron emission tomography (PET) is a non-invasive imaging modality that is widely used to observe metabolic process in vivo by tracking the interactions between PET probes and biomarkers. Facilitated by the recent development in the instrumentation and synthetic chemistry, clinical application of PET has been proven to be vital in theranostic uses. It possesses the advantages of high sensitivity, quantitative images, and great tissue penetration capability, all of which make it one of the most powerful molecular imaging techniques currently available in clinical use.

In order to visualize biochemical processes in vivo, corresponding PET probes are needed which could be synthesized based on PET radionuclides and biomolecules such as antibodies, proteins and peptides. ^{18}F is the most broadly used radionuclides in PET due to the high positron enrichment, high specific activity and clinically attractive half-life (~110min). However, the low concentration of ^{18}F and low reactivity make it challenging to be incorporated into biomolecules. This becomes more problematic when biomolecules become larger. It is also difficult to separate labeled large biomolecules (such as proteins) from unlabeled ones. As a result, the presence of unlabeled compound could saturate targeted receptors causing blocking effect in PET imaging. Therefore, the **goal of this dissertation** is to develop a highly efficient method for rapid construction of PET probes, especially large biomolecule based PET probes.

To achieve this goal, we **hypothesize** that a radiolabeling method based on the biorthogonal tetrazine-*trans*-cyclooctene (TTCO) ligation can enable fast reaction at submicromolar concentration, which will allow efficient construction of PET agents in high specific activity. In brief, biomolecules were modified with different tetrazine derivatives while the *trans*-cyclooctene (TCO) derivatives were radiolabeled with PET imaging radioisotopes such as ^{18}F or ^{64}Cu. The fast reaction rate between tetrazines and TCOs allowed us to form radio labeled biomolecules in seconds at low concentrations. The labeling strategy was applied to peptides and proteins to construct novel PET probes. The prepared PET probes showed uncompromised binding affinity and good targeting property and pharmacokinetics in PET imaging studies. We also explored the pre-targeting concept and showed the potential of using radiolabeled TTCO ligation for in vivo reaction.

ACKNOWLEDGEMENTS

Among all those people I would like to acknowledge, I want to first thank my advisor Dr. Zibo Li who supported and guided me in the past few years. Thank you for providing such a space for me to fail and grow and learn to be a researcher. I would also like to thank the other members in my committee, Dr. Rihe Liu, Dr. David Lalush, Dr. Yen-Yu Ian Shih and Dr. Paul Dayton for all the constructive suggestions and creative thinking during the presentation. I am also grateful to Dr. Rihe Liu, Dr. Xin Ming from Wake Forest University, Dr. Joeseph Fox from University of Delaware and all the members in their labs for supporting me with all the experimental resources.

To all the members in our lab, past and present, thank you for the extensive help in every aspect in our work. I could not have made it through these years without your support and guidance. Thanks to Dr. Hui Wang for teaching me so many knowledge and skills on biological part and did tons of injections for my work. I would also like to give my gratefulness to all the staffs in the radiochemistry and small animal imaging facility cores for providing massive access and resources that I need.

Thank you to the Department of Biomedical Engineering for a great graduate studying experience. I had many valuable memories in the courses I took and the seminars I attended. I would like to acknowledge Dr. Shawn Gomez and Vilma Berg for their effort in helping me through the application, transferring and graduation.

I would also like to thank all my friends both in LA and Chapel Hill who helped me balance my life and work. It would not be easy studying and living abroad without all of the accompanies.

The last but not least, I want to give my special thanks to my family. I am extremely grateful to my father Jun and mother Ru who devoted themselves in my education for the past 30 years and provided me the best opportunities as a student. It was their encouragement that made up my mind to pursue the PhD. Thanks also to my wife Mengqi for supporting me and share all my emotions during the highs and lows of my life. I could not have made this without her. I would also like to acknowledge my cat, Mooncake, who pleased me every time I came home and urge me to go back to work when I was too relaxed playing with him.

TABLE OF CONTENTS

LIST OF TABLES xiii

LIST OF SCHEMES xiv

LIST OF FIGURES xvi

LIST OF ABBREVIATIONS xxiii

Chapter 1 INTRODUCTION 1

  1.1 Positron Emission Tomography 1

  1.2 Radionuclide Selection 2

  1.3 Radiopharmaceuticals in Clinical and Translational Use 4

    1.3.1 Metabolism Related PET Probes 4

    1.3.2 Receptor Related PET Probes 5

  1.4 Challenges in PET Tracer Construction 7

  REFERENCES 10

Chapter 2 CURRENT STRATEGIES FOR ^{18}F LABELING OF BIOMOLECULES 14

  2.1 Overview 14

  2.2 Direct Labeling Methods 14

    2.2.1 ^{18}F Labeling via C-F Bond 14

    2.2.2 ^{18}F Labeling via B-F Bond 16

    2.2.3 ^{18}F Labeling via Si-F Bond 17

2.2.4 ^{18}F Labeling via AlF chelation 18
2.3 Indirect Labeling Methods 19
2.3.1 ^{18}F Labeling using amine selective prosthetic groups 19
2.3.2 ^{18}F Labeling using thiol selective prosthetic groups 21
2.3.3 ^{18}F Labeling using Cu-Catalyzed Azide-Alkyne Cycloaddition 22
2.3.4 ^{18}F Labeling using Strain-promoted Azide-Alkyne Click Reaction 24
2.3.5 ^{18}F Labeling using Staudinger Ligation 26
2.3.6 ^{18}F Labeling using Inverse Electron Demand Diels-Alder Click Reaction 26
2.4 Limitations 28
REFERENCES 29
Chapter 3 THE DEVELOPMENT OF RADIOLABELED TCOS AND TETRAZINES 34
3.1 Introduction on Tetrazine *Trans*-cyclooctene Ligation 34
3.2 Results and Discussion 35
3.2.1 ^{18}F Labeling of *Trans*-cyclooctenes 35
3.2.2 ^{64}Cu Labeling of *Trans*-cyclooctenes 40
3.2.3 ^{64}Cu Labeling of Tetrazines 43
3.3 Conclusion 45
3.4 Materials and Methods 46
3.4.1 General 46
3.4.2 Radiochemistry 47
3.4.3 *In Vitro* Stability and Reactivity for TTCO Ligation 48
REFERENCES 49
Chapter 4 BIOMOLECULES BASED PET PROBE CONSTRUCTION AND IMAGING USING TTCO LIGATION 50

4.1 Introduction of the Biomolecules 50

4.2 Radiolabeled RGD Peptide for Integrin $\alpha_v\beta_3$ Targeted Imaging 50

4.2.1 ^{18}F-TCO-DiPhTz-RGDyK 51

4.2.2 ^{18}F-sTCO-DiPhTz-RGDyK 54

4.2.3 ^{18}F-dTCO-DiPhTz-RGDyK 56

4.2.4 ^{18}F-sTCO-MePhTz-RGDyK 58

4.2.5 ^{18}F-sTCO-DiolTz-RGDyK 61

4.3 Radiolabeled NT Peptide for NTSR1 Targeted Imaging 63

4.3.1 ^{18}F-sTCO-DiPhTz-NT 64

4.3.2 ^{18}F-sTCO-DiolTz-NT 67

4.3.3 ^{18}F-sTCO-MePhTz-NT 69

4.3.4 ^{18}F-dTCO-MePhTz-NT 71

4.3.5 ^{18}F-oTCO-MePhTz-NT 73

4.3.6 ^{64}Cu-dTCO-PEG-DOTA-MePhTz-NT 75

4.3.7 Effect of TTCO system on Binding Affinity of the PET Probes 77

4.4 Radiolabeled PSMA Ligand for Prostate Cancer Imaging 79

4.4.1 ^{18}F-oTCO-MePhTz-PSMA 80

4.4.2 ^{18}F-sTCO-DiPhTz-PSMA 83

4.5 Other Radiolabeled Peptides for PET Imaging 86

4.5.1 ^{18}F-sTCO-DiPhTz-Exendin 86

4.5.2 ^{18}F-sTCO-DiPhTz-BBN 89

4.6 Radiolabeled HER2 Protein Ligands for HER2 Targeted Imaging 91

4.6.1 ^{18}F-oTCO-MePhTz-HER2 92

4.7 Effect of TTCO System on Pharmacokinetic of PET Probes 94

4.8 Conclusion 99

4.9 Materials and Methods 100

4.9.1 General 100

4.9.2 Chemistry and Radiochemistry 100

4.9.3 Small Animal PET Imaging 102

4.9.4 *In Vitro* Cell Binding Assay 102

4.9.5 Octanol-Water Partition Coefficient 103

4.9.6 Statistical Analysis 103

REFERENCES 104

Chapter 5 EXPLORATION OF PRE-TARGETING CONCEPT USING TTCO LIGATION 110

5.1 Introduction to Pretargeting 110

5.2 Results and Discussion 112

5.2.1 Pretargeting with ^{18}F *Trans*-cyclooctene and Tetrazine-peptide 112

5.2.2 Pretargeting with ^{64}Cu Tetrazine and TCO-antibody 114

5.2.3 Pretargeting with ^{18}F TCO-8Tetrazine and TCO-antibody 116

5.3 Conclusion 119

5.4 Materials and Methods 119

5.4.1 General 119

5.4.2 Chemistry and Radiochemistry 120

5.4.3 Pretargeted Small Animal PET Imaging 120

5.4.4 Statistical Analysis 121

REFERENCES 122

Chapter 6 OTHER PET PROBES CONSTRUCTION PROJECTS 124

6.1 ^{18}F-NHC-BF$_3$ Adducts as Water Stable Radio-Prosthetic Groups for PET Imaging 124

6.1.1 Introduction 124

6.1.2 Results and Discussion 124

6.2 Preparation of ^{18}F-NHC-BF$_3$ Conjugates and Their Applications in PET Imaging 125

6.2.1 Introduction 125

6.2.2 Results and Discussion 125

6.3 Synthesis and *In vivo* Stability Studies of ^{18}F-Zwitterionic Phosphonium Aryltrifluoroborate/Indomethacin Conjugates 126

6.3.1 Introduction 126

6.3.2 Results and Discussion 126

6.4 The efficiency of ^{18}F labelling of a prostate specific membrane antigen ligand via strain-promoted azide-alkyne reaction: reaction speed versus hydrophilicity 127

6.4.1 Introduction 127

6.4.2 Results and Discussion 127

6.5 Molecular Imaging of P-glycoprotein in Chemoresistant Tumors Using a Dual-Modality PET/Fluorescence Probe 129

6.5.1 Introduction 129

6.5.2 Results and Discussion 130

6.6 Development of ^{18}F-AlF-NOTA-NT as PET Agents of Neurotensin Receptor-1 Positive Pancreatic Cancer 131

6.6.1 Introduction 131

6.6.2 Results and Discussion 132

REFERENCES 134

Chapter 7 SUMMARY 137

7.1 Summary of Current Work 137

7.2 Innovation of Current Studies 139

7.3 Future Work 139

LIST OF TABLES

Table 1.1 Commonly used radionuclides in PET 2

Table 1.2 Relationship between reaction rate constant and reaction time if both reactants are at 1μM concentration.. 9

Table 2.1 Reaction rate constant range for common ^{18}F-biomolecule labeling reactions 28

Table 4.1 Tumor to muscle uptake ratio of ^{18}F-sTCO with different NT-tetrazine derivatives in H1299 xenografts at 1 and 4h post injection 95

Table 4.2 Tumor to muscle uptake ratio of MePhTzNT with different TCO derivatives in PC3 xenografts at 1 and 4h post injection 95

LIST OF SCHEMES

Scheme 2.1 Direct ^{18}F labeling methods via C-F bond 15

Scheme 2.2 Direct ^{18}F labeling methods via B-F bond 16

Scheme 2.3 Direct ^{18}F labeling methods via Si-F bond 17

Scheme 2.4 Direct ^{18}F labeling method via AlF chelation 18

Scheme 2.5 Indirect ^{18}F labeling methods using amine selective prosthetic groups 20

Scheme 2.6 Indirect ^{18}F labeling methods using thiol selective prosthetic groups 21

Scheme 2.7 Indirect ^{18}F labeling methods using Cu-catalyzed azide-alkyne cycloaddition 23

Scheme 2.8 Indirect ^{18}F labeling methods using strain-promoted azide-alkyne click reaction 25

Scheme 2.9 Indirect ^{18}F labeling methods using Staudinger ligation 26

Scheme 2.10 Indirect ^{18}F labeling methods using inverse electron demand Diels-Alder click reaction 27

Scheme 3.1 Labeling scheme of ^{18}F-TCO 35

Scheme 3.2 Labeling scheme of ^{18}F-sTCO 36

Scheme 3.3 Labeling scheme of ^{18}F-dTCO 37

Scheme 3.4 Labeling scheme of ^{18}F-oTCO 39

Scheme 3.5 Labeling scheme of ^{64}Cu-sTCO-PEG-DOTA 40

Scheme 3.6 Labeling scheme of ^{64}Cu-dTCO-PEG-DOTA 42

Scheme 3.7 Labeling scheme of ^{64}Cu-Tz-NOTA 43

Scheme 3.8 Labeling scheme of ^{64}Cu-Tz-PEG-NOTA 44

Scheme 4.1 Synthesis scheme of ^{18}F-TCO-DiPhTz-RGDyK 51

Scheme 4.2 Synthesis scheme of ^{18}F-sTCO-DiPhTz-RGDyK 54

Scheme 4.3 Synthesis scheme of ^{18}F-dTCO-DiPhTz-RGDyk 56

Scheme 4.4 Synthesis scheme of ^{18}F-sTCO-MePhTz-RGDyK.. 58

Scheme 4.5 Synthesis scheme of ^{18}F-sTCO-DiolTz-RGDyK 61

Scheme 4.6 Synthesis scheme of ^{18}F-sTCO-DiPhTz-NT 64

Scheme 4.7 Synthesis scheme of ^{18}F-sTCO-DiolTz-NT 67

Scheme 4.8 Synthesis scheme of ^{18}F-sTCO-MePhTz-NT... 69

Scheme 4.9 Synthesis scheme of ^{18}F-dTCO-MePhTz-NT 71

Scheme 4.10 Synthesis scheme of ^{18}F-oTCO-MePhTz-NT 73

Scheme 4.11 Synthesis scheme of ^{64}Cu-dTCO-PEG-DOTA-MePhTz-NT 75

Scheme 4.12 Synthesis scheme of ^{18}F-oTCO-MePhTz-PSMA... 80

Scheme 4.13 Synthesis scheme of ^{18}F-sTCO-DiPhTz-PSMA 83

Scheme 4.14 Synthesis scheme of ^{18}F-sTCO-DiPhTz-Exendin.. 86

Scheme 4.15 Synthesis scheme of ^{18}F-sTCO-DiPhTz-BBN 89

LIST OF FIGURES

Figure 3.1 HPLC profile of a) purified ^{18}F-TCO. b) ^{19}F-TCO. c) ^{18}F-TCO after incubation in PBS for 1h at 37°C. d) Crude of ^{18}F-TCO ligation with DiPhTz-RGDyK 36

Figure 3.2 HPLC profile of a) purified ^{18}F-sTCO. b) ^{19}F-sTCO. c) ^{18}F-sTCO after incubation in PBS for 1h at 37°C. d) Crude of ^{18}F-sTCO ligation with DiPhTz-RGDyK 37

Figure 3.3 HPLC profile of a) purified ^{18}F-dTCO. b) ^{19}F-dTCO. c) ^{18}F-dTCO after incubation in PBS for 1h at 37°C. d) Crude of ^{18}F-dTCO ligation with DiPhTz-RGDyK 38

Figure 3.4 HPLC profile of a) purified ^{18}F-oTCO. b) ^{19}F-oTCO. c) ^{18}F-oTCO after incubation in PBS for 1h at 37°C. d) Crude of ^{18}F-oTCO ligation with DiPhTz-RGDyK 40

Figure 3.5 HPLC profile of a) purified ^{64}Cu-sTCO-PEG-DOTA. b) sTCO-PEG-DOTA. c) ^{64}Cu-sTCO-PEG-DOTA after incubation in PBS for 1h at 37°C. d) Crude of ^{64}Cu-sTCO-PEG-DOTA ligation with DiPhTz-RGDyK 41

Figure 3.6 HPLC profile of a) purified ^{64}Cu-dTCO-PEG-DOTA. b) dTCO-PEG-DOTA. c) ^{64}Cu-dTCO-PEG-DOTA after incubation in PBS for 1h at 37°C. d) Crude of ^{64}Cu-dTCO-PEG-DOTA ligation with DiPhTz-RGDyK........ 42

Figure 3.7 HPLC profile of a) purified ^{64}Cu-Tz-NOTA. b) Tz-NOTA. c) ^{64}Cu-Tz-NOTA after incubation in PBS for 1h at 37°C. d) Crude of ^{64}Cu-Tz-NOTA ligation with TCO-F 44

Figure 3.8 HPLC profile of a) purified ^{64}Cu-Tz-PEG-NOTA. b) Tz-PEG-NOTA. c) ^{64}Cu-Tz-PEG-NOTA after incubation in PBS for 1h at 37°C. d) Crude of ^{64}Cu-Tz-PEG-NOTA ligation with TCO-F 45

Figure 4.1 a) HPLC profile of crude reaction between DiPhTz-NHS and RGDyK. b) HPLC profile of purified DiPhTz-RGDyK. c) Mass spectrum of purified DiPhTz-RGDyK 52

Figure 4.2 HPLC profile of a) purified ^{18}F-TCO-DiPhTz-RGDyK. b) ^{19}F-TCO-DiPhTz-RGDyK. c) crude of ^{18}F-TCO ligation with DiPhTz-RGDyK. d) Mass spectrum of purified ^{19}F-TCO-DiPhTz-RGDyK 53

Figure 4.3 Representative PET/CT images of U87MG tumor bearing mice at a) 1h and b) 4h post injection of ^{18}F-TCO-DiPhTz-RGDyK.

c) Quantitative uptake of the major organs determined from the PET images. Tumor regions are highlighted in orange circle 54

Figure 4.4 HPLC profile of a) purified ^{18}F-sTCO-DiPhTz-RGDyK. b) ^{19}F-sTCO-DiPhTz-RGDyK. c) crude of ^{18}F-sTCO ligation with DiPhTz-RGDyK. d) Mass spectrum of purified ^{19}F-sTCO-DiPhTz-RGDyK............. 55

Figure 4.5 Representative PET/CT images of U87MG tumor bearing mice at a) 1h and b) 4h post injection of ^{18}F-sTCO-DiPhTz-RGDyK. c) Quantitative uptake of the major organs determined from the PET images. Tumor regions are highlighted in orange circle 56

Figure 4.6 HPLC profile of a) purified ^{18}F-dTCO-DiPhTz-RGDyK. b) ^{19}F-dTCO-DiPhTz-RGDyK. c) crude of ^{18}F-dTCO ligation with DiPhTz-RGDyK. d) Mass spectrum of purified ^{19}F-dTCO-DiPhTz-RGDyK. 57

Figure 4.7 Representative PET/CT images of U87MG tumor bearing mice at a) 1h and b) 4h post injection of ^{18}F-dTCO-DiPhTz-RGDyK. c) Quantitative uptake of the major organs determined from the PET images. Tumor regions are highlighted in orange circle 58

Figure 4.8 a) HPLC profile of crude reaction between MePhTz-NHS and RGDyK. b) HPLC profile of purified MePhTz-RGDyK. c) Mass spectrum of purified MePhTz-RGDyK 59

Figure 4.9 HPLC profile of a) purified ^{18}F-sTCO-MePhTz-RGDyK. b) ^{19}F-sTCO-MePhTz-RGDyK. c) crude of ^{18}F-sTCO ligation with MePhTz-RGDyK. d) Mass spectrum of purified ^{19}F-sTCO-MePhTz-RGDyK.................. 60

Figure 4.10 Representative PET/CT images of U87MG tumor bearing mice at a) 1h and b) 4h post injection of ^{18}F-sTCO-MePhTz-RGDyK. c) Quantitative uptake of the major organs determined from the PET images. Tumor regions are highlighted in orange circle 60

Figure 4.11 a) HPLC profile of crude reaction between DiolTz-NHS and RGDyK. b) HPLC profile of purified DiolTz-RGDyK. c) Mass spectrum of purified DiolTz-RGDyK.. 61

Figure 4.12 HPLC profile of a) purified ^{18}F-sTCO-DiolTz-RGDyK. b) ^{19}F-sTCO-DiolTz-RGDyK. c) crude of ^{18}F-sTCO ligation with DiolTz-RGDyK. d) Mass spectrum of purified ^{19}F-sTCO-DiolTz-RGDyK....................... 62

Figure 4.13 Representative PET/CT images of U87MG tumor bearing mice at a) 1h and b) 4h post injection of ^{18}F-sTCO-DiolTz-RGDyK. c) Quantitative uptake of the major organs determined from the PET images. Tumor regions are highlighted in orange circle 63

Figure 4.14 a) HPLC profile of crude reaction between DiPhTz-NHS and NT. b) HPLC profile of purified DiPhTz-NT. c) Mass spectrum of purified DiPhTz-NT 65

Figure 4.15 HPLC profile of a) purified ^{18}F-sTCO-DiPhTz-NT. b) ^{19}F-sTCO-DiPhTz-NT. c) crude of ^{18}F-sTCO ligation with DiPhTz-NT. d) Mass spectrum of purified ^{19}F-sTCO-DiPhTz-NT 65

Figure 4.16 Representative PET/CT images of AsPC1 tumor bearing mice at a) 1h and b) 4h post injection of ^{18}F-sTCO-DiPhTz-NT. c) Quantitative uptake of the major organs determined from the PET images. Tumor regions are highlighted in orange circle 66

Figure 4.17 a) HPLC profile of crude reaction between DiolTz-NHS and NT. b) HPLC profile of purified DiolTz-NT. c) Mass spectrum of purified DiolTz-NT 67

Figure 4.18 HPLC profile of a) purified ^{18}F-sTCO-DiolTz-NT. b) ^{19}F-sTCO-DiolTz-NT. c) crude of ^{18}F-sTCO ligation with DiolTz-NT. d) Mass spectrum of purified ^{19}F-sTCO-DiolTz-NT 68

Figure 4.19 Representative PET/CT images of H1299 tumor bearing mice at a) 1h and b) 4h post injection of ^{18}F-sTCO-DiolTz-NT. c) Quantitative uptake of the major organs determined from the PET images. Tumor regions are highlighted in orange circle 68

Figure 4.20 a) HPLC profile of crude reaction between MePhTz-NHS and NT. b) HPLC profile of purified MePhTz-NT. c) Mass spectrum of purified MePhTz-NT 70

Figure 4.21 HPLC profile of a) purified ^{18}F-sTCO-MePhTz-NT. b) ^{19}F-sTCO-MePhTz-NT. c) crude of ^{18}F-sTCO ligation with MePhTz-NT. d) Mass spectrum of purified ^{19}F-sTCO-MePhTz-NT 70

Figure 4.22 Representative PET/CT images of PC3 tumor bearing mice at a) 0.5h and b) 3.5h post injection of ^{18}F-sTCO-MePhTz-NT. c) Quantitative uptake of the major organs determined from the PET images. Tumor regions are highlighted in orange circle 71

Figure 4.23 HPLC profile of a) purified ^{18}F-dTCO-MePhTz-NT. b) ^{19}F-dTCO-MePhTz-NT. c) crude of ^{18}F-dTCO ligation with MePhTz-NT. d) Mass spectrum of purified ^{19}F-dTCO-MePhTz-NT 72

Figure 4.24 Representative PET/CT images of PC3 tumor bearing mice at a) 0.5h and b) 3.5h post injection of ^{18}F-dTCO-MePhTz-NT. c) Quantitative uptake of the major organs determined from the

PET images. Tumor regions are highlighted in orange circle 73

Figure 4.25 HPLC profile of a) purified ^{18}F-oTCO-MePhTz-NT. b) ^{19}F-oTCO-MePhTz-NT. c) crude of ^{18}F-oTCO ligation with MePhTz-NT. d) Mass spectrum of purified ^{19}F-oTCO-MePhTz-NT.................................. 74

Figure 4.26 Representative PET/CT images of PC3 tumor bearing mice at a) 0.5h and b) 3.5h post injection of ^{18}F-oTCO-MePhTz-NT. c) Quantitative uptake of the major organs determined from the PET images. Tumor regions are highlighted in orange circle 75

Figure 4.27 HPLC profile of a) purified ^{64}Cu-dTCO-PEG-DOTA-MePhTz-NT. b) dTCO-PEG-DOTA-MePhTz-NT. c) crude of ^{64}Cu-dTCO-PEG-DOTA ligation with MePhTz-NT. d) Mass spectrum of purified dTCO-PEG-DOTA-MePhTz-NT 76

Figure 4.28 Representative PET/CT images of PC3 tumor bearing mice at a) 1h and b) 4h post injection of ^{64}Cu-dTCO-PEG-DOTA-MePhTz-NT. c) Quantitative uptake of the major organs determined from the PET images. Tumor regions are highlighted in orange circle 77

Figure 4.29 Competitive cell binding assays of ^{19}F-sTCO-MePhTz-NT, ^{19}F-sTCO-DiPhTz-NT, ^{19}F-sTCO-DiolTz-NT and original NT20.3 peptide....................... 78

Figure 4.30 Competitive cell binding assays of ^{19}F-sTCO-MePhTz-NT, ^{19}F-dTCO-MePhTz-NT, ^{19}F-oTCO-MePhTz-NT and original NT20.3 peptide 79

Figure 4.31 a) HPLC profile of crude reaction between MePhTz-NHS and PSMA. b) HPLC profile of purified MePhTz-PSMA. c) Mass spectrum of purified MePhTz-PSMA 81

Figure 4.32 HPLC profile of a) purified ^{18}F-oTCO-MePhTz-PSMA. b) ^{19}F-oTCO-MePhTz-PSMA. c) crude of ^{18}F-oTCO ligation with MePhTz-PSMA. d) Mass spectrum of purified ^{19}F-oTCO-MePhTz-PSMA 81

Figure 4.33 Representative PET/CT images of LnCaP tumor bearing mice at a) 1h and b) 4h post injection of ^{18}F-oTCO-MePhTz-PSMA. c) Quantitative uptake of the major organs determined from the PET images. Tumor regions are highlighted in orange circle.. 82

Figure 4.34 a) HPLC profile of crude reaction between DiPhTz-NHS and PSMA. b) HPLC profile of purified DiPhTz-PSMA. c) Mass spectrum of purified DiPhTz-PSMA... 84

Figure 4.35 HPLC profile of a) purified ^{18}F-sTCO-DiPhTz-PSMA. b) ^{19}F-sTCO-DiPhTz-PSMA. c) crude of ^{18}F-sTCO ligation with

DiPhTz-PSMA. d) Mass spectrum of purified ^{19}F-sTCO-DiPhTz-PSMA 85

Figure 4.36 Representative PET/CT images of LnCaP tumor bearing mice at a) 1h and b) 4h post injection of ^{18}F-sTCO-DiPhTz-PSMA. c) Quantitative uptake of the major organs determined from the PET images. Tumor regions are highlighted in orange circle 85

Figure 4.37 a) HPLC profile of crude reaction between DiPhTz-NHS and Exendin. b) HPLC profile of purified DiPhTz-Exendin. c) Mass spectrum of purified DiPhTz-Exendin 87

Figure 4.38 HPLC profile of a) purified ^{18}F-sTCO-DiPhTz-Exendin. b) ^{19}F-sTCO-DiPhTz-Exendin4. c) crude of ^{18}F-sTCO ligation with DiPhTz-Exendin. d) Mass spectrum of purified ^{19}F-sTCO-DiPhTz-Exendin 88

Figure 4.39 Representative PET/CT images of INS1 tumor bearing mice at a) 1h and b) 4h post injection of ^{18}F-sTCO-DiPhTz-Exendin. c) Quantitative uptake of the major organs determined from the PET images. Tumor regions are highlighted in orange circle 88

Figure 4.40 a) HPLC profile of crude reaction between DiPhTz-NHS and BBN. b) HPLC profile of purified DiPhTz-BBN. c) Mass spectrum of purified DiPhTz-BBN 89

Figure 4.41 HPLC profile of a) purified ^{18}F-sTCO-DiPhTz-BBN. b) ^{19}F-sTCO-DiPhTz-BBN. c) crude of ^{18}F-sTCO ligation with DiPhTz-BBN. d) Mass spectrum of purified ^{19}F-sTCO-DiPhTz-BBN 90

Figure 4.42 Representative PET/CT images of PC3 tumor bearing mice at a) 1h and b) 4h post injection of ^{18}F-sTCO-DiPhTz-BBN. c) Quantitative uptake of the major organs determined from the PET images. Tumor regions are highlighted in orange circle 91

Figure 4.43 Picture of PD-10 elutions during purification of MePhTz modified HER2 protein 93

Figure 4.44 Representative PET/CT images of SKOV3 tumor bearing mice at a) 1h and b) 4h post injection of ^{18}F-oTCO-MePhTz-HER2. c) Quantitative uptake of the major organs determined from the PET images. Tumor regions are highlighted in orange circle 94

Figure 4.45 Electropherogram and autoradiography of ^{18}F-sTCO-DiPhTz in mouse plasma 98

Figure 4.46 Electropherogram and autoradiography of ^{18}F-sTCO-DiPhTz in hemopexin and transferrin. 99

Figure 5.1 Representative PET/CT images of U87MG tumor bearing mice at a) 1h and b) 4h post injection of ^{18}F-sTCO. c) Quantitative uptake of the major organs determined from the PET images. Representative PET/CT images of U87MG tumor bearing mice injected with ^{18}F-sTCO 1h after pretargeting of DiPhTz-RGDyK. Images were acquired at d) 1h and e) 4h post injection of ^{18}F-sTCO. f) Quantitative uptake of the major organs determined from the PET images. Tumor regions are highlighted in orange circle 114

Figure 5.2 Representative PET/CT images of Fadu tumor bearing mice at a) 1h and b) 4h post injection of ^{64}Cu-Tz-PEG-NOTA. c) Quantitative uptake of the major organs determined from the PET images. Representative PET/CT images of Fadu tumor bearing mice injected with ^{64}Cu-Tz-PEG-NOTA 24h after pretargeting of TCO-15D3. Images were acquired at d) 1h and e) 4h post injection of ^{64}Cu-Tz-PEG-NOTA. f) Quantitative uptake of the major organs determined from the PET images. Tumor regions are highlighted in orange circle.. 115

Figure 5.3 Representative PET/CT images of Fadu tumor bearing mice at a) 1h and b) 4h post injection of ^{18}F-TCO-8Tz. c) Quantitative uptake of the major organs determined from the PET images. Representative PET/CT images of Fadu tumor bearing mice at a) 1h and b) 4h post injection of ^{18}F-TCO-8Tz-TCO-15D3. c) Quantitative uptake of the major organs determined from the PET images. Tumor regions are highlighted in orange circle.. 117

Figure 5.4 Representative PET/CT images of Fadu tumor bearing mice injected with ^{18}F-TCO-8Tz 48h after pretargeting of TCO-15D3. Images were acquired at a) 1h and b) 4h post injection of ^{18}F-TCO-8Tz. c) Quantitative uptake of the major organs determined from the PET images. Tumor regions are highlighted in orange circle 118

Figure 5.5 Representative PET/CT images of Fadu tumor bearing mice injected with ^{18}F-TCO-8Tz 10min after intratumorally administration of TCO-15D3 (right tumor). Images were acquired at a) 1h and b) 4h post injection of ^{18}F-TCO-8Tz. c) Quantitative uptake of the major organs determined from the PET images. Tumor regions are highlighted in orange circle.. 119

Figure 6.1 Graphical abstract of ^{18}F labeling of NHC-BF$_3$ adduct and PET images of the constructed PET tracer. Sources: Adapted from Mengzhe et al (*5*). Reproduced by permission of The Royal Society of Chemistry.............. 125

Figure 6.2 Graphical abstract of the synthesis of ^{18}F-NHC-BF$_3$-biomolecule and PET images of the constructed PET tracer. Sources: Adapted from

Mengzhe et al (*8*). Published by The Royal Society of Chemistry 126

Figure 6.3 Graphical abstract of ^{18}F labeling of zwitterionic phosphonium arytrifluoroborate-Indomethacin and PET images of the constructed PET tracer. Sources: Adapted from Mengzhe et al (*15*). Reproduced by permission of The Royal Society of Chemistry 127

Figure 6.4 Graphical abstract of ^{18}F-BCN-PSMA, ^{18}F-ODIBO-PSMA and corresponding PET images of the constructed PET tracer. Sources: Adapted from Mengzhe et al (*19*). Reproduced by permission of The Royal Society of Chemistry 129

Figure 6.5 Graphical abstract of ^{64}Cu-DOTA-Pab-IR800 and corresponding PET images. Sources: Adapted from Mengzhe et al (*23*). Reprinted with permission from Mol. pharmaceutics 2017, 14, 10, 3391-3398. Copyright 2017 American Chemical Society 131

Figure 6.6 Graphical abstract of ^{18}F-AlF-NOTA-NT synthesis and corresponding PET images. Sources: Adapted from Mengzhe et al (*29*). Reprinted with permission from Mol. Pharmaceutics 2018, 15, 8, 3093-3100. Copyright 2018 American Chemical Society 133

LIST OF ABBREVIATIONS

%ID/g	Percentage of injected dose per gram
ADIBO	Azadibenzocyclooctyne
Arg	Arginine
Asn	Asparagine
Asp	Aspartic acid
ATSM	Diacetyl-bis(N^4-methylthiosemicarbazone)
BBN	Bombesin
BCN	Bicyclo[6.1.0]nonyne
BPH	Benign prostatic hyperplasia
CT	Computed tomorgraphy
DiolTz	2,2'-(1,2,4,5-tetrazine-3,6-diyl)bis(ethan-1-ol)
DIPEA	N,N-Diisopropylethylamine
DiPhTz	3,6-diphenyl-1,2,4,5-tetrazine
DMSO	Dimethyl sulfoxide
DNA	Deoxyribonucleic acid
DOTA	1,4,7,10-Tetraazacyclododecane-1,4,7,10-tetraacetic acid
dTCO	dioxolane-fused *trans*-cyclooctene
ECM	Extracellular matrix
EGFR	Epidermal growth factor receptor
ERK	Extracellular signal-regulated kinase
F-Py-TFP	6-fluoronicotinic acid tetrafluorophenyl ester

FBA	4-fluorobenzaldehyde
FBBA	*N*-(4-fluorobenzyl)-2-bromoacetamide
FBEM	*N*-[2-(4-fluorobenzamideo)ethyl]maleimide
FEA	Fluoroethylazide
FES	Fluoroestradiol
FLT	Fluorothymidine
FNPB	4-fluoro-3-nitro-*N*-2-prop-1-ynylbenzamide
FPOS	2-(4-(2-(fluoroethoxy)phenyl)-5-(methylsulfonyl)-1,3,4-oxadiazole
FSA	Fluoro-*N*-(prop-2-ynyl)benzamide
GLP-1R	Glucagon-like peptide-1 receptor
Glu	Glutamic acid
Gly	Glycine
HER2	Human epidermal growth factor receptor 2
HFB	Hexafluorobenzene
IC_{50}	Half maximal inhibitory conecntration
IEDDA	Inverse electron demand Diels-Alder click reaction
Ile	Isoleucine
Leu	Leucine
Lys	Lysine
mAb	Monoclonal antibody
MAPK	Mitogen-activated protein kinase
MeCN	Acetonitrile
MePhTz	3-methyl-6-phenyl-1,2,4,5-tetrazine

NaOH	Sodium hydroxide
NFP	4-nitrophenyl-2-fluoropropionate
NHC	N-Heterocyclic Carbene
NHS	*N*-Hydroxysuccinimide
NOTA	1,4,7-Triazacyclononane-1,4,7-triacetic acid
NT	Neurotensin
NTR	Neurotensin receptor
ODIBO	Oxa-dibenzocyclooctyne
oTCO	trans-5-oxocene
PBS	Phosphate-buffered saline
PEG	Polyethylene glycol
PET	Positron emission tomorgraphy
PI3K	Phosphoinositide 3-kinase
Pro	Proline
PSA	Prostate specific antigen
PSMA	Prostate specific membrane antigen
RGDyK	Cyclo(- Arg - Gly - Asp - D - Tyr - Lys)
ROI	Region of interest
RP-HPLC	Reverse phase high performance liquid chromatography
SD	Standard deviation
SFB	N-succinimidyl 4-fluorobenzoate
SiFA-A	*p*-(di-*tert*-butyl fluorosilyl)benzaldehyde
SSTR	Somatostatin receptor

sTCO	Strained *trans*-cyclooctene
TAC	Time-activity curve
TBAF	Tetra-*n*-butylammonium fluoride
TCO	*trans*-cyclooctene
TFA	Triethylamine
Tle	Tert-leucine
TTCO	Tetrazine-*trans*-cyclooctene
Tyr	Tyrosine
Tz	Tetrazine

Chapter 1 INTRODUCTION

1.1 Positron Emission Tomography

Positron Emission Tomography (PET) is a non-invasive molecular imaging technique that allows the visualization, characterization and measurement of biological process. PET requires a probe that consists of positron emitting radionuclide and a targeting moiety that specifically participates in the targeting biological process. Once the tracer is administered to the subject, the targeting moiety mainly contributes to the biodistribution of the tracer while the imaging is made possible by the special property of positrons. The emitted positron tends to undergo annihilation when collides with a negatively charged electron nearby. This annihilation will produce two 511 keV γ-rays that are 180 degree apart and these γ-rays will be detected by the ring shaped scintillation detectors in a PET scanner. A coincident signal is recorded if the detectors achieve two γ-rays simultaneously and this signal is further converted to visible light and electrical current by photomultiplier tubes. The coincident events are then reconstructed into 3-dimensional image which represent the spatial distribution of the radionuclide in the subject.

Due to the high energy of the γ-rays produced by the annihilation, there is minimum penetration depth limitation in human bodies, which is one of the advantages of PET over other imaging modalities such as optical imaging. Furthermore, the high specific activity of PET tracers and high sensitivity of the γ-ray detection enables the picomolar sensitivity of PET imaging. With trace amount of PET tracer injected, we could evaluate their biological functions without affecting the natural system. Additionally, PET is a quantitative imaging modality that is capable of measuring the PET tracer concentration in certain regions with high accuracy. When combined with other anatomical imaging modalities such as computed tomography (CT), regions of interests (ROIs) can be drawn on PET images to obtain quantitative data. These data can be further recorded along with time to measure the changes of PET tracer concentration using dynamic scans and can be used as an index to measure the radiation exposure to patients(*1-3*). Moreover, enzyme activity, metabolic rate and perfusions can also be quantified by analyzing the kinetics of PET imaging data (*4-6*).

1.2 Radionuclide Selection

Since the radionuclides are the source of the PET imaging signal, the selection of radionuclide is important and highly affected by their physical and chemical properties and the availability of the radionuclides (*2,7*). Some of the commonly used radionuclides in PET are shown in Table 1.1.

Table 1.1 Commonly used radionuclides in PET

Radionuclide	Half-life	β^+ decay %	E_{max} ($\beta^{+)}$/MeV
^{11}C	20.4min	99.8	0.96
^{18}F	109min	96.7	0.63
^{15}O	2.1min	99.9	1.7
^{13}N	9.97min	99.8	1.2
^{66}Ga	9.5h	56	4.2
^{68}Ga	67.6min	89	1.9
^{62}Cu	9.8min	98	2.9
^{64}Cu	12.7h	17.4	0.65
^{124}I	4.17d	23	2.1

^{76}Br	16.2h	54.7	3.9
^{86}Y	14.7h	31.9	3.1
^{94m}Tc	52min	70.2	2.4
^{52}Fe	8.2h	57	0.80

As shown in Table 1.1, the half-life of these radionuclides ranges from a few minutes to several days. The criteria for choosing the suitable radionuclides is based on the radiolabeling procedure, biological half-life of the ligand and the transportation time from labeling site to imaging site. For example, if it requires a lengthy procedure to synthesize the tracer or the cyclotron for radionuclide production is not on imaging site, it may not be possible to use radionuclides with short half-life such as ^{11}C. In some extreme conditions like ^{15}O or ^{13}N with very short half-life, the radionuclides shall be used right after production from the cyclotron or only after instant but high yield synthesis. Additionally, the biological half-life of targeting moiety is an important factor for the selection of suitable radionuclides. Long half-life isotopes such as ^{64}Cu or ^{89}Zr are better suited for radiolabeling of antibodies since it may take hours or days for antibodies to accumulate in targeting sites and achieve good target to background concentration ratio. However, this may induce high doses of radiation exposure. For molecules with relative lower molecular sizes, as the time required to get receptor binding equilibrium of these molecules is within a few minutes or hours, ^{18}F or ^{11}C are more suitable.

Other than physical half-life, the positron energy and abundance are also two important indexes. The positron abundance represents the percentage of the decay in positron modes, which is related to how much agent we need to inject in PET scan. The positron energy determines the distance that positron could travel after decay, which will directly affect the resolution of the images acquired. For radionuclides with high positron energy such as ^{68}Ga or ^{124}I, the large positron range will lead to relatively low resolution. Some other factors including chemical incorporation condition and specific activity shall be taken into consideration as well when choosing the radionuclides. In the following chapters, we will mainly focus on the incorporation of ^{18}F to biomolecules since it has high positron abundance and relatively low positron energy. More importantly, the 109min half-life is clinical attractive since it allows reasonable synthesis length and transportation time while avoids high radiation exposure towards patient.

1.3 Radiopharmaceuticals in Clinical and Translational Use

In addition to selecting suitable radionuclides, the application of PET highly depends on the availability of radiopharmaceuticals. In general, PET tracers fall into two categories namely "**Metabolism Related**" and "**Receptor Related**". Some clinical used PET tracers or those under development are listed below as representative examples.

1.3.1 Metabolism Related PET Probes

Upregulated metabolism rate has been observed in many cancers and inflammation sites. ^{18}F labeled glucose analog ^{18}F-fluorodeoxyglucose (^{18}F-FDG) can reflect the glycolysis level thus further represents the metabolism of tissues (*8*). After being taken up by the cell, ^{18}F-FDG will undergo phosphorylation and form ^{18}F-FDG-6-phophate like normal glucose. However, due to the substitution of the hydroxyl group at the C-2 position by ^{18}F, further glycolysis is prevented and the molecule is trapped inside the cell before radioactive decay. Different from measuring the metabolism rate, monitoring the DNA synthesis is another way for tumor detection. ^{18}F-fluorothymidine (^{18}F-FLT) is one of a promising PET agent for this purpose. ^{18}F-FLT is phosphorylated to 3'-fluorothymidine monophosphate by thymidine kinase 1 after entering the cell. The phosphorylated product is further accumulated in the cell due to the lack of 3'-hydroxy group (*9*).

Hypoxia is another factor found in many tumors and is a sign of recurrence or metastasis (*10*). It is also a well-established index to evaluate the resistance to systematic cancer therapies (*11,12*). Generally, hypoxia imaging PET agents undergo reduction after entering the cells and release radicals. In the presence of sufficient O_2, this process is reversible and the PET agents are free to leave the cells. However, in hypoxia conditions, this process is irreversible and the radicals will bind to intracellular macromolecules and trapped in the cells. Examples of hypoxia PET imaging agents include ^{18}F-fluoromisonidasole (^{18}F-FMISO) and Copper(II)-diacetyl-bis(N4-methylthiosemicarbazone) (Cu-ATSM).

1.3.2 Receptor Related PET Probes

The second category of PET agents is based on target receptor system. In order to evaluate the target expression profile, the corresponding ligands can be radiolabeled, which will accumulate in areas with receptor expression. Representative examples are listed below. Somatostatin receptors (SSTR) are a group of G protein-coupled transmembrane receptors that can be internalized after binding to certain specific ligands (*13*). Among them, SSTR2 and SSTR5 are overexpressed in many types of tumors including breast cancer and neuroendocrine tumors (*14,15*). Due to the heterogeneity of the SSTR expression in tumors, molecular imaging targeting SSTR can be a useful tool to evaluate the SSTR expression in the whole picture. Several octreotide (a peptide that mimics the nature somatostatin) analogues are radiolabeled with ^{68}Ga via DOTA chelation to form PET tracers. ^{68}Ga-DOTATOC and ^{68}Ga-DOTATATE are two widely used candidate and both of them show uptake proportional to SSTR expression (*16,17*). Kratochwil etc used ^{68}Ga-DOTATOC to predict the response to peptide receptor radionuclide therapy in neuroendocrine tumor metastasis while Ezziddin and coworkers chose the same PET tracer to compare with the tumor dose when conducting radionuclide therapy using ^{177}Lu-DOTATATE (*18,19*). All these studies showed significant correlation between tumor uptake of the PET tracer and the tumor dosimetry demonstrating the value of targeted PET imaging of somatostatin receptors.

Estrogen receptors are proteins found inside the cells that play key roles in cell growth, proliferation and differentiation (*20*). They have been chosen as target for therapy and imaging in various kinds of cancers such as breast cancer, endometrial and ovarian cancer (*21-23*). An ^{18}F labeled PET tracer ^{18}F-Fluoroestradiol (^{18}F-FES) has been extensively studied to evaluate the estrogen receptor expression in breast cancer and showed high correlation between the tumor uptake and biopsy results (*24,25*). Additionally, the uptake of ^{18}F-FES also showed predictive value in the response to endocrine therapy which makes it a useful tool for customized cancer therapy (*26*).

Receptor tyrosine kinases are a family of cell surface receptors that show high affinity to growth factors, cytokines and hormones. They have attracted great attention in oncology since many of them are approved to be overexpressed in different cancers and some of their inhibitors were chosen as PET imaging probes and therapeutic drugs (*27*). We will mainly discuss the epidermal growth factor receptor (EGFR) and human epidermal growth factor receptor 2 (HER2) which are two widely used biomarkers in cancer imaging. One of the major categories of PET tracers used to image these tyrosine kinases is radiolabeled drugs and analogues. PET imaging of these compounds not only provides information about the biomarker expression level but also the drug accumulation in the tumor, which further helps in the design of therapy plans. Several EGFR targeted drugs such as erlotinib and geftinib have been radiolabeled with either ^{11}C or ^{18}F for PET probe construction and evaluated in animal models (*28-30*). Among them, ^{11}C-erlotinib was tested in non-small cell lung cancer patients to identify the tumor accumulation of erlotinib and was demonstrated to be predictive to erlotinib therapy response (*31*). The second category of receptors tyrosine kinases targeted PET tracer is radiolabeled antibodies. Due to the slow kinetics of antibodies binding to targeting sites, antibodies are usually labeled with radionuclides with relatively long half-life such as ^{64}Cu and ^{89}Zr via chelation method. Several clinical studies were performed using ^{64}Cu/^{89}Zr-DOTA-trastuzumab to detect both primary and metastatic breast cancer lesions and showed reasonable tumor uptake (*32-34*). EGFR targeted antibody cetuximab was also labeled with either ^{64}Cu or ^{89}Zr and evaluated in human malignant mesothelioma tumors for EGFR mapping (*35-37*).

Angiogenesis also plays important roles in progression of aggressive tumors and many drugs that inhibit this process are being used in cancer therapies. PET imaging of angiogenesis thus provides vital information on the response of such drugs in patients. One biomarker of angiogenesis is the integrin $\alpha_v\beta_3$, which is a cell surface receptor that allows the signal transmission between the cells and extracellular matrix and contributes to the endothelial cell migration (*38*). RGD peptides show high binding affinity to integrin $\alpha_v\beta_3$ and have been extensively explored in constructing PET tracers. Examples with clinical data such as ^{68}Ga labeled ^{68}Ga-NOTA-RGD, ^{18}F labeled RGD dimer ^{18}F-FPRGD2 and ^{18}F-alfatide showed considerable tumor uptake in lung cancer and renal cancer patients with reasonable target to background contrast (*39-41*).

1.4 Challenges in PET Tracer Construction

As we discussed above, PET imaging is a useful tool in various aspects and PET agent plays critical roles in order to accurately monitor the biological processes. A PET tracer can be constructed by conjugating radionuclides to targeting motif. Although ^{18}F is the most broadly used in PET isotope due to its high positron efficiency, low positron energy and clinically attractive half-life, **one major challenge in PET probe construction is the synthesis of ^{18}F labeled high-molecular-weight biomolecules with high specific activity**. Due to the slow rates for conventional conjugation chemistry, a large excess of macrobiomolecules are often required to obtain high yield. Since the unlabeled macrobiomolecules cannot be separated from the radiolabeled ones, the specific activity of the final tracer is low.

As shown in Table 1.2, one important factor for incorporation of ^{18}F into biomolecules at low concentrations is the reaction kinetic. Fast and novel labeling methods in ^{18}F-radiochemistry are therefore necessary. **Since the tetrazine-*trans*-cyclooctene (TTCO) ligation shows extremely fast reaction kinetic, my dissertation focuses on the development of a platform for fast and efficient ^{18}F labeling of biomolecules with high specific activity. In this dissertation, the TTCO ligation systems are first subjected to ^{18}F labeling to demonstrate the feasibility in radiochemistry. Then the systems are applied to several types of biomolecules for PET probes construction and the probes are evaluated both in vitro and in vivo. Additionally, the potential of using the TTCO ligation for pre-targeting imaging strategy is also explored. I believe personalized medicine will be the trend for future therapeutic service and various PET probes will be needed and developed as supporting tools. The TTCO ligation system can serve as a general platform for customized PET probes construction and be tailored to different applications.**

Table 1.2 Relationship between reaction rate constant and reaction time if both reactants are at 1µM concentration

k (L/(M•s))	$t_{1/2}$
10^{6}	**1 sec**
10^{4}	**1.7 min**
10^{2}	**2.8 h**
1	**12 days**
10^{-2}	**3 years**

REFERENCES

1. Escalona S, Blasco JA, Reza MM, Andradas E, Gómez N. A systematic review of FDG-PET in breast cancer. *Medical Oncology.* 2010;27:114-129.
2. Shoghi K. Quantitative small animal PET. *The Quarterly Journal of Nuclear Medicine and Molecular Imaging.* 2009;53:365-373.
3. West CML, Jones T, Price P. The potential of positron-emission tomography to study anticancer-drug resistance. *Nature Reviews Cancer.* 2004;4:457.
4. Kumakura Y, Cumming P. PET Studies of Cerebral Levodopa Metabolism: A Review of Clinical Findings and Modeling Approaches. *The Neuroscientist.* 2009;15:635-650.
5. Morris ED, Endres CJ, Schmidt KC, Christian BT, Muzic RF, Fisher RE. CHAPTER 23 - Kinetic Modeling in Positron Emission Tomography. In: Wernick MN, Aarsvold JN, eds. *Emission Tomography*. San Diego: Academic Press; 2004:499-540.
6. Smith MF. Advances in rubidium PET and integrated imaging with CT angiography. *Current Cardiology Reports.* 2008;10:135-141.
7. Serdons K, Verbruggen A, Bormans GM. Developing new molecular imaging probes for PET. *Methods.* 2009;48:104-111.
8. Bustamante E, Pedersen PL. High aerobic glycolysis of rat hepatoma cells in culture: role of mitochondrial hexokinase. *Proceedings of the National Academy of Sciences of the United States of America.* 1977;74:3735-3739.
9. Wagner M, Seitz U, Buck A, et al. 3′-[^{18}F]Fluoro-3′-Deoxythymidine ([^{18}F]-FLT) as Positron Emission Tomography Tracer for Imaging Proliferation in a Murine B-Cell Lymphoma Model and in the Human Disease. *Cancer Research.* 2003;63:2681.
10. Brown JM. The Hypoxic Cell. *Cancer Research.* 1999;59:5863.
11. Graeber TG, Osmanian C, Jacks T, et al. Hypoxia-mediated selection of cells with diminished apoptotic potential in solid tumours. *Nature.* 1996;379:88-91.
12. Höckel M, Schlenger K, Aral B, Mitze M, Schäffer U, Vaupel P. Association between Tumor Hypoxia and Malignant Progression in Advanced Cancer of the Uterine Cervix. *Cancer Research.* 1996;56:4509.
13. Cescato R, Schulz S, Waser B, et al. Internalization of SST2, SST3, and SST5 Receptors: Effects of Somatostatin Agonists and Antagonists. *Journal of Nuclear Medicine.* 2006;47:502-511.

14. Frati A, Rouzier R, Lesieur B, et al. Expression of Somatostatin Type-2 and -4 Receptor and Correlation with Histological Type in Breast Cancer. *Anticancer Research.* 2014;34:3997-4003.

15. Herder WWd, Hofland LJ, Lely AJvd, Lamberts SWJ. Somatostatin receptors in gastroentero-pancreatic neuroendocrine tumours. *Endocrine-related cancer Endocr Relat Cancer Endocr Relat Cancer.* 2003;10:451-458.

16. Kaemmerer D, Peter L, Lupp A, et al. Molecular imaging with ^{68}Ga-SSTR PET/CT and correlation to immunohistochemistry of somatostatin receptors in neuroendocrine tumours. *European Journal of Nuclear Medicine and Molecular Imaging.* 2011;38:1659.

17. Miederer M, Seidl S, Buck A, et al. Correlation of immunohistopathological expression of somatostatin receptor 2 with standardised uptake values in ^{68}Ga-DOTATOC PET/CT. *European Journal of Nuclear Medicine and Molecular Imaging.* 2009;36:48-52.

18. Ezziddin S, Lohmar J, Yong-Hing CJ, et al. Does the Pretherapeutic Tumor SUV in ^{68}Ga DOTATOC PET Predict the Absorbed Dose of ^{177}Lu Octreotate? *Clinical Nuclear Medicine.* 2012;37.

19. Kratochwil C, Stefanova M, Mavriopoulou E, et al. SUV of [^{68}Ga]DOTATOC-PET/CT Predicts Response Probability of PRRT in Neuroendocrine Tumors. *Molecular Imaging and Biology.* 2015;17:313-318.

20. Shao W, Brown M. Advances in estrogen receptor biology: prospects for improvements in targeted breast cancer therapy. *Breast Cancer Research.* 2003;6:39.

21. Shanle EK, Xu W. Selectively targeting estrogen receptors for cancer treatment. *Advanced Drug Delivery Reviews.* 2010;62:1265-1276.

22. Tsujikawa T, Yoshida Y, Maeda H, et al. Oestrogen-related tumour phenotype: positron emission tomography characterisation with ^{18}F-FDG and ^{18}F-FES. *The British Journal of Radiology.* 2012;85:1020-1024.

23. Yoshida Y, Kurokawa T, Tsujikawa T, Okazawa H, Kotsuji F. Positron emission tomography in ovarian cancer: ^{18}F-deoxy-glucose and 16α-^{18}F-fluoro-17β-estradiol PET. *Journal of Ovarian Research.* 2009;2:7.

24. Amir E, Clemons M, Purdie CA, et al. Tissue confirmation of disease recurrence in breast cancer patients: Pooled analysis of multi-centre, multi-disciplinary prospective studies. *Cancer Treatment Reviews.* 2012;38:708-714.

25. van Kruchten M, de Vries EGE, Brown M, et al. PET imaging of oestrogen receptors in patients with breast cancer. *The Lancet Oncology.* 2013;14:e465-e475.

26. Dehdashti F, Mortimer JE, Trinkaus K, et al. PET-based estradiol challenge as a predictive biomarker of response to endocrine therapy in women with estrogen-receptor-positive breast cancer. *Breast Cancer Research and Treatment.* 2009;113:509-517.

27. Mammatas LH, Verheul HMW, Hendrikse NH, Yaqub M, Lammertsma AA, Menke-van der Houven van Oordt CW. Molecular imaging of targeted therapies with positron emission tomography: the visualization of personalized cancer care. *Cellular Oncology.* 2015;38:49-64.

28. Bahce I, Smit EF, Lubberink M, et al. Development of [^{11}C]erlotinib Positron Emission Tomography for *In vivo* Evaluation of EGF Receptor Mutational Status. *Clinical Cancer Research.* 2013;19:183.

29. Su H, Seimbille Y, Ferl GZ, et al. Evaluation of [^{18}F]gefitinib as a molecular imaging probe for the assessment of the epidermal growth factor receptor status in malignant tumors. *European Journal of Nuclear Medicine and Molecular Imaging.* 2008;35:1089-1099.

30. Zhang M-R, Kumata K, Hatori A, et al. [^{11}C]Gefitinib ([^{11}C]Iressa): Radiosynthesis, In Vitro Uptake, and In Vivo Imaging of Intact Murine Fibrosarcoma. *Molecular Imaging and Biology.* 2010;12:181-191.

31. Memon AA, Weber B, Winterdahl M, et al. PET imaging of patients with non-small cell lung cancer employing an EGF receptor targeting drug as tracer. *British Journal Of Cancer.* 2011;105:1850.

32. Dijkers EC, Oude Munnink TH, Kosterink JG, et al. Biodistribution of ^{89}Zr-trastuzumab and PET Imaging of HER2-Positive Lesions in Patients With Metastatic Breast Cancer. *Clinical Pharmacology & Therapeutics.* 2010;87:586-592.

33. Mortimer JE, Bading JR, Colcher DM, et al. Functional Imaging of Human Epidermal Growth Factor Receptor 2–Positive Metastatic Breast Cancer Using ^{64}Cu-DOTA-Trastuzumab PET. *Journal of Nuclear Medicine.* 2014;55:23-29.

34. Tamura K, Kurihara H, Yonemori K, et al. ^{64}Cu-DOTA-Trastuzumab PET Imaging in Patients with HER2-Positive Breast Cancer. *Journal of Nuclear Medicine.* 2013;54:1869-1875.

35. Achmad A, Hanaoka H, Yoshioka H, et al. Predicting cetuximab accumulation in KRAS wild-type and KRAS mutant colorectal cancer using ^{64}Cu-labeled cetuximab positron emission tomography. *Cancer Science.* 2012;103:600-605.

36. Nayak TK, Garmestani K, Milenic DE, Baidoo KE, Brechbiel MW. HER1-targeted ^{86}Y-panitumumab possesses superior targeting characteristics than ^{86}Y-cetuximab for PET imaging of human malignant mesothelioma tumors xenografts. *PloS one.* 2011;6:e18198-e18198.

37. Perk LR, Visser GWM, Vosjan MJWD, et al. ^{89}Zr as a PET Surrogate Radioisotope for Scouting Biodistribution of the Therapeutic Radiometals ^{90}Y and ^{177}Lu in Tumor-Bearing Nude Mice After Coupling to the Internalizing Antibody Cetuximab. *Journal of Nuclear Medicine.* 2005;46:1898-1906.

38. Brooks PC, Clark RA, Cheresh DA. Requirement of vascular integrin $\alpha_v\beta_3$ for angiogenesis. *Science.* 1994;264:569.

39. Kim JH, Lee JS, Kang KW, et al. Whole-Body Distribution and Radiation Dosimetry of ^{68}Ga-NOTA-RGD, a Positron Emission Tomography Agent for Angiogenesis Imaging. *Cancer Biotherapy and Radiopharmaceuticals.* 2011;27:65-71.

40. Wan W, Guo N, Pan D, et al. First Experience of ^{18}F-Alfatide in Lung Cancer Patients Using a New Lyophilized Kit for Rapid Radiofluorination. *Journal of Nuclear Medicine.* 2013;54:691-698.

41. Withofs N, Signolle N, Somja J, et al. ^{18}F-FPRGD2 PET/CT Imaging of Integrin $\alpha_v\beta_3$ in Renal Carcinomas: Correlation with Histopathology. *Journal of Nuclear Medicine.* 2015;56:361-364.

Chapter 2 CURRENT STRATEGIES FOR ^{18}F LABELING OF BIOMOLECULES

2.1 Overview

PET provides functional information on molecular level by tracking the interaction between PET probes and biomarkers. In order to visualize such interaction, PET probes generally include both radionuclides and biomolecules such as antibodies, proteins or peptides with specific bindings to biomarkers of interest. Since ^{18}F is the most frequently used radionuclide for PET imaging, much effort has been devoted into exploring the methods to introduce ^{18}F to different types of biomolecules in the past few decades. **In this chapter, we highlight the major breakthroughs of ^{18}F labeling of biomolecules and classify them into two categories: 1) direct labeling methods in which ^{18}F is directed attached to the biomolecules via C-F, B-F, Si-F bonds or chelation of AlF; 2) indirect labeling methods where an ^{18}F labeled prosthetic group is synthesized and further conjugates to biomolecules**.

2.2 Direct Labeling Methods

In the direct labeling methods, the introduction of ^{18}F into biomolecules usually occurs in the last or second last step of the radiolabeling, which can minimize the synthetic time and simplify the synthetic steps. This is important since the relative short half-life of ^{18}F limits the time frame and available methods for biomolecules ^{18}F labeling.

2.2.1 ^{18}F Labeling via C-F Bond

Since most of the biomolecules possess carbon based backbones, the most straightforward strategy for ^{18}F labeling of these biomolecules is to create a carbon-fluorine bond. For aromatic biomolecules, one common method to introduce ^{18}F is nucleophilic aromatic substitution. In this case, a suitable leaving group is required to be modified to the biomolecules before radiolabeling. As shown in Scheme 2.1A, trimethylammonium and nitro group are two major leaving groups that were studied. For example, Becaud and coworkers synthesized a biomolecule precursor containing trimethylammonium group and successfully radiolabeled with ^{18}F at yield up to 90% (*1*). Nitro group has also been explored by Jacobsen etc who prepared nitro modified RGD peptide and the nitro group was substituted by ^{18}F at yield ranges from 9% to 19% under mild condition (*2*). Although these methods were proved to be feasible to incorporate ^{18}F into biomolecules, both of them required relatively large amounts of biomolecules as substrate and potentially decreased the specific activity of the final tracer.

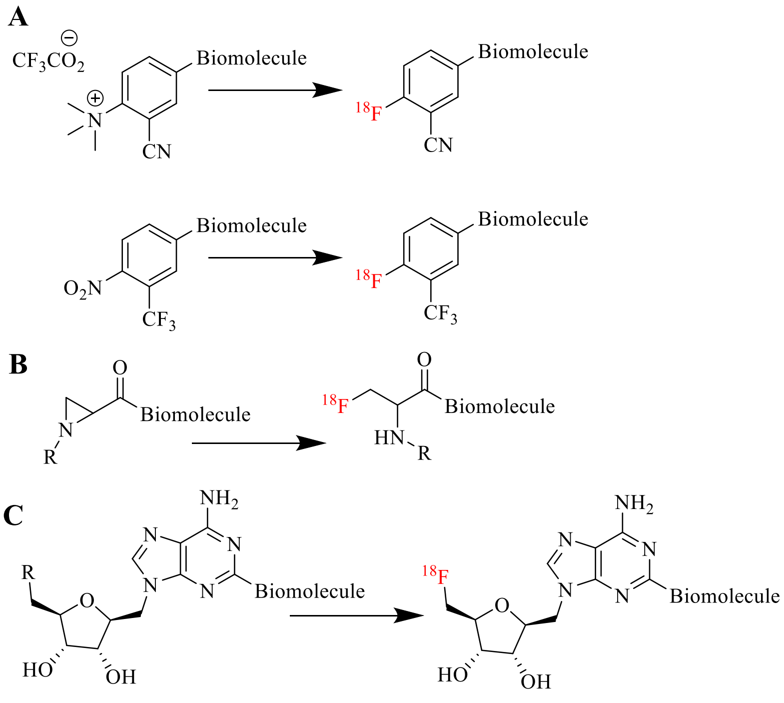

Scheme 2.1 Direct ^{18}F labeling methods via C-F bond

Other than nucleophilic aromatic substitution reaction, methods regarding aliphatic C-F bond formation have also been explored. As shown in Scheme 2.1B, a ring opening reaction of activated aziridines was introduced by Roehn's group and several substrates were screened to optimize the labeling condition and suitable activating group (*3*). The radiochemical yield was reported by be as high as 87%. However, this method required polar organic solvents and high temperature which limits the application in biomolecules such as proteins or antibodies.

Taking the advantage of some natural fluorination involved reaction is another strategy to form carbon-fluorine bond in radiochemistry. Fluorinase enzyme can catalyze the reaction between fluoride ion and certain substrates and has been utilized in ^{18}F labeling by conjugating the corresponding substrates to biomolecule of interest (*4,5*). This method could obtain the product at around 12% yield within 30min but the narrow scope of substrates available was its main disadvantage.

2.2.2 ^{18}F Labeling via B-F Bond

Boron-fluorine bond is brought into attention in ^{18}F fluorination due to its high bond dissociation energy. The first application was reported by Perrin and coworkers who mixed arylboronic ester with aqueous carrier added ^{18}F and successfully obtained ^{18}F labeled compound with moderate yield (Scheme 2.2A)(*6*). This method was further explored in several studies in which the biomolecules were modified with boronic ester to allow ^{18}F incorporation (*7,8*).

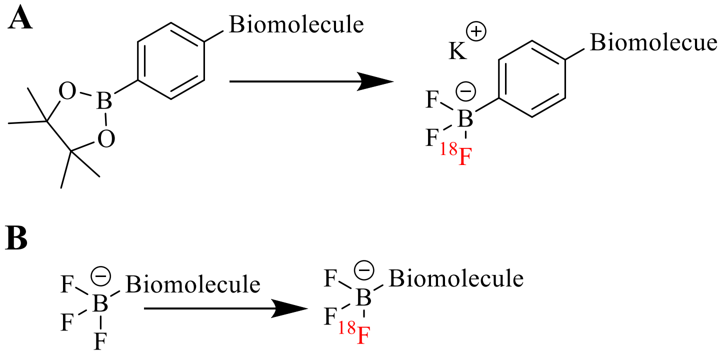

Scheme 2.2 Direct ^{18}F labeling methods via B-F bond

Additionally, boron-fluorine bond can also be formed prior to the radiolabeling and incorporate the ^{18}F through isotope exchange method afterwards (Scheme 2.2B). This mechanism allowed the kit-like ^{18}F labeling strategy and was demonstrated by using trifluoroborate modified biomolecules (*9*). An advanced method based on this mechanism was also reported: Perrin's group used ^{18}F without drying to radiolabel a zwitterionic organotrifluoroborate analogue and was able to obtain reasonable yield (*10,11*). This method was soon adapted to construct several PET agents and showed promising tumor uptake (*12*). The outstanding property of this method is that it avoids the azeotropic drying of ^{18}F and saved much time. However, acidic condition is needed during the labeling process and defluorination may happen in some cases.

2.2.3 ^{18}F Labeling via Si-F Bond

The third category of direct ^{18}F labeling is forming Si-F bond through either substitution or isotope exchange. The substitution method was initially reported by Ting's team who radiofluorinated the triethoxysilane modified biomolecule with high yield (Scheme 2.3A) (*6*). Although the resulting PET tracer showed moderate stability in water, which already showed great improvement compared with the first generation ^{18}F-fluorotrimethylsilane (*13*), it was still not stable enough for most PET applications.

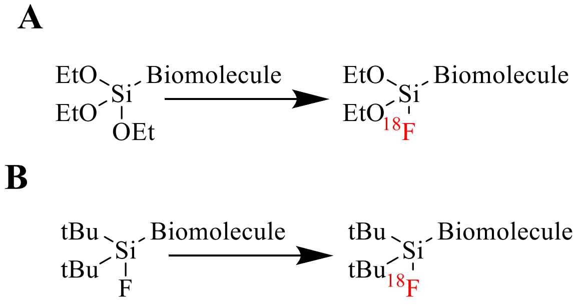

Scheme 2.3 Direct ^{18}F labeling methods via Si-F bond

To solve this problem, an isotope exchange method was developed using di-*tert*-butyl fluorosilane as precursor (Scheme 2.3B). This evolved method allowed the construction of PET tracer with 50~90% yield and compatible with aqueous conditions. Mishra etc and Niedermoser etc successfully applied this strategy to radiolabeled ligands that could specifically target to serotonin receptors and somatostatin receptors, respectively (*14,15*). However, this method shares the disadvantage with all of the isotope exchange methods that may results in low specific activity due to the introduction of ^{19}F.

2.2.4 ^{18}F Labeling via AlF chelation

Most of the ^{18}F labeling protocols required lengthy procedures which usually start with the trap/release and azeotropic drying of ^{18}F in complicated modules. These steps involve multiple synthetic procedures and high-performance liquid chromatography (HPLC) purification, which may eventually take 1 to 2 hours. A straightforward ^{18}F labeling approach was developed according to the fact that the chelator 1,4,7-triazacyclononane-1,4,7-triacetic acid (NOTA) could form stable chelation complex with aluminum fluoride under certain conditions (Scheme 2.4) (*16*). Due to the excellent binding affinity of fluoride to Al, the ^{18}F-metal complex is rather stable in vivo, which offers an efficient way to generate ^{18}F labeled biomolecule PET tracer effectively.

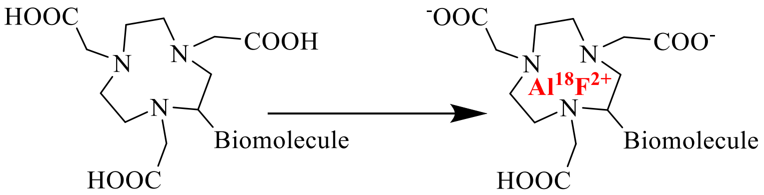

Scheme 2.4 Direct ^{18}F labeling method via AlF chelation

This approach has broadened the possibility of ^{18}F labeling of biomolecules and numerous studies using this method was reported. For instance, RGD peptide was radiolabeled with such strategy with around 25% yield, NTR targeted ligand NT20.3 was ^{18}F fluorinated and evaluated in pancreatic cancer model while octreotide analogue was reported to be radiolabeled under different conditions to investigate the effects of temperature and pH (*17-19*). Although the chelation chemistry shows great efficiency and allows the synthesis without HPLC purification, it requires high temperature and acidic condition which may be harsh to some of the biomolecules.

2.3 Indirect Labeling Methods

As we mentioned before, most of the direct labeling methods are performed under harsh conditions that biomolecules can be denatured or lose binding affinity during labeling process. One alternative way to radiolabel the biomolecules with ^{18}F is through indirect labeling method. Generally, an organic prosthetic group is first ^{18}F fluorinated under the non-physiological conditions. Then the purified ^{18}F labeled prosthetic group is conjugated to biomolecules under mild condition.

2.3.1 ^{18}F Labeling using amine selective prosthetic groups

Prosthetic groups are molecules that are radiolabeled with radionuclides while retaining another functional group to be attached to biomolecules. Since most of the biomolecules (such as peptide, proteins and antibodies) consist of amino acids, free amines are abundant and are commonly chosen as labeling sites as long as they do not participate in binding with the target. So several prosthetic groups were designed with a functional group that was selectively reactive to amine. The most widely used amine selective prosthetic group is ^{18}F-*N*-succinimidyl-4-fluorobenzoate (^{18}F-SFB). ^{18}F-SFB conjugates with the biomolecules by acylation of the free amines on the biomolecules. The first application of ^{18}F-SFB was developed by Dr. Zalutsky and Dr. Vaidyanathan who radiolabeled the ^{18}F-SFB at 25% yield and conjugated it to a monoclonal antibody fragment to obtain the final agent in 40~60% yield (*20*). Afterwards, more studies were conducted to increase the labeling yield and optimize the synthesis procedures (*21,22*). As shown in Scheme 2.5A, other prosthetic groups that can react with the amines on biomolecules via acylation were developed, including ^{18}F-6-fluoronicotinic acid tetrafluorophenyl ester (^{18}F-Py-

TFP) and ^{18}F-4-nitrophenyl-2-fluoropropionate (^{18}F-NFP). ^{18}F-Py-TFP has been tested in ^{18}F fluorination of RGD peptide and albumin while ^{18}F-NFP was also utilized in radiolabeling of RGD and PET imaging of $\alpha_v\beta_3$ in patients (*23*).

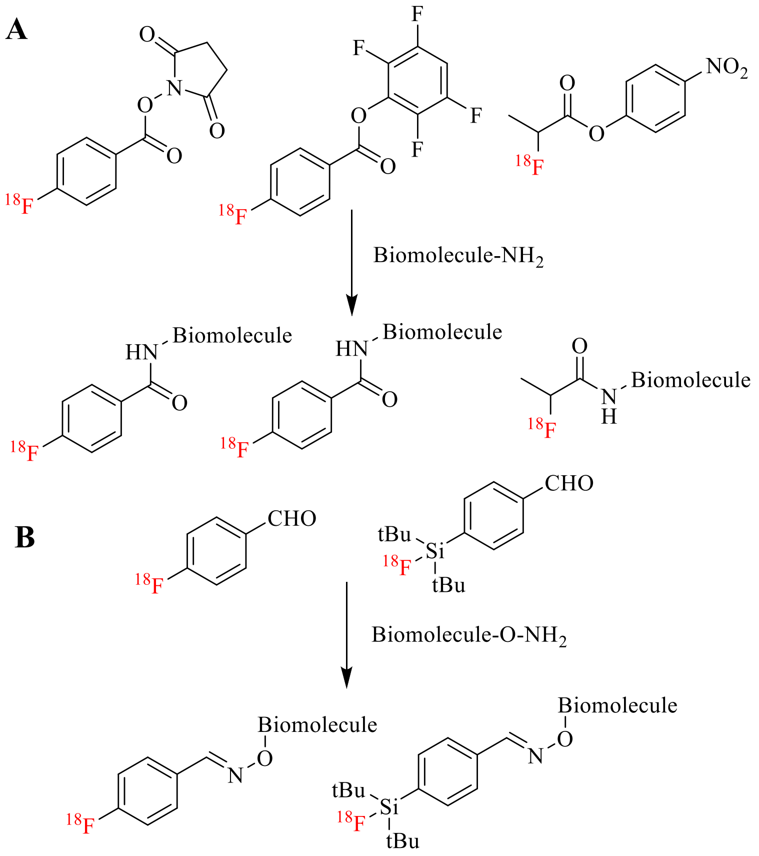

Scheme 2.5 Indirect ^{18}F labeling methods using amine selective prosthetic groups

In addition to amine acylation, oximes formation reaction is also considered when designing amine selective prosthetic groups for aminooxy-functionalized biomolecules. As shown in Scheme 2.5B, ^{18}F-4-fluorobenzaldehyde (^{18}F-FBA) and ^{18}F-*p*-(di-*tert*-butyl fluorosilyl)benzaldehyde (^{18}F-SiFA-A) are two examples that takes advantages of this reaction. Glaser and coworkers synthesized ^{18}F-FBA and conjugated to RGD peptide to yield ^{18}F labeled RGD with high specific activity (*24*). On the other hand, Schirrmacher etc radiolabeled ^{18}F-SiFA-A via isotope exchange method discussed in the previous section and further conjugated to Tyr^3-octreotate under ambient condition (*25*). Although amine selective prosthetic groups offer the possibility to radiolabel the unmodified biomolecule directly, the reaction rate is rather low and requires relative large amounts of substrates. Furthermore, the prosthetic groups will be randomly labeled on the biomolecule without site specificity. Thus, biomolecules with amine binding sites are not suitable for this labeling strategy.

2.3.2 ^{18}F Labeling using thiol selective prosthetic groups

Other than amine, thiol is another commonly seen functional group in biomolecules. Although ^{18}F-SFB showed possibility to react with thiol through acylation, more specific conjugation methods are needed to selectively react with thiol other than amine.

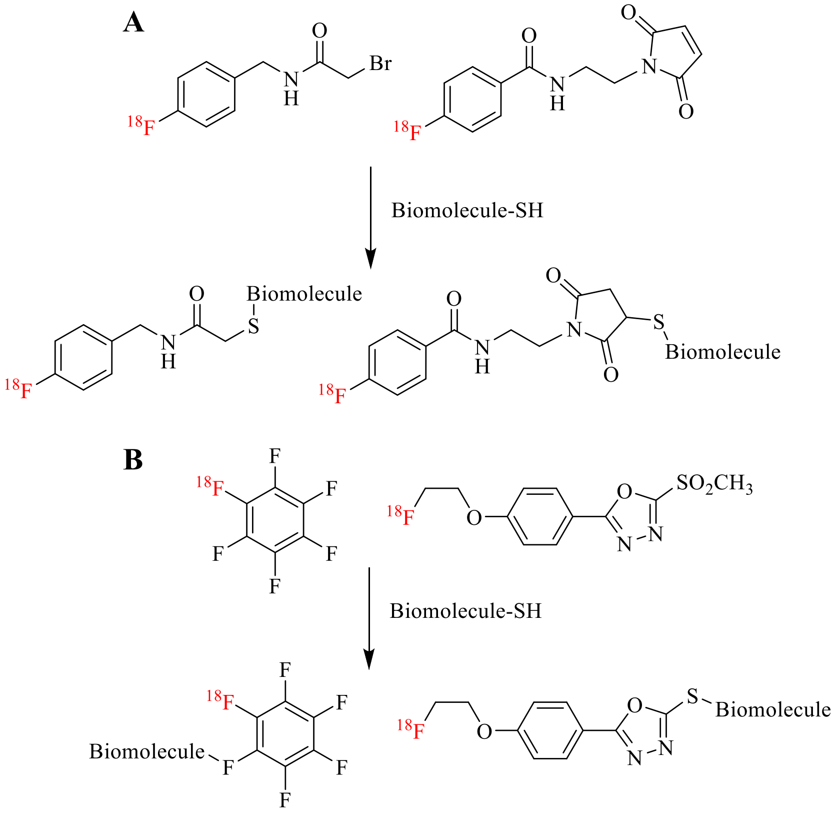

Scheme 2.6 Indirect ^{18}F labeling methods using thiol selective prosthetic groups

As shown in Scheme 2.6A, ^{18}F-*N*-(4-fluorobenzyl)-2-bromoacetamide (^{18}F-FBBA) and ^{18}F-*N*-[2-(4-fluorobenzamideo)ethyl]maleimide (^{18}F-FBEM) are two candidates that specifically react with thiol functionalized biomolecules (*26,27*). Maleimide alkylated thiol through Michael addition and was broadly used in radiolabeling of cysteine or methionine containing biomolecules. A variety of maleimide functionalized prosthetic groups were reported and conjugated to biomolecules for PET tracer construction (*28-31*). However, the maleimide-thiol bond suffers from some extent of instability under physiological conditions. Thus some more stable conjugation methods are explored and shown in Scheme 2.6B. ^{18}F-2-(4-(2-(fluoroethoxy)phenyl)-5-(methylsulfonyl)-1,3,4-oxadiazole (^{18}F-FPOS) was synthesized by Chiotellis's group and used as prosthetic group to ^{18}F fluorinate an affibody under ambient condition (*32*). The resulting PET probe showed improved stability compared with the maleimide-thiol conjugated analogue. Additionally, ^{18}F-hexafluorobenzene (^{18}F-HFB) was brought into attention by Dr. Jacobsen due to its unique structure (*33*). This prosthetic group was radiolabeled with ^{18}F via isotope exchange method and could be involved in a thiol-substitution reaction with multiply thiol containing biomolecules. This strategy enabled the synthesis of ^{18}F labeled biomolecule multimers and was indeed used to construct RGD dimer PET tracer by the same group. However, all these thiol-based labeling methods require relatively large amounts of biomolecules and may result in low specific activity.

2.3.3 ^{18}F Labeling using Cu-Catalyzed Azide-Alkyne Cycloaddition

In the past few decades, bioorthogonal reactions have become a unique tool in diverse fields including nuclear medicine. Since bioorthogonal chemistry can occur without interfering with biological process, it is highly suitable for biomolecule radiolabeling. The copper catalyzed azide-alkyne cycloaddition was introduced by Dr. Meldal and Dr. Sharpless in 2002 and soon expanded its application in radiolabeling. Different from the above mentioned prosthetic groups which are selective to certain functional groups on the biomolecule, the prosthetic group can be either the azide moiety or the alkyne moiety in this reaction while the counter part is modified to the biomolecules.

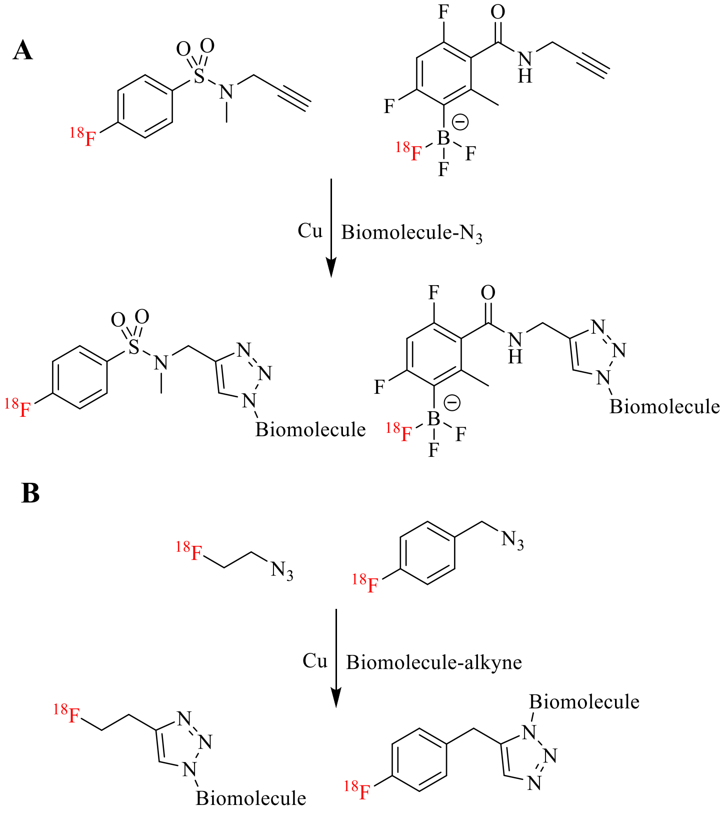

Scheme 2.7 Indirect ^{18}F labeling methods using Cu-catalyzed azide-alkyne cycloaddition

Due to the high volatility of the ^{18}F labeled aliphatic alkynes, researchers turned to radiolabel the aryl compounds with alkyne function group. The first alkyne based prosthetic group was ^{18}F-fluoro-*N*-(prop-2-ynyl)benzamide (^{18}F-FSA) (Scheme 2.7A), which was used to radiolabel several azide modified biomolecules including human serum albumin, phosphopeptide and oligonucleotide (*34,35*). Additionally, ^{18}F-4-fluoro-3-nitro-*N*-2-prop-1-ynylbenzamide (^{18}F-FNPB) was reported by Li etc as an efficient and stable prosthetic group for Cu-catalyzed azide-alkyne cycloaddition reaction. This molecule was radiolabeled in 58% yield and was utilized in peptide labeling (*36*).

While various ^{18}F labeled alkyne derivatives were developed, only a few azide derivatives were ^{18}F fluorinated. Similar to the case in alkyne, an aliphatic ^{18}F-fluoroethylazide (^{18}F-FEA) (Scheme 2.7B) was the first to be synthesized by co-distillation with acetonitrile (*37,38*). It was then subjected to radiolabel of RGD peptide but the yield was somehow low due to the interaction between ^{18}F-FEA and the copper catalyst (*39*). Additionally, the high volatility also limited its application. As shown in Scheme 2.7B, an azido aryl ^{18}F prosthetic group, ^{18}F-4-fluorobenzylazide was synthesized in reasonable yield and was used to radiolabel SiRNA derivatives and single-stranded DNA aptamers (*40-42*). Although the aryl analogue was not as volatile as the aliphatic version, the synthesis procedure is complicated requiring multiple steps or complex set ups. Overall, the Cu-catalyzed azide-alkyne cycloaddition provides a new pathway for ^{18}F labeling of biomolecules and shows improved efficiency compared with the previous discussed methods. However, some drawbacks still exist such as the involvement of copper and complicated purification procedures.

2.3.4 ^{18}F Labeling using Strain-promoted Azide-Alkyne Click Reaction

To overcome the limitation of using copper in the azide-alkyne conjugation, azide based metal-free click reactions have been developed including covalent ligation of azides to strain-promoted cycloaddition to alkynes (*43-46*). Due to the bent triple bond in the strained ring, the cyclooctyne can react with azide in the absence of copper catalyst. Similar to the copper catalyst cycloaddtion, the ^{18}F labeled prosthetic group can be either cyclooctyne or azide in this click reaction. Initially, the cyclooctyne was radiolabeled with ^{18}F-SFB to form ^{18}F-azadibenzocyclooctyne (^{18}F-ADIBO) as prosthetic group. ^{18}F-ADIBO was further coupled with azide modified peptide $A_{20}FMDV_2$ to construct $\alpha_v\beta_6$ targeting PET tracer (*47*). Additionally, our laboratory and collaborators reported the synthesis of ^{18}F-oxa-dibenzocyclooctyne (^{18}F-ODIBO)

(Scheme 2.8A), which is one of the most reactive cyclooctynes (>45 $M^{-1}s^{-1}$), and conjugated to PSMA-azide via strain-promoted azide-cyclooctyne click reaction (*48*). Similar to the ^{18}F-ADIBO, the radiochemistry worked out well but the constructed PET tracer did not show significant binding to the target. The poor pharmacokinetic property might be the result of the increased hydrophobicity introduced by the dibenzocyclooctyne moiety. To address this, our group developed a ^{18}F-bicyclo[6.1.0]nonyne (^{18}F-BCN) which was less reactive to azide but more hydrophilic compared with ^{18}F-ODIBO (Scheme 2.8A). The labeling condition was optimized and the PET tracer showed favorable tumor uptake and tumor to background ratio (*48*).

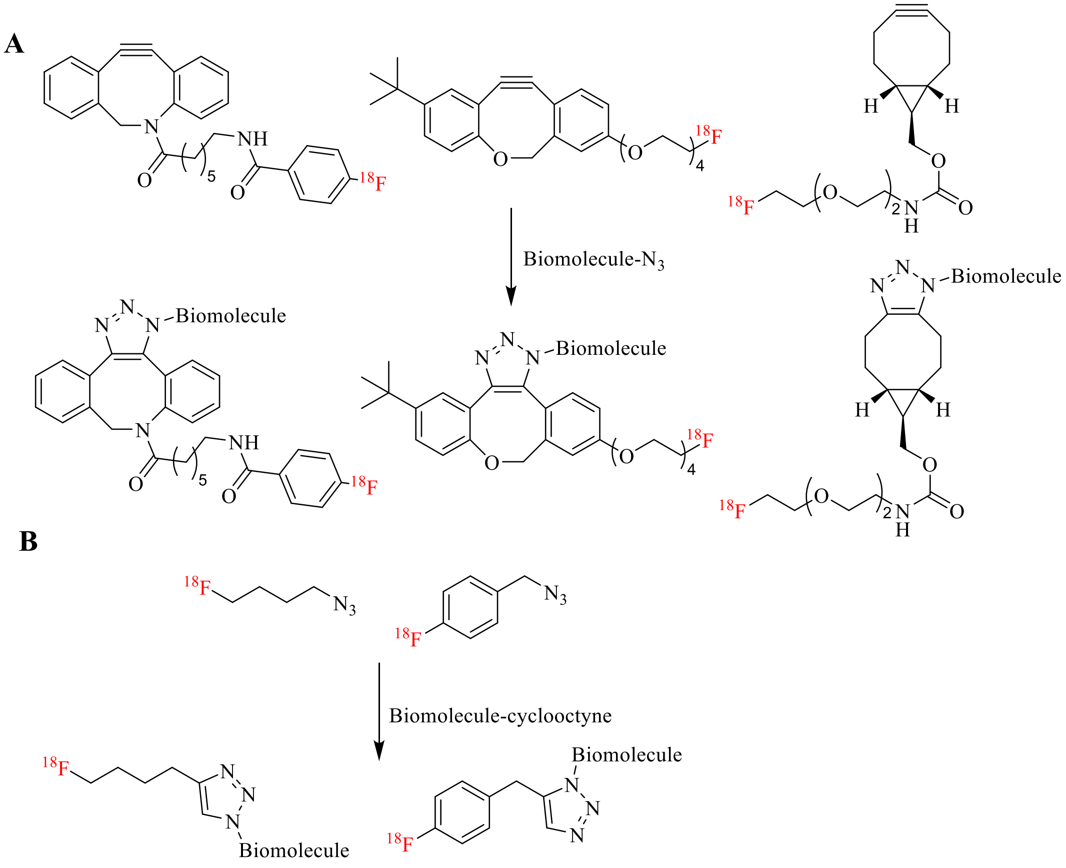

Scheme 2.8 Indirect ^{18}F labeling methods using strain-promoted azide-alkyne click reaction

Since there is not much difference in the azide moiety between the copper catalyzed cycloaddition and the strain promoted click reaction, ^{18}F labeled azide prosthetic group developed in the copper catalyzed cycloaddition could be directly used in the strain promoted click reaction. As shown in Scheme 2.8B, ^{18}F-4-fluorobenzylazide and ^{18}F-fluorobutylazide were used to label ADIBO modified bombesin derivatives (*49*).

2.3.5 ^{18}F Labeling using Staudinger Ligation

Staudinger ligation is a reaction between azide and phosphine that was first reported in 1919 (*50*). Since the reaction can occur at room temperature with high yield, it is potentially suitable for ^{18}F labeling of biomolecules. As shown in Scheme 2.9A, Pretze's group was able to radiolabel phosphine at reasonable yield, which could be readily conjugated with azide modified biomolecules. Furthermore, the previously discussed ^{18}F-FEA was used as azide prosthetic group and radiolabeled diarylphosphine modified amino acid derivatives. Although the Staudinger ligation could be carried out under biomolecule friendly condition, it suffered from low kinetics (~2.0 x 10^{-3} $M^{-1}s^{-1}$) and phosphines are oxygen sensitive (*51,52*).

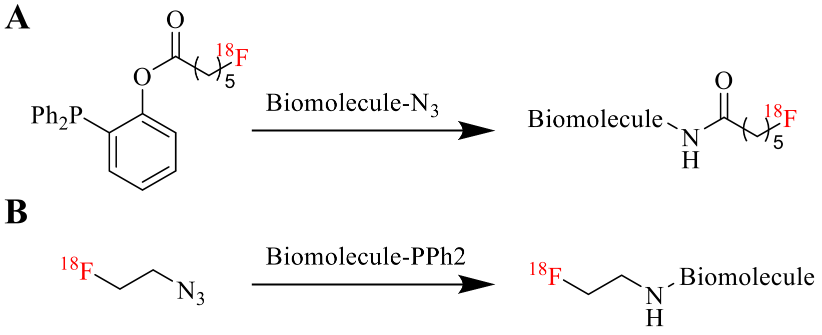

Scheme 2.9 Indirect ^{18}F labeling methods using Staudinger ligation

2.3.6 ^{18}F Labeling using Inverse Electron Demand Diels-Alder Click Reaction

Inverse electron demand Diels-Alder click reaction (IEDDA) involves the reactions between tetrazine and dienophiles such as norbornene, BCN and *trans*-cyclooctene (TCO). The IEDDA reaction can proceeds without any catalyst and under both organic and aqueous conditions. More importantly, the reaction kinetics can be as high as 3.3 x 10^6 $M^{-1}s^{-1}$ which makes it suitable for labeling with short-lived radioisotopes at dilute concentrations (*53*).

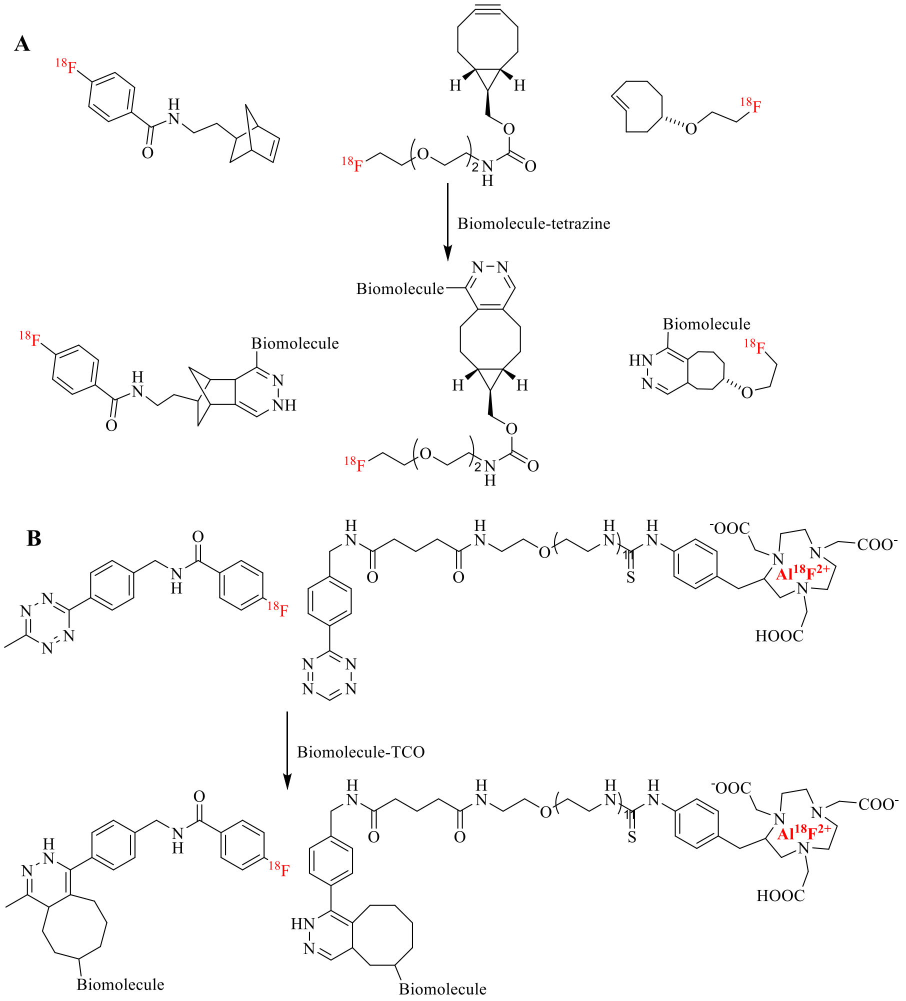

Scheme 2.10 Indirect ^{18}F labeling methods using inverse electron demand Diels-Alder click reaction

Li and coworkers synthesized ^{18}F fluorinated BCN to label tetrazine modified oligonucleotide with high yield within 3min (*54*). Although both norbornene and BCN have been used as dienophile in the reaction, *trans*-cyclooctene derivatives remained the most reactive dienophile towards tetrazine. As shown in Scheme 2.10A, our group first introduced the ^{18}F labeled *trans*-cyclooctene and applied it to the radiolabeling of dipyridyl tetrazine functionalized RGD peptide (*55,56*). In the following chapters we will discuss the details of using tetrazine *trans*-cyclooctene ligation to radiolabel biomolecules.

Furthermore, the ^{18}F labeled tetrazine moieties have also been developed. Liang's group synthesized an ^{18}F labeled tetrazine by reacting tetrazine-amine with ^{18}F-SFB (Scheme 2.10B) (*57*). The resulting prosthetic group was coupled with TCO modified anti-Class-II and anti-CD11B dimers with reasonable tumor uptake. AlF chelation strategy was also utilized to radiolabel tetrazine by Meyer and coworkers. The ^{18}F-AlF-NOTA-tetrazine was ligated to TCO bearing antibodies and the resulting tracer successfully localized the pancreatic cancer xenografts (*58*).

2.4 Limitations

In this chapter, a variety of methods have been explored for biomolecule ^{18}F-labeling. **As shown in Table 2.1, a major limitation of these labeling methods is the relatively low reaction rate constant which prevents them to ^{18}F-label large biomolecules with high specific activity. On the contrary, the TTCO ligation we proposed here has extremely fast reaction kinetic and holds the great potential for large biomolecule ^{18}F-labeling.** In the following chapters, we report the development of radiolabeling method based on TTCO ligation and explore the utilization of this reaction for PET probe construction.

Table 2.1 Reaction rate constant range for common ^{18}F-biomolecule labeling reactions

Reactions	*k* (L/(M•s))
Acyl transfer	**10^{-2}~10^{-1}**
Cyclooctyne click chemistry	**10^{-1}~10**
TTCO ligation	**10^{3}~10^{6}**

REFERENCES

1. Becaud J, Mu L, Karramkam M, et al. Direct One-Step ^{18}F-Labeling of Peptides via Nucleophilic Aromatic Substitution. *Bioconjugate Chemistry.* 2009;20:2254-2261.

2. Jacobson O, Zhu L, Ma Y, et al. Rapid and Simple One-Step F-18 Labeling of Peptides. *Bioconjugate Chemistry.* 2011;22:422-428.

3. Roehn U, Becaud J, Mu L, et al. Nucleophilic ring-opening of activated aziridines: A one-step method for labeling biomolecules with fluorine-18. *Journal of Fluorine Chemistry.* 2009;130:902-912.

4. Sun H, Yeo WL, Lim YH, et al. Directed Evolution of a Fluorinase for Improved Fluorination Efficiency with a Non-native Substrate. *Angewandte Chemie International Edition.* 2016;55:14277-14280.

5. Thompson S, Zhang Q, Onega M, et al. A Localized Tolerance in the Substrate Specificity of the Fluorinase Enzyme enables "Last-Step" ^{18}F Fluorination of a RGD Peptide under Ambient Aqueous Conditions. *Angewandte Chemie.* 2014;126:9059-9064.

6. Ting R, Adam MJ, Ruth TJ, Perrin DM. Arylfluoroborates and Alkylfluorosilicates as Potential PET Imaging Agents: High-Yielding Aqueous Biomolecular ^{18}F-Labeling. *Journal of the American Chemical Society.* 2005;127:13094-13095.

7. auf dem Keller U, Bellac CL, Li Y, et al. Novel Matrix Metalloproteinase Inhibitor [^{18}F]Marimastat-Aryltrifluoroborate as a Probe for *In vivo* Positron Emission Tomography Imaging in Cancer. *Cancer Research.* 2010;70:7562.

8. Li Y, Liu Z, Lozada J, et al. Single step ^{18}F-labeling of dimeric cycloRGD for functional PET imaging of tumors in mice. *Nuclear Medicine and Biology.* 2013;40:959-966.

9. Liu Z, Li Y, Lozada J, et al. Kit-like ^{18}F-labeling of RGD-^{19}F-Arytrifluroborate in high yield and at extraordinarily high specific activity with preliminary in vivo tumor imaging. *Nuclear Medicine and Biology.* 2013;40:841-849.

10. Liu Z, Lin K-S, Bénard F, et al. One-step ^{18}F labeling of biomolecules using organotrifluoroborates. *Nature Protocols.* 2015;10:1423.

11. Liu Z, Pourghiasian M, Radtke MA, et al. An Organotrifluoroborate for Broadly Applicable One-Step ^{18}F-Labeling. *Angewandte Chemie International Edition.* 2014;53:11876-11880.

12. Liu Z, Chen H, Chen K, et al. Boramino acid as a marker for amino acid transporters. *Science advances.* 2015;1:e1500694-e1500694.

13. Rosenthal MS, Bosch AL, Nickles RJ, Gatley SJ. Synthesis and some characteristics of no-carrier added [^{18}F]fluorotrimethylsilane. *The International Journal of Applied Radiation and Isotopes.* 1985;36:318-319.

14. Hazari PP, Schulz J, Vimont D, et al. A New SiF–Dipropargyl Glycerol Scaffold as a Versatile Prosthetic Group to Design Dimeric Radioligands: Synthesis of the [^{18}F]BMPPSiF Tracer to Image Serotonin Receptors. *ChemMedChem.* 2014;9:337-349.

15. Niedermoser S, Chin J, Wängler C, et al. In Vivo Evaluation of ^{18}F-SiFAlin–Modified TATE: A Potential Challenge for ^{68}Ga-DOTATATE, the Clinical Gold Standard for Somatostatin Receptor Imaging with PET. *Journal of Nuclear Medicine.* 2015;56:1100-1105.

16. McBride WJ, Sharkey RM, Karacay H, et al. A Novel Method of ^{18}F Radiolabeling for PET. *Journal of Nuclear Medicine.* 2009;50:991-998.

17. Guo N, Lang L, Li W, et al. Quantitative analysis and comparison study of [^{18}F]AlF-NOTA-PRGD2, [^{18}F]FPPRGD2 and [^{68}Ga]Ga-NOTA-PRGD2 using a reference tissue model. *PloS one.* 2012;7:e37506-e37506.

18. Laverman P, D'Souza CA, Eek A, et al. Optimized labeling of NOTA-conjugated octreotide with F-18. *Tumor Biology.* 2012;33:427-434.

19. Wang M, Zhang H, Wang H, et al. Development of [^{18}F]AlF-NOTA-NT as PET Agents of Neurotensin Receptor-1 Positive Pancreatic Cancer. *Molecular Pharmaceutics.* 2018;15:3093-3100.

20. Vaidyanathan G, Zalutsky MR. Labeling proteins with fluorine-18 using N-succinimidyl 4-[^{18}F]fluorobenzoate. *International Journal of Radiation Applications and Instrumentation Part B Nuclear Medicine and Biology.* 1992;19:275-281.

21. Hou S, Phung DL, Lin W-Y, Wang M-w, Liu K, Shen CK-F. Microwave-assisted one-pot synthesis of N-succinimidyl-4[^{18}F]fluorobenzoate ([^{18}F]SFB). *Journal of visualized experiments : JoVE.* 2011:2755.

22. Tang G, Tang X, Wang X. A facile automated synthesis of N-succinimidyl 4-[^{18}F]fluorobenzoate ([^{18}F]SFB) for ^{18}F-labeled cell-penetrating peptide as PET tracer. *Journal of Labelled Compounds and Radiopharmaceuticals.* 2010;53:543-547.

23. Basuli F, Zhang X, Woodroofe CC, Jagoda EM, Choyke PL, Swenson RE. Fast indirect fluorine-18 labeling of protein/peptide using the useful 6-fluoronicotinic acid-2,3,5,6-tetrafluorophenyl prosthetic group: A method comparable to direct fluorination. *Journal of Labelled Compounds and Radiopharmaceuticals.* 2017;60:168-175.

24. Glaser M, Morrison M, Solbakken M, et al. Radiosynthesis and Biodistribution of Cyclic RGD Peptides Conjugated with Novel [^{18}F]Fluorinated Aldehyde-Containing Prosthetic Groups. *Bioconjugate Chemistry.* 2008;19:951-957.

25. Schirrmacher E, Wängler B, Cypryk M, et al. Synthesis of p-(Di-tert-butyl[^{18}F]fluorosilyl)benzaldehyde ([^{18}F]SiFA-A) with High Specific Activity by Isotopic Exchange: A Convenient Labeling Synthon for the ^{18}F-Labeling of N-amino-oxy Derivatized Peptides. *Bioconjugate Chemistry.* 2007;18:2085-2089.

26. Cai W, Zhang X, Wu Y, Chen X. A Thiol-Reactive ^{18}F-Labeling Agent, N-[2-(4-^{18}F-Fluorobenzamido)Ethyl]Maleimide, and Synthesis of RGD Peptide-Based Tracer for PET Imaging of $\alpha_v\beta_3$ Integrin Expression. *Journal of Nuclear Medicine.* 2006;47:1172-1180.

27. Dolle F, Hinnen F, Vaufrey F, Tavitian B, Crouzel C. A general method for labeling oligodeoxynucleotides with ^{18}F for in vivo PET imaging. *Journal of Labelled Compounds and Radiopharmaceuticals.* 1997;39:319-330.

28. Berndt M, Pietzsch J, Wuest F. Labeling of low-density lipoproteins using the ^{18}F-labeled thiol-reactive reagent N-[6-(4-[^{18}F]fluorobenzylidene)aminooxyhexyl]maleimide. *Nuclear Medicine and Biology.* 2007;34:5-15.

29. de Bruin B, Kuhnast B, Hinnen F, et al. 1-[3-(2-[^{18}F]Fluoropyridin-3-yloxy)propyl]pyrrole-2,5-dione: Design, Synthesis, and Radiosynthesis of a New [^{18}F]Fluoropyridine-Based Maleimide Reagent for the Labeling of Peptides and Proteins. *Bioconjugate Chemistry.* 2005;16:406-420.

30. Toyokuni T, Walsh JC, Dominguez A, et al. Synthesis of a New Heterobifunctional Linker, N-[4-(Aminooxy)butyl]maleimide, for Facile Access to a Thiol-Reactive ^{18}F-Labeling Agent. *Bioconjugate Chemistry.* 2003;14:1253-1259.

31. Yue X, Yan X, Wu C, et al. One-Pot Two-Step Radiosynthesis of a New ^{18}F-Labeled Thiol Reactive Prosthetic Group and Its Conjugate for Insulinoma Imaging. *Molecular Pharmaceutics.* 2014;11:3875-3884.

32. Chiotellis A, Sladojevich F, Mu L, et al. Novel chemoselective ^{18}F-radiolabeling of thiol-containing biomolecules under mild aqueous conditions. *Chemical Communications.* 2016;52:6083-6086.

33. Jacobson O, Yan X, Ma Y, Niu G, Kiesewetter DO, Chen X. Novel Method for Radiolabeling and Dimerizing Thiolated Peptides Using ^{18}F-Hexafluorobenzene. *Bioconjugate Chemistry.* 2015;26:2016-2020.

34. Ramenda T, Kniess T, Bergmann R, Steinbach J, Wuest F. Radiolabelling of proteins with fluorine-18 via click chemistry. *Chemical Communications.* 2009:7521-7523.

35. Ramenda T, Steinbach J, Wuest F. 4-[^{18}F]Fluoro-N-methyl-N-(propyl-2-yn-1-yl)benzenesulfonamide ([^{18}F]F-SA): a versatile building block for labeling of peptides, proteins and oligonucleotides with fluorine-18 via Cu(I)-mediated click chemistry. *Amino Acids.* 2013;44:1167-1180.

36. Li Y, Liu Y, Zhang L, Xu Y. One-step radiosynthesis of 4-[^{18}F]flouro-3-nitro-N-2-propyn-1-yl-benzamide ([^{18}F]FNPB): a new stable aromatic porosthetic group for efficient labeling of peptides with fluorine-18. *Journal of Labelled Compounds and Radiopharmaceuticals.* 2012;55:229-234.

37. Glaser M, Årstad E. “Click Labeling” with 2-[^{18}F]Fluoroethylazide for Positron Emission Tomography. *Bioconjugate Chemistry.* 2007;18:989-993.

38. Kobus D, Giesen Y, Ullrich R, Backes H, Neumaier B. A fully automated two-step synthesis of an ^{18}F-labelled tyrosine kinase inhibitor for EGFR kinase activity imaging in tumors. *Applied Radiation and Isotopes.* 2009;67:1977-1984.

39. Glaser M, Årstad E, Gaeta A, Nairne J, Trigg W, Robins EG. Copper-mediated reduction of 2-[^{18}F]fluoroethyl azide to 2-[^{18}F]fluoroethylamine. *Journal of Labelled Compounds and Radiopharmaceuticals.* 2012;55:326-331.

40. Jacobson O, Weiss ID, Wang L, et al. ^{18}F-Labeled Single-Stranded DNA Aptamer for PET Imaging of Protein Tyrosine Kinase-7 Expression. *Journal of Nuclear Medicine.* 2015;56:1780-1785.

41. Mercier F, Paris J, Kaisin G, et al. General Method for Labeling siRNA by Click Chemistry with Fluorine-18 for the Purpose of PET Imaging. *Bioconjugate Chemistry.* 2011;22:108-114.

42. Thonon D, Kech C, Paris J, Lemaire C, Luxen A. New Strategy for the Preparation of Clickable Peptides and Labeling with 1-(Azidomethyl)-4-[^{18}F]-fluorobenzene for PET. *Bioconjugate Chemistry.* 2009;20:817-823.

43. de Almeida G, Sletten EM, Nakamura H, Palaniappan KK, Bertozzi CR. Thiacycloalkynes for Copper-Free Click Chemistry. *Angewandte Chemie International Edition.* 2012;51:2443-2447.

44. Dommerholt J, Schmidt S, Temming R, et al. Readily Accessible Bicyclononynes for Bioorthogonal Labeling and Three-Dimensional Imaging of Living Cells. *Angewandte Chemie International Edition.* 2010;49:9422-9425.

45. Kuzmin A, Poloukhtine A, Wolfert MA, Popik VV. Surface Functionalization Using Catalyst-Free Azide−Alkyne Cycloaddition. *Bioconjugate Chemistry.* 2010;21:2076-2085.

46. Ning X, Guo J, Wolfert MA, Boons G-J. Visualizing Metabolically Labeled Glycoconjugates of Living Cells by Copper-Free and Fast Huisgen Cycloadditions. *Angewandte Chemie International Edition.* 2008;47:2253-2255.

47. Hausner SH, Abbey CK, Bold RJ, et al. Targeted *In vivo* Imaging of Integrin $\alpha_v\beta_6$ with an Improved Radiotracer and Its Relevance in a Pancreatic Tumor Model. *Cancer Research.* 2009;69:5843.

48. Wang M, McNitt CD, Wang H, et al. The efficiency of ^{18}F labelling of a prostate specific membrane antigen ligand via strain-promoted azide–alkyne reaction: reaction speed versus hydrophilicity. *Chemical Communications.* 2018;54:7810-7813.

49. Campbell-Verduyn LS, Mirfeizi L, Schoonen AK, Dierckx RA, Elsinga PH, Feringa BL. Strain-Promoted Copper-Free "Click" Chemistry for ^{18}F Radiolabeling of Bombesin. *Angewandte Chemie International Edition.* 2011;50:11117-11120.

50. Staudinger H, Meyer J. Über neue organische Phosphorverbindungen III. Phosphinmethylenderivate und Phosphinimine. *Helvetica Chimica Acta.* 1919;2:635-646.

51. Agard NJ, Baskin JM, Prescher JA, Lo A, Bertozzi CR. A Comparative Study of Bioorthogonal Reactions with Azides. *ACS Chemical Biology.* 2006;1:644-648.

52. Köhn M, Breinbauer R. The Staudinger Ligation—A Gift to Chemical Biology. *Angewandte Chemie International Edition.* 2004;43:3106-3116.

53. Wang M, Svatunek D, Rohlfing K, et al. Conformationally Strained trans-Cyclooctene (sTCO) Enables the Rapid Construction of ^{18}F-PET Probes via Tetrazine Ligation. *Theranostics.* 2016;6:887-895.

54. Li X-G, Roivainen A, Bergman J, et al. Enabling [^{18}F]-bicyclo[6.1.0]nonyne for oligonucleotide conjugation for positron emission tomography applications: [^{18}F]-anti-microRNA-21 as an example. *Chemical Communications.* 2015;51:9821-9824.

55. Liu S, Hassink M, Selvaraj R, et al. Efficient ^{18}F labeling of cysteine-containing peptides and proteins using tetrazine-trans-cyclooctene ligation. *Molecular imaging.* 2013;12:121-128.

56. Selvaraj R, Liu S, Hassink M, et al. Tetrazine-trans-cyclooctene ligation for the rapid construction of integrin $\alpha_v\beta_3$ targeted PET tracer based on a cyclic RGD peptide. *Bioorganic & Medicinal Chemistry Letters.* 2011;21:5011-5014.

57. Rashidian M, Wang L, Edens JG, et al. Enzyme-Mediated Modification of Single-Domain Antibodies for Imaging Modalities with Different Characteristics. *Angewandte Chemie International Edition.* 2016;55:528-533.

58. Meyer J-P, Houghton JL, Kozlowski P, et al. ^{18}F-Based Pretargeted PET Imaging Based on Bioorthogonal Diels–Alder Click Chemistry. *Bioconjugate Chemistry.* 2016;27:298-301.

Chapter 3 THE DEVELOPMENT OF RADIOLABELED TCOS AND TETRAZINES[1]

3.1 Introduction on Tetrazine *Trans*-cyclooctene Ligation

To evaluate the potential of using TTCO ligation for PET probe construction, we first explored the possibility of generating radiolabeled TCOs and tetrazines. Tetrazine *trans*-cyclooctene ligation (TTCO) is an inverse electron demand Diels-Alder bioorthogonal reaction and only produces N_2 as byproduct upon cycloaddition (*1*). Saur et al. reported the quantitative kinetics between tetrazines and a series of dienophiles and demonstrated that *trans*-cyclooctene was the most reactive dienophile with exceptionally fast reaction speed (*2*). Since Saur's tetrazine substrates showed poor water stability thus unsuitable for biological application, our collaborator Dr. Fox's group developed 3,6-diaryl-*s*-tetrazine which offered excellent combination of rapid reactivity and stability for bioconjugation. The reaction rate between *trans*-cyclooctene and the *s*-tetrazine derivatives can be up to 2000 M^{-1} s^{-1} and reactive in cell media and cell lysate (*3*). The extremely fast reaction rate and biocompatibility make TTCO ligation a potential method for the rapid conjugation of radionuclides to biomolecules.

To great effect, Robillard and coworkers modified tetrazine moiety with DOTA and radiolabeled with ^{111}In for tumor imaging (*4*). Zeglis et al. used tetrazine bearing amino acids for ^{89}Zr labeling of peptides applying a *trans*-cyclooctene which was modified with deferrioxamine, a chelating agent for zirconium (*5*). However, these studies mainly utilized radiometal labeling

---

[1] This chapter is partly adapted from two published research articles. The original citation are as follows:
Wang M, Svatunek D, Rohlfing K, et al. Conformationally Strained trans-Cyclooctene (sTCO) Enables the Rapid Construction of ^{18}F-PET Probes via Tetrazine Ligation. Theranostics. 2016;6:887-895.
Wang M, Vannam R, Lambert WD, et al. Hydrophilic ^{18}F-labeled trans-5-oxocene (oxoTCO) for efficient construction of PET agents with improved tumor-to-background ratios in neurotensin receptor (NTR) imaging. Chemical Communications. 2019;55:2485-2488.

and few studies reported the ^{18}F labeled PET probes based on TTCO ligation. **Here we describe the ^{18}F labeling of TCO derivatives for efficient labeling of biomolecules, especially proteins that use to be challenge to ^{18}F-label. Some chelator modified TCO and tetrazine analogues were also synthesized and labeled with radiometals for other potential applications**.

3.2 Results and Discussion

3.2.1 ^{18}F Labeling of *Trans*-cyclooctenes

3.2.1.1 ^{18}F-TCO

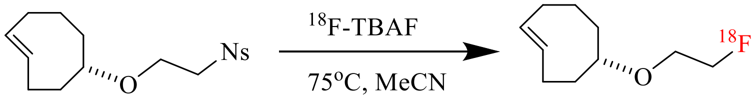

Scheme 3.1 Labeling scheme of ^{18}F-TCO

To radiolabel the *trans*-cyclooctene moiety with ^{18}F, we started from the first generation of *trans*-cyclooctene. By treating TCO-nosylate with ^{18}F-TBAF in acetonitrile at 75°C for 15min, we were able to obtain ^{18}F-TCO in 15.5 ± 2.5% isolation yield with over 99% radiochemical purity after HPLC purification (Fig 3.1a). The identity of the ^{18}F-TCO was confirmed by comparing the retention time with an independently synthesized ^{19}F-TCO standard (Fig 3.1b). Prior to reacting with tetrazines, we first tested the *in vitro* stability of ^{18}F-TCO. After incubation in 1x PBS for 1h, the radio purity remained at 82.2% (Fig 3.1c). Considering the extreme fast reaction kinetics of TTCO ligation, the stability was reasonable for PET probe construction in aqueous solution. To test the reactivity of the ^{18}F labeled TCO towards tetrazine, tetrazine modififed RGDyK peptide was used as a model to ligate with ^{18}F-TCO. As shown in Fig 3.1d, after mixing the ^{18}F-TCO with DiPhTz-RGDyK, the radio peak of ^{18}F-TCO disappeared, indicating a complete consumption of ^{18}F-TCO in the TTCO ligation. The ligation produced conjugates as a mixture of isomers (retention time at 14.9 and 15.2 min). It is worthy to point out that the *trans*-cyclooctene derivatives were not stable under acidic condition. So the TFA introduced during the tetrazine-biomolecule synthesis might result in some decomposed radio impurities in the TTCO ligation process.

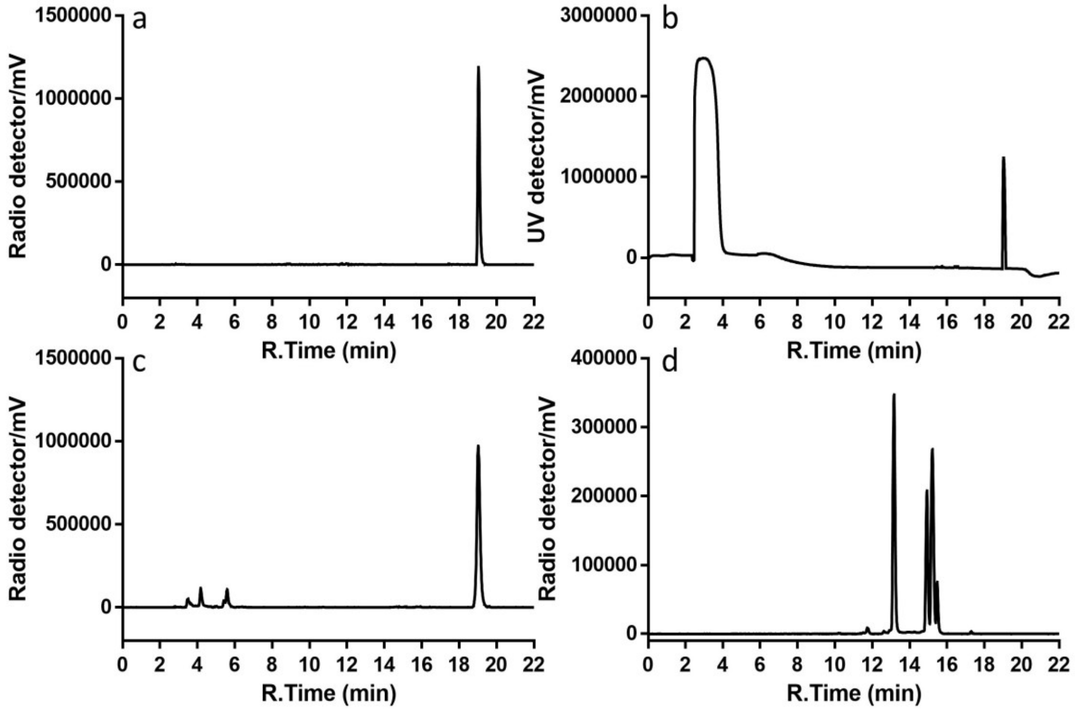

Figure 3.1 HPLC profile of a) purified ^{18}F-TCO. b) ^{19}F-TCO. c) ^{18}F-TCO after incubation in PBS for 1h at 37°C. d) Crude of ^{18}F-TCO ligation with DiPhTz-RGDyK

3.2.1.2 ^{18}F-sTCO

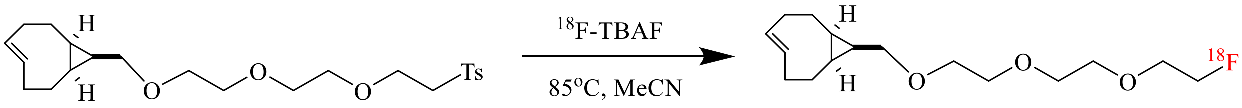

Scheme 3.2 Labeling scheme of ^{18}F-sTCO

With the success of the ^{18}F labeled TCO in hand, we turned to radiolabel the second generation of the *trans*-cyclooctene with faster reaction kinetic, sTCO. sTCO was a conformationally strained *trans*-cyclooctene for which rate constants as fast as 3.3 x 10^6 $M^{-1}s^{-1}$ (*6*). This exceptional kinetics enabled it to be the highly reactive dienophile for TTCO ligation.

The sTCO-tosylate precursor was dissolved in anhydrous acetonitrile and heated with ^{18}F-TBAF at 85°C for 10min. ^{18}F-sTCO was obtained at 29.3 ± 5.1% isolation yield with 99%

radiochemical purity (Fig 3.2a). An ^{19}F-sTCO standard was used to confirm the identity of the radiolabeled ^{18}F-sTCO (Fig 3.2b). The *in vitro* stability of ^{18}F-sTCO was tested by incubation in 1X PBS for 1h and the result gave 97.5% of intact ^{18}F-sTCO after incubation, which showed improved stability compared with ^{18}F-TCO (Fig 3.2c). We also evaluated the hydrophilicity of ^{18}F-sTCO and the log *P* value was 0.95 ± 0.02. As shown in Fig 3.2d, two new peaks were observed in the crude reaction between ^{18}F-sTCO and DiPhTz-RGDyK while no ^{18}F-sTCO was left. This result demonstrated that ^{18}F-sTCO remained the reactivity towards tetrazine after fluorination. The relatively clean background in the reaction might result from the higher stability of ^{18}F-sTCO.

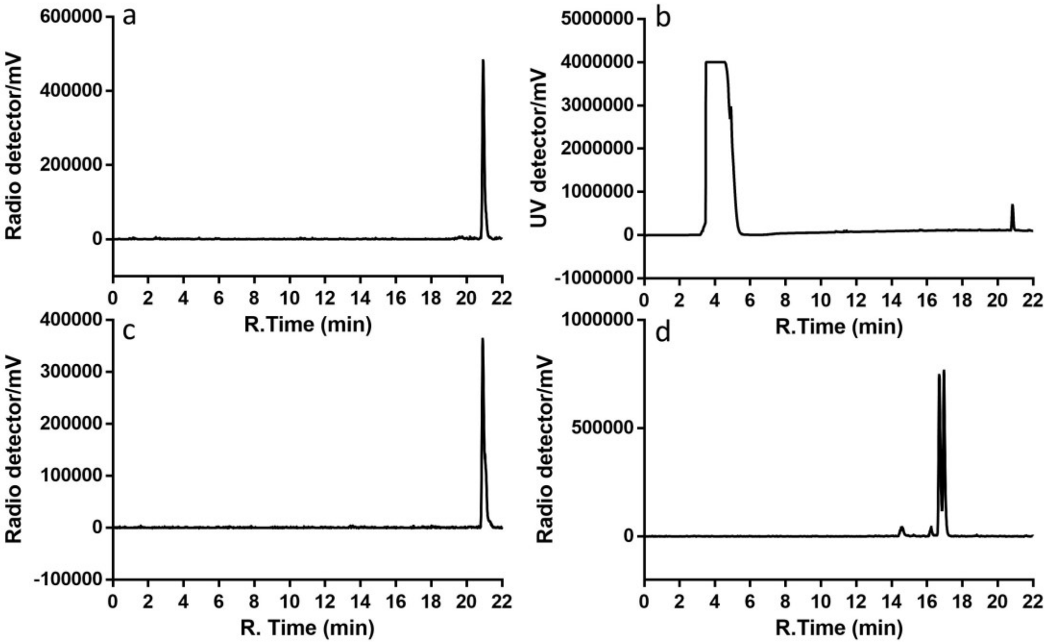

Figure 3.2 HPLC profile of a) purified ^{18}F-sTCO. b) ^{19}F-sTCO. c) ^{18}F-sTCO after incubation in PBS for 1h at 37^{o}C. d) Crude of ^{18}F-sTCO ligation with DiPhTz-RGDyK

3.2.1.3 ^{18}F-dTCO

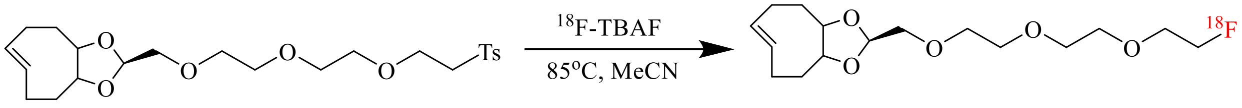

Scheme 3.3 Labeling scheme of ^{18}F-dTCO

Since the precursor for ^{18}F-sTCO suffered from stability issue, we further explored a more stable derivative precursor with slightly lower rate constant to sTCO. Conformationally-strained dioxolane-fused *trans*-cyclooctene (dTCO) could react with tetrazine with a second order rate k_2=3.7 x 10^5 $M^{-1}s^{-1}$ (*7*).

The ^{18}F labeling protocol for dTCO was similar to sTCO with labeling yield of 11.4 ± 0.9% and 99% radiochemical purity after HPLC purification (Fig 3.3a and 3.3b). The partition coefficient of the relative hydrophilic ^{18}F-dTCO was measured and the log *P* value was 0.91 ± 0.02 which demonstrated the slightly more hydrophilic than ^{18}F-sTCO. After incubation in 1X PBS for 1h, the radiochemical purity of ^{18}F-dTCO was 86.2%, which was similar to most *trans*-cyclooctene derivatives except sTCO (Fig 3.3c). The reactivity towards tetrazine after ^{18}F fluorination was confirmed by mixing with DiPhTz-RGDyK. As shown in Fig 3.3d, a complete ligation between DiPhTz-RGDyk and ^{18}F-dTCO occurred within seconds while only one major product peak was observed indicating a high yield of the ligation.

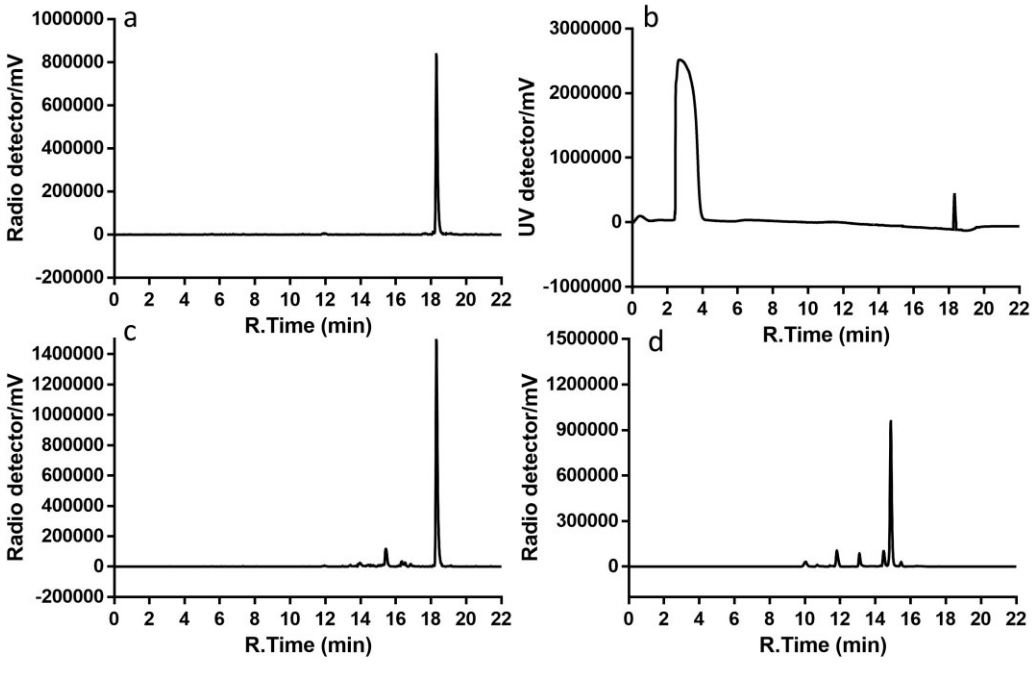

Figure 3.3 HPLC profile of a) purified ^{18}F-dTCO. b) ^{19}F-dTCO. c) ^{18}F-dTCO after incubation in PBS for 1h at 37^{o}C. d) Crude of ^{18}F-dTCO ligation with DiPhTz-RGDyK

3.2.1.4 ^{18}F-oTCO

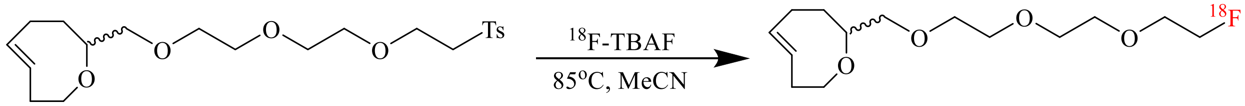

Scheme 3.4 Labeling scheme of ^{18}F-oTCO

Due to the relatively high hydrophobicity of both ^{18}F-sTCO and ^{18}F-dTCO, which might lead to hepatic clearance pathway with higher background signal in PET imaging, an oxygen-containing TCO derivatives with improved water solubility properties has been described (*8*). The developed *trans*-5-oxocene (oTCO) was shown to have enhanced reactivity compared to TCO and enhanced hydrophgilicity relative to TCO, sTCO and dTCO.

Radiochemical synthesis was modeled after our previously described procedure for prepaing ^{18}F-sTCO. oTCO-tosylate was radiolabeled with ^{18}F-TBAF to provide ^{18}F-oTCO with 15.2 ± 1.9% isolation yield. The purity and identity were confirmed by HPLC and ^{19}F-oTCO standard (Fig 3.4a and 3.4b). Efforts to improve the radiochemical yield by increasing the concentration of precursor or prolonging the reaction time were unsuccessful. While the radiochemical yield for tosylate displacement was moderate, it is high enough to be useful and is in alignment with yields obtained in many procedures for ^{18}F probe construction (*9*). After incubation for 1 h in PBS, the radiochemical purity of 6was 85.2%, indicating a level of stability that was good but not as high as a cold oTCO compound stored under similar conditions (Fig 3.4c)(*8*). In a previous study, we found that TCO decomposes more rapidly under conditions conducive to radical formation, and it may be that the radiolysis contributes to the decomposition of ^{18}F-oTCO. The log *P* value of ^{18}F-oTCO was 0.57 ± 0.02, which was significantly lower than those for ^{18}F-sTCO and ^{18}F-dTCO. Fig 3.4d showed the reaction crude between ^{18}F-oTCO and DiPhTz-RGDyK. The major peak shift demonstrated that ^{18}F-oTCO retained the reactivity towards tetrazine after radiolabeling.

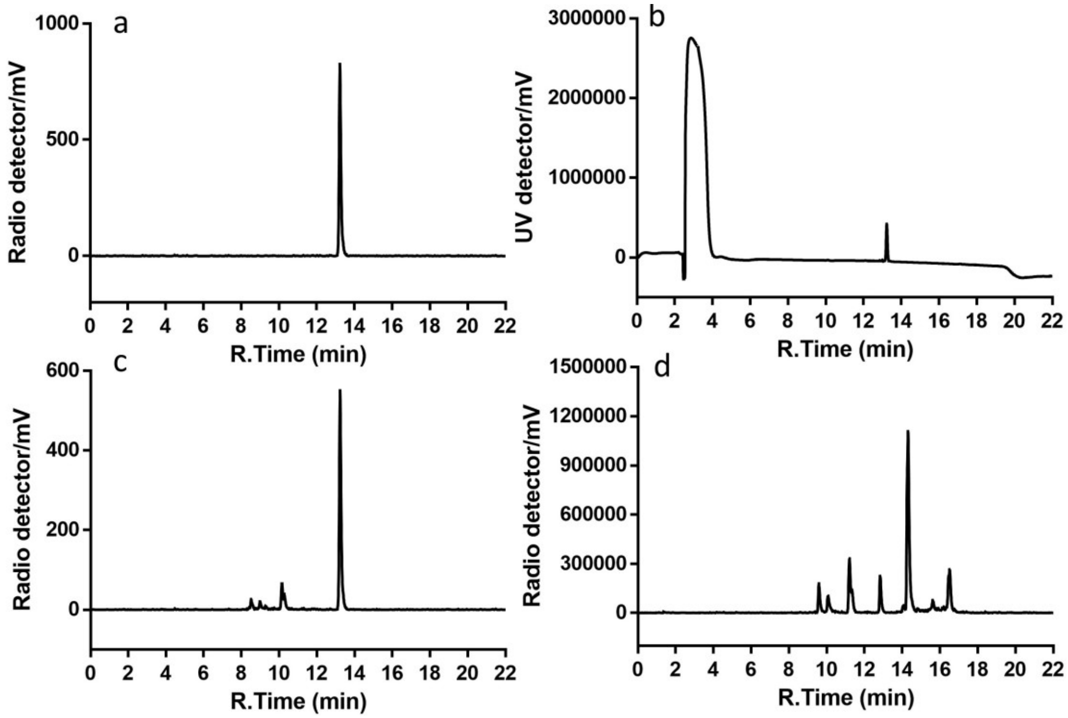

Figure 3.4 HPLC profile of a) purified ^{18}F-oTCO. b) ^{19}F-oTCO. c) ^{18}F-oTCO after incubation in PBS for 1h at 37^{o}C. d) Crude of ^{18}F-oTCO ligation with DiPhTz-RGDyK

3.2.2 ^{64}Cu Labeling of *Trans*-cyclooctenes

3.2.2.1 ^{64}Cu-sTCO-PEG-DOTA

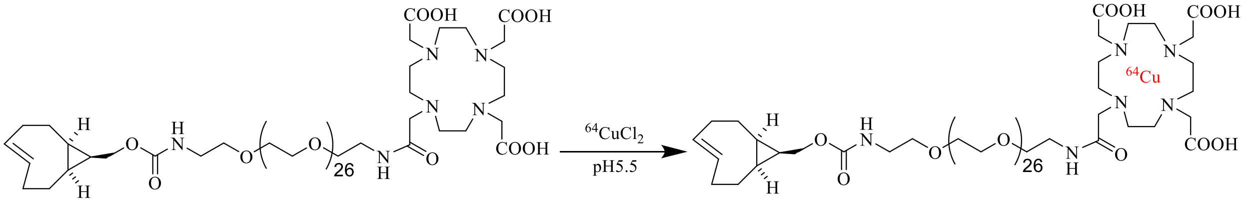

Scheme 3.5 Labeling scheme of ^{64}Cu-sTCO-PEG-DOTA

Despite of labeling the *trans*-cyclooctene derivatives with ^{18}F, which was mainly used for PET imaging, we also tested the labeling with radiometals for potential radiotherapy applications.

Starting from the most reactive *trans*-cyclooctene derivatives, we modified the sTCO with DOTA which was one of the most widely used chelator for radiometal labeling. The sTCO-PEG-DOTA was labeled with ^{64}Cu efficiently in 0.25M NH_4OAc buffer with isolation yield of

43.4 ± 5.8% (Fig 3.5a). The radiochemical purity was over 99% after initial purification and remained at 93.3% after 1h incubation in 1X PBS (Fig 3.5c). The improved stability compared with ^{18}F labeled version might be due to the lower specific activity and few radiolysis. We would like to point out that the *trans*-cyclooctene derivatives were sensitive to pH, which was essential for radiometal chelating process. Thus, optimizing the labeling condition for *trans*-cyclooctene derivatives radiometal labeling is necessary in future studies. We also evaluated whether the ^{64}Cu labeled sTCO-PEG-DOTA remained the reactivity towards tetrazine by treating it with DiPhTz-RGDyK. As shown in Fig 3.5d, ^{64}Cu-sTCO-PEG-DOTA was completely consumed within seconds indicating the ligation between ^{64}Cu-sTCO-PEG-DOTA and DiPhTz-RGDyK.

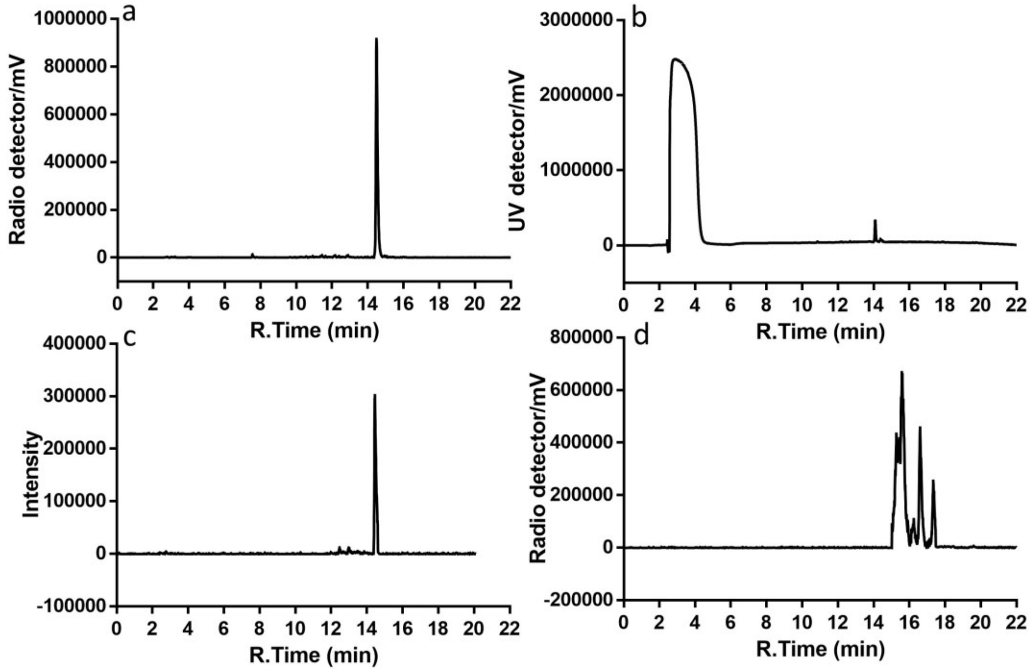

Figure 3.5 HPLC profile of a) purified ^{64}Cu-sTCO-PEG-DOTA. b) sTCO-PEG-DOTA. c) ^{64}Cu-sTCO-PEG-DOTA after incubation in PBS for 1h at 37°C. d) Crude of ^{64}Cu-sTCO-PEG-DOTA ligation with DiPhTz-RGDyK

3.2.2.2 ^{64}Cu-dTCO-PEG-DOTA

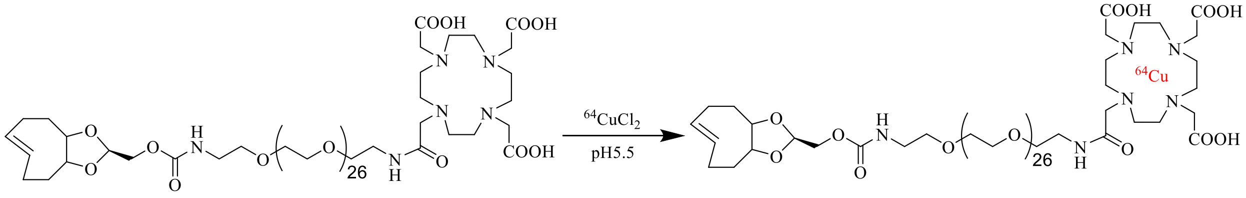

Scheme 3.6 Labeling scheme of ^{64}Cu-dTCO-PEG-DOTA

The more hydrophilic dTCO was also modified with DOTA and subjected to ^{64}Cu labeling. Under the same labeling protocol, dTCO-PEG-DOTA was able to be radiolabeled with ^{64}Cu at 42.9 ± 9.7% isolation yield and 99% purity after HPLC purification (Fig 3.6a). The stability in 1X PBS at 1h time point was 90.3% (Fig 3.6c). The reactivity towards tetrazine after ^{64}Cu labeling was demonstrated by ligation with DiPhTz-RGDyK. In Fig 3.6d, a new peak appeared with no ^{64}Cu-dTCO-PEG-DOTA left indicating the ^{64}Cu labeling of dTCO-PEG-DOTA did not compromise its reactivity for TTCO ligation.

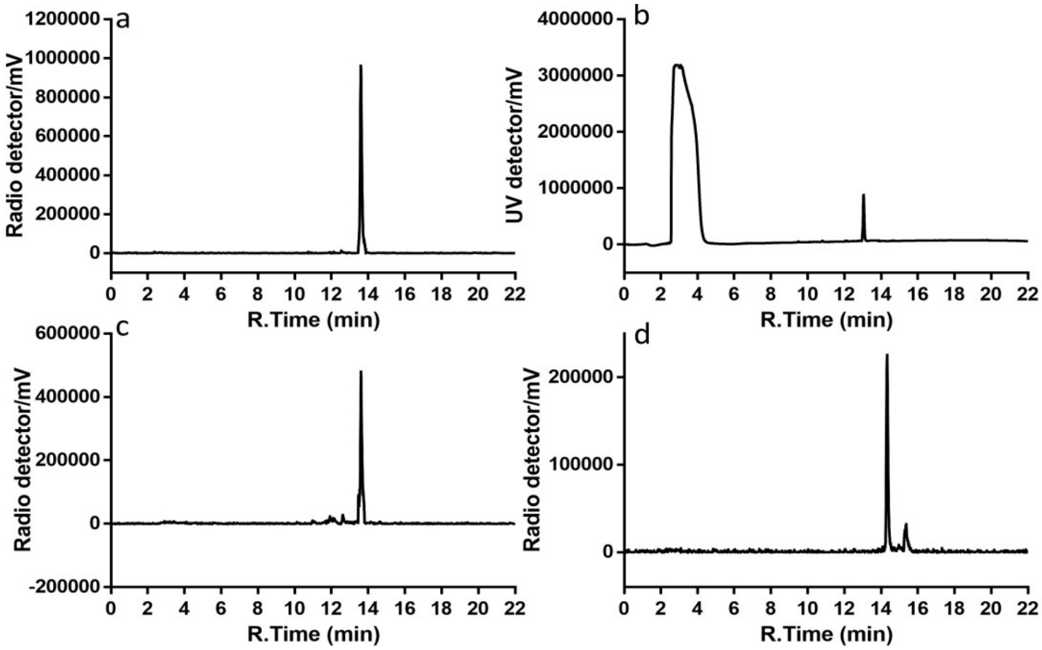

Figure 3.6 HPLC profile of a) purified ^{64}Cu-dTCO-PEG-DOTA. b) dTCO-PEG-DOTA. c) ^{64}Cu-dTCO-PEG-DOTA after incubation in PBS for 1h at 37°C. d) Crude of ^{64}Cu-dTCO-PEG-DOTA ligation with DiPhTz-RGDyK

3.2.3 ^{64}Cu Labeling of Tetrazines

3.2.3.1 ^{64}Cu-Tz-NOTA

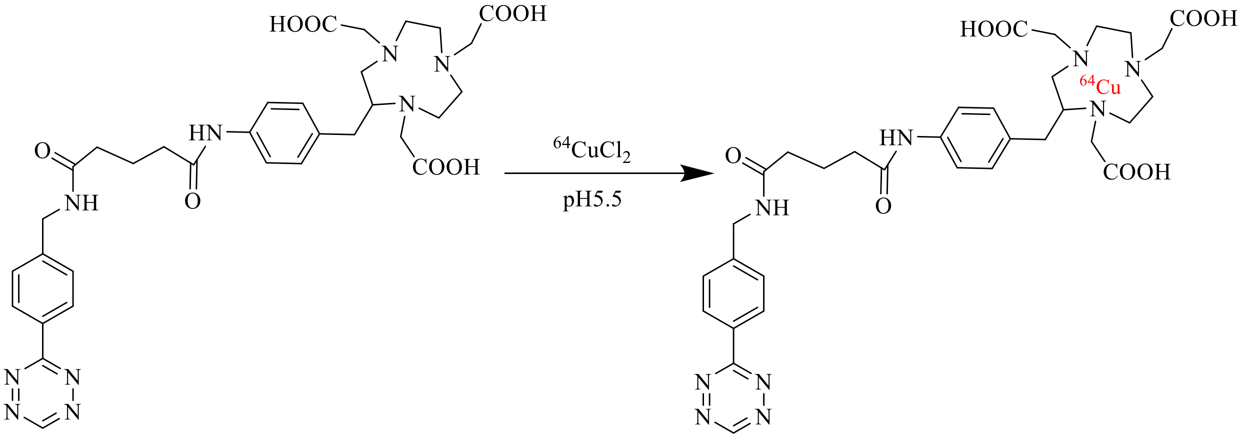

Scheme 3.7 Labeling scheme of ^{64}Cu-Tz-NOTA

Similar to *trans*-cyclooctene, we also modified tetrazine moiety with NOTA for radiometal chelation. The first candidate we chose was Tz-NOTA where chelator NOTA was directly conjugated to Tz-NHS. As can be seen in Fig 3.7a, Tz-NOTA could be successfully labeled with ^{64}Cu under the same condition as sTCO-PEG-DOTA/dTCO-PEG-DOTA. The isolation yield was 62.6 ± 7.7% and remained 94.5% stability after 1h incubation in 1X PBS (Fig 3.7a, 3.7c). The reactivity of ^{64}Cu-Tz-NOTA was tested by treating it with TCO-F and the result was shown in Fig 3.7d. A fully consumption of ^{64}Cu-Tz-NOTA was observed with additional peaks showing up indicating the reactivity for TTCO ligation was remained after ^{64}Cu labeling of the tetrazine moiety.

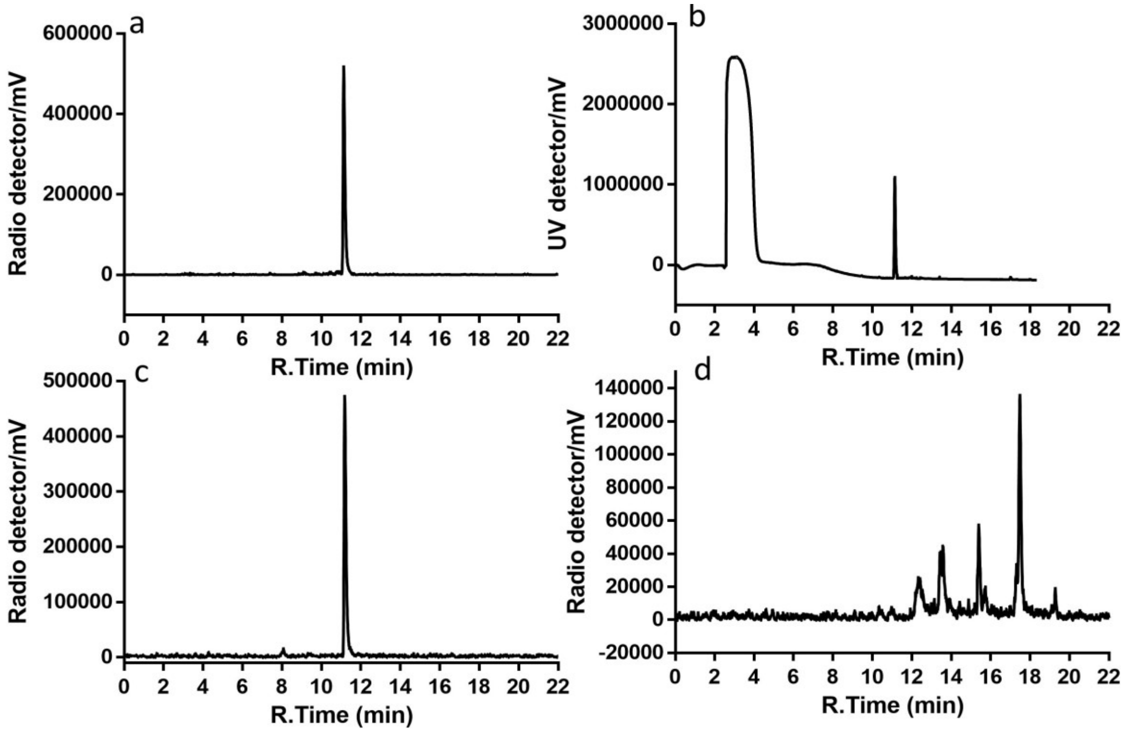

Figure 3.7 HPLC profile of a) purified ^{64}Cu-Tz-NOTA. b) Tz-NOTA. c) ^{64}Cu-Tz-NOTA after incubation in PBS for 1h at 37^{o}C. d) Crude of ^{64}Cu-Tz-NOTA ligation with TCO-F

3.2.3.2 ^{64}Cu-Tz-PEG-NOTA

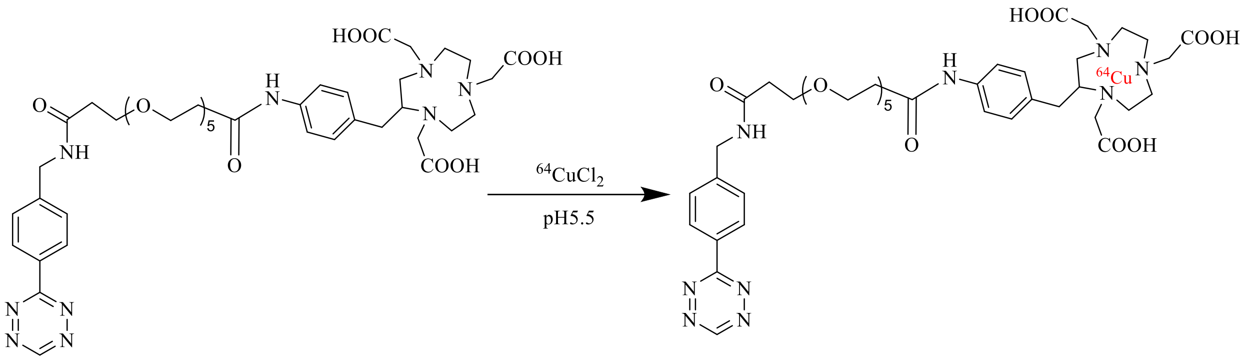

Scheme 3.8 Labeling scheme of ^{64}Cu-Tz-PEG-NOTA

In order to avoid steric hinderance when labeling large biomolecules with TTCO ligation, we added a space linker between the radiolabeling moiety NOTA and the TTCO ligation moiety tetrazine. Fig 3.8a and Fig 3.8c showed the radio HPLC profile of freshly prepared ^{64}Cu-Tz-PEG-NOTA and that after 1h incubation in PBS. The isolated labeling yield was 50.3 ± 9.8% and 1h stability was 95.8%. Similarly, adding in TCO-F to purified ^{64}Cu-Tz-PEG-NOTA led to completely consumption of ^{64}Cu-Tz-PEG-NOTA and the ligation products with some impurities, which proved the retaining of the reactivity towards TCO after radiolabeling (Fig 3.8d).

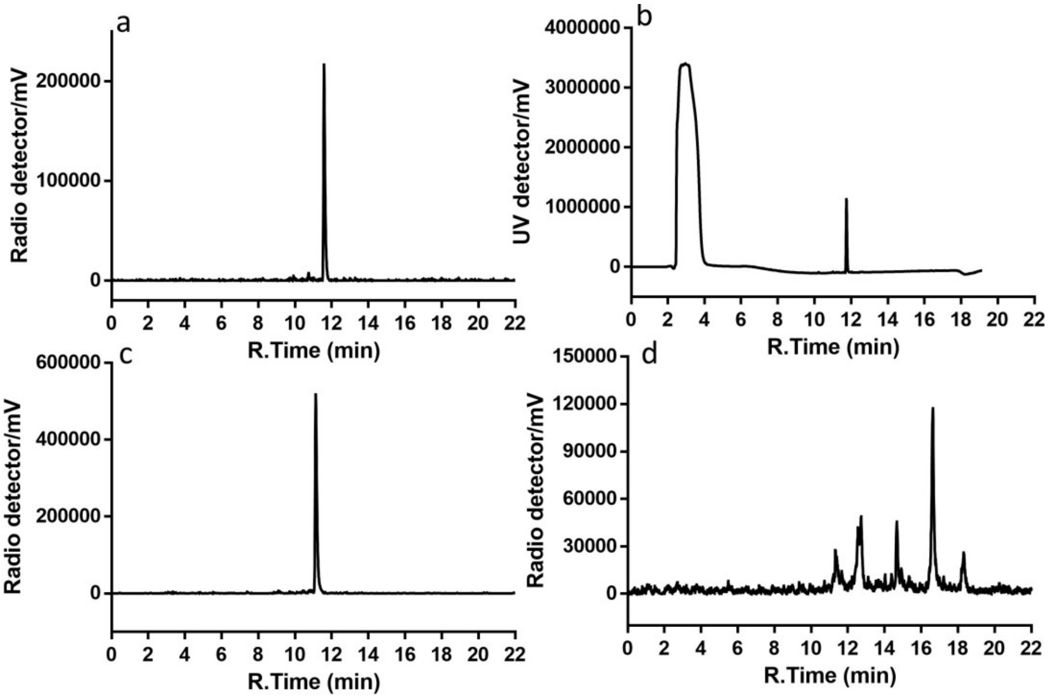

Figure 3.8 HPLC profile of a) purified ^{64}Cu-Tz-PEG-NOTA. b) Tz-PEG-NOTA. c) ^{64}Cu-Tz-PEG-NOTA after incubation in PBS for 1h at 37^{o}C. d) Crude of ^{64}Cu-Tz-PEG-NOTA ligation with TCO-F

3.3 Conclusion

We have demonstrated the feasibility of radiolabeling several TCO derivatives with ^{18}F. All ^{18}F-TCOs were achieved with reasonable yield for further construction of PET probes after simple purification. The TCO derivatives were also successfully labeled with radiometal ^{64}Cu for potential imaging and therapeutic applications. Additionally, we also proved that the tetrazine moiety could be labeled with ^{64}Cu, which represents another pathway for radiolabeling of biomolecules. All radiolabeled compounds retained their reactivity for TTCO ligation. **These results lay solid ground for using TTCO ligation for biomolecule radiolabeling.**

3.4 Materials and Methods

3.4.1 General

All commercially available reagents were purchased and used without further purification. All *trans*-cyclooctene and tetrazine-NHS ester derivatives were kindly provided by Dr. Joseph M. Fox from University of Delaware. Briefly, *trans*-cyclooctene derivatives were prepared from *cis*-cyclooctenes using photochemical flow-reaction (*10*). Analytical reversed-phase HPLC using a Kinetex 5µ C18 column (250 x 4.6mm) was performed on a SPD-M30A photodiode array detector (Shimadzu) and model 105S single-channel radiation detector (Carroll & Ramsey Associates). Radio HPLC analyses were carried out at 1 mL/min flow rate. The mobile phase was 0.1% TFA in water for solvent A and 0.1% TFA in acetonitrile for solvent B. The mobile phase was kept at 95% solvent A and 5% solvent B from 0~2min and ramped to 5% solvent A and 95% solvent B in 20min. For HPLC analyses and purification of *trans*-cyclooctene derivatives, the solvents were switched to TFA free solvents. Mass spectrometry was obtained on Advion Expression CMS mass spectrometer.

^{18}F-TBAF was synthesized using the following protocol: Targeted water containing ^{18}F was passed through a pre-conditioned QMA anion exchange cartridge for ^{18}F trapping. The ^{18}F was released by eluting the QMA cartridge with a mixture of 123 µL of 20% tetrabutylammonium bicarbonate and 477 µL of anhydrous acetonitrile. The elution was azeotropically dried at 100 ^{o}C under nitrogen and vacuum for 3 times. The obtained ^{18}F-TBAF was dissolved in anhydrous acetonitrile for further use.

3.4.2 Radiochemistry

3.4.2.1 ^{18}F-TCO

TCO-nosylate (2mg, 5.9 μmol) was dissolved in 30 μL anhydrous acetonitrile and then allowed to react with ^{18}F-TBAF (200 mCi) at 75°C for 15min. The reaction was quenched with 1 mL water. The mixture was then passed through a pre-conditioned Sep-Pak cartridge (Sep-Pak Plus light alumina) followed by RP-HPLC purification. The desired fraction containing product was collected and decay corrected yield was calculated. An aliquot of the product was loaded on RP-HPLC for quality control.

3.4.2.2 ^{18}F –sTCO/^{18}F-dTCO/^{18}F-oTCO

sTCO-tosylate, dTCO-tosylate or oTCO-tosylate (2 mg) was dissolved in 30 μL anhydrous acetonitrile and then added with 200mCi ^{18}F-TBAF. The reaction was kept at 85°C for 10min before quenching with 1 mL water. The mixture was then passed through a pre-conditioned Sep-Pak cartridge (Sep-Pak Plus light alumina) followed by RP-HPLC purification. The desired fraction containing product was collected for further use. After measuring the decay corrected yield, an aliquot of the product was taken for quality control on RP-HPLC.

3.4.2.3 ^{64}Cu-dTCO-PEG-DOTA/^{64}Cu-sTCO-PEG-DOTA

1 mCi of ^{64}Cu was added to dTCO-PEG-DOTA or sTCO-PEG-DOTA (10 μg in 20 μL water) and the pH was adjusted to 5.5 with 0.25 M NH_4OAc. The mixture was incubated at 40°C for 40min with constant shaking before loading on RP-HPLC for analysis and purification. The desired fraction containing product was collected for further use. The decay corrected yield was calculated and a portion of the product was used as quality control.

3.4.2.4 ^{64}Cu-Tz-PEG-NOTA/^{64}Cu-Tz-NOTA

10 µg of Tz-PEG-NOTA or Tz-NOTA in 20 µL DMSO was added with 1 mCi of ^{64}Cu. The pH of mixture was adjusted to 5.5 using 0.25 M NH_4OAc. The reaction was kept at 40°C for 40min with constant shaking followed by RP-HPLC analysis and purification. The desired fraction containing product was collected and decay corrected yield was calculated. An aliquot of the product was loaded on RP-HPLC for quality control.

3.4.3 *In Vitro* Stability and Reactivity for TTCO Ligation

Each radiolabeled compound collected from RP-HPLC was subjected to rotary evaporation to remove the organic solvent and the pH was adjusted to neutral using NaOH solution. After reconstituted in 1X PBS, a fraction of the radiolabeled compound (~1 mCi) was mixed with 10 nmol of either DiPhTz-RGDyK or ^{19}F-TCO and loaded on RP-HPLC for TTCO ligation reactivity analysis. Another fraction of the radiolabeled compound (~100 µCi) were incubated in 37°C in PBS for 1h and loaded on RP-HPLC for stability analysis.

REFERENCES

1. Boger DL. Diels-Alder reactions of heterocyclic aza dienes. Scope and applications. *Chemical Reviews.* 1986;86:781-793.

2. Thalhammer F, Wallfahrer U, Sauer J. Reaktivität einfacher offenkettiger und cyclischer dienophile bei Diels-Alder-reaktionen mit inversem elektronenbedarf. *Tetrahedron Letters.* 1990;31:6851-6854.

3. Blackman ML, Royzen M, Fox JM. Tetrazine Ligation: Fast Bioconjugation Based on Inverse-Electron-Demand Diels−Alder Reactivity. *Journal of the American Chemical Society.* 2008;130:13518-13519.

4. Rossin R, Renart Verkerk P, van den Bosch SM, et al. In Vivo Chemistry for Pretargeted Tumor Imaging in Live Mice. *Angewandte Chemie International Edition.* 2010;49:3375-3378.

5. Zeglis BM, Emmetiere F, Pillarsetty N, Weissleder R, Lewis JS, Reiner T. Building Blocks for the Construction of Bioorthogonally Reactive Peptides via Solid-Phase Peptide Synthesis. *ChemistryOpen.* 2014;3:48-53.

6. Wang M, Svatunek D, Rohlfing K, et al. Conformationally Strained trans-Cyclooctene (sTCO) Enables the Rapid Construction of ^{18}F-PET Probes via Tetrazine Ligation. *Theranostics.* 2016;6:887-895.

7. Darko A, Wallace S, Dmitrenko O, et al. Conformationally strained trans-cyclooctene with improved stability and excellent reactivity in tetrazine ligation. *Chemical Science.* 2014;5:3770-3776.

8. Lambert WD, Scinto SL, Dmitrenko O, et al. Computationally guided discovery of a reactive, hydrophilic trans-5-oxocene dienophile for bioorthogonal labeling. *Organic & Biomolecular Chemistry.* 2017;15:6640-6644.

9. Jacobson O, Kiesewetter DO, Chen X. Fluorine-18 Radiochemistry, Labeling Strategies and Synthetic Routes. *Bioconjugate Chemistry.* 2015;26:1-18.

10. Royzen M, Yap GPA, Fox JM. A Photochemical Synthesis of Functionalized trans-Cyclooctenes Driven by Metal Complexation. *Journal of the American Chemical Society.* 2008;130:3760-3761.

Chapter 4 BIOMOLECULES BASED PET PROBE CONSTRUCTION AND IMAGING USING TTCO LIGATION[1]

4.1 Introduction of the Biomolecules

Given the fact that *trans*-cyclooctene and tetrazine can be radiolabeled at reasonable yield and maintain high reactivity towards the other counterpart, we step further to evaluate their application in biomolecule radiolabeling. **In this chapter, we apply the TTCO radiolabeling method to construct two types of biomolecules:** small peptides and proteins with larger molecular weight. Our ultimate goal is to establish **the TTCO ligation method as a general tool for PET probes construction, which may also solve the challenges on radiolabel protein with ^{18}F.**

We first test the TTCO ligation using peptides with small molecular weight, which include RGD, NT20.3 and PSMA ligand.

4.2 Radiolabeled RGD Peptide for Integrin $\alpha_v\beta_3$ Targeted Imaging

RGD is a tripeptide with Arg-Gly-Asp sequence and has high binding affinity and specificity to integrin $\alpha_v\beta_3$ (*1*). Integrins are transmembrane receptors, which contain alpha and beta subunits and mediate the adhesion of cells to extra-cellular matrix (ECM) (*2*). Integrins, especially integrin $\alpha_v\beta_3$, show significant up-regulation on activated endothelial cells and mediated the migration of cells during angiogenesis, which is essential for tumor growing (*3*-*5*).

---

[1] This chapter is partly adapted from two published research articles. The original citation are as follows:
Wang M, Svatunek D, Rohlfing K, et al. Conformationally Strained trans-Cyclooctene (sTCO) Enables the Rapid Construction of ^{18}F-PET Probes via Tetrazine Ligation. Theranostics. 2016;6:887-895.
Wang M, Vannam R, Lambert WD, et al. Hydrophilic ^{18}F-labeled trans-5-oxocene (oxoTCO) for efficient construction of PET agents with improved tumor-to-background ratios in neurotensin receptor (NTR) imaging. Chemical Communications. 2019;55:2485-2488.

$\alpha_v\beta_3$ is reported to be overexpressed in various malignant tumors including glioma and breast cancer and its expression level correlates with the tumor grade (*6-8*). Inhibition of the $\alpha_v\beta_3$ integrin has been found to induce apoptosis of both activated endothelial cells and $\alpha_v\beta_3$ positive tumor cells without affecting pre-existing blood vessels (*9*). Furthermore, $\alpha_v\beta_3$ targeting molecules show great potential to deliver various therapeutic agents to tumor tissues. Molecular imaging of $\alpha_v\beta_3$ provides valuable information about the expression level and can help in selecting patients for appropriate anti-$\alpha_v\beta_3$ treatment as well as monitoring the treatment efficacy. RGD peptide was a well-established targeting reagent to integrin $\alpha_v\beta_3$ and several RGD based PET probes have been investigated including ^{18}F-Galacto-RGD, ^{68}Ga-NOTA-RGD and ^{18}F-Alfatide etc (*10-13*).

4.2.1 ^{18}F-TCO-DiPhTz-RGDyK

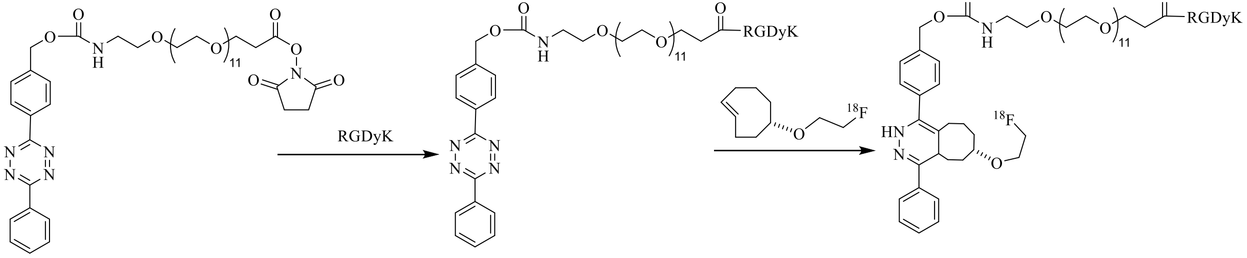

Scheme 4.1 Synthesis scheme of ^{18}F-TCO-DiPhTz-RGDyK

We started with the most well-established $\alpha_v\beta_3$ targeting agent RGDyK as a model peptide. The peptide was modified with diphenyl-*s*-tetrazine (DiPhTz) since it was reported to show improved metabolic stability compared with the first generation dipyridyl-*s*-tetrazine (*14*). We then radiolabeled it with ^{18}F-TCO described in the previous chapter for PET probe construction and further evaluated its pharmacokinetics in vivo.

As shown in Fig 4.1a, only two peaks were observed in the HPLC profile of the crude reaction. The peak with 15.1min retention time was the product while the peak with 19.5min retention time was DiPhTz-NHS. No starting material RGDyK was observed indicating the complete consumption of RGDyK. Fig 4.1b showed the HPLC profile of purified DiPhTz-RGDyK. DiPhTz-RGDyK (2.1mg, 1.4 µmol) was obtained as white powder after lyophilization with 87.5% yield. The product identity was confirmed by LC-MS (Fig 4.1c, *m/z* : $[M+H]^+$, Calcd for $C_{70}H_{105}N_{14}O_{23}$ is 1510.7; found 1510.8)

^{18}F-TCO labeling was reported in the previous chapter. After mixed with DiPhTz-RGDyK for 10 seconds at room temperature, the TTCO ligation was completed and the ^{18}F-TCO-DiPhTz-RGDyK was obtained at 49.2 ± 1.4% isolation yield and over 99% radiochemical purity after HPLC purification. The identity of the collected radio peak was confirmed by comparing the retention time with the independently synthesized ^{19}F-TCO-DiPhTz-RGDyK and LC-MS (Fig 4.2).

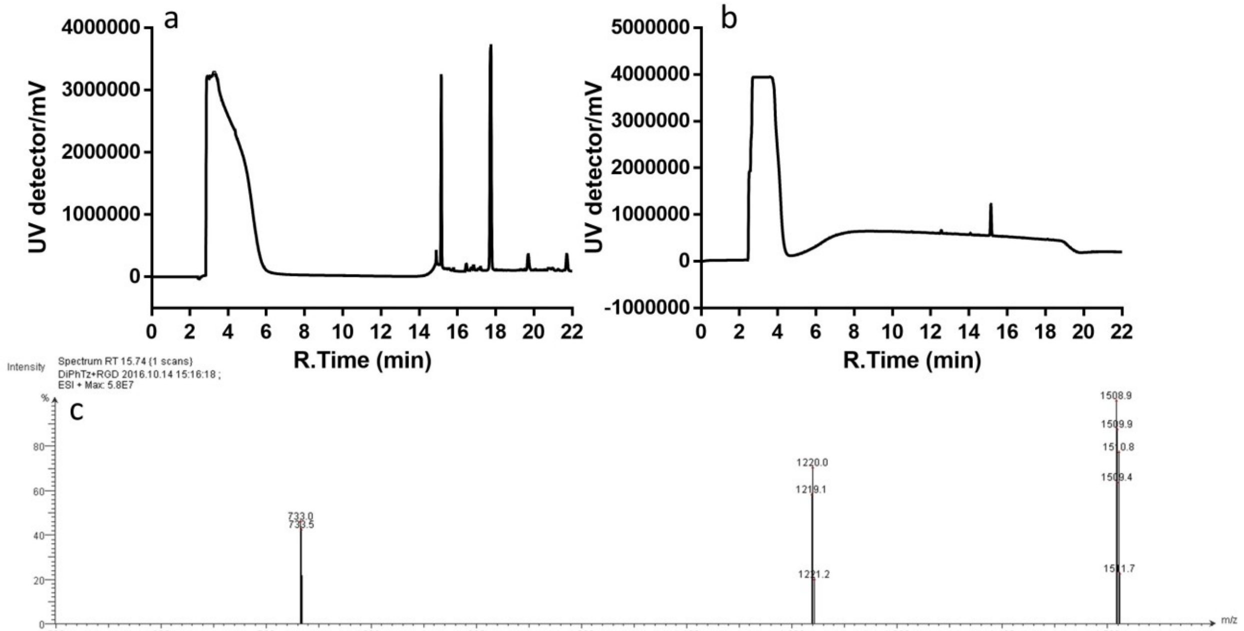

Figure 4.1 a) HPLC profile of crude reaction between DiPhTz-NHS and RGDyK. b) HPLC profile of purified DiPhTz-RGDyK. c) Mass spectrum of purified DiPhTz-RGDyK

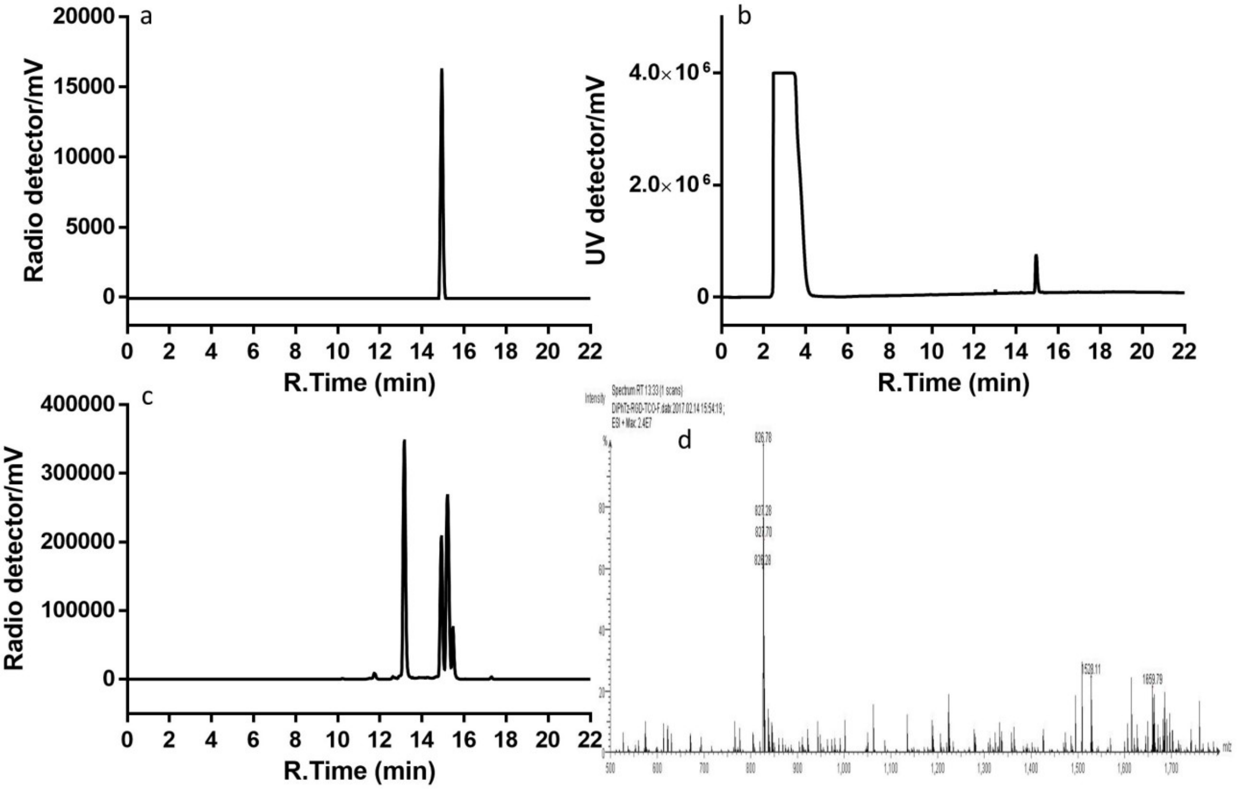

Figure 4.2 HPLC profile of a) purified ^{18}F-TCO-DiPhTz-RGDyK. b) ^{19}F-TCO-DiPhTz-RGDyK. c) crude of ^{18}F-TCO ligation with DiPhTz-RGDyK. d) Mass spectrum of purified ^{19}F-TCO-DiPhTz-RGDyK

The in vivo behavior of ^{18}F-TCO-DiPhTz-RGDyK was evaluated in $\alpha_v\beta_3$ positive human U87MG tumor-bearing mice (n=3). As shown in Fig 4.3, high and persistent tumor accumulation was observed at both 1h and 4h post injection. The tumor uptake increased from 3.9 ± 0.3 %ID/g at 1h post injection to 4.1 ± 0.4 %ID/g at 4h post injection. Though a relative high background signal was observed, this result indicated that the peptide based PET probe could be successfully constructed via TTCO ligation and showed reasonable tumor targeting efficiency and biodistribution.

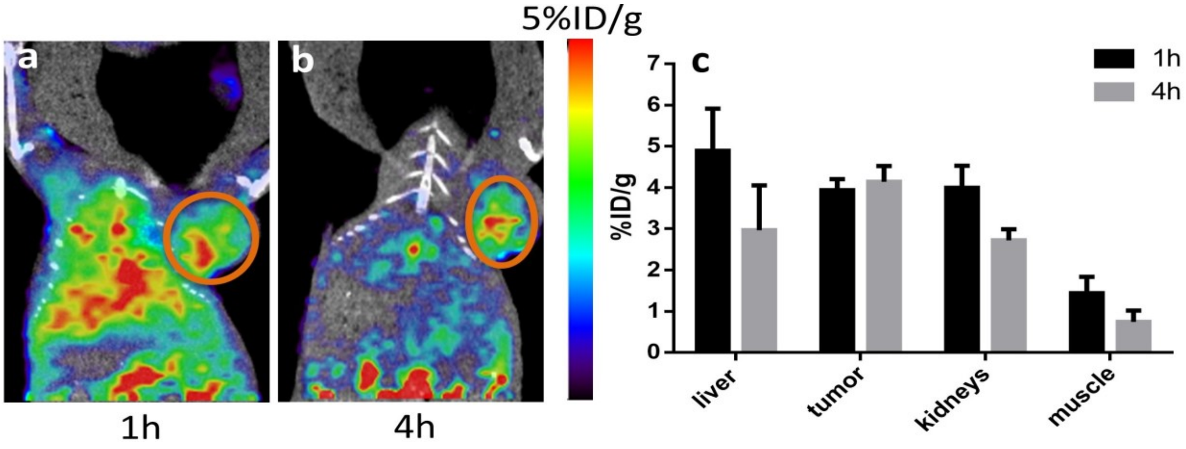

Figure 4.3 Representative PET/CT images of U87MG tumor bearing mice at a) 1h and b) 4h post injection of ^{18}F-TCO-DiPhTz-RGDyK. c) Quantitative uptake of the major organs determined from the PET images. Tumor regions are highlighted in orange circle

4.2.2 ^{18}F-sTCO-DiPhTz-RGDyK

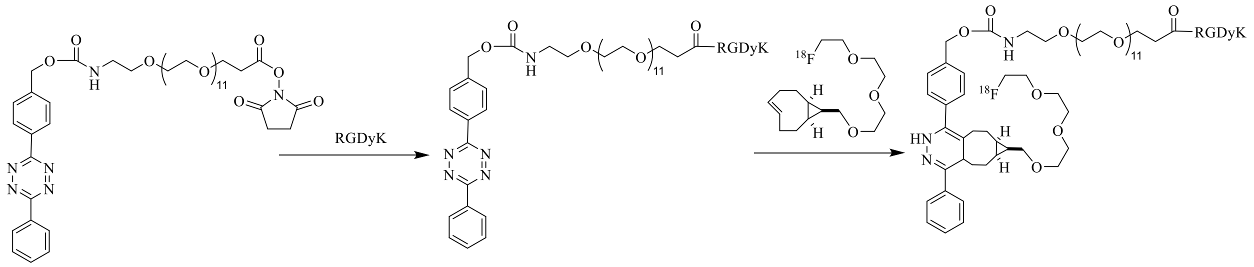

Scheme 4.2 Synthesis scheme of ^{18}F-sTCO-DiPhTz-RGDyK

With this encouraging result in hand, we further switched the ^{18}F-TCO to the second generation ^{18}F-sTCO since it was the most reactive dienophiles currently known towards tetrazine (*15*). As shown in Fig 4.4, DiPhTz-RGDyK was successfully radiolabeled with ^{18}F-sTCO at 49.6 ± 4.5% isolation yield in just 10 seconds. One of the two major radio peaks appeared in the HPLC profile matched the corresponding ^{19}F-sTCO-DiPhTz-RGDyK (Fig 4.4b and 4.4d) and the other one was likely the stereoisomers (*16*). The ^{18}F-sTCO-DiPhTz-RGDyK can be obtained at over 99% radiochemical purity after HPLC purification (Fig 4.4a).

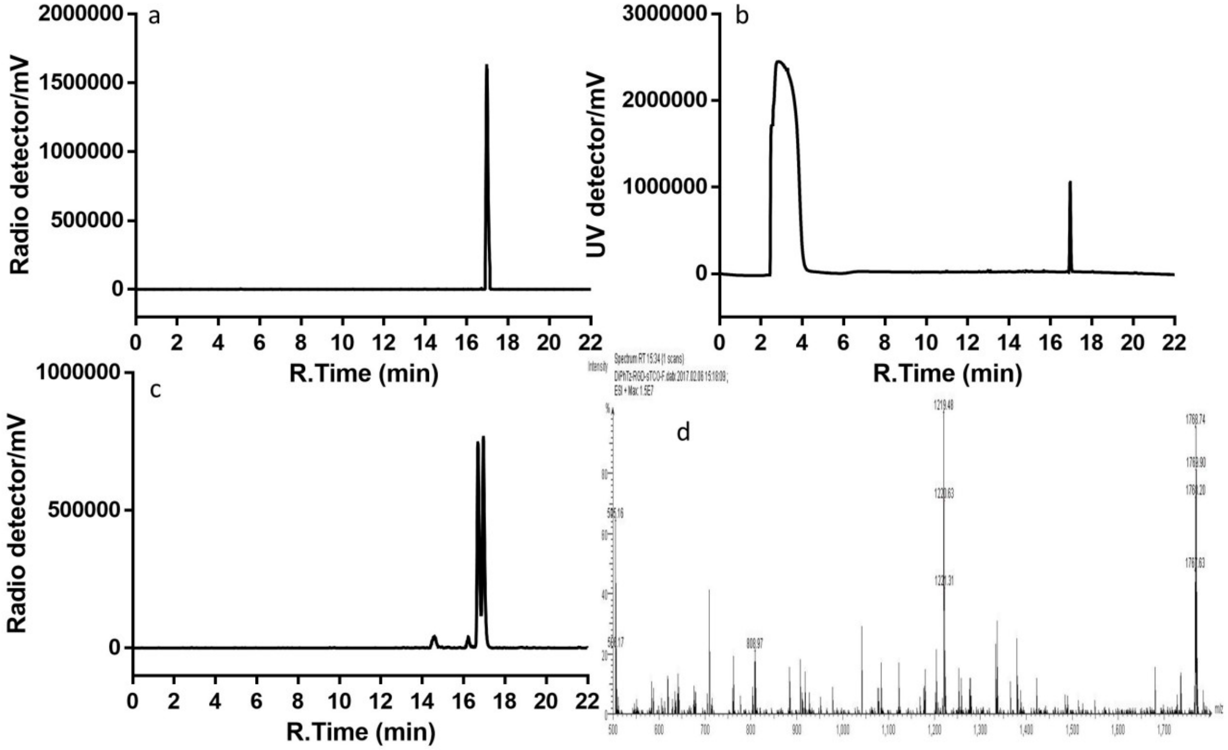

Figure 4.4 HPLC profile of a) purified ^{18}F-sTCO-DiPhTz-RGDyK. b) ^{19}F-sTCO-DiPhTz-RGDyK. c) crude of ^{18}F-sTCO ligation with DiPhTz-RGDyK. d) Mass spectrum of purified ^{19}F-sTCO-DiPhTz-RGDyK

Similar to ^{18}F-TCO-DiPhTz-RGDyK, the constructed ^{18}F-sTCO-DiPhTz-RGDyK was also intravenously injected into U87MG tumor bearing mice and subjected to static PET scan at 1 and 4h post injection. As can be seen in Fig 4.5, clear tumor uptake was observed as early as 1h post injection and the tumor became the brightest spot at 4h post injection. The quantitative uptake of major organs derived from the PET images were shown in Fig 4.5c. The tumor uptake was 6.9 ± 0.5 %ID/g and increased to 8.9 ±0.5 %ID/g at 1 and 4h post injection, respectively. The tumor to liver and tumor to kidney ratio was 1.6 and 2.4 at 4h post injection, respectively. Although the DiPhTz and sTCO system resulted in higher tumor uptake, high background signal was also observed which led to relatively poor tumor to background contrast.

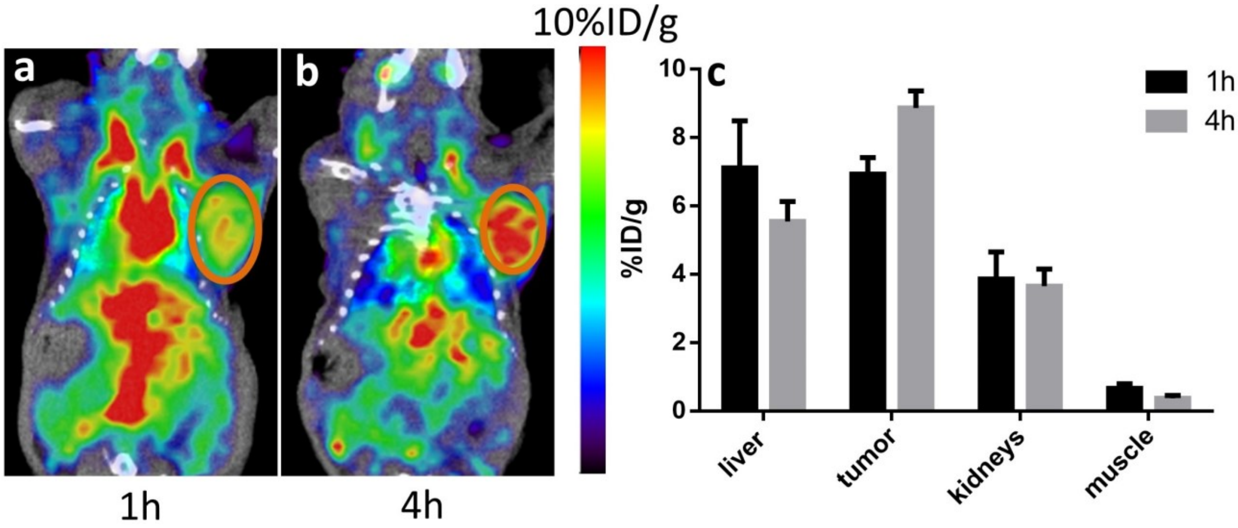

Figure 4.5 Representative PET/CT images of U87MG tumor bearing mice at a) 1h and b) 4h post injection of ^{18}F-sTCO-DiPhTz-RGDyK. c) Quantitative uptake of the major organs determined from the PET images. Tumor regions are highlighted in orange circle

4.2.3 ^{18}F-dTCO-DiPhTz-RGDyK

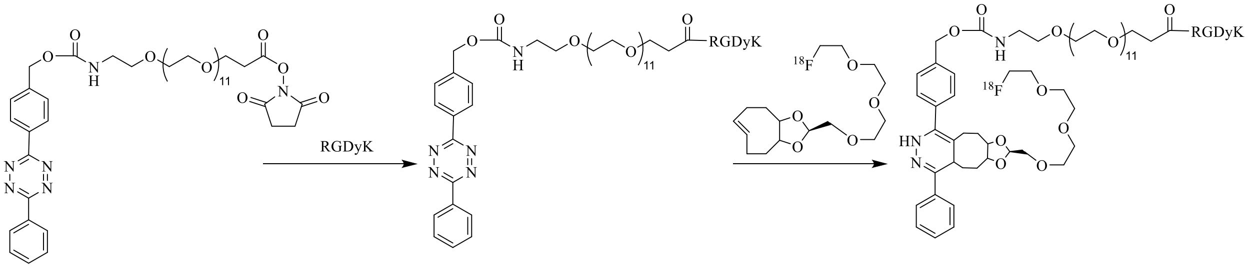

Scheme 4.3 Synthesis scheme of ^{18}F-dTCO-DiPhTz-RGDyk

Since the sTCO was too reactive and its precursor suffered from stability issue, we further exchanged the TCO moiety with another analogue dTCO which was less reactive but more stable than sTCO. The ^{18}F-dTCO was ligated with the DiPhTz-RGDyK in a few seconds and the isolation yield of the product was 53.2 ± 9.1%. The product showed 99% radiochemical purity after purification and was confirmed by the corresponding ^{19}F version (Fig 4.6).

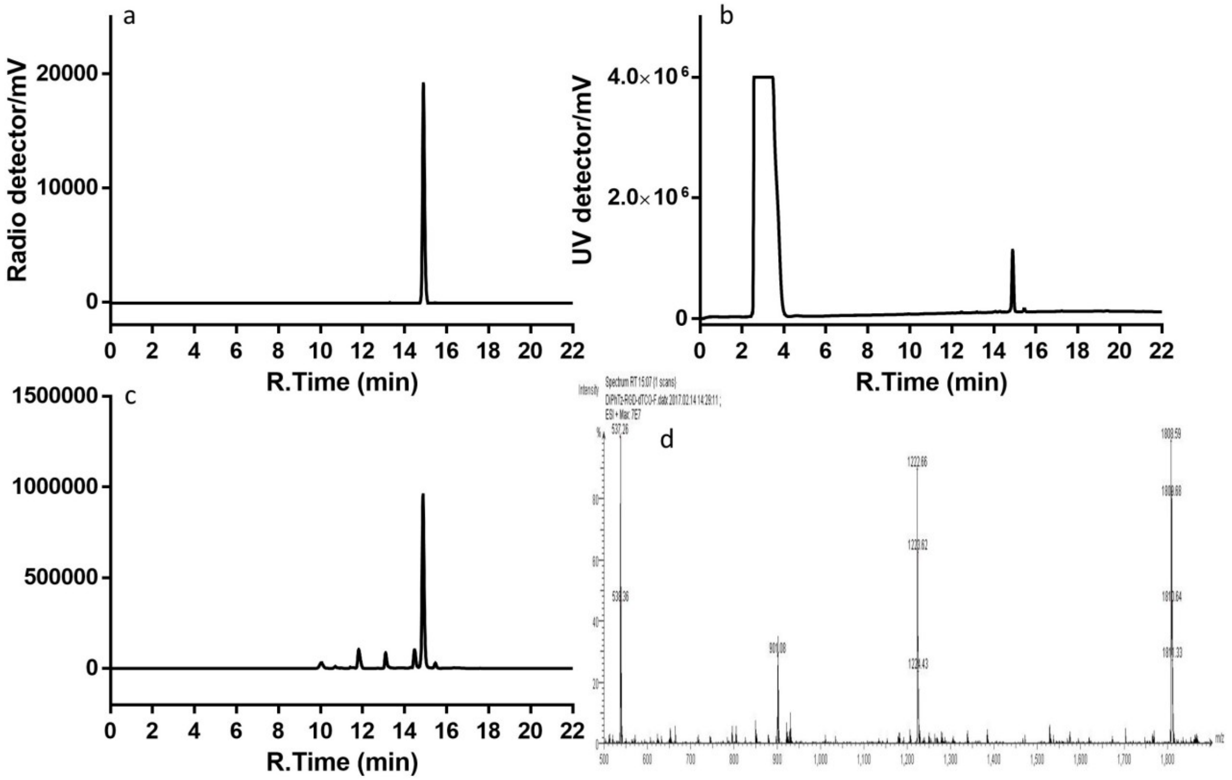

Figure 4.6 HPLC profile of a) purified ^{18}F-dTCO-DiPhTz-RGDyK. b) ^{19}F-dTCO-DiPhTz-RGDyK. c) crude of ^{18}F-dTCO ligation with DiPhTz-RGDyK. d) Mass spectrum of purified ^{19}F-dTCO-DiPhTz-RGDyK.

The PET images of U87MG xenografts after injection of ^{18}F-dTCO-DiPhTz-RGDyK was shown in Fig 4.7. The result was consistent to the probes constructed with DiPhTz-RGDyK and the other two TCOs. Persistent blood circulation of the probe was observed with increased tumor uptake over the 4h period. The tumor uptake was 4.4 ± 0.3 %ID/g and 4.6 ± 0.5 %ID/g at 1 and 4h post injection, respectively. This result more firmly proved our statement that the DiPhTz-TCOs ligation could be used in peptide based PET probes construction.

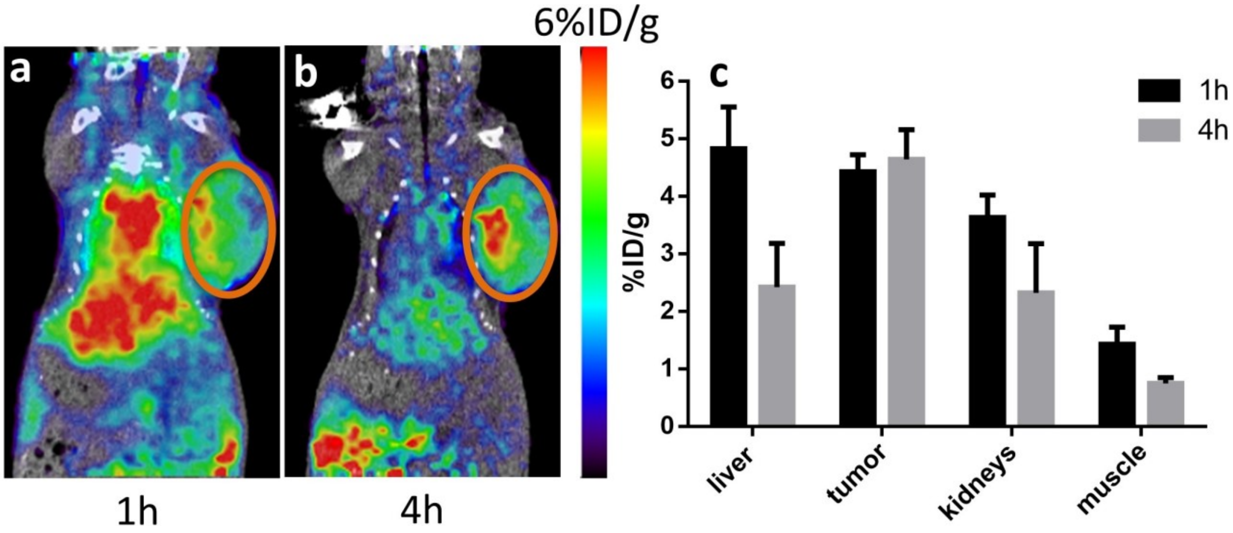

Figure 4.7 Representative PET/CT images of U87MG tumor bearing mice at a) 1h and b) 4h post injection of ^{18}F-dTCO-DiPhTz-RGDyK. c) Quantitative uptake of the major organs determined from the PET images. Tumor regions are highlighted in orange circle

4.2.4 ^{18}F-sTCO-MePhTz-RGDyK

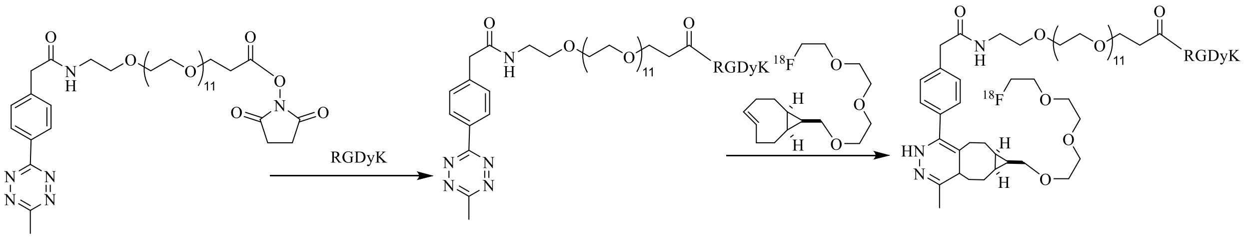

Scheme 4.4 Synthesis scheme of ^{18}F-sTCO-MePhTz-RGDyK

After validating different *trans*-cyclooctene motifs, we then explored how the tetrazine moiety will affect the PET probe construction and biodistribution. We started from the ^{18}F-sTCO-DiPhTz-RGDyK and replaced the DiPhTz with a more hydrophilic MePhTz analogue. MePhTz-RGDyK was synthesized from MePhTz-NHS and RGDyK peptide (Fig 4.8). The UV peak at 13min corresponds to the desired product and the identity was confirmed by LC-MS *m/z*: $[M+2H]^{2+}$ calcd $C_{65}H_{104}N_{14}O_{22}$ for 716.81; found 716.88.

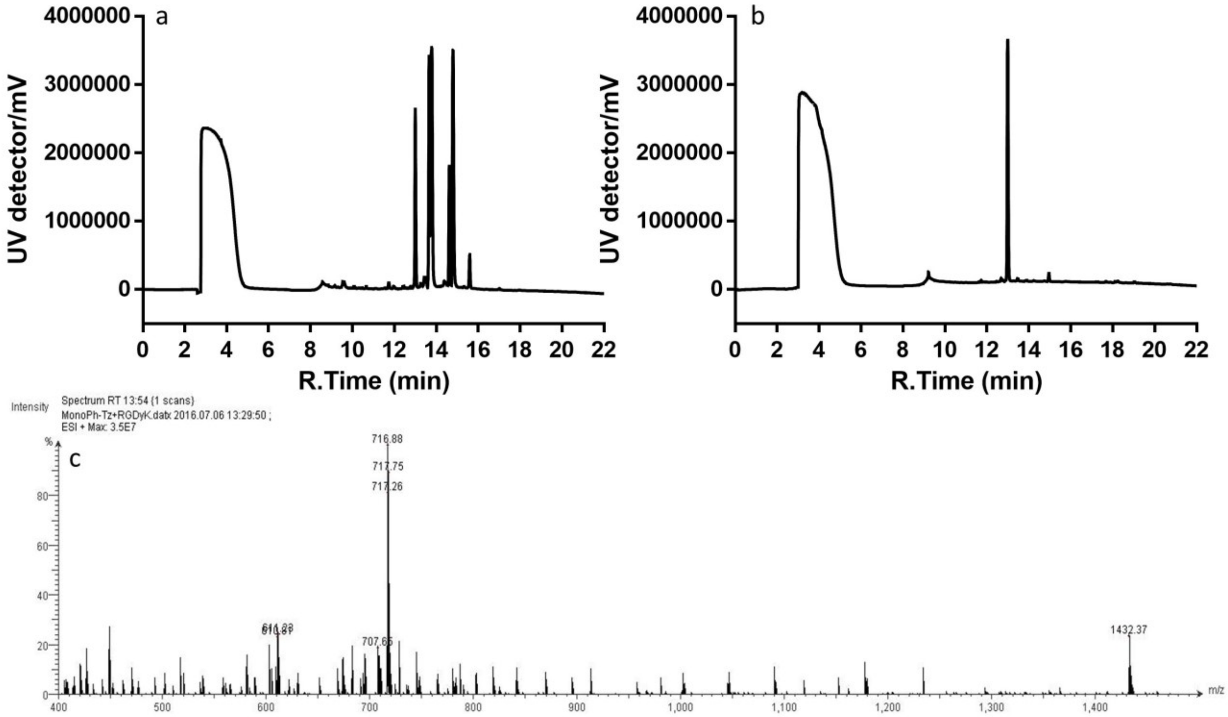

Figure 4.8 a) HPLC profile of crude reaction between MePhTz-NHS and RGDyK. b) HPLC profile of purified MePhTz-RGDyK. c) Mass spectrum of purified MePhTz-RGDyK

RGDyK modified with the new MePhTz could still be radiolabeled with ^{18}F-sTCO with 40.0 ± 4.6% isolation yield indicating the TTCO ligation allowed some buffer range for modification of both tetrazine and *trans*-cyclooctene sides. The purified ^{18}F-sTCO-MePhTz-RGDyK showed 99% radiochemical purity and the identity was confirmed by the ^{19}F “cold” standard (Fig 4.9).

As shown in Fig 4.10, the in vivo behavior of ^{18}F-sTCO-MePhTz-RGDyK was evaluated in U87MG xenograft. Although it demonstrated prominent tumor uptake at early time point (1.8 ± 0.4 %ID/g), a fast clearance from tumor was observed at 4h post injection (1.1 ± 0.0 %ID/g). This result demonstrated the feasibility of using different tetrazine to construct PET probes via TTCO ligation.

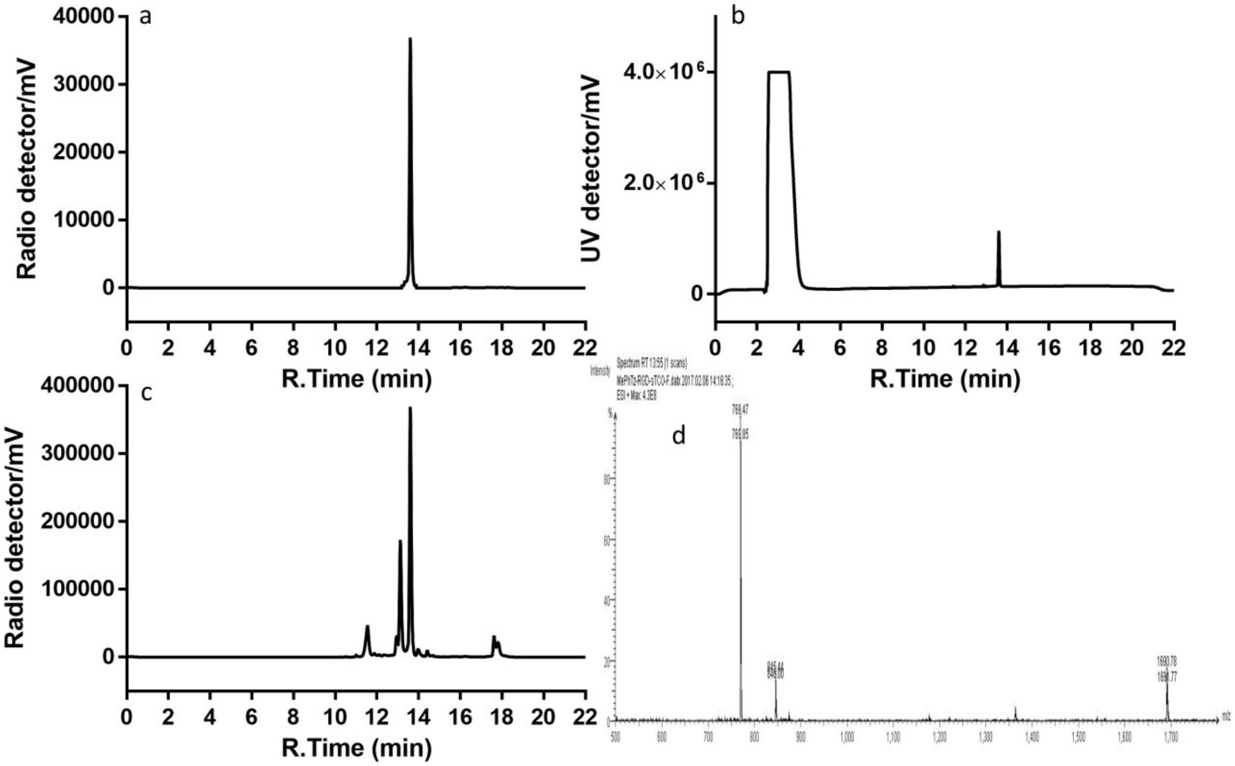

Figure 4.9 HPLC profile of a) purified ^{18}F-sTCO-MePhTz-RGDyK. b) ^{19}F-sTCO-MePhTz-RGDyK. c) crude of ^{18}F-sTCO ligation with MePhTz-RGDyK. d) Mass spectrum of purified ^{19}F-sTCO-MePhTz-RGDyK

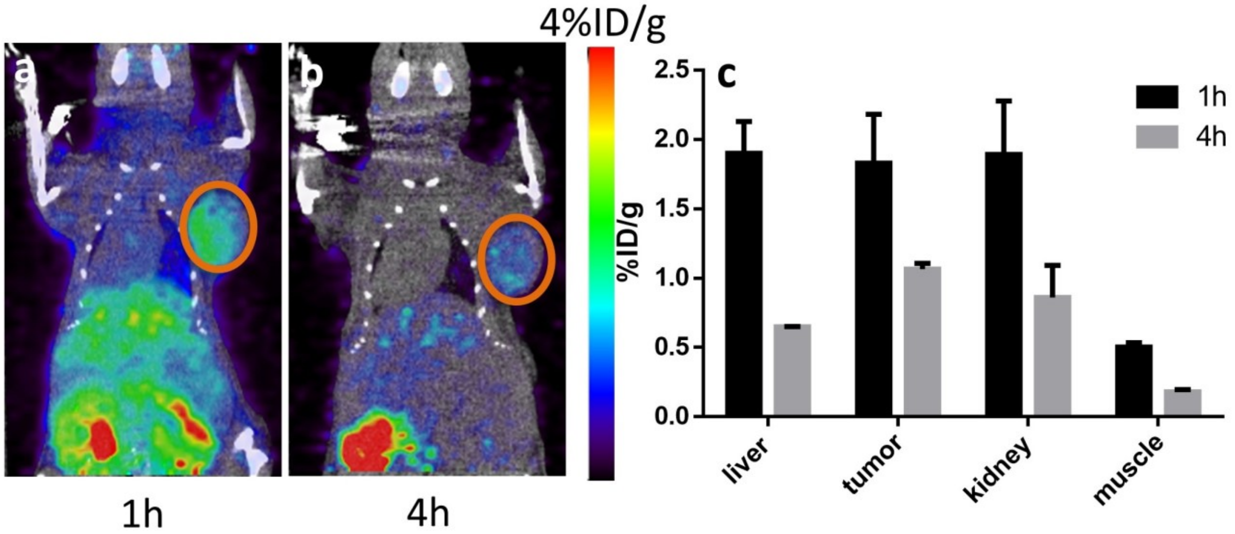

Figure 4.10 Representative PET/CT images of U87MG tumor bearing mice at a) 1h and b) 4h post injection of ^{18}F-sTCO-MePhTz-RGDyK. c) Quantitative uptake of the major organs determined from the PET images. Tumor regions are highlighted in orange circle

4.2.5 ^{18}F-sTCO-DiolTz-RGDyK

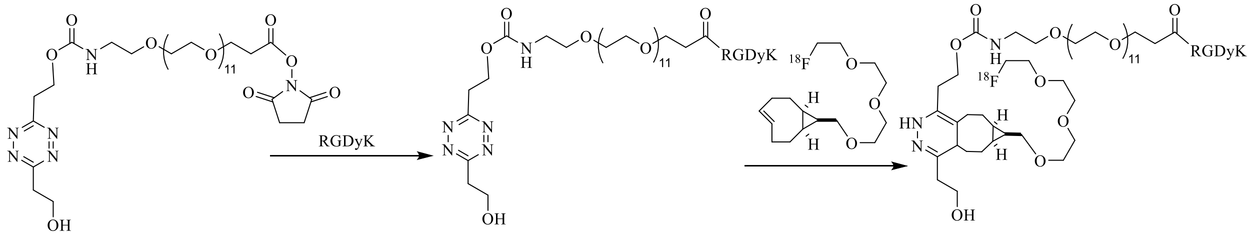

Scheme 4.5 Synthesis scheme of ^{18}F-sTCO-DiolTz-RGDyK

We also substituted the original tetrazine moiety with another tetrazine analogue DiolTz to further validate our statement. The DiolTz was conjugated with RGDyK via amide bond similarly to the DiPhTz and MePhTz analogues. The HPLC profiles of the crude and purified DiolTz-RGDyK were shown in Fig 4.11. LC-MS demonstrated the identity with *m/z*: [M+H+K]$^{2+}$ calcd $C_{61}H_{103}N_{14}O_{24}K$ for 727.78; found 727.92.

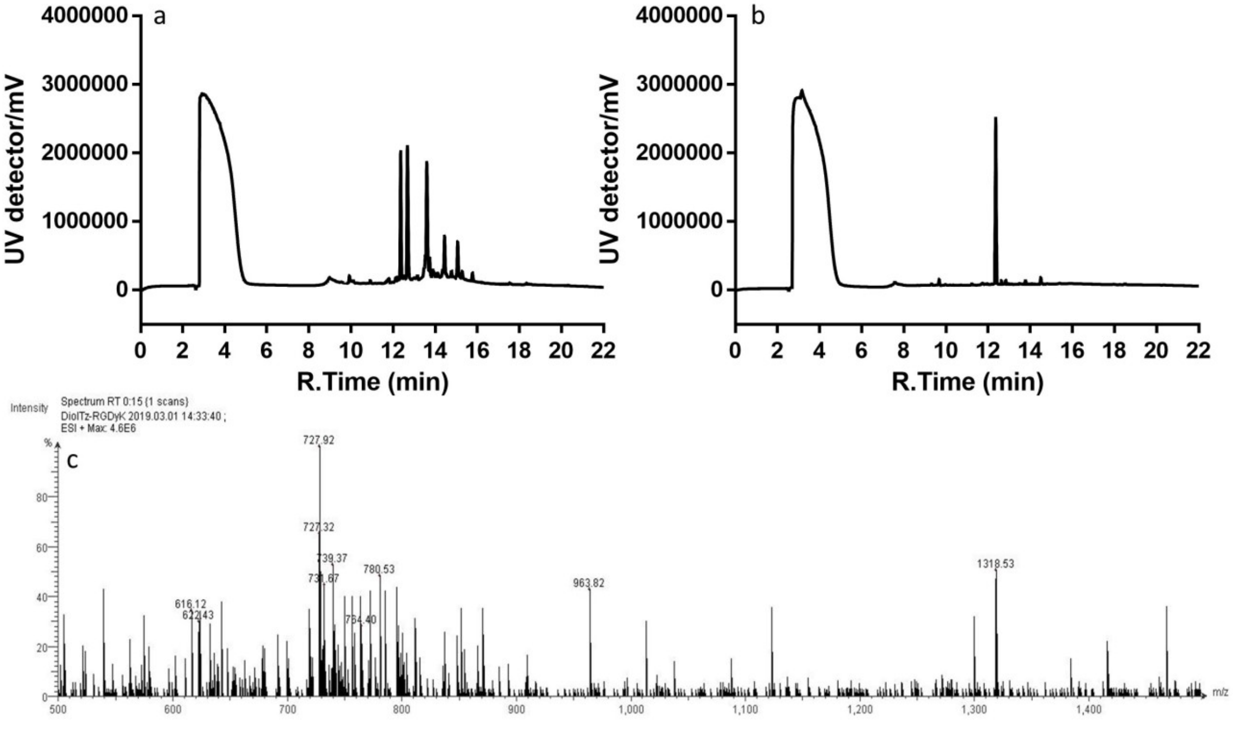

Figure 4.11 a) HPLC profile of crude reaction between DiolTz-NHS and RGDyK. b) HPLC profile of purified DiolTz-RGDyK. c) Mass spectrum of purified DiolTz-RGDyK

Similar to MePhTz-RGDyK, the newly constructed DiolTz-RGDyK could also be radio fluorinated by ^{18}F-sTCO via TTCO ligation and the isolation yield was 41.6 ± 1.5%. The product was appeared as isomers with 2 close radio peaks and the later one had the retention time matched with the ^{19}F-sTCO-DiolTz-RGDyK standard. The product can be readily purified with over 99% radiochemical purity (Fig 4.12).

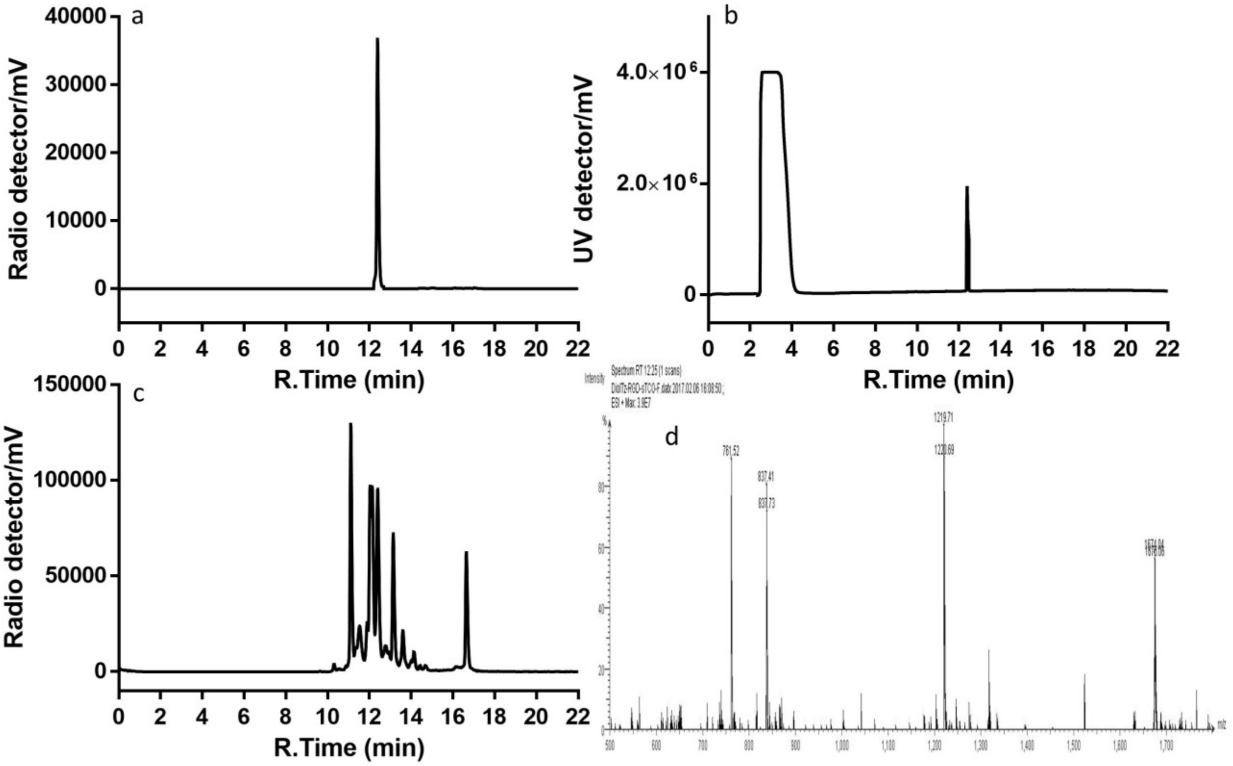

Figure 4.12 HPLC profile of a) purified ^{18}F-sTCO-DiolTz-RGDyK. b) ^{19}F-sTCO-DiolTz-RGDyK. c) crude of ^{18}F-sTCO ligation with DiolTz-RGDyK. d) Mass spectrum of purified ^{19}F-sTCO-DiolTz-RGDyK

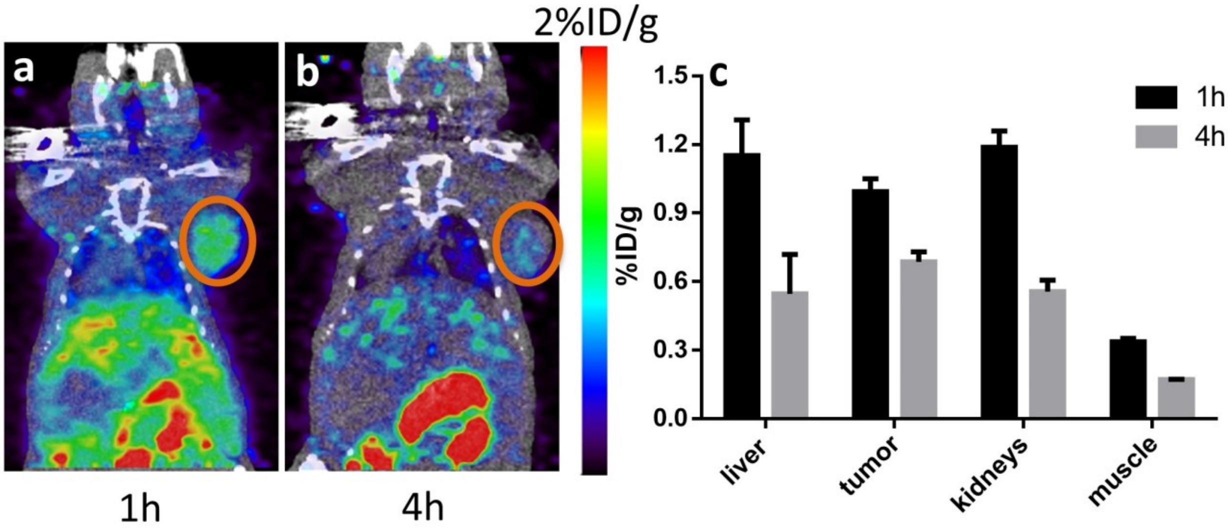

Figure 4.13 Representative PET/CT images of U87MG tumor bearing mice at a) 1h and b) 4h post injection of ^{18}F-sTCO-DiolTz-RGDyK. c) Quantitative uptake of the major organs determined from the PET images. Tumor regions are highlighted in orange circle

The biodistribution of ^{18}F-sTCO-DiolTz-RGDyK in U87MG xenografts was similar to that of ^{18}F-sTCO-MePhTz-RGDyK. As can be seen in Fig 4.13, the tumor was clearly localized with slightly lower absolute tumor uptake at both time points (1.0 ± 0.1 %ID/g and 0.7 ± 0.0 %ID/g at 1 and 4h post injection, respectively). These results further demonstrated that replacing the tetrazines will not affect the tumor targeting efficiency.

4.3 Radiolabeled NT Peptide for NTSR1 Targeted Imaging

The second model peptide we used was NT20.3 which was an agonist of neurotensin receptor 1 (NTSR1). NTSRs are transmembrane G protein-coupled receptors and consist with 3 subtypes, NTSR1, NTSR2 and NTSR3. The NTSR1 that we are looking into can cause phosphorylation of various proteins such as ERK and lead to cellular proliferation when activated by its agonist (*17-19*). Overexpression of NTSR1 has been demonstrated in several cancer types such as 91% of invasive ductal breast carcinomas, 60% of lung adenocarcinomas, 75% of ductal pancreatic adenocarcinomas, 90% of malignant mesothelioma, prostate cancer and colon adenocarcinomas (*20-26*). The selective and high expression of NTSR1 make it a promising target for both diagnostic and treatment applications. The natural full length of neurotensin peptide NT contains 13 amino acids with the sequence of pGlu-Leu-Tyr-Glu-Asn-Lys-Pro-Arg-Arg-Pro-Tyr-Ile-Leu-OH (*27*). The core sequence to mimic its natural effect is NT (8-13). However due to the stability issue, a sequence modification was introduced to NT (8-13) and NT20.3 was created with sequence of Ac-Lys-Pro-Me-Arg-Arg-Pro-Tyr-Tle-Leu-OH (*28*). In this section we radiolabel these peptides with our TTCO ligation platform and evaluate their in vivo behavior in several tumor models.

4.3.1 ^{18}F-sTCO-DiPhTz-NT

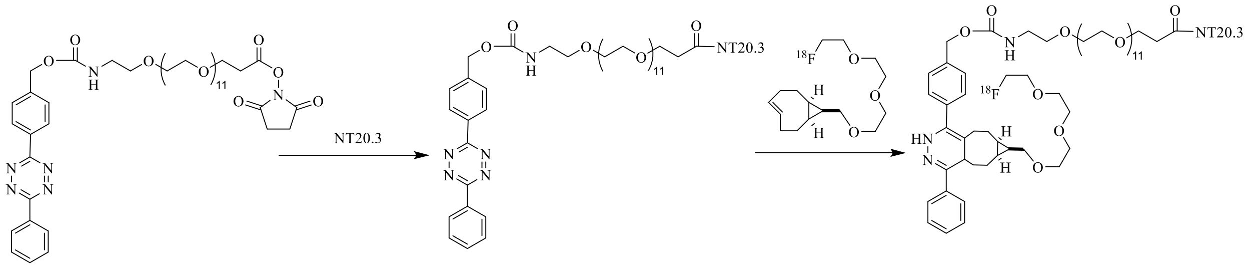

Scheme 4.6 Synthesis scheme of ^{18}F-sTCO-DiPhTz-NT

We first radiolabel the NT20.3 peptide with the sTCO-DiPhTz system. Figure 4.14 showed the modification of NT20.3 with DiPhTz-NHS. The major peak at 15.2min correspond the DiPhTz-NT and can be obtained at 99% purity after HPLC purification. The identity was confirmed by LC-MS *m/z*: $[M+2H]^{2+}$ calcd $C_{95}H_{152}N_{20}O_{26}$ for 995.18; found 995.15. The hydrophilicity of the probe was evaluated by measuring the octanol-water partition coefficient and the resulting logP value was -0.69 ± 0.03.

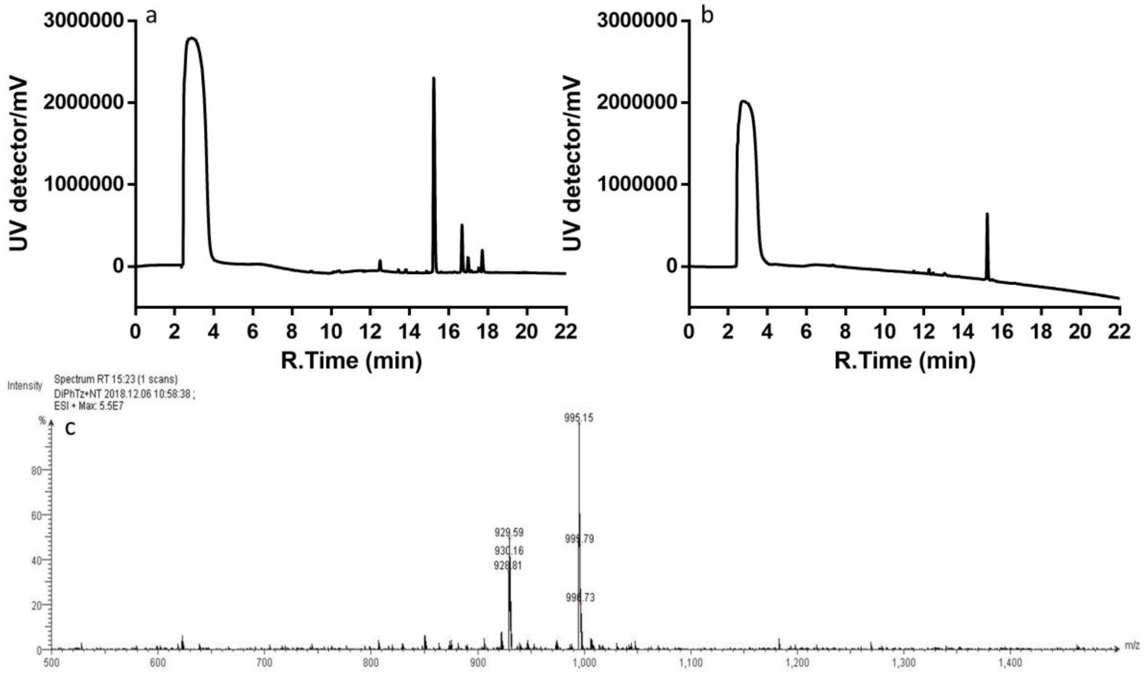

Figure 4.14 a) HPLC profile of crude reaction between DiPhTz-NHS and NT. b) HPLC profile of purified DiPhTz-NT. c) Mass spectrum of purified DiPhTz-NT

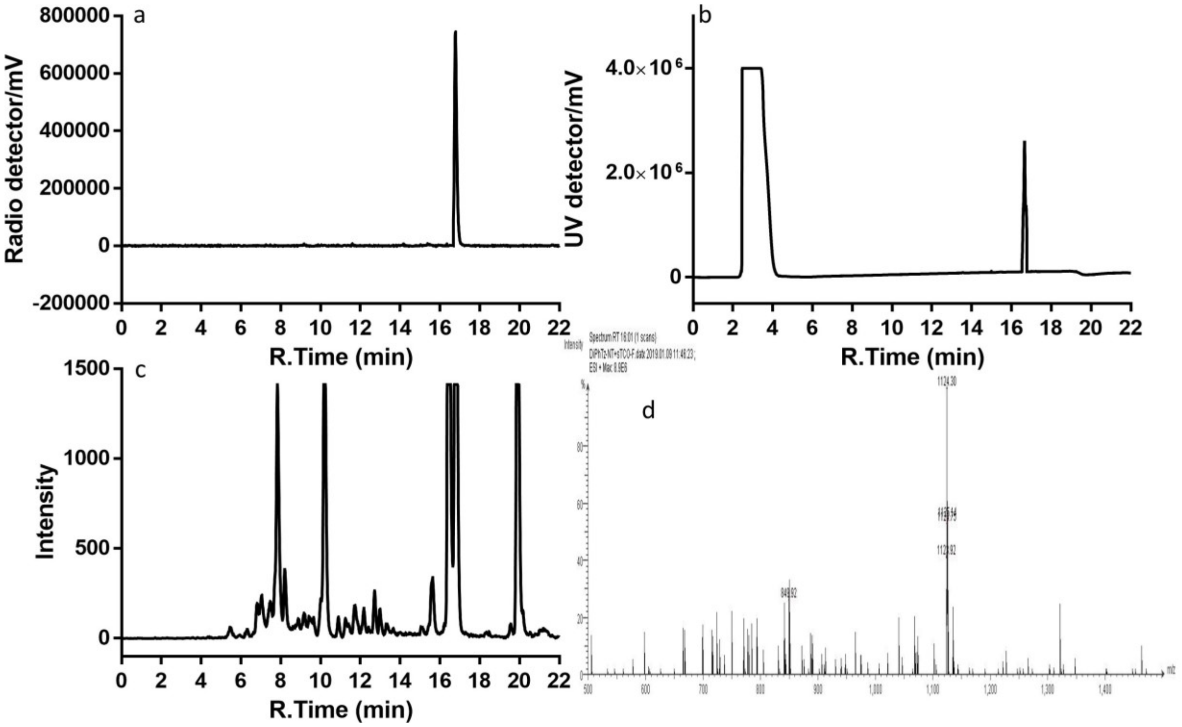

Figure 4.15 HPLC profile of a) purified ^{18}F-sTCO-DiPhTz-NT. b) ^{19}F-sTCO-DiPhTz-NT. c) crude of ^{18}F-sTCO ligation with DiPhTz-NT. d) Mass spectrum of purified ^{19}F-sTCO-DiPhTz-NT

^{18}F-sTCO-DiPhTz-NT was synthesized in the same pattern as ^{18}F-sTCO-DiPhTz-RGDyK with 42.7 ± 6.2% isolation yield and 99% radiochemical purity after purification. An independently prepared ^{19}F-sTCO-DiPhTz-NT was synthesized to confirm the identity of the obtained radio tracer. The HPLC profile of purified tracer and reaction crude was shown in Fig 4.15.

The targeting efficiency of constructed PET probe was evaluated in NTSR1 positive pancreatic cancer model AsPC1 xenograft. As shown in Fig 4.16, the tumor uptake was 4.3 ± 0.1 %ID/g at 1h post injection and maintained at 4.6 ± 0.1 %ID/g at 4h p.i. Though the absolute tumor uptake was enhanced compared with our previously reported NT analogue based PET probe, the overall contrast was decreased due the high signal from blood pool (*29*). Nevertheless, this result proved that the TTCO ligation could be served as a platform to construct PET probes for various kinds of peptide ligand.

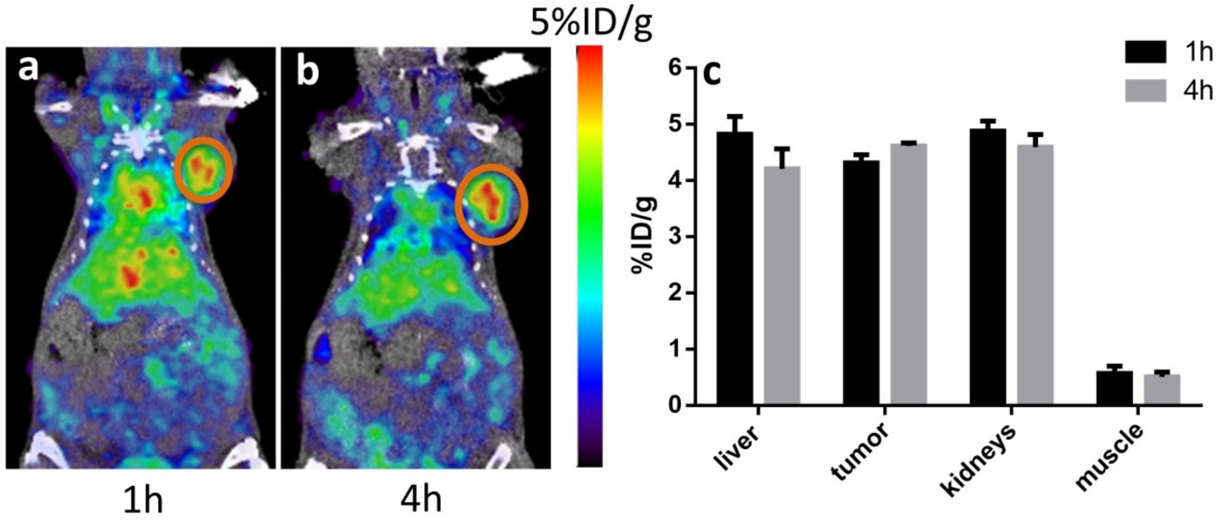

Figure 4.16 Representative PET/CT images of AsPC1 tumor bearing mice at a) 1h and b) 4h post injection of ^{18}F-sTCO-DiPhTz-NT. c) Quantitative uptake of the major organs determined from the PET images. Tumor regions are highlighted in orange circle

4.3.2 ^{18}F-sTCO-DiolTz-NT

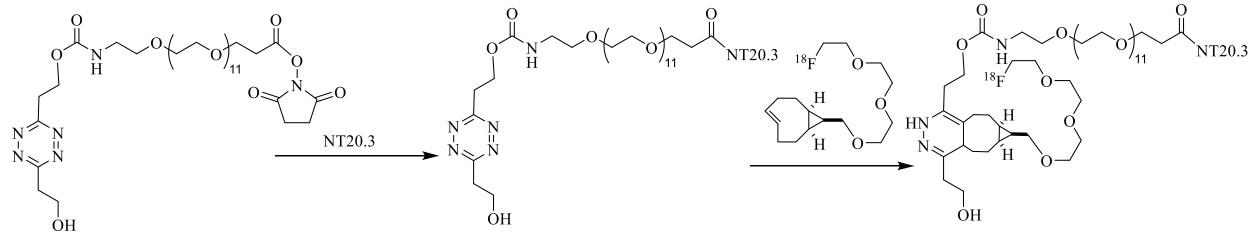

Scheme 4.7 Synthesis scheme of ^{18}F-sTCO-DiolTz-NT

We also screened several TTCO system combinations for NT20.3 based PET probe construction. As shown in Fig 4.17, DiolTz-NT was synthesized via amide bond conjugation and purified by RP-HPLC. The peak with 14.1min retention time showed the correct *m/z*: $[M+2H]^{2+}$ calcd $C_{86}H_{150}N_{20}O_{27}$ for 948.12; found 948.05.

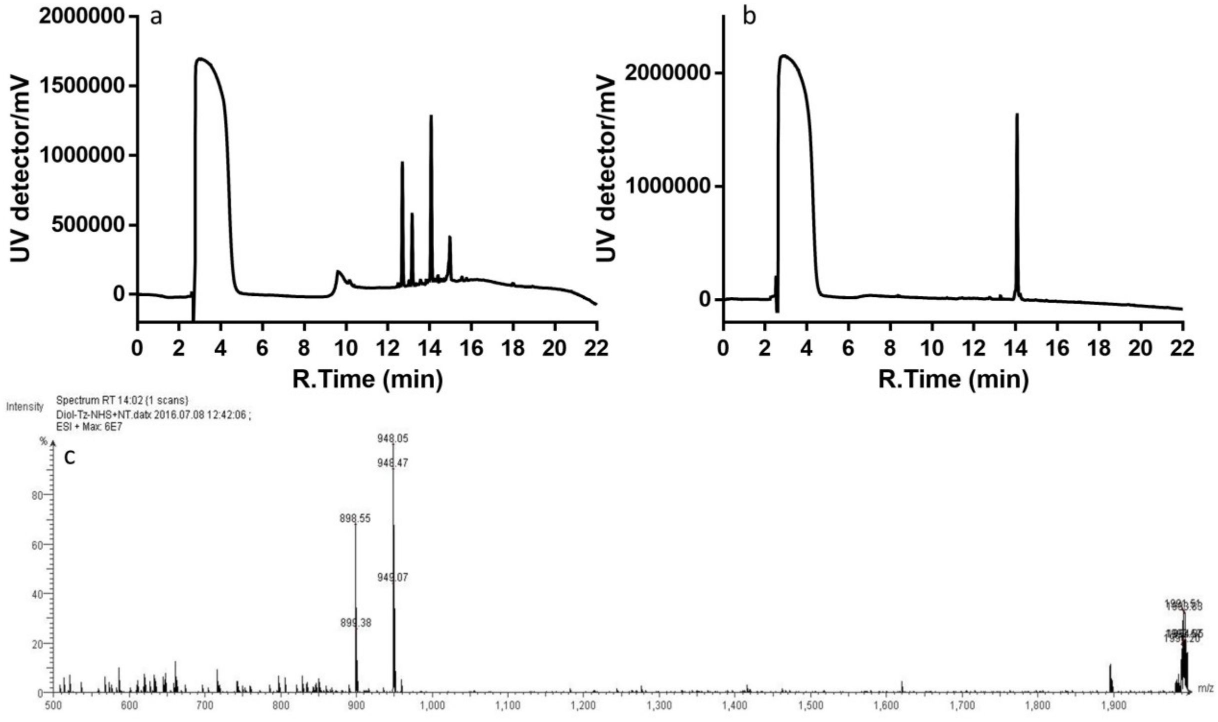

Figure 4.17 a) HPLC profile of crude reaction between DiolTz-NHS and NT. b) HPLC profile of purified DiolTz-NT. c) Mass spectrum of purified DiolTz-NT

Not surprisingly, the DiolTz-NT was also successfully radiolabeled with ^{18}F-sTCO in a few seconds under mild condition and the isolation yield was calculated to be 41.1 ± 9.3%. The radiochemical purity of the purified PET tracer was determined to be 99% and the identity was confirmed by the corresponding ^{19}F standard (Fig 4.18). The logP of this tracer was -0.98 ± 0.08, which is more hydrophilic than ^{18}F-sTCO-MePhTz-NT and ^{18}F-sTCO-DiPhTz-NT.

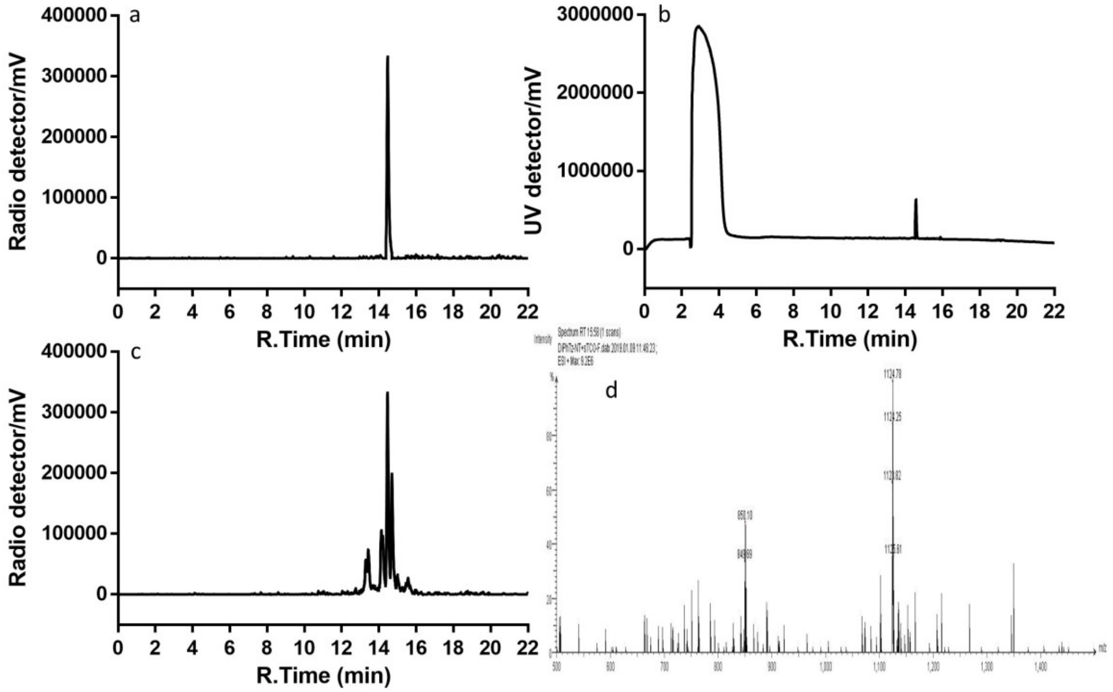

Figure 4.18 HPLC profile of a) purified ^{18}F-sTCO-DiolTz-NT. b) ^{19}F-sTCO-DiolTz-NT. c) crude of ^{18}F-sTCO ligation with DiolTz-NT. d) Mass spectrum of purified ^{19}F-sTCO-DiolTz-NT

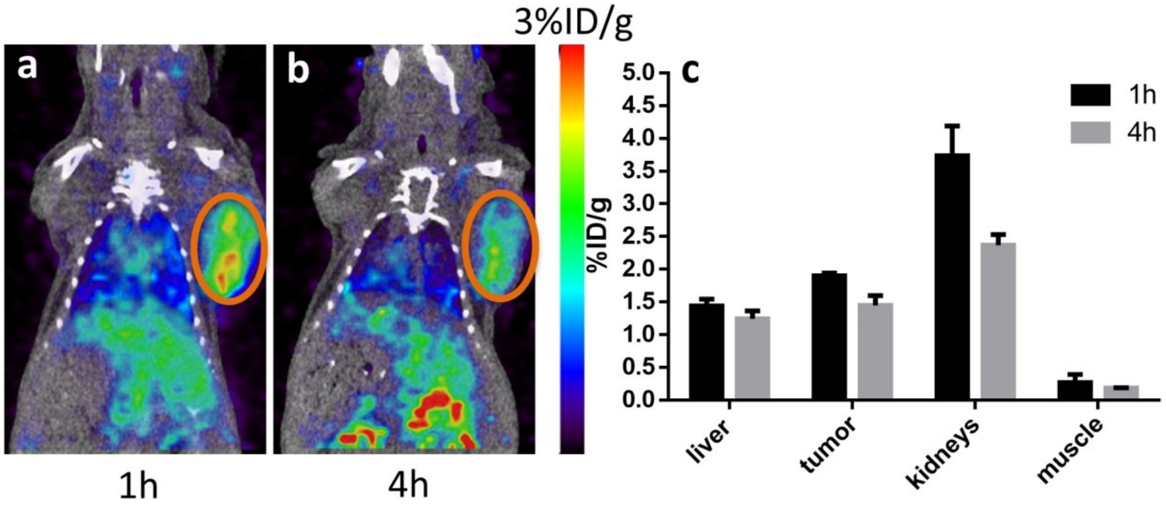

Figure 4.19 Representative PET/CT images of H1299 tumor bearing mice at a) 1h and b) 4h post injection of ^{18}F-sTCO-DiolTz-NT. c) Quantitative uptake of the major organs determined from the PET images. Tumor regions are highlighted in orange circle

The constructed ^{18}F-sTCO-DiolTz-NT was subjected to static PET scan in H1299 tumor models. As can be seen in Fig 28, it showed clear tumor uptake at 1 and 4h post injection with uptakes of 1.9 ± 0.0 %ID/g and 1.4 ± 0.2 %ID/g, respectively. The tumor to muscle ratio was 7.9 ± 2.5 and 7.9 ± 0.8 at 1 and 4h post injection. These data were consistent with the previous results obtained from RGDyK and demonstrated that TTCO ligation can be used to construct various small molecular peptide based PET probes.

4.3.3 ^{18}F-sTCO-MePhTz-NT

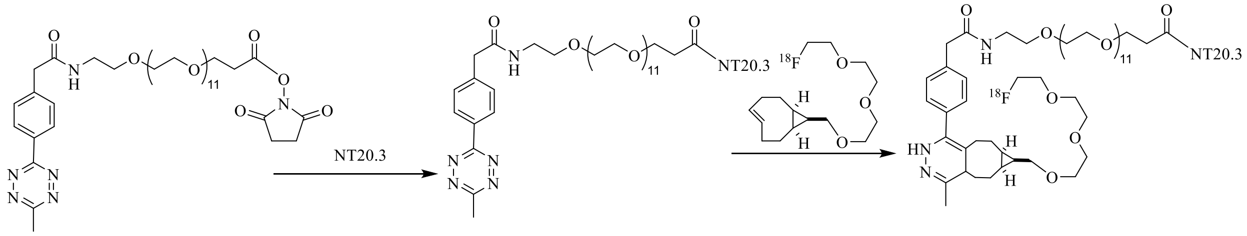

Scheme 4.8 Synthesis scheme of ^{18}F-sTCO-MePhTz-NT

Despite of DiolTz, another hydrophilic tetrazine analogue MePhTz was engineered on NT20.3 for TTCO ligation test and the constructed PET probe was subjected to PET imaging. The MePhTz-NT was synthesized in a similar pattern to MePhTz-RGDyK. The UV peak at 14.3min on the HPLC showed the correct *m/z*: $[M+2H]^{2+}$ calcd $C_{90}H_{150}N_{20}O_{25}$ for 956.15; found 956.00 (Fig 4.20).

The ^{18}F-sTCO-MePhTz-NT could be rapidly prepared by mixing the ^{18}F-sTCO with MePhTz-NT and incubation at room temperature for 10 seconds. The isolation yield was 51.8 ± 5.8% and the identity of the collected radio tracer was confirmed by coinjection with the ^{19}F-sTCO-MePhTz-NT standard. The purified tracer showed over 99% radiochemical purity (Fig 4.21). The octanol-water partition coefficient of ^{18}F-sTCO with MePhTz-NT was measured and the logP value was -0.87 ± 0.09.

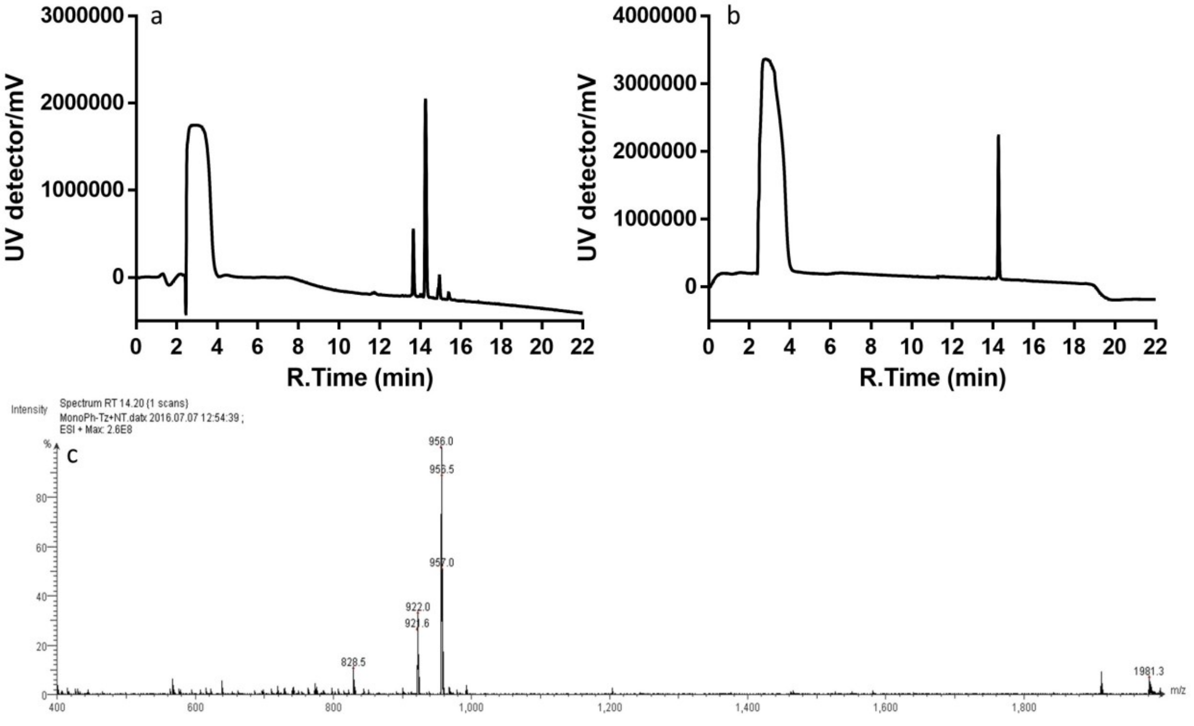

Figure 4.20 a) HPLC profile of crude reaction between MePhTz-NHS and NT. b) HPLC profile of purified MePhTz-NT. c) Mass spectrum of purified MePhTz-NT

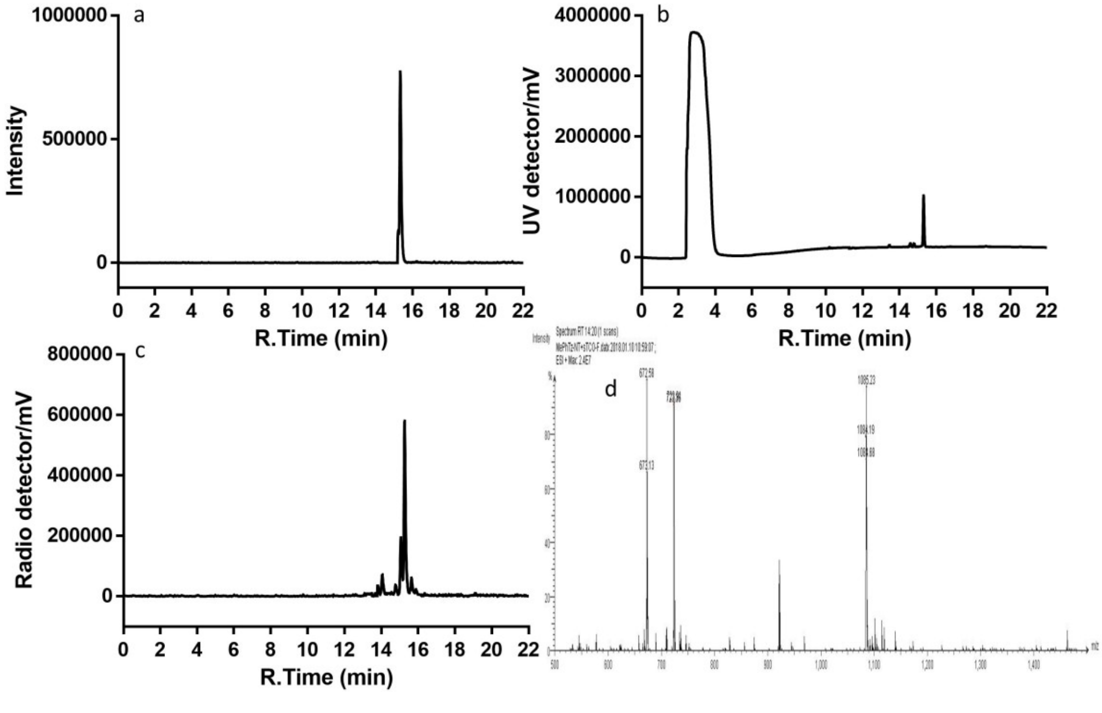

Figure 4.21 HPLC profile of a) purified ^{18}F-sTCO-MePhTz-NT. b) ^{19}F-sTCO-MePhTz-NT. c) crude of ^{18}F-sTCO ligation with MePhTz-NT. d) Mass spectrum of purified ^{19}F-sTCO-MePhTz-NT

We then evaluated the targeting efficiency and pharmacokinetics of ^{18}F-sTCO-MePhTz-NT in PC3 tumor bearing mice. As can be seen in Fig 4.22, tumors were clearly visualized at both time points, indicating a reasonable targeting efficiency in vivo. The tumor uptake was 1.5 ± 0.1 %ID/g and 1.2 ± 0.2 %ID/g at 0.5h and 3.5h post injection, respectively. Relatively low background signal was observed with a tumor to muscle ratio of 6.5 ± 1.5 at 0.5h and 6.4 ± 0.5 at 3.5h post injection. These data further demonstrated that several combinations of TTCO system could be utilized to construct PET probes with different pharmacokinetics while maintaining reasonable targeting efficiency.

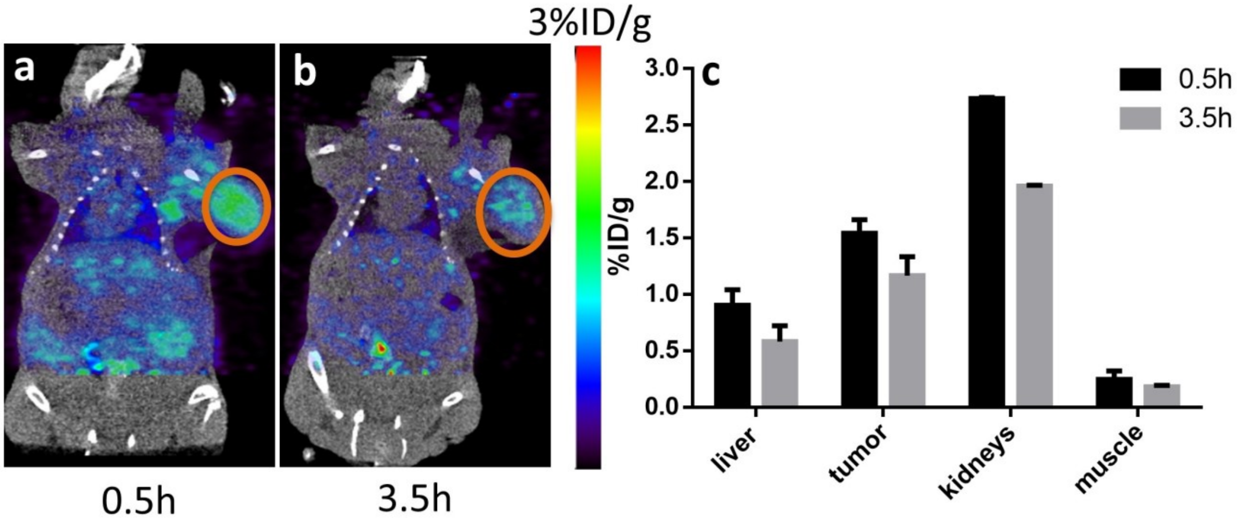

Figure 4.22 Representative PET/CT images of PC3 tumor bearing mice at a) 0.5h and b) 3.5h post injection of ^{18}F-sTCO-MePhTz-NT. c) Quantitative uptake of the major organs determined from the PET images. Tumor regions are highlighted in orange circle

4.3.4 ^{18}F-dTCO-MePhTz-NT

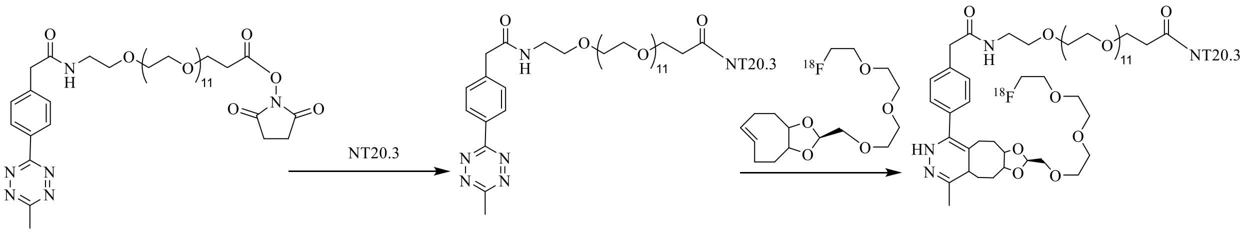

Scheme 4.9 Synthesis scheme of ^{18}F-dTCO-MePhTz-NT

With the conclusion that the hydrophilic MePhTz can be used in TTCO ligation, we then combined it with several newly developed hydrophilic *trans*-cyclooctenes and applied in NT20.3 peptide based PET probe construction.

The first TCO candidate we choose was ^{18}F-dTCO. ^{18}F-dTCO was successfully ligated to MePhTz-NT with 71.3 ± 1.2% isolation yield and the radiochemical purity could reach 99% after initial HPLC purification. The identity was confirmed by an independently synthesized ^{19}F version of the probe (Fig 4.23). The logP value of ^{18}F-dTCO-MePhTz-NT was -1.59 ± 0.01 while that of ^{18}F-sTCO-MePhTz-NT was -1.10 ± 0.04, indicating the more hydrophilic TCO motif would lead to a more hydrophilic TTCO ligation product.

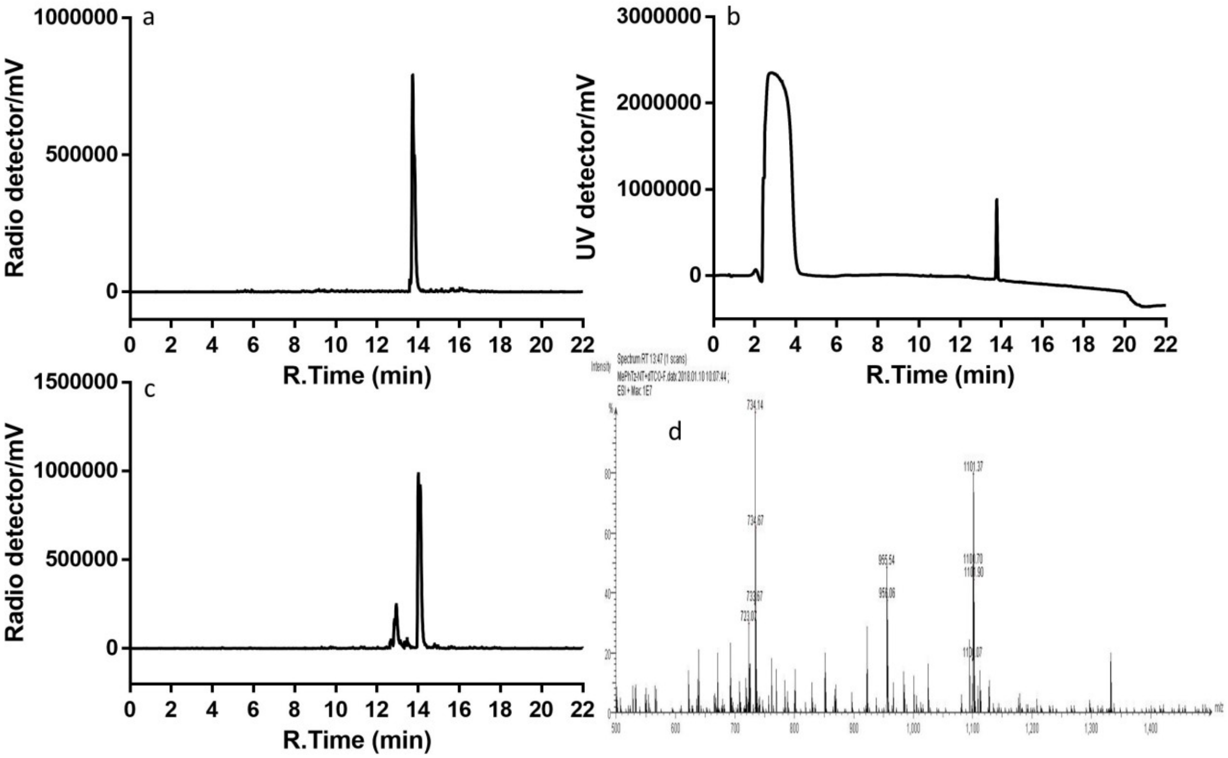

Figure 4.23 HPLC profile of a) purified ^{18}F-dTCO-MePhTz-NT. b) ^{19}F-dTCO-MePhTz-NT. c) crude of ^{18}F-dTCO ligation with MePhTz-NT. d) Mass spectrum of purified ^{19}F-dTCO-MePhTz-NT

We then evaluated the targeting efficiency and pharmacokinetics of ^{18}F-dTCO-MePhTz-NT in PC3 tumor bearing mice. As can be seen in Fig 4.24, the tumor uptake was 2.1 ± 0.4

%ID/g and 0.9 ± 0.2 %ID/g at 0.5 and 3.5h post injection, respectively. The tumor to muscle ratio was 3.8 ± 0.9 at 0.5h and 11.9 ± 4.3 at 3.5h post injection, respectively.

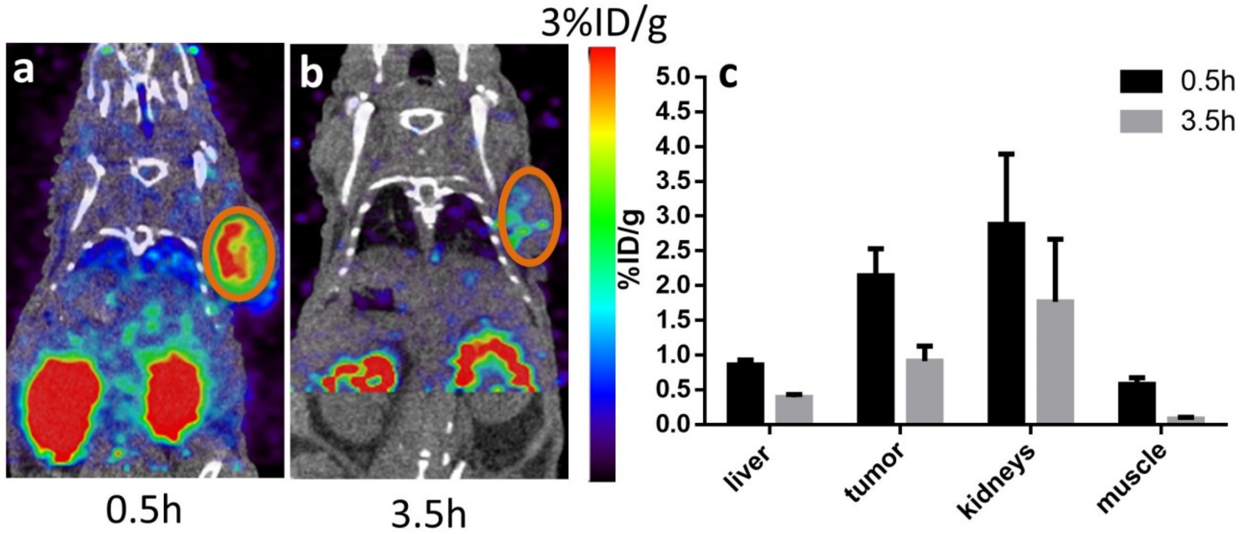

Figure 4.24 Representative PET/CT images of PC3 tumor bearing mice at a) 0.5h and b) 3.5h post injection of ^{18}F-dTCO-MePhTz-NT. c) Quantitative uptake of the major organs determined from the PET images. Tumor regions are highlighted in orange circle

4.3.5 ^{18}F-oTCO-MePhTz-NT

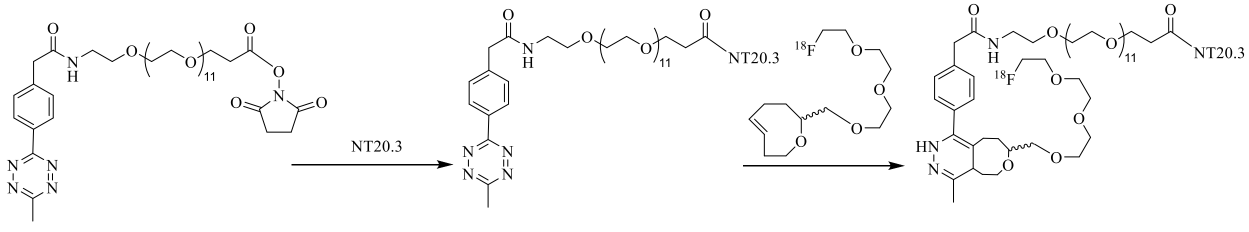

Scheme 4.10 Synthesis scheme of ^{18}F-oTCO-MePhTz-NT

We then introduced *trans*-5-oxocene (oTCO), which was significantly more hydrophilic than both dTCO and sTCO, to the TTCO ligation. The logP value for ^{18}F-oTCO was 0.57 ± 0.02. The ^{18}F-oTCO derived probe ^{18}F-oTCO-MePhTz-NT was prepared by mixing ^{18}F-oTCO with MePhTz-NT under mild condition and allowed to react for 10 seconds. As shown in Fig 4.25, no ^{18}F-oTCO was left indicating a complete consumption of it and the isolation yield was 72.0 ± 3.3%. The radiochemical purity was over 99% after HPLC purification. The logP of ^{18}F-oTCO-

MePhTz-NT was -2.47 ± 0.05, which was much more hydrophilic than ^{18}F-sTCO-MePhTz-NT and ^{18}F-dTCO-MePhTz-NT.

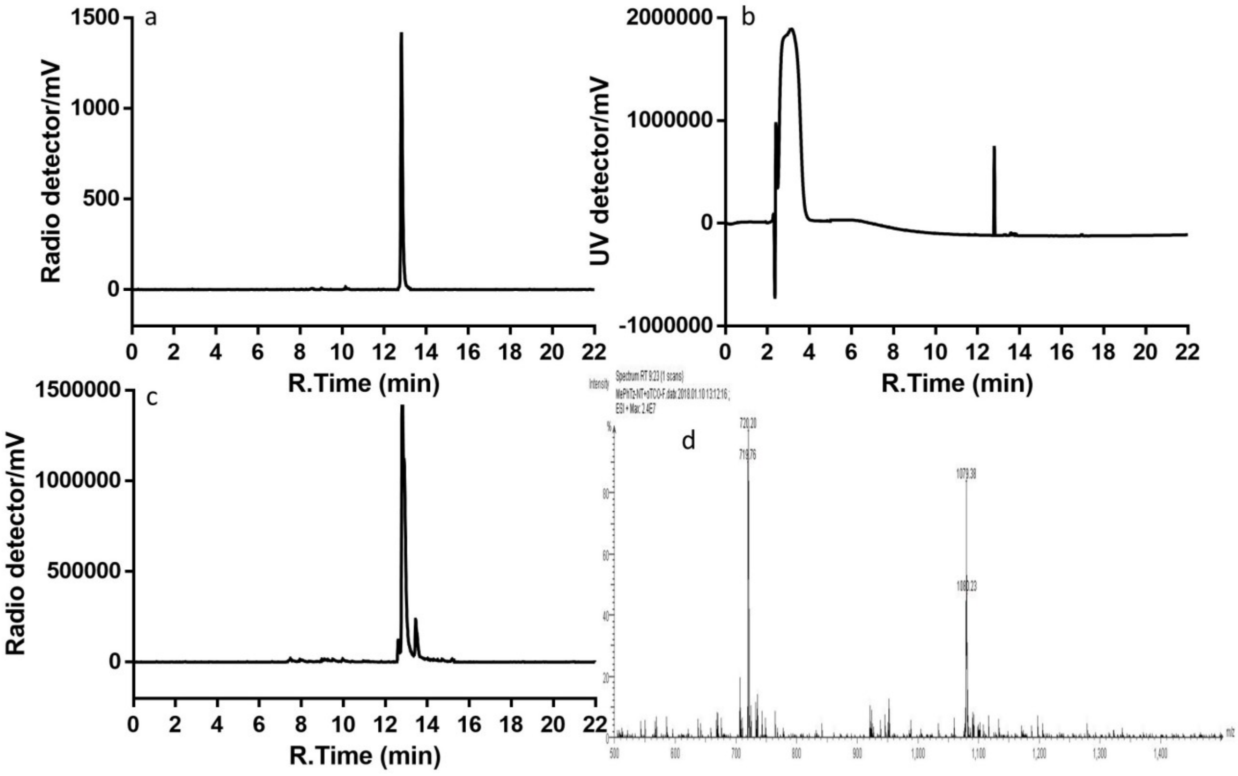

Figure 4.25 HPLC profile of a) purified ^{18}F-oTCO-MePhTz-NT. b) ^{19}F-oTCO-MePhTz-NT. c) crude of ^{18}F-oTCO ligation with MePhTz-NT. d) Mass spectrum of purified ^{19}F-oTCO-MePhTz-NT

This PET probe constructed from a more hydrophilic *trans*-cyclooctene was also evaluated in the same PC3 tumor xenografts. As shown in Fig 4.26, tumor regions could be clearly localized with uptake of 1.7 ± 0.1 %ID/g and 1.1 ± 0.1 %ID/g at 0.5h and 3.5h post injection. Although there was not much difference in the absolute tumor uptake between this more hydrophilic PET probe and the previously reported sTCO and dTCO derived probes, the tumor to muscle ratio was significantly improved. The tumor to muscle ratio was 15.8 ± 2.2 at 0.5h and 16.2 ± 2.3 at 3.5h post injection. Given that the tumor uptake of ^{18}F-oTCO-MePhTz-NT was not significantly higher, it could be concluded that the high tumor to background ratio was due to the fast clearance rate at non-specific binding regions such as muscle and liver.

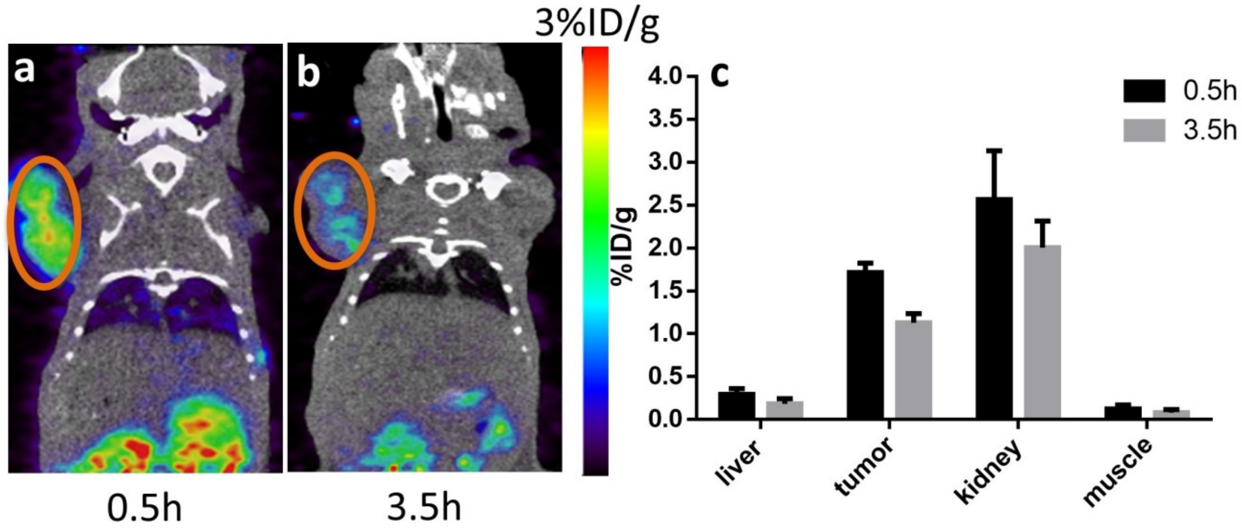

Figure 4.26 Representative PET/CT images of PC3 tumor bearing mice at a) 0.5h and b) 3.5h post injection of ^{18}*F-oTCO-MePhTz-NT. c) Quantitative uptake of the major organs determined from the PET images. Tumor regions are highlighted in orange circle*

4.3.6 ^{64}Cu-dTCO-PEG-DOTA-MePhTz-NT

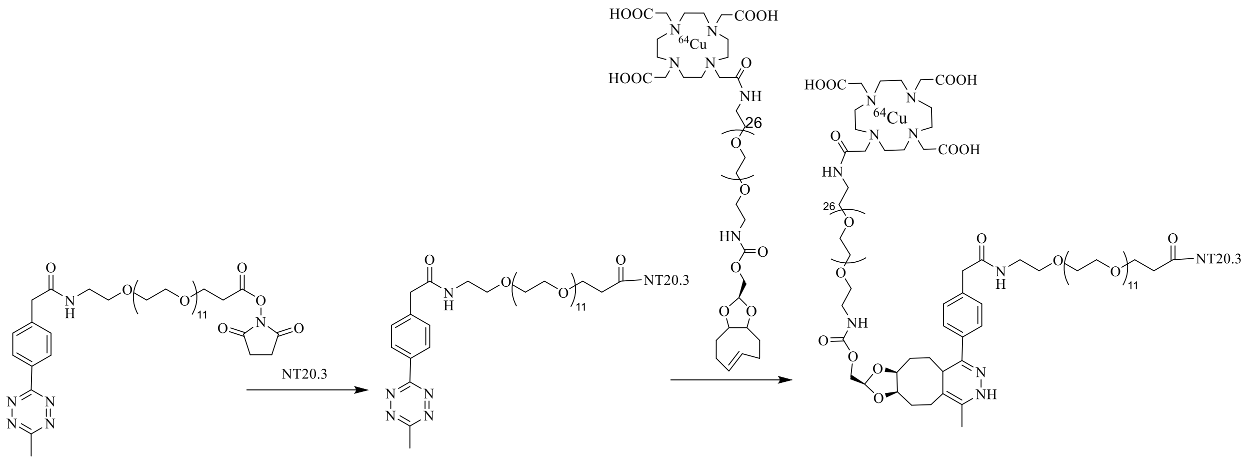

Scheme 4.11 Synthesis scheme of ^{64}*Cu-dTCO-PEG-DOTA-MePhTz-NT*

As we mentioned in the previous chapter, the TTCO ligation could be used not only in construction of ^{18}F labeled biomolecules but also in attaching radiometals and held potential for synthesis of therapeutic radio pharmaceuticals. So here we used the ^{64}Cu labeled dTCO-PEG-DOTA and applied it radiolabel biomolecule MePhTz-NT and evaluated its biodistribution.

As shown in Fig 4.27, ^{64}Cu-dTCO-PEG-DOTA could be successfully conjugated to MePhTz-NT through TTCO ligation and the isolation yield was 58.0 ± 1.7%. The tracer was obtained at 99% radiochemical purity after initial purification and the identity was confirmed by comparing the retention time with dTCO-PEG-DOTA-MePhTz-NT.

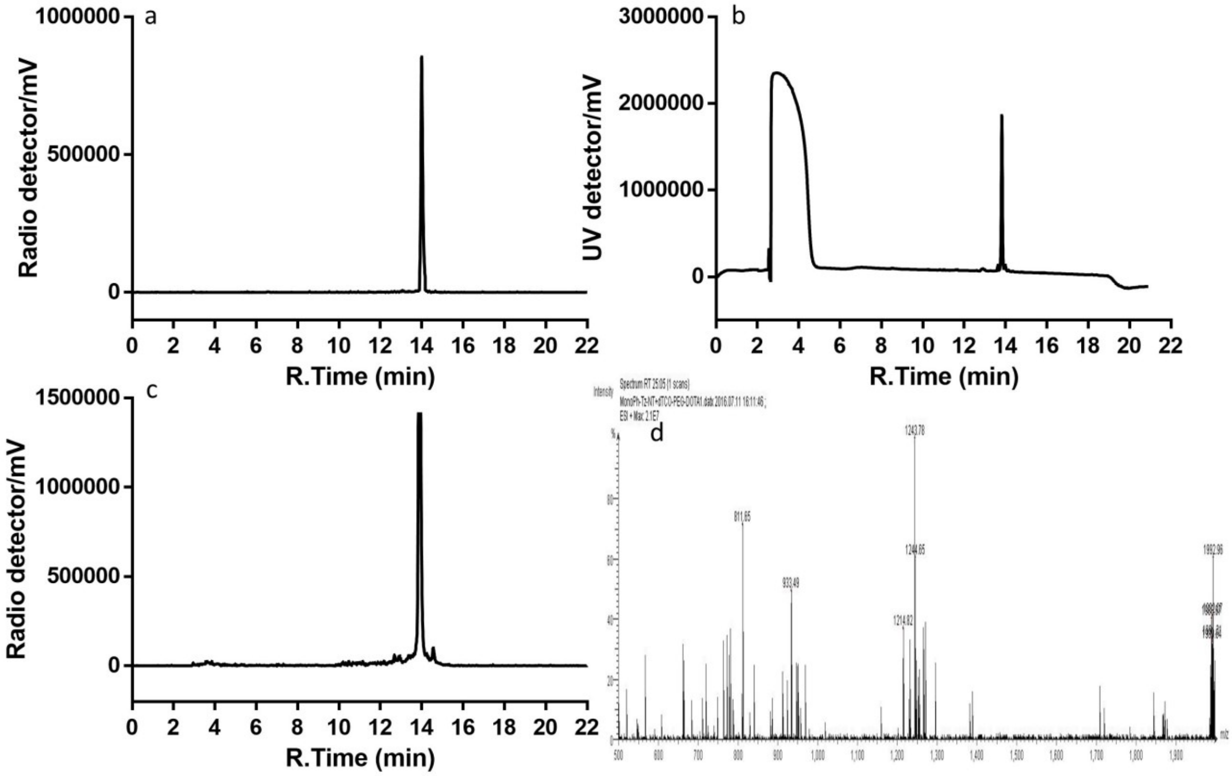

Figure 4.27 HPLC profile of a) purified ^{64}Cu-dTCO-PEG-DOTA-MePhTz-NT. b) dTCO-PEG-DOTA-MePhTz-NT. c) crude of ^{64}Cu-dTCO-PEG-DOTA ligation with MePhTz-NT. d) Mass spectrum of purified dTCO-PEG-DOTA-MePhTz-NT

The PET images of PC3 tumor bearing mice after intravenously injected with ^{64}Cu-dTCO-PEG-DOTA-MePhTz-NT were shown in Fig 4.28. Tumor was still clearly visualized at both time points with uptake of 0.9 ± 0.1 %ID/g and 0.9 ± 0.1 %ID/g at 1 and 4h post injection, respectively. Although this tracer showed decent tumor to background contrast, the absolute tumor uptake was not high enough for therapeutic applications. Thus, future works will be focused on increasing the tumor uptake of this TTCO ligation constructed radiometal PET tracer.

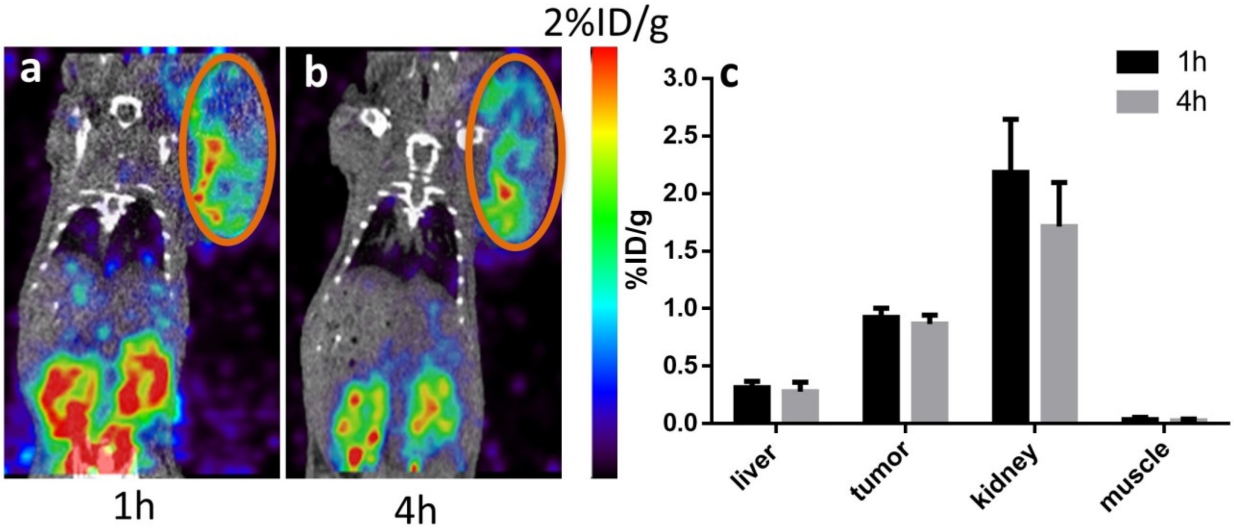

Figure 4.28 Representative PET/CT images of PC3 tumor bearing mice at a) 1h and b) 4h post injection of ^{64}*Cu-dTCO-PEG-DOTA-MePhTz-NT. c) Quantitative uptake of the major organs determined from the PET images. Tumor regions are highlighted in orange circle*

4.3.7 Effect of TTCO system on Binding Affinity of the PET Probes

Although reasonable targeting efficiency has been observed in several PET probes, the binding affinity of the TTCO ligation constructed PET probes still needs to be evaluated as the tumor uptake could be affected by many factors. Since we have synthesized several NT20.3 conjugates with different combination of tetrazines and *trans*-cyclooctenes, we took them as an example and compared their binding affinity with the unmodified NT20.3 peptide.

As shown in Fig 4.29, PET probes with different tetrazine moieties were evaluated. ^{19}F-sTCO-MePhTz-NT, ^{19}F-sTCO-DiPhTz-NT and ^{19}F-sTCO-DiolTz-NT inhibited the binding of ^{125}I-NT (20.3) to H1299 cells in a dose-dependent manner. The IC_{50} value of ^{19}F-sTCO-MePhTz-NT, ^{19}F-sTCO-DiPhTz-NT, ^{19}F-sTCO-DiolTz-NT and parent peptide NT20.3 was 62.3 ± 3.4 nM, 73.0 ± 1.5 nM, 78.6 ± 1.7 nM and 16.7 ± 2.1 nM, respectively. This result demonstrated that the TTCO ligation slightly compromised the binding affinity to NTSR1 but the binding affinity between the modified compounds did not share much difference.

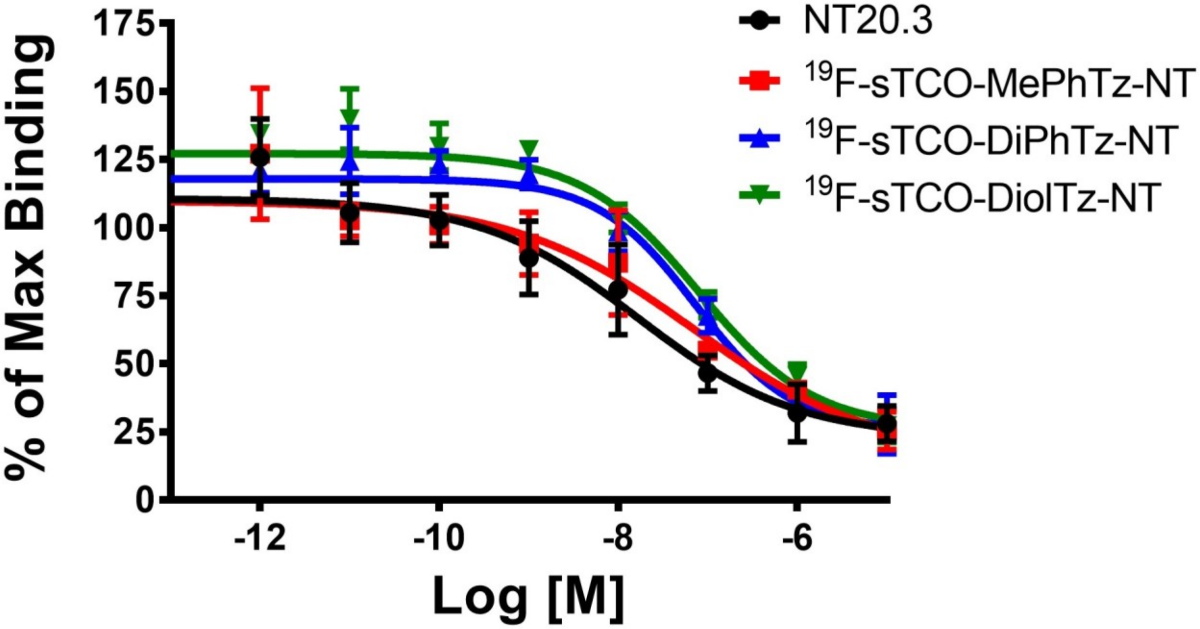

Figure 4.29 Competitive cell binding assays of ^{19}F-sTCO-MePhTz-NT, ^{19}F-sTCO-DiPhTz-NT, ^{19}F-sTCO-DiolTz-NT and original NT20.3 peptide

Additionally, the NTSR1 binding affinities of PET probes with different TCO motifs were tested in NTR1 positive prostate cancer cell PC3 and the results were shown in Fig 4.30. ^{19}F-sTCO-MePhTz-NT, ^{19}F-dTCO-MePhTz-NT and ^{19}F-oTCO-MePhTz-NT showed comparable binding affinity with the unmodified NT20.3 peptide. The IC_{50} value for ^{19}F-sTCO-MePhTz-NT, ^{19}F-dTCO-MePhTz-NT, ^{19}F-oTCO-MePhTz-NT and parent NT20.3 was 20.5 ± 14.1 nM, 15.4 ± 3.4 nM, 31.6 ± 7.1 nM and 16.2 ± 2.7 nM, respectively.

These data demonstrated that neither the tetrazine nor the TCO moiety would affect the binding affinity of the parent biomolecules and further supported the hypothesis that TTCO ligation could be served as a platform for high specific biomolecular based PET probe construction

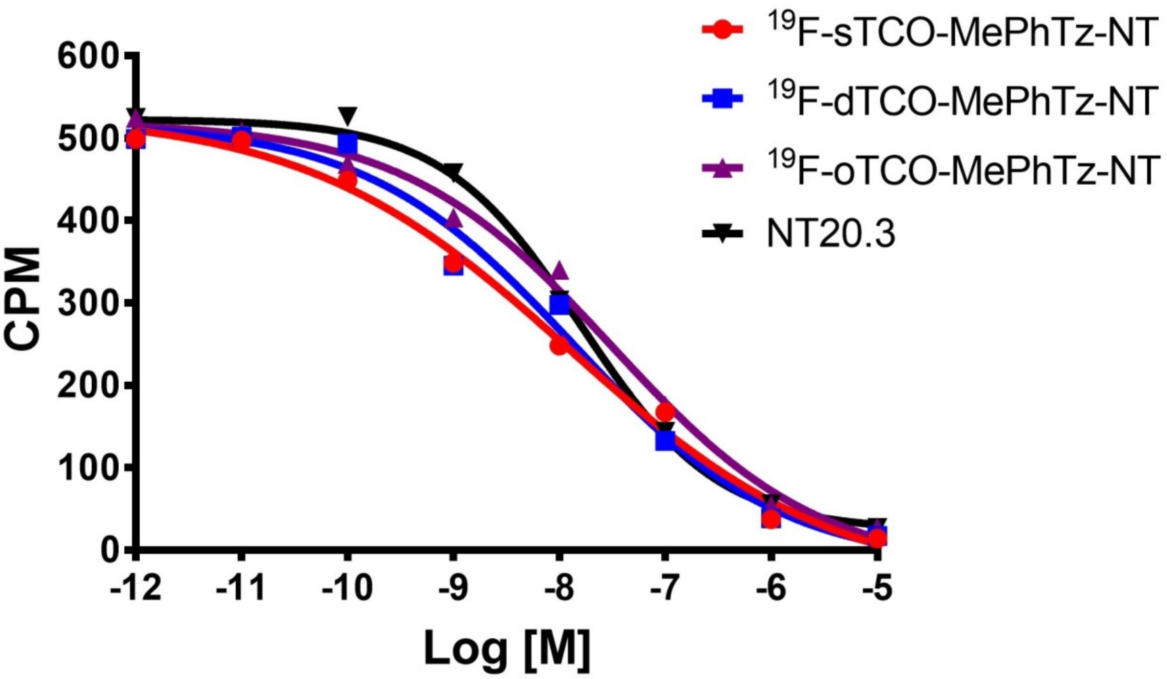

Figure 4.30 Competitive cell binding assays of ^{19}F-sTCO-MePhTz-NT, ^{19}F-dTCO-MePhTz-NT, ^{19}F-oTCO-MePhTz-NT and original NT20.3 peptide

4.4 Radiolabeled PSMA Ligand for Prostate Cancer Imaging

Additionally, we also include a prostate specific membrane antigen (PSMA) ligand, Glu-urea-Lys, as an example to test in the TTCO ligation system. Prostate cancer is currently the most common cancer in male at Europe and the United States. Over 161 thousand newly reported prostate cancer occurred in US during 2017, which accounted for 19% of the new cancer cases nationwide (*30*). The current standard procedure for early diagnosis of prostate cancer includes digital rectal exam, blood test of prostate specific antigen (PSA) and biopsy (*31*). However, the digital rectal exam is only sensitive to advanced stage of prostate cancer and biopsy suffers from heterogeneity of tumors (*32,33*). The PSA test result may be misleading since it can be affected by benign prostatic hypertrophy (BPH) (*34,35*). PSMA is a transmembrane protein that is highly overexpressed on massive types of prostate tumor models (*36-38*). Additionally, enhanced expression is particularly found in poorly differentiated, metastatic and hormone-refractory carcinomas making it ideal target for prostate cancer imaging (*37,39*). Although some radiolabeled anti-PSMA antibodies has be approved by FDA, they only target the intracellular epitope of PSMA and cannot access into viable tumor cells, which limited their performance (*40*). On the contrary, the Glu-urea-Lys based small molecule PSMA inhibitor binds to the extracellular domain of PSMA and can be internalized and endosomally recycled, which lead to increased tumor uptake (*41-43*). Several PET tracers were established based on this ligand including ^{18}F-DCFPyL, ^{68}Ga-PSMA-11 and ^{68}Ga-PSMA-617 etc (*44-46*). So here we utilize this ligand as another representative small biomolecule to test our TTCO radiolabeling system.

4.4.1 ^{18}F-oTCO-MePhTz-PSMA

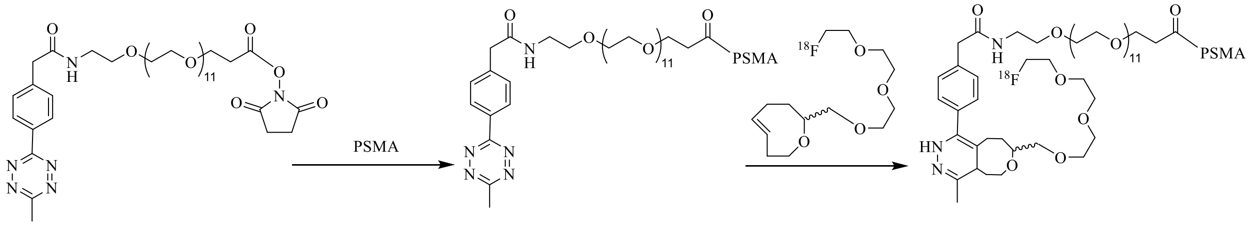

Scheme 4.12 Synthesis scheme of ^{18}F-oTCO-MePhTz-PSMA

As shown in Fig 4.31, the side chain of lysine in the PSMA ligand was modified with MePhTz via amide bond. The UV peak at 12.4min showed the correct *m/z*: $[M+H]^{2+}$ calcd $C_{50}H_{83}N_{8}O_{21}$ for 1132.24; found 1131.90. Similar to other peptides, PSMA ligand was also successfully radio fluorinated through TTCO ligation and the ^{18}F-oTCO labeling yield was 46.7 ± 1.4%. The identity of the tracer was confirmed by comparing with the ^{19}F standard and the radiochemical purity was over 99% (Fig 4.32).

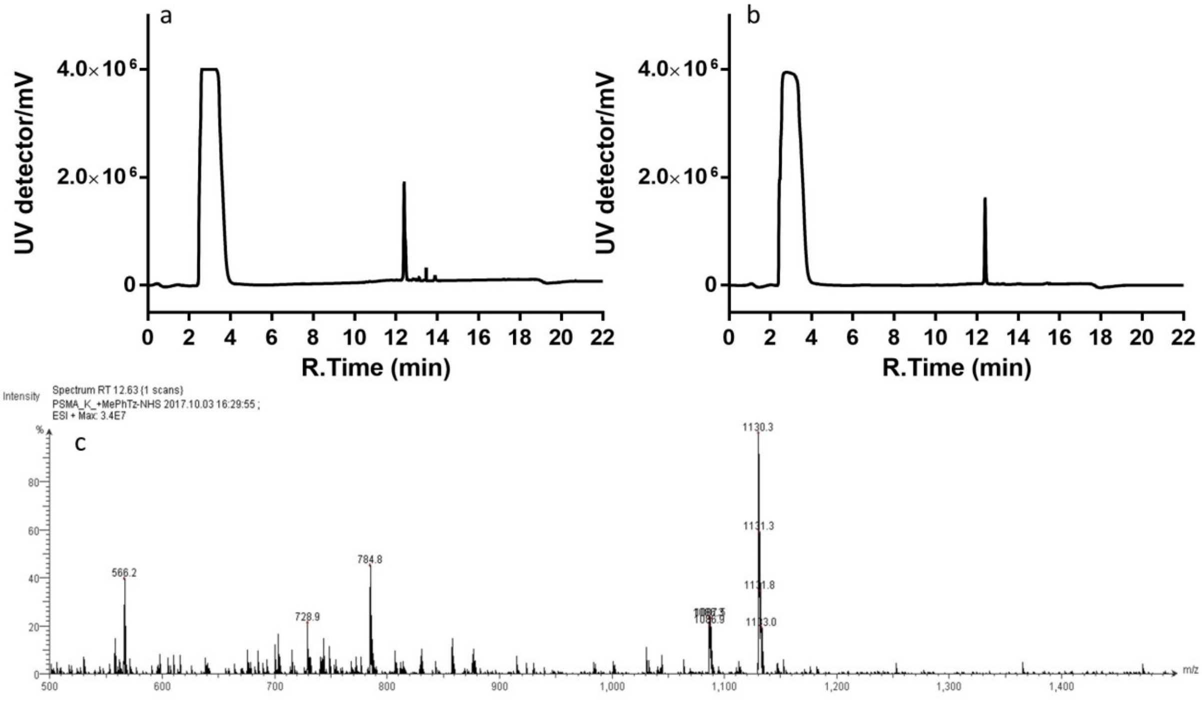

Figure 4.31 a) HPLC profile of crude reaction between MePhTz-NHS and PSMA. b) HPLC profile of purified MePhTz-PSMA. c) Mass spectrum of purified MePhTz-PSMA

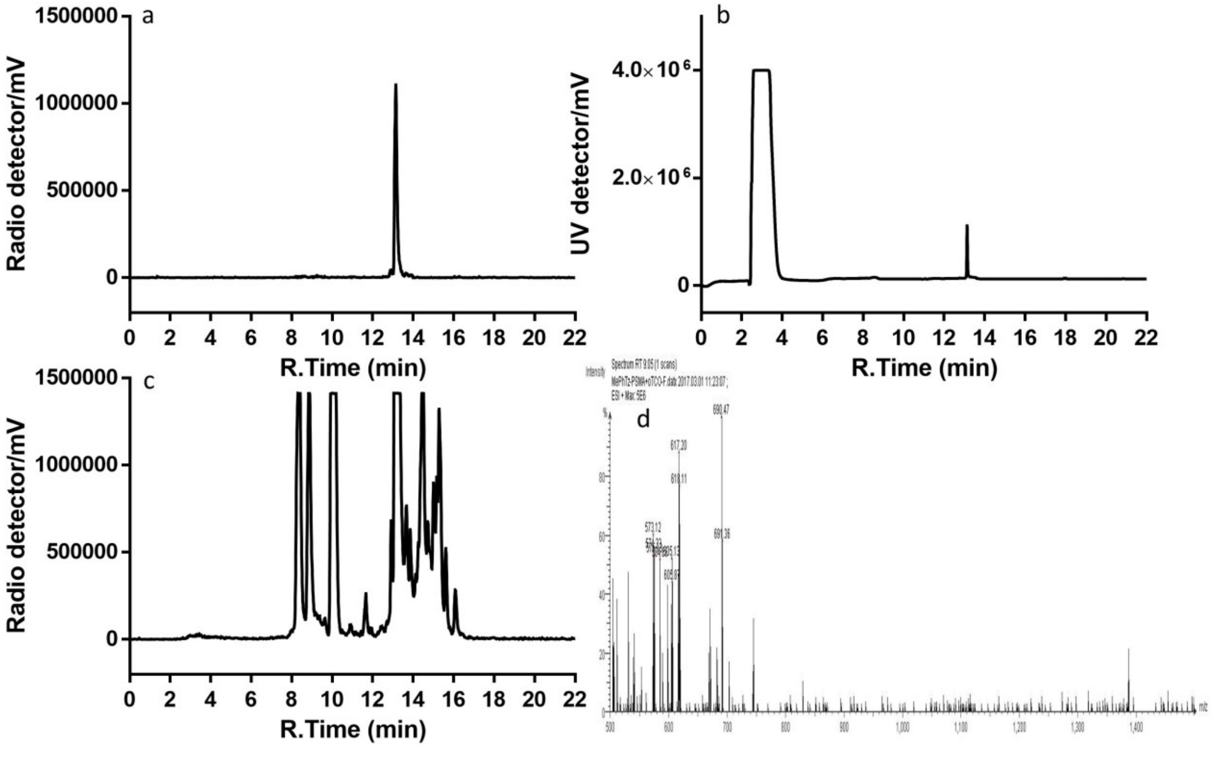

Figure 4.32 HPLC profile of a) purified ^{18}F-oTCO-MePhTz-PSMA. b) ^{19}F-oTCO-MePhTz-PSMA. c) crude of ^{18}F-oTCO ligation with MePhTz-PSMA. d) Mass spectrum of purified ^{19}F-oTCO-MePhTz-PSMA

The constructed ^{18}F-oTCO-MePhTz-PSMA was intravenously injected into PSMA positive LnCaP tumor bearing mice for static PET scan. As can be seen in Fig 4.33, the tumor was clearly spotted at 1h post injection with reasonable tumor to background contrast. The tumor uptake was 0.9 ± 0.2 %ID/g at 1h post injection. However, the tracer was rapidly cleared out through renal metabolic pathways and the tumor uptake was only 0.3 ± 0.1 %ID/g at 4h post injection. The fast clearance rate was consistent to the previously discussed probes constructed through MePhTz-oTCO ligation. Additionally, the small molecular weight PSMA ligand its self also has relatively short in vivo half-life and may contribute to the fast clearance from the tumor site. Nevertheless, these results demonstrated that small biomolecules could be efficiently constructed into PET probes with good contrast using our TTCO ligation method.

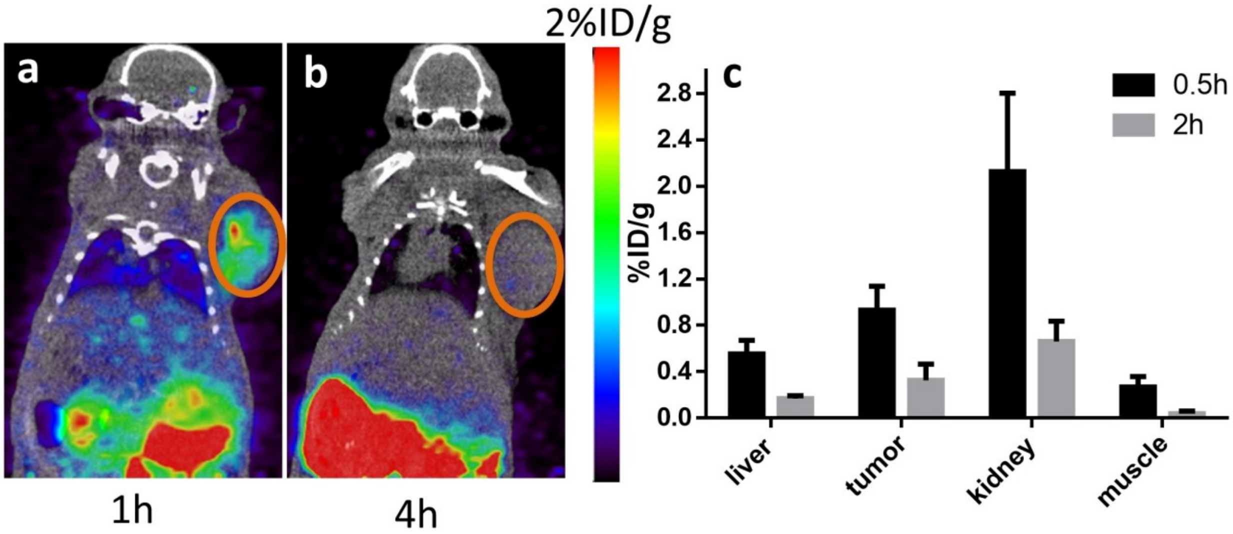

Figure 4.33 Representative PET/CT images of LnCaP tumor bearing mice at a) 1h and b) 4h post injection of ^{18}F-oTCO-MePhTz-PSMA. c) Quantitative uptake of the major organs determined from the PET images. Tumor regions are highlighted in orange circle

4.4.2 ^{18}F-sTCO-DiPhTz-PSMA

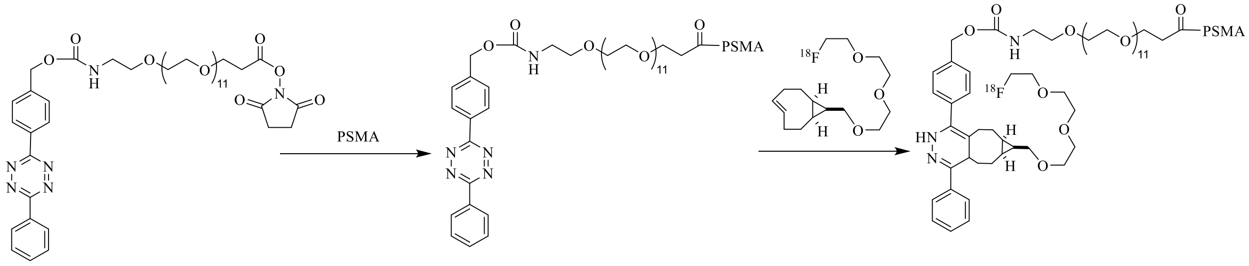

Scheme 4.13 Synthesis scheme of ^{18}*F-sTCO-DiPhTz-PSMA*

Although the ^{18}F-oTCO-MePhTz-PSMA showed reasonable tumor to background contrast, the absolute tumor uptake was much lower than other ^{18}F labeled PSMA ligand. Given that the PSMA ligand could also be used as therapeutic agents, we further applied the sTCO-DiPhTz ligation to it aiming to increase the tumor uptake. The DiPhTz-PSMA was synthesized under the protocol similar to DiPhTz-RGDyK and DiPhTz-NT. A correct LC-MS result was found for UV peak at 16.9min. *m/z*: $[M+H]^{2+}$ calcd $C_{55}H_{85}N_8O_{22}$ for 1210.31; found 1210.11 (Fig 4.34).

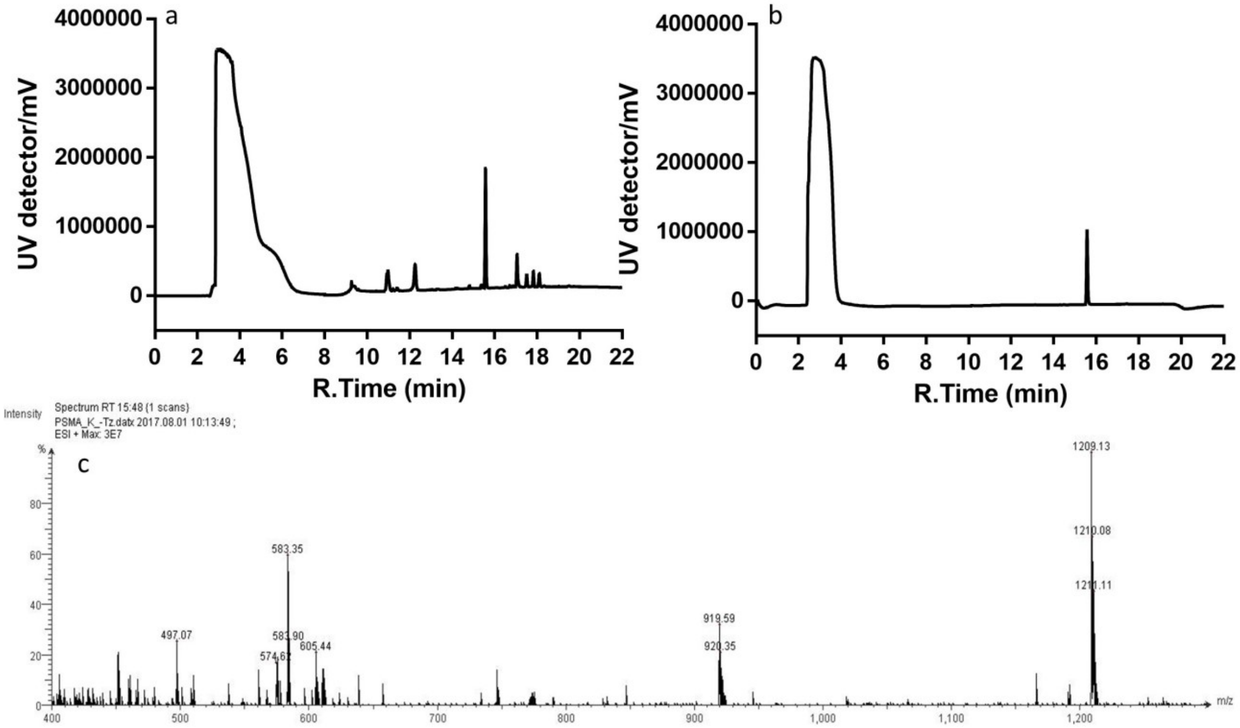

Figure 4.34 a) HPLC profile of crude reaction between DiPhTz-NHS and PSMA. b) HPLC profile of purified DiPhTz-PSMA. c) Mass spectrum of purified DiPhTz-PSMA

DiPhTz-PSMA was readily labeled with ^{18}F-sTCO in a few seconds under mild condition. The isolation yield was 53.5 ± 6.7% decay corrected and the radiochemical purity was 99% after initial HPLC purification. The identity was confirmed by coinjection with the corresponding ^{19}F standard (Fig 4.35). We then tested the in vivo behavior of the ^{18}F-sTCO-DiPhTz-PSMA in LnCaP tumor xenografts. As shown in Fig 4.36, the tumor uptake was 3.3 ± 0.6 %ID/g at 1h post injection and maintained at 3.2 ± 0.7 %ID/g at 4h post injection. Although this uptake was significantly higher than that of using oTCO-MePhTz labeled tracer, it is still slightly lower than the widely used ^{18}F labeled PSMA inhibitor ^{18}F-DCFPyL (*47*). So future work will be focused on increasing the tumor uptake of the TTCO ligated PSMA inhibitor for theranostic applications.

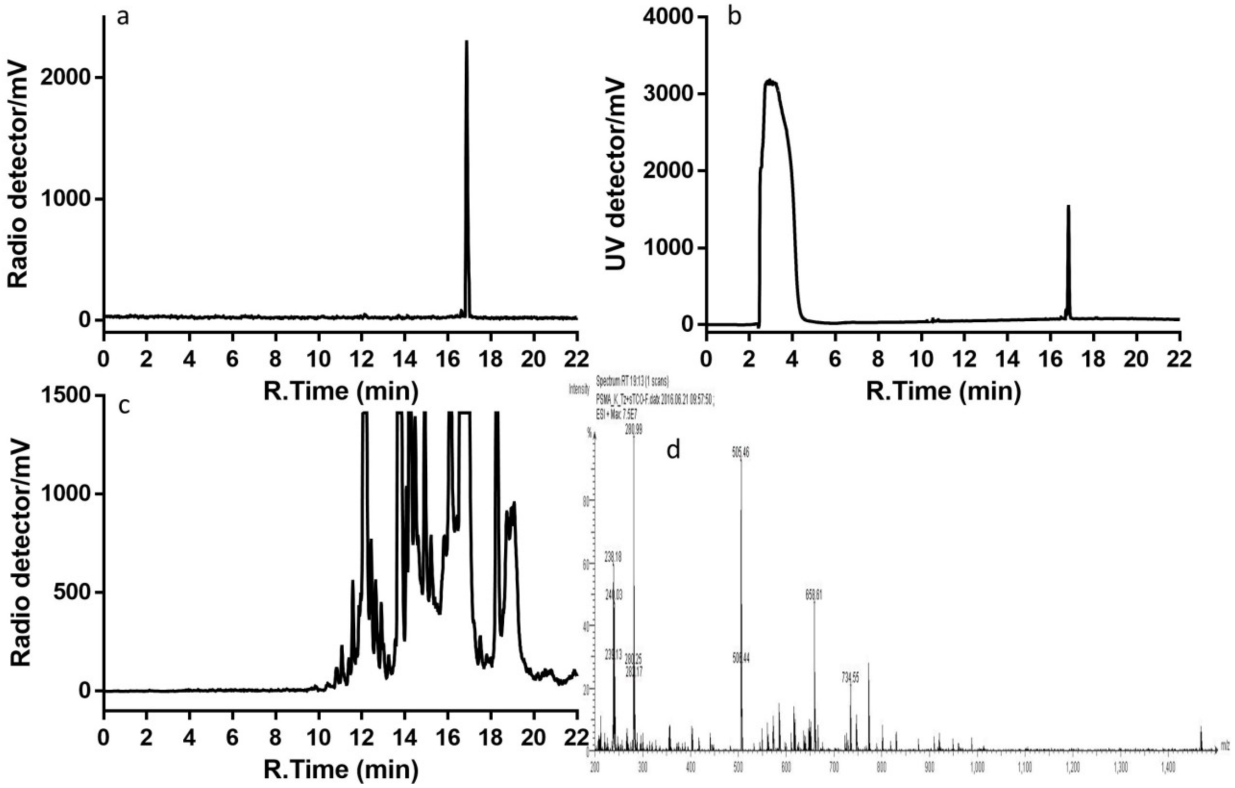

Figure 4.35 HPLC profile of a) purified ^{18}F-sTCO-DiPhTz-PSMA. b) ^{19}F-sTCO-DiPhTz-PSMA. c) crude of ^{18}F-sTCO ligation with DiPhTz-PSMA. d) Mass spectrum of purified ^{19}F-sTCO-DiPhTz-PSMA

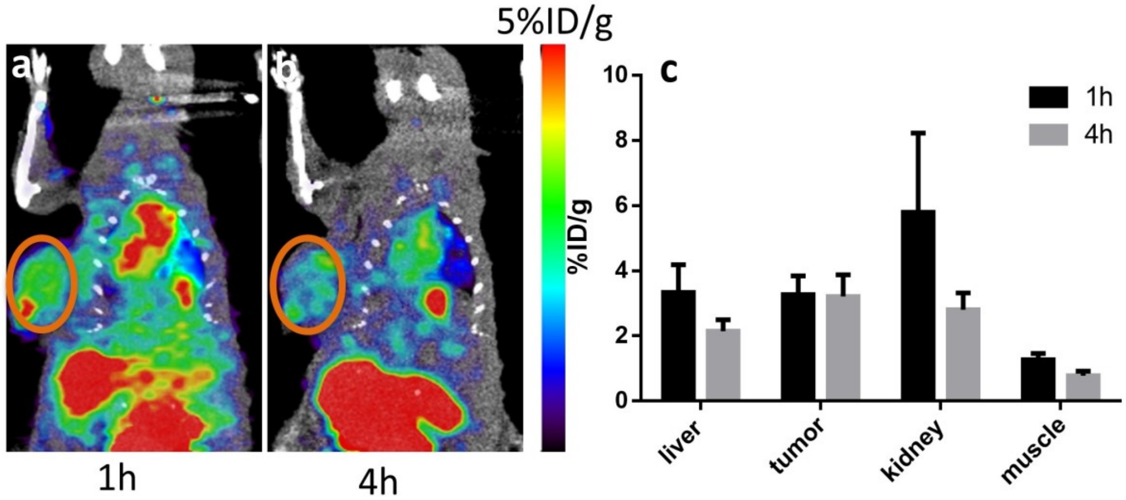

Figure 4.36 Representative PET/CT images of LnCaP tumor bearing mice at a) 1h and b) 4h post injection of ^{18}F-sTCO-DiPhTz-PSMA. c) Quantitative uptake of the major organs determined from the PET images. Tumor regions are highlighted in orange circle

4.5 Other Radiolabeled Peptides for PET Imaging

4.5.1 ^{18}F-sTCO-DiPhTz-Exendin

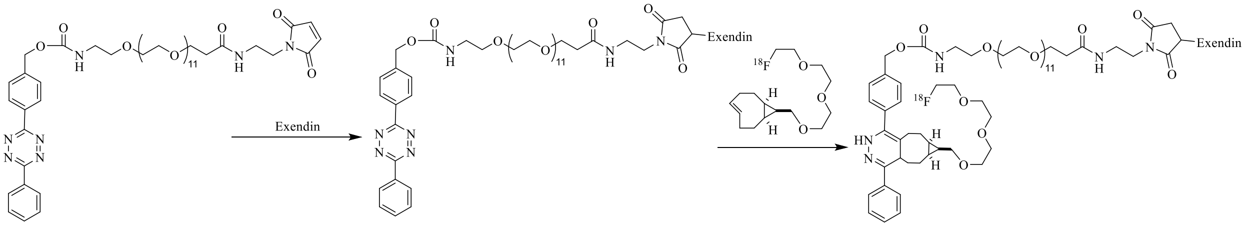

Scheme 4.14 Synthesis scheme of ^{18}F-sTCO-DiPhTz-Exendin

Additionally, ^{18}F-sTCO-DiPhTz-Exendin was designed as another candidate to validate the feasibility for peptide based PET probe construction via TTCO ligation. Exendin peptide tends to target the glucagon-like peptide 1 receptor (GLP-1R), which is mainly expressed in β-cells and commonly used as target for insulinoma imaging (*48,49*). The DiPhTz-Exendin was synthesized by converting the DiPhTz-NHS to DiPhTz-maleimide and conjugating with the Exendin peptide via thiol-maleimide bond. The HPLC profile of the reaction crude and purified DiPhTz-Exendin was shown in Fig 4.37 and was confirmed by MALDI-TOF.

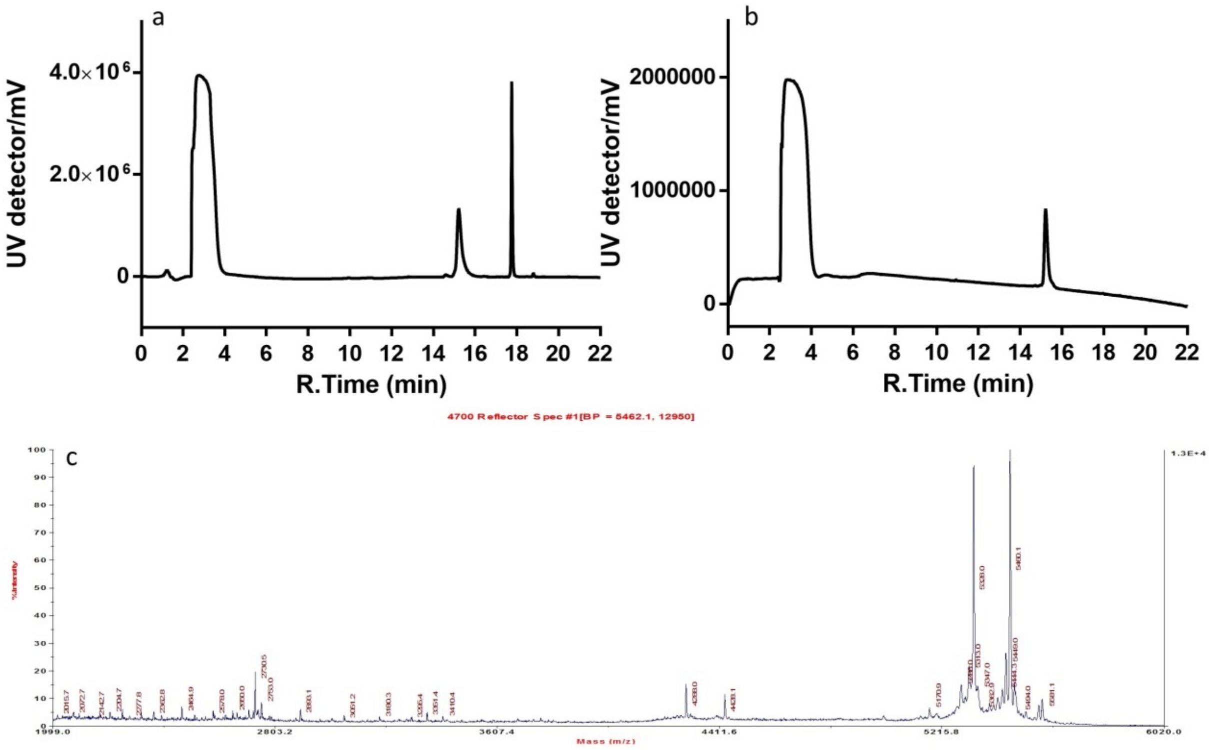

Figure 4.37 a) HPLC profile of crude reaction between DiPhTz-NHS and Exendin. b) HPLC profile of purified DiPhTz-Exendin. c) Mass spectrum of purified DiPhTz-Exendin

The DiPhTz-Exendin was radiolabeled with ^{18}F-sTCO under the same protocol as previously discussed at 40.1 ± 1.1 % isolation yield and 99% radiochemical purity after purification (Fig 4.38). The following small animal PET study was conducted in INS1 tumor xenografts and the images were shown in Fig 4.39. In this case the tumor uptake increased from 8.2 ± 2.9 %ID/g at 1h post injection to 11.4 ± 4.7 %ID/g at 4h post injection. This was consistent to what we observed in the RGDyK and NT probes, which further proved that TTCO ligation system could be used to radiolabel different types of peptide.

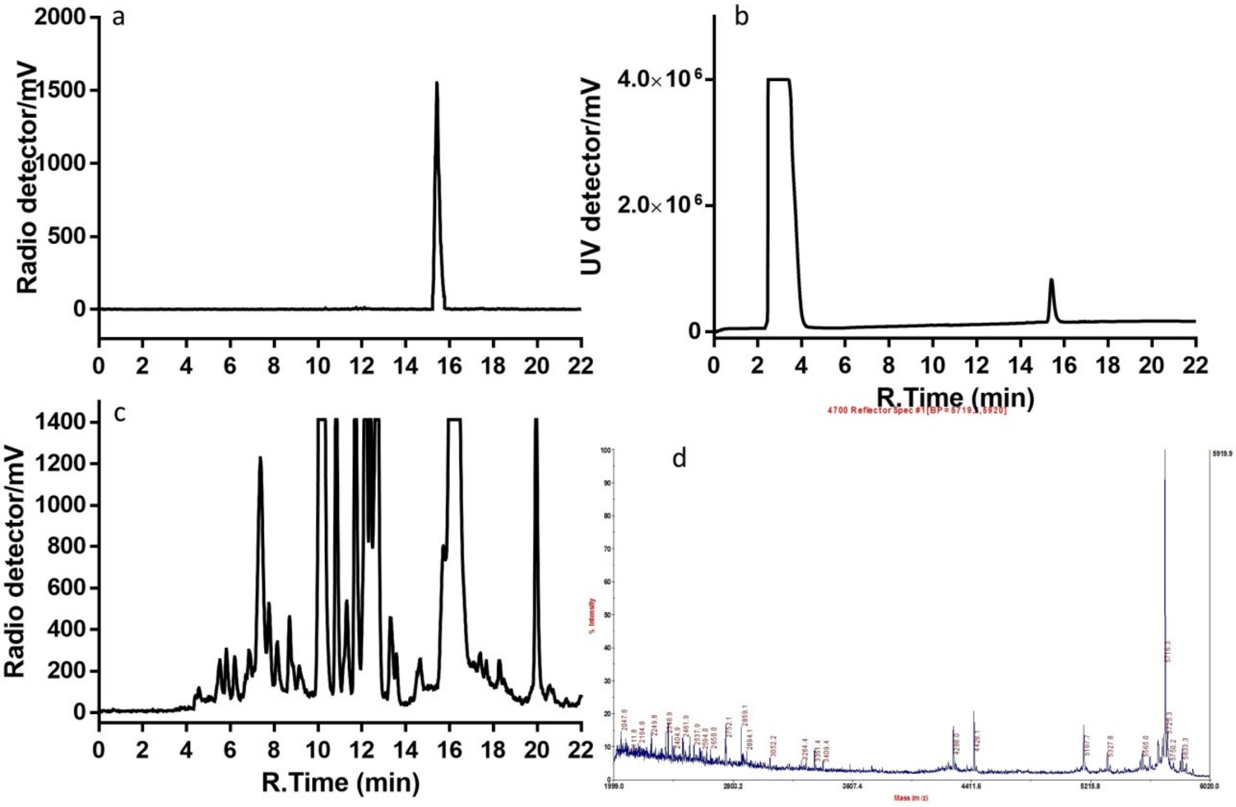

Figure 4.38 HPLC profile of a) purified ^{18}F-sTCO-DiPhTz-Exendin. b) ^{19}F-sTCO-DiPhTz-Exendin4. c) crude of ^{18}F-sTCO ligation with DiPhTz-Exendin. d) Mass spectrum of purified ^{19}F-sTCO-DiPhTz-Exendin

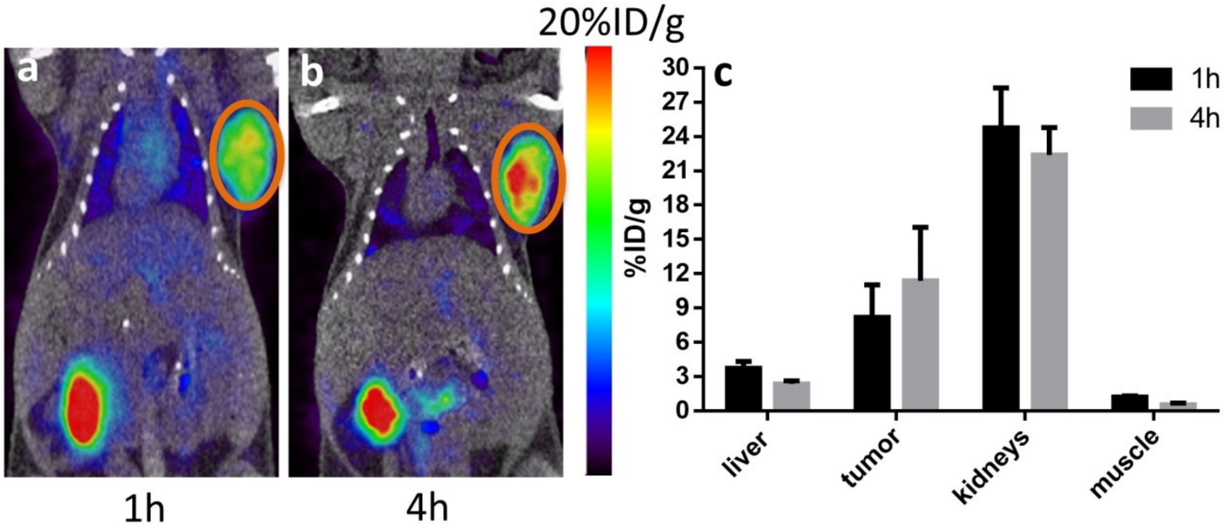

Figure 4.39 Representative PET/CT images of INS1 tumor bearing mice at a) 1h and b) 4h post injection of ^{18}F-sTCO-DiPhTz-Exendin. c) Quantitative uptake of the major organs determined from the PET images. Tumor regions are highlighted in orange circle

4.5.2 ^{18}F-sTCO-DiPhTz-BBN

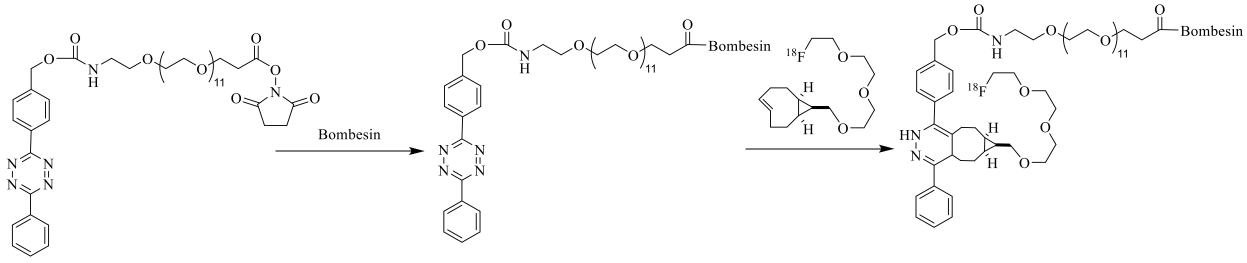

Scheme 4.15 Synthesis scheme of ^{18}F-sTCO-DiPhTz-BBN

We also designed a bombesin based ^{18}F-sTCO-DiPhTz-BBN probe and evaluated the in vivo behavior. Bombesin has a short in vivo half-life and is quickly proteolytically degraded in less than 30min (*50*). The DiPhTz-BBN was synthesized via amide bond between DiPhTz-NHS and BBN and the identity was confirmed by LC-MS *m/z*: $[M+H+K]^{2+}$ calcd $C_{92}H_{140}N_{19}O_{25}SK$ for 991.64; found 991.48 (Fig 4.40).

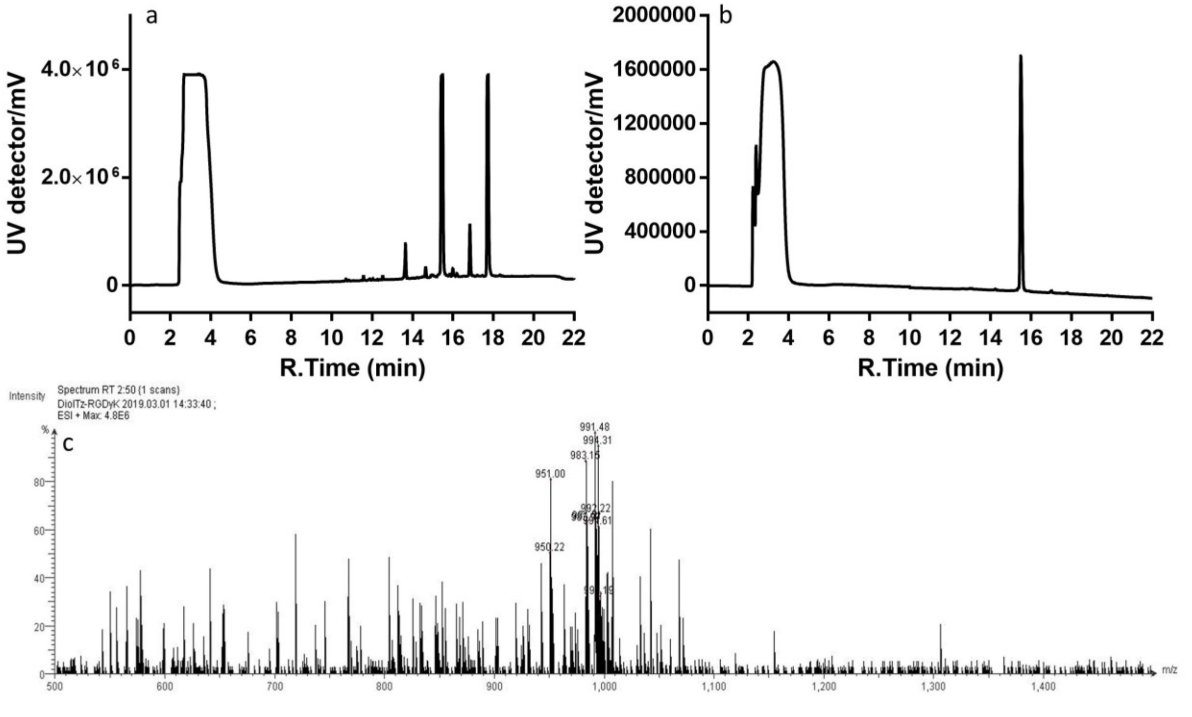

Figure 4.40 a) HPLC profile of crude reaction between DiPhTz-NHS and BBN. b) HPLC profile of purified DiPhTz-BBN. c) Mass spectrum of purified DiPhTz-BBN

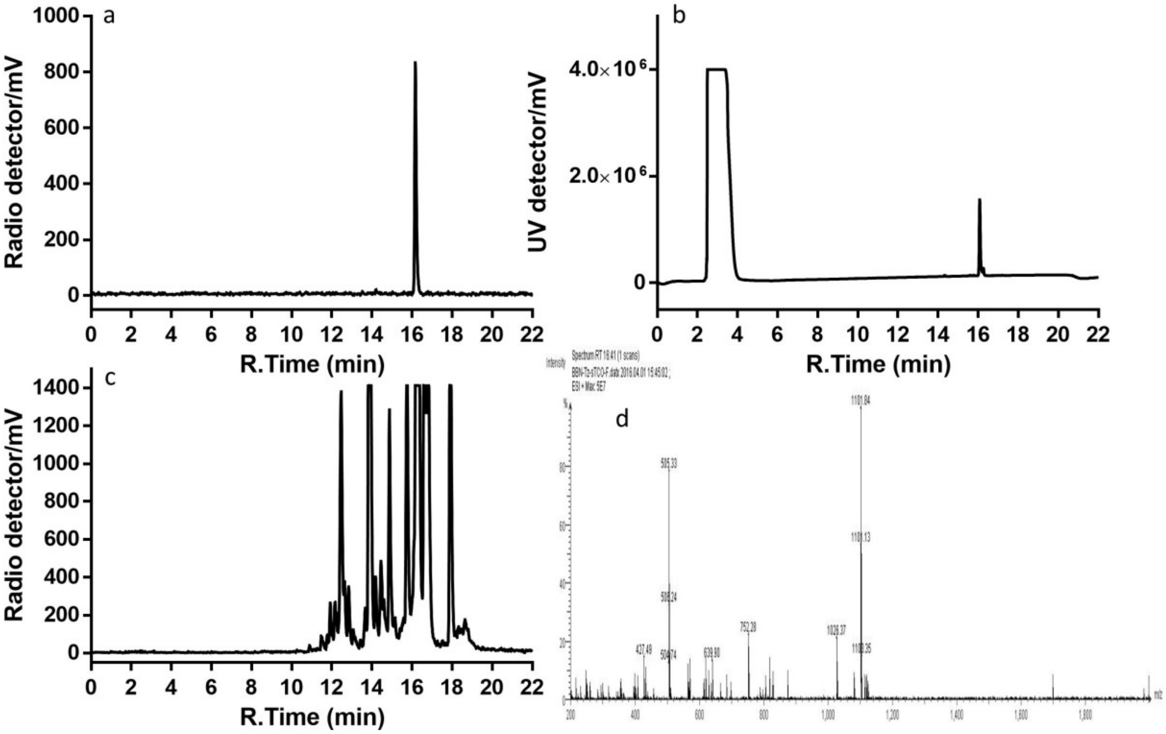

Figure 4.41 HPLC profile of a) purified ^{18}F-sTCO-DiPhTz-BBN. b) ^{19}F-sTCO-DiPhTz-BBN. c) crude of ^{18}F-sTCO ligation with DiPhTz-BBN. d) Mass spectrum of purified ^{19}F-sTCO-DiPhTz-BBN

The prepared DiPhTz-BBN was subjected to ^{18}F-sTCO labeling and the isolation yield was 46.2 ± 3.9% and the radiochemical purity after HPLC purification was over 99%. The identity of the radiolabeled compound was confirmed by comparing the retention time with the corresponding ^{19}F version (Fig 4.41).

^{18}F-sTCO-DiPhTz-BBN was tested in prostate cancer model PC3 xenografts and the PET images were shown in Fig 4.42. The tumor uptake decreased from 3.2 ± 0.8 %ID/g at 1h post injection to 2.2 ± 0.3 %ID/g at 4h post injection.

All the above results proved that the TTCO system provided a promising platform for peptide based biomolecule radiolabeling and PET probe construction. Several peptide candidates were screened and the PET probes demonstrated reasonable targeting efficiency.

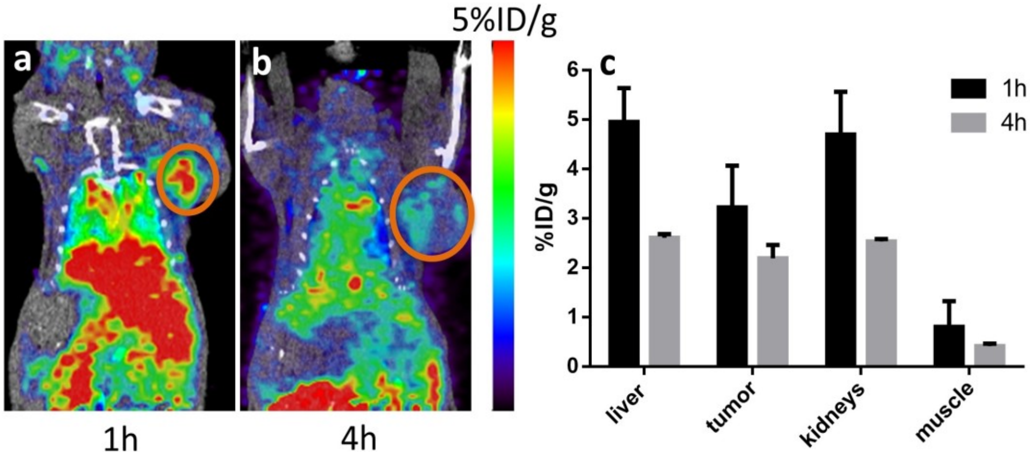

Figure 4.42 Representative PET/CT images of PC3 tumor bearing mice at a) 1h and b) 4h post injection of ^{18}*F-sTCO-DiPhTz-BBN. c) Quantitative uptake of the major organs determined from the PET images. Tumor regions are highlighted in orange circle*

4.6 Radiolabeled HER2 Protein Ligands for HER2 Targeted Imaging

In addition to the peptide based biomolecules, we also utilize the TTCO ligation to radiolabel large biomolecules such as proteins. The protein we used was a human epidermal growth factor receptor 2 (HER2) ligand which was generated by Dr. Rihe Liu's group in School of Pharmacy, University of North Carolina at Chapel Hill. HER2 receptor belongs to the ErbBs family and is a transmembrane receptor that activates intracellular signaling pathways in response to extracellular signals (*51,52*). This receptor plays a key role in cell development, proliferation and differentiation via two main signaling pathways (MAPK and PI3k) (*53,54*). The overexpression of this receptor on the cell surface was reported in several cancers including lung, gastric, ovarian, prostate and breast cancer and is always associated with poor prognosis and short survival (*55,56*). Since this receptor participates in the proliferation and migration of the cancer cells, it has been reported that monoclonal antibodies (mAbs) that specifically bind to HER2 receptor and inhibit its binding with natural ligand EGF could significantly improve patient survival in breast cancer (*57,58*). However, as only 15 to 30% of breast cancer patients are HER2 positive, the assessment of receptor expression is critical for patient selection and tumor recurrence monitor (*59,60*). The standard procedure to evaluate HER2 expression level in clinic is biopsy, which suffers from the heterogeneous bias and discordance between primary and metastatic sites (*61-63*). To address these issues, PET imaging provides an alternative approach to determine the HER2 expression on the whole picture non-invasively. Several anti-HER2 mAbs such as trastuzumab and pertuzumab have been developed into PET tracers by radiolabeling with ^{89}Zr, ^{64}Cu or ^{111}In (*64-67*). Although they showed desired imaging properties, the low tumor penetration, slow clearance and high radiation exposure were still concerns before applying to further clinical applications. So we aim to use a HER2 targeting protein (~12.5 kDa) and construct it into PET tracer using our TTCO radiolabeling platform.

4.6.1 ^{18}F-oTCO-MePhTz-HER2

We used the HER2 targeting ligand with 12.5 kDa molecular weight, which was kindly provided by our collaborator Dr. Rihe Liu from School of Pharmacy, UNC. The MePhTz was conjugated to HER2 proteins by reacting with amine groups on the proteins and purified by size exclusive PD-10 column. As shown in Fig 4.43, tetrazine's red color was observed in the 3-4mL elution fraction from the PD-10 column, in which the proteins were eluted off according to the manufacture's manual. This suggested that the tetrazine was successfully conjugated to the Her2 protein. Different reaction ratio between tetrazine and HER2 protein was also explored (protein to tetrazine ratio of 1:5, 1:10 and 1:20). Although higher reaction ratio will lead to better labeling yield in the following step, the protein binding affinity will be affected by over modification.

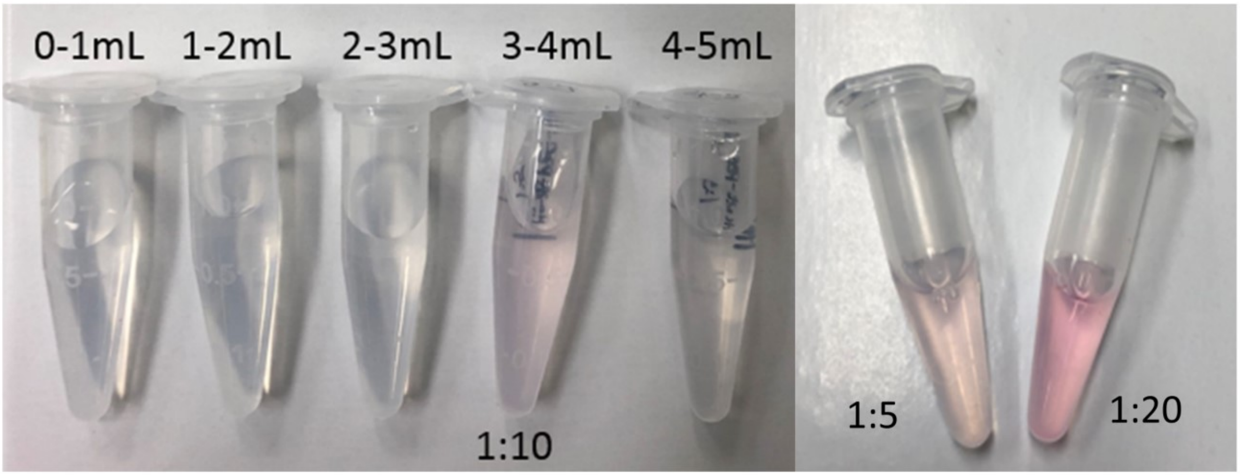

Figure 4.43 Picture of PD-10 elutions during purification of MePhTz modified HER2 protein

The MePhTz-HER2 could also be successfully radio fluorinated with ^{18}F-oTCO through TTCO ligation. The isolation yield increased with respect to the reaction ratio between tetrazine and HER2 proteins, which may be the result of more tetrazines were attached per protein molecule when using higher reaction ratio. The isolation yield was 3.6 ± 1.4% for 5:1 tetrazine to protein ratio samples, 7.7 ± 1.5 for 10:1 tetrazine to protein ratio samples and 11.7 ± 1.1 for 20:1 tetrazine to protein ratio samples.

In order to minimize the affection of tetrazine to HER2 protein, we used the 5:1 tetrazine to protein ratio samples to evaluate in HER2 positive breast cancer tumor xenografts SKOV3. As shown in Fig 4.44, The tumor was clearly visualized at both time points with uptake of 4.8 ± 1.0 %ID/g and 4.1 ± 0.8 %ID/g at 1 and 4h post injection, respectively. While the tumor uptake remained stable over 4h, the uptake of other major organs such as liver and kidney decreased significantly leading to an enhanced tumor to background ratio. **These results proved that the TTCO ligation could be applied to radiolabel large biomolecules such as proteins with ^{18}F and the constructed PET tracer retained good target binding capability**.

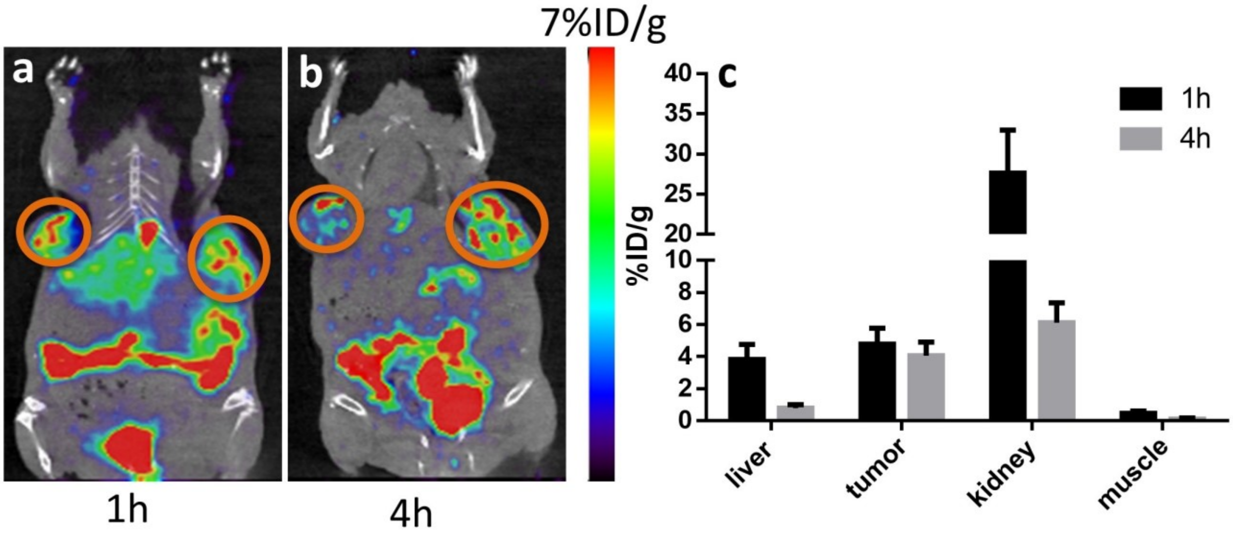

Figure 4.44 Representative PET/CT images of SKOV3 tumor bearing mice at a) 1h and b) 4h post injection of ^{18}*F-oTCO-MePhTz-HER2. c) Quantitative uptake of the major organs determined from the PET images. Tumor regions are highlighted in orange circle*

4.7 Effect of TTCO System on Pharmacokinetic of PET Probes

As we can see from the previous results, different combinations of tetrazine and *trans*-cyclooctene derived PET probes showed significantly different biodistributions. In general, more hydrophilic TTCO system resulted in less background signal and better tumor to background contrast. Taking the NT20.3 based PET probes as examples, we calculated the tumor to muscle uptake ratio of three PET probes with the same *trans*-cyclooctene but different tetrazine moiety. As shown in Table 4.1, the tumor to muscle ratio was significantly improved when more hydrophilic ^{18}F-sTCO-MePhTz and ^{18}F-sTCO-DiolTz systems were used. The hydrophilicity was determined by measuring the octanol-water partition coefficient of each tracer.

Table 4.1 Tumor to muscle uptake ratio of ^{18}F-sTCO with different NT-tetrazine derivatives in H1299 xenografts at 1 and 4h post injection

Tumor/Muscle	1h post injection	4h post injection	logP
^{18}F-sTCO-MePhTz-NT	**6.1 ± 1.0**	**6.4 ± 0.4**	**-0.9 ± 0.1**
^{18}F-sTCO-DiolTz-NT	**7.9 ± 2.5**	**7.9 ± 0.8**	**-1.0 ± 0.1**
^{18}F-sTCO-DiPhTz-NT	**1.6 ± 0.4**	**2.9 ± 0.1**	**-0.7 ± 0.0**

Similar phenomenon was observed when more hydrophilic *trans*-cyclooctene motifs were chosen while using the same tetrazine. Table 4.2 showed the tumor to muscle ratio and the partition coefficient of three MePhTz-NT based PET tracers. The most hydrophilic ^{18}F-oTCO derived PET probe showed the highest tumor to muscle ratio at both time points. Although ^{18}F-dTCO-MePhTz-NT gave lower ratio compared with ^{18}F-sTCO-MePhTz-NT at the first time point, the ratio significantly increased at 4h post injection. Given that the tumor uptake of ^{18}F-oTCO-MePhTz-NT was not the highest among the three compounds, it can be concluded that the high tumor to background ratio is due to low uptake in the muscle. These results proved that the more hydrophilic TTCO system derived PET probe showed improved tumor to background contrast. **In general, although the TTCO ligation could be used to construct biomolecular based PET probes with reasonable targeting efficiency, various factors may impact the pharmacokinetic of the PET probes, which need to be tested in vivo.**

Table 4.2 Tumor to muscle uptake ratio of MePhTzNT with different TCO derivatives in PC3 xenografts at 1 and 4h post injection

Tumor/Muscle	1h post injection	4h post injection	logP
^{18}F-sTCO-MePhTz-NT	**6.5 ± 1.5**	**6.4 ± 0.5**	**-0.9 ± 0.1**
^{18}F-dTCO-MePhTz-NT	**3.8 ± 0.9**	**11.9 ± 4.3**	**-1.6 ± 0.0**
^{18}F-oTCO-MePhTz-NT	**15.8 ± 2.2**	**16.2 ± 2.3**	**-2.5 ± 0.1**

Another interesting finding we would like to point out is that sTCO-DiPhTz system derived PET probes showed enhanced blood circulation time. As demonstrated in RGDyK, NT and Exendin derived probes, the DiPhTz-sTCO system leads to conjugates with improved blood circulation leading to higher levels of tumor uptake at late time point. We then investigated whether this phenomenon was mainly caused by the tetrazine or the *trans*-cyclooctene moiety. When switching the sTCO to other *trans*-cyclooctene agents such as TCO and dTCO in the sTCO-DiPhTz-RGDyK system, similar result with long lasting blood pool signal and increased tumor uptake was observed. These data demonstrated that the TCO motif might only have minor impact on the enhanced blood circulation time effect and some modifications were allowed to maintain the long lasting in vivo half-life of the constructed PET probes. On the contrary, blood pool signal was reduced significantly when DiPhTz was exchanged with either MePhTz or DiolTz in the sTCO-DiPhTz system. Although the tumor could still be localized in both scenarios, the tumor uptake decreased as time passed. This difference from the DiPhTz-sTCO system constructed probes proved that the structure of the tetrazine may play the key role in the blood circulation enhancement phenomenon.

However, it is also noteworthy to point out that the improved blood circulation time not always lead to stable or increased tumor uptake. The uptake can be affected by various factors such as target affinity, dissociation rates, clearance rates and stability etc. The ^{18}F-sTCO-DiPhTz-BBN showed decreased tumor uptake even when the blood pool signal was high. Since bombesin has a short in vivo half-life and is proteolytically degraded in less than 30min (*50*). The signal in the blood pool might come from the intact ^{18}F-sTCO-DiPhTz moiety while the targeting moiety already got degraded.

To have a better understanding of enhanced blood circulation of the sTCO-DiPhTz system, we injected tracer ^{18}F-sTCO-DiPhTz into normal mice and collected the blood at 1h post injection. After separation of the blood cells and plasma, 95.3% of the radio activity was left in the plasma, indicating the tracer may bind to proteins in the plasma. The plasma was then subjected to electrophoresis and autoradiography. As shown in Figure 4.45, the autoradiography revealed the presence of ^{18}F-sTCO-DiPhTz binding proteins as radioactive band (instead of monomeric ^{18}F-sTCO-DiPhTz) which coincided with the protein band visualized by Coomassie blue staining. Due to the abundance of proteins in mouse plasma, the radioactive band was identified as a mixture of hemopexin and transferrin by MALDI-TOF/TOF. In order to further confirm the identity of the binding protein, we incubated ^{18}F-sTCO-DiPhTz with pure hemopexin and transferrin individually followed by electrophoresis and autoradiography. As shown in Figure 4.46, ^{18}F-sTCO-DiPhTz binding can be seen on both proteins, whereas hemopexin showed stronger radioactive signal than transferrin. This suggested that the sTCO-DiPhTz system may bind to plasma proteins like hemopexin and transferrin, thus prolonged its circulation time in blood.

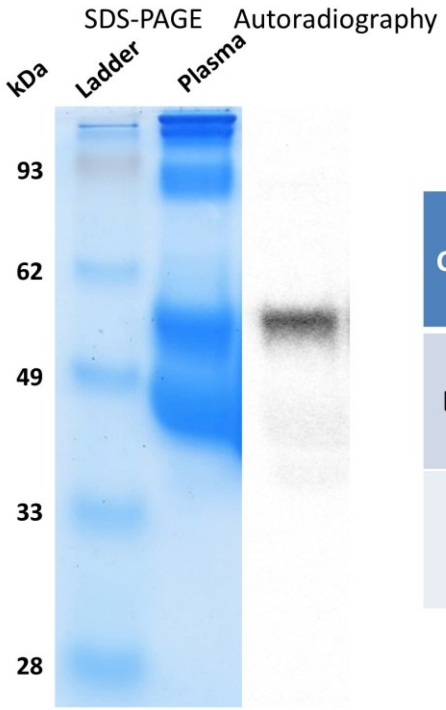

Component	Percentage of activity
Blood Cells	4.66%
Blood Plasma	95.34%

Figure 4.45 Electropherogram and autoradiography of ^{18}*F-sTCO-DiPhTz in mouse plasma.*

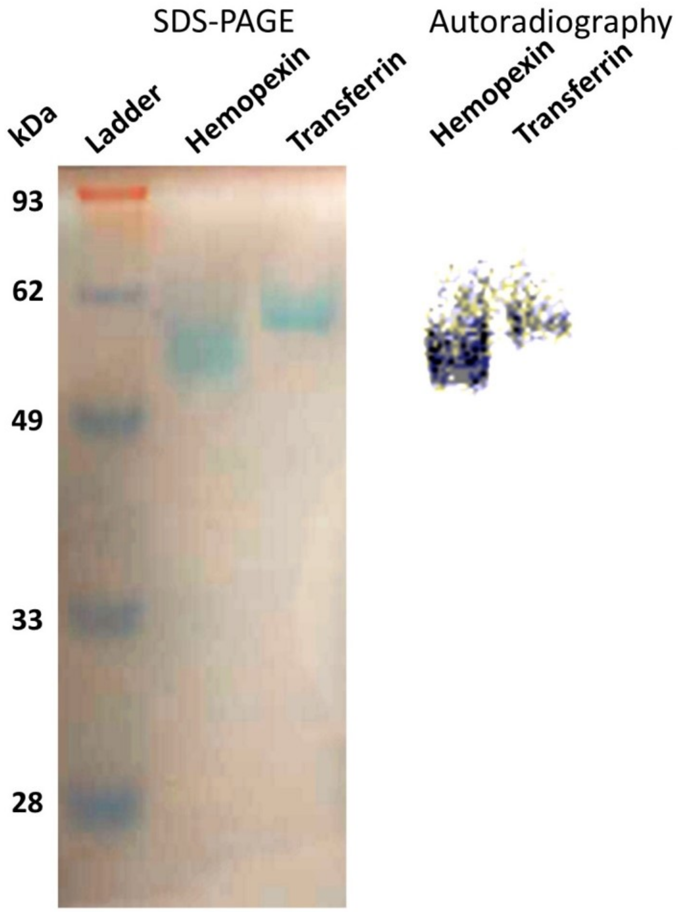

Figure 4.46 Electropherogram and autoradiography of ^{18}*F-sTCO-DiPhTz in hemopexin and transferrin.*

4.8 Conclusion

In this chapter, we have demonstrated that the TTCO ligation could be successfully applied to radiofluorinate biomolecules with different molecular weights for PET probe construction. All candidates were labeled with reasonable isolation yield and high purity after purification. The constructed PET probes showed reasonable tumor targeting efficiency with different biodistribution patterns. The DiPhTz-sTCO system showed long lasting blood circulation time while the more hydrophilic tetrazine and *trans*-cyclooctene systems showed higher tumor to background contrast. **In summary, TTCO ligation is a versatile radiolabeling method to construct PET probes based on both small and large biomolecules.** However, it is worthwhile to point out that this labeling method is still far from clinical use. More systematic evaluation on the stability, toxicity, pharmacokinetic and dosimetry in primates etc. are necessary before clinical trial. Additionally, the synthesis procedure needs to be optimized and adapted to integrated modules.

4.9 Materials and Methods

4.9.1 General

All chemicals were procured through commercially available sources and used without further purification. All *trans*-cyclooctene and tetrazine-NHS ester derivatives were kindly provided by Dr. Joseph M. Fox from University of Delaware and the HER2 ligand was provided by Dr. Rihe Liu from School of Pharmacy at University of North Carolina at Chapel Hill. RGDyK and NT20.3 peptide was purchased from C.S.Bio (CA, USA). PSMA ligand Glu-urea-Lys was obtained from FutureChem (Seoul, Korea). Analytical RP-HPLC was equipped with a Kinetex 5µ C18 column (250 x 4.6mm), a SPD-M30A photodiode array detector (Shimadzu) and model 105S single-channel radiation detector (Carroll & Ramsey Associates). The flow rate was 1 mL/min for radio-HPLC analysis while the mobile phase was 0.1% TFA in water for solvent A and 0.1% TFA in acetonitrile for solvent B. The mobile phase was kept at 95% solvent A and 5% solvent B from 0~2min and ramped to 5% solvent A and 95% solvent B in 20min. Mass spectrometry was obtained on Advion Expression CMS mass spectrometer.

4.9.2 Chemistry and Radiochemistry

All peptides and PSMA ligand except Exendin4 were modified with tetrazine derivatives under the same protocol. Briefly, peptides or PSMA ligand (1 µmol) was dissolved in 30 µL of anhydrous DMSO. Tetrazine-NHS analogues (1.5 eq) were dissolved in another 30 µL of anhydrous DMSO and mixed with the peptides or PSMA ligand solution. DIPEA (5 µL) was added to the mixture and stirred for 2h at room temperature. The reaction was quenched with 1 mL 5% acetic acid and the crude was analyzed and purified by RP-HPLC. For Exendin4 derivative, DiPhTz-NHS was first converted to DiPhTz-mal. 2 μmol of DiPhTz-NHS was dissolved in 30 μL dry DMSO followed by the addition of 3 μmol of N-(2-Aminoethyl)maleimide in 30 μL of dry DMSO. After adding in 5 μL of DIPEA, the crude was incubated at room temperature for 2h and purified using RP-HPLC. DiPhTz-Mal was collected and lyophilized for storage. Exendin4 (1 μmol) was dissolved in 50 μL of 1X PBS before adding in 1.5 eq DiPhTz-mal in another 50 μL of 1X PBS. The pH was adjusted to neutral and the mixture was incubated at room temperature for 1h. The reaction was quenched with 1 mL 5% acetic acid and the crude was analyzed and purified using RP-HPLC. The ^{19}F standard of each tracer was synthesized by mixing 0.1 μmol of peptide/PSMA ligand-tetrazine analogue and 0.1 μmol of ^{19}F-TCO derivatives. The mixture was incubated at room temperature for 1min and loaded on RP-HPLC for analysis and purification.

HER2 ligand was conjugated with MePhTz-NHS under a modified protocol. HER2 ligand (500 μg, 40nmol) was prepared in 1X PBS and adjusted to pH 8.5 using borate buffer. MePhTz-NHS (5, 10 or 20 eq) was dissolved in 50 μL Milli-Q water and added to the HER2 ligand solution. The mixture was incubated at 4^{o}C overnight and purified by size-exclusive PD-10 column using 1X PBS as elution buffer. The elution fraction containing MePhTz-HER2 was collected for further use.

Radio TTCO ligation was carried out in a similar pattern to the non-radioactive version. Briefly, 185 MBq of ^{18}F-TCO analogues or 37 MBq of ^{64}Cu-TCO analogues was mixed with 5 nmol of peptide/PSMA ligand-tetrazine derivatives and incubated at room temperature for 10 seconds. The crude was then subjected to radio HPLC purification. The collected fraction containing product was rotary evaporated to remove organic solvent and reconstituted in 1X PBS for further use. For HER2 ligand radiolabeling, 185 MBq of ^{18}F-oTCO purified by RP-HPLC was rotary evaporated to remove the organic solvent. The pH was adjusted to neutral using 0.1 N NaOH and 1X PBS. After mixing with 1 nmol of MePhTz-HER2 for 10 seconds, the crude was purified with PD-10 column and the 4th milliliter was collected as product.

4.9.3 Small Animal PET Imaging

All animal procedures were performed according to protocol approved by the UNC Institutional Animal Care and Use Committee. Generally, tumor bearing mice were anesthetized under 2% isoflurane/oxygen and intravenously injected with 3.7 MBq of each PET tracer. At 1 and 4 h post injection, 10min static emission scans were acquired using small animal PET scanner (GE eXplre Vista or SuperArgus). The regions of interest (ROIs) were manually drawn and converted to %ID/g based on the assumption of 1g/mL tissue density.

4.9.4 *In Vitro* Cell Binding Assay

The NTSR1 binding of NT related tracers was evaluated using a competitive binding assay according to our previously reported method (*68*). PC3 or H1299 cells were incubated with ^{125}I-NT(8-13) and various concentrations (0.001-10000 nM) of ^{19}F version of tetrazine-NT-TCO analogues and NT(8-13). After 1h of incubation at 37°C, the cells were washed with PBS for three times and lysed with 0.1 N NaOH. The activity on the cells was measured by γ-counter (PerkinElmer). Nonlinear regression was performed with GraphPad Prism 6 and the best-fit inhibitory concentration (IC_{50}) was calculated. Experiments were performed on triplicate samples.

4.9.5 Octanol-Water Partition Coefficient

185 kBq of each ^{18}F tracer was diluted in 500 µL PBS and 500 µL octanol. After vigorous mixing for 10min, the mixture was centrifuged (5min, 5000 rpm) to separate the aqueous and organic phases. The activity in aliquots of the organic and aqueous layers were measured by γ-counter (PerkinElmer).

4.9.6 Statistical Analysis

Analyzed data were presented as mean ± standard deviation (SD).

REFERENCES

1. Pierschbacher MD, Ruoslahti E. Cell attachment activity of fibronectin can be duplicated by small synthetic fragments of the molecule. *Nature.* 1984;309:30-33.

2. Stupack D. The biology of integrins. *Oncology.* 2007;21:6-12.

3. Chen X. Integrin Targeted Imaging and Therapy. *Theranostics.* 2011;2011:28-29.

4. Takada Y, Ye X, Simon S. The integrins. *Genome Biology.* 2007;8:215.

5. Zitzmann S, Ehemann V, Schwab M. Arginine-Glycine-Aspartic Acid (RGD)-Peptide Binds to Both Tumor and Tumor-Endothelial Cells ***in Vivo***. *Cancer Research.* 2002;62:5139.

6. Puduvalli VK. Inhibition of Angiogenesis as a Therapeutic Strategy against Brain Tumors. In: Kirsch M, Black PM, eds. *Angiogenesis in Brain Tumors*. Boston, MA: Springer US; 2004:307-336.

7. Sengupta S, Chattopadhyay N, Mitra A, Ray S, Dasgupta S, Chatterjee A. Role of $\alpha_v\beta_3$ integrin receptors in breast tumor. *Journal of Experimental & Clinical Cancer Research.* 2001;20:585-590.

8. Bello L, Francolini M, Marthyn P, et al. $\alpha_v\beta_3$ and $\alpha_v\beta_5$ Integrin Expression in Glioma Periphery. *Neurosurgery.* 2001;49:380-390.

9. Taga T, Suzuki A, Gonzalez-Gomez I, et al. α_v-Integrin antagonist EMD 121974 induces apoptosis in brain tumor cells growing on vitronectin and tenascin. *International Journal of Cancer.* 2002;98:690-697.

10. Beer AJ, Schwaiger M. PET Imaging of $\alpha_v\beta_3$ Expression in Cancer Patients. In: Shah K, ed. *Molecular Imaging: Methods and Protocols*. Totowa, NJ: Humana Press; 2011:183-200.

11. Haubner R, Kuhnast B, Mang C, et al. [^{18}F]Galacto-RGD: Synthesis, Radiolabeling, Metabolic Stability, and Radiation Dose Estimates. *Bioconjugate Chemistry.* 2004;15:61-69.

12. Jeong JM, Hong MK, Chang YS, et al. Preparation of a Promising Angiogenesis PET Imaging Agent: ^{68}Ga-Labeled c(RGDyK)–Isothiocyanatobenzyl-1,4,7-Triazacyclononane-1,4,7-Triacetic Acid and Feasibility Studies in Mice. *Journal of Nuclear Medicine.* 2008;49:830-836.

13. Lang L, Li W, Guo N, et al. Comparison Study of [^{18}F]FAl-NOTA-PRGD2, [^{18}F]FPPRGD2, and [^{68}Ga]Ga-NOTA-PRGD2 for PET Imaging of U87MG Tumors in Mice. *Bioconjugate Chemistry.* 2011;22:2415-2422.

14. Selvaraj R, Giglio B, Liu S, et al. Improved Metabolic Stability for ^{18}F PET Probes Rapidly Constructed via Tetrazine trans-Cyclooctene Ligation. *Bioconjugate Chemistry.* 2015;26:435-442.

15. Wang M, Svatunek D, Rohlfing K, et al. Conformationally Strained trans-Cyclooctene (sTCO) Enables the Rapid Construction of ^{18}F-PET Probes via Tetrazine Ligation. *Theranostics.* 2016;6:887-895.

16. Taylor MT, Blackman ML, Dmitrenko O, Fox JM. Design and Synthesis of Highly Reactive Dienophiles for the Tetrazine–trans-Cyclooctene Ligation. *Journal of the American Chemical Society.* 2011;133:9646-9649.

17. Kisfalvi K, Guha S, Rozengurt E. Neurotensin and EGF induce synergistic stimulation of DNA synthesis by increasing the duration of ERK signaling in ductal pancreatic cancer cells. *Journal of Cellular Physiology.* 2005;202:880-890.

18. Leyton J, Garcia-Marin L, Jensen RT, Moody TW. Neurotensin causes tyrosine phosphorylation of focal adhesion kinase in lung cancer cells. *European Journal of Pharmacology.* 2002;442:179-186.

19. McNeil GP, Dobner PR, Harrison RJ. Synergistic activation of neurotensin/neuromedin N gene expression by c-Jun and glucocorticoids: novel effects of Fos family proteins. *Molecular Endocrinology.* 1995;9:981-993.

20. Alifano M, Loi M, Camilleri-Broet S, Dupouy S, Régnard JF, Forgez P. Neurotensin expression and outcome of malignant pleural mesothelioma. *Biochimie.* 2010;92:164-170.

21. Gui X, Guzman G, Dobner PR, Kadkol SS. Increased neurotensin receptor-1 expression during progression of colonic adenocarcinoma. *Peptides.* 2008;29:1609-1615.

22. Souazé F, Dupouy S, Viardot-Foucault V, et al. Expression of Neurotensin and NT1 Receptor in Human Breast Cancer: A Potential Role in Tumor Progression. *Cancer Research.* 2006;66:6243.

23. Alifano M, Souazé F, Dupouy S, et al. Neurotensin Receptor 1 Determines the Outcome of Non–Small Cell Lung Cancer. *Clinical Cancer Research.* 2010;16:4401.

24. Reubi JC, Waser B, Friess H, Büchler M, Laissue J. Neurotensin receptors: a new marker for human ductal pancreatic adenocarcinoma. *Gut.* 1998;42:546.

25. Sehgal I, Powers S, Huntley B, Powis G, Pittelkow M, Maihle NJ. Neurotensin is an autocrine trophic factor stimulated by androgen withdrawal in human prostate cancer. *Proceedings of the National Academy of Sciences.* 1994;91:4673.

26. Valerie NCK, Casarez EV, DaSilva JO, et al. Inhibition of Neurotensin Receptor 1 Selectively Sensitizes Prostate Cancer to Ionizing Radiation. *Cancer Research.* 2011;71:6817.

27. Granier C, Van Rietschoten J, Kitabgi P, Poustis C, Freychet P. Synthesis and Characterization of Neurotensin Analogues for Structure/Activity Relationship Studies. *European Journal of Biochemistry.* 1982;124:117-125.

28. Alshoukr F, Prignon A, Brans L, et al. Novel DOTA-Neurotensin Analogues for ^{111}In Scintigraphy and ^{68}Ga PET Imaging of Neurotensin Receptor-Positive Tumors. *Bioconjugate Chemistry.* 2011;22:1374-1385.

29. Wu Z, Li L, Liu S, et al. Facile Preparation of a Thiol-Reactive ^{18}F-Labeling Agent and Synthesis of ^{18}F-DEG-VS-NT for PET Imaging of a Neurotensin Receptor–Positive Tumor. *Journal of Nuclear Medicine.* 2014;55:1178-1184.

30. Siegel RL, Miller KD, Jemal A. Cancer statistics, 2017. *CA: A Cancer Journal for Clinicians.* 2017;67:7-30.

31. Zeller JL, Lynm C, Glass RM. Grading of Prostate Cancer. *JAMA.* 2007;298:1596-1596.

32. Chodak G, Keller P, HW S. Assessment of screening for prostate cancer using the digital rectal examination. *The Journal of Urology.* 1989;141:1136-1138.

33. Essink-Bot M-L, de Koning HJ, Nijs HGT, Kirkels WJ, van der Maas PJ, Schröder FH. Short-Term Effects of Population-Based Screening for Prostate Cancer on Health-Related Quality of Life. *JNCI: Journal of the National Cancer Institute.* 1998;90:925-931.

34. D'Amico AV, Roehrborn CG. Effect of 1 mg/day finasteride on concentrations of serum prostate-specific antigen in men with androgenic alopecia: a randomised controlled trial. *The Lancet Oncology.* 2007;8:21-25.

35. Linn M, Ball R, A M. Prostate-specific antigen screening: friend or foe? *Urologic Nursing.* 2007;27:481-489.

36. Mannweiler S, Amersdorfer P, Trajanoski S, Terrett JA, King D, Mehes G. Heterogeneity of Prostate-Specific Membrane Antigen (PSMA) Expression in Prostate Carcinoma with Distant Metastasis. *Pathology & Oncology Research.* 2009;15:167-172.

37. Silver DA, Pellicer I, Fair WR, Heston WD, Cordon-Cardo C. Prostate-specific membrane antigen expression in normal and malignant human tissues. *Clinical Cancer Research.* 1997;3:81.

38. Trover JK, Beckett ML, Wright Jr GL. Detection and characterization of the prostate-specific membrane antigen (PSMA) in tissue extracts and body fluids. *International Journal of Cancer.* 1995;62:552-558.

39. Perner S, Hofer MD, Kim R, et al. Prostate-specific membrane antigen expression as a predictor of prostate cancer progression. *Human Pathology.* 2007;38:696-701.

40. Bander NH. Technology Insight: monoclonal antibody imaging of prostate cancer. *Nature Clinical Practice Urology.* 2006;3:216.

41. Afshar-Oromieh A, Malcher A, Eder M, et al. PET imaging with a [^{68}Ga]gallium-labelled PSMA ligand for the diagnosis of prostate cancer: biodistribution in humans and first evaluation of tumour lesions. *European Journal of Nuclear Medicine and Molecular Imaging.* 2013;40:486-495.

42. Ghosh A, Heston WDW. Tumor target prostate specific membrane antigen (PSMA) and its regulation in prostate cancer. *Journal of Cellular Biochemistry.* 2004;91:528-539.

43. Rajasekaran SA, Anilkumar G, Oshima E, et al. A Novel Cytoplasmic Tail MXXXL Motif Mediates the Internalization of Prostate-specific Membrane Antigen. *Molecular Biology of the Cell.* 2003;14:4835-4845.

44. Eder M, Schäfer M, Bauder-Wüst U, et al. ^{68}Ga-Complex Lipophilicity and the Targeting Property of a Urea-Based PSMA Inhibitor for PET Imaging. *Bioconjugate Chemistry.* 2012;23:688-697.

45. Rowe SP, Macura KJ, Mena E, et al. PSMA-Based [^{18}F]DCFPyL PET/CT Is Superior to Conventional Imaging for Lesion Detection in Patients with Metastatic Prostate Cancer. *Molecular Imaging and Biology.* 2016;18:411-419.

46. Weineisen M, Schottelius M, Simecek J, et al. ^{68}Ga- and ^{177}Lu-Labeled PSMA I&T: Optimization of a PSMA-Targeted Theranostic Concept and First Proof-of-Concept Human Studies. *Journal of Nuclear Medicine.* 2015;56:1169-1176.

47. Robu S, Schmidt A, Eiber M, et al. Synthesis and preclinical evaluation of novel ^{18}F-labeled Glu-urea-Glu-based PSMA inhibitors for prostate cancer imaging: a comparison with ^{18}F-DCFPyl and ^{18}F-PSMA-1007. *EJNMMI Research.* 2018;8:30.

48. Körner M, Stöckli M, Waser B, Reubi JC. GLP-1 Receptor Expression in Human Tumors and Human Normal Tissues: Potential for In Vivo Targeting. *Journal of Nuclear Medicine.* 2007;48:736-743.

49. Tornehave D, Kristensen P, Rømer J, Knudsen LB, Heller RS. Expression of the GLP-1 Receptor in Mouse, Rat, and Human Pancreas. *Journal of Histochemistry & Cytochemistry.* 2008;56:841-851.

50. Yang Y-S, Zhang X, Xiong Z, Chen X. Comparative in vitro and in vivo evaluation of two ^{64}Cu-labeled bombesin analogs in a mouse model of human prostate adenocarcinoma. *Nuclear Medicine and Biology.* 2006;33:371-380.

51. Patricia VE, Rosalía ICR, Maria FC, Roxana S. ErbB-2 nuclear function in breast cancer growth, metastasis and resistance to therapy. *Endocrine-Related Cancer.* 2016;23:T243-T257.

52. Toss A, Venturelli M, Peterle C, Piacentini F, Cascinu S, Cortesi L. Molecular Biomarkers for Prediction of Targeted Therapy Response in Metastatic Breast Cancer: Trick or Treat? *International Journal of Molecular Sciences.* 2017;18.

53. Moasser MM. The oncogene HER2: its signaling and transforming functions and its role in human cancer pathogenesis. *Oncogene.* 2007;26:6469.

54. Olayioye MA, Neve RM, Lane HA, Hynes NE. The ErbB signaling network: receptor heterodimerization in development and cancer. *The EMBO Journal.* 2000;19:3159.

55. Gebhart G, Flamen P, De Vries EGE, Jhaveri K, Wimana Z. Imaging Diagnostic and Therapeutic Targets: Human Epidermal Growth Factor Receptor 2. *Journal of Nuclear Medicine.* 2016;57:81S-88S.

56. Schmidt KT, Chau CH, Price DK, Figg WD. Precision Oncology Medicine: The Clinical Relevance of Patient-Specific Biomarkers Used to Optimize Cancer Treatment. *The Journal of Clinical Pharmacology.* 2016;56:1484-1499.

57. Gu G, Dustin D, Fuqua SAW. Targeted therapy for breast cancer and molecular mechanisms of resistance to treatment. *Current Opinion in Pharmacology.* 2016;31:97-103.

58. Luque-Cabal M, García-Teijido P, Fernández-Pérez Y, Sánchez-Lorenzo L, Palacio-Vázquez I. Mechanisms behind the Resistance to Trastuzumab in HER2-Amplified Breast Cancer and Strategies to Overcome It. *Clinical Medicine Insights: Oncology.* 2016;10s1:CMO.S34537.

59. Burstein HJ. The Distinctive Nature of HER2-Positive Breast Cancers. *New England Journal of Medicine.* 2005;353:1652-1654.

60. Mitri Z, Constantine T, O'Regan R. The HER2 Receptor in Breast Cancer: Pathophysiology, Clinical Use, and New Advances in Therapy. *Chemotherapy research and practice.* 2012;2012:743193-743193.

61. Becker S, Becker-Pergola G, Fehm T, Wallwiener D, Solomayer E-F. Her2 Expression on Disseminated Tumor Cells from Bone Marrow of Breast Cancer Patients. *Anticancer Research.* 2005;25:2171-2175.

62. Brown A, Wickerham DL, Romond E, et al. Real-World Performance of HER2 Testing—National Surgical Adjuvant Breast and Bowel Project Experience. *JNCI: Journal of the National Cancer Institute.* 2002;94:852-854.

63. Perez EA, Suman VJ, Davidson NE, et al. HER2 Testing by Local, Central, and Reference Laboratories in Specimens From the North Central Cancer Treatment Group N9831 Intergroup Adjuvant Trial. *Journal of Clinical Oncology.* 2006;24:3032-3038.

64. Cai Z, Chattopadhyay N, Yang K, et al. ^{111}In-labeled trastuzumab-modified gold nanoparticles are cytotoxic in vitro to HER2-positive breast cancer cells and arrest tumor growth in vivo in athymic mice after intratumoral injection. *Nuclear Medicine and Biology.* 2016;43:818-826.

65. Jiang D, Im H-J, Sun H, et al. Radiolabeled pertuzumab for imaging of human epidermal growth factor receptor 2 expression in ovarian cancer. *European Journal of Nuclear Medicine and Molecular Imaging.* 2017;44:1296-1305.

66. N Tinianow J, Pandya DN, Pailloux SL, et al. Evaluation of a 3-hydroxypyridin-2-one (2,3-HOPO) Based Macrocyclic Chelator for ^{89}Zr^{4+} and Its Use for ImmunoPET Imaging of HER2 Positive Model of Ovarian Carcinoma in Mice. *Theranostics.* 2016;6:511-521.

67. Ulaner GA, Hyman DM, Ross DS, et al. Detection of HER2-Positive Metastases in Patients with HER2-Negative Primary Breast Cancer Using ^{89}Zr-Trastuzumab PET/CT. *Journal of Nuclear Medicine.* 2016;57:1523-1528.

68. Wang M, Vannam R, Lambert WD, et al. Hydrophilic ^{18}F-labeled trans-5-oxocene (oxoTCO) for efficient construction of PET agents with improved tumor-to-background ratios in neurotensin receptor (NTR) imaging. *Chemical Communications.* 2019;55:2485-2488.

Chapter 5 EXPLORATION OF PRE-TARGETING CONCEPT USING TTCO LIGATION

5.1 Introduction to Pretargeting

Due to the extremely high specificity and binding affinity, antibodies can be served as an excellent targeting vector in both imaging and therapy. Tons of antibody based radiopharmaceuticals have been developed and evaluated in PET imaging and radionuclide therapy (*1*). However, one limitation of antibodies is that the large size and relatively slow pharmacokinetic always requires several days or even weeks before reaching the equilibrium and optimal biodistribution in vivo. To match with this time period, radioisotopes with half-life that are compatible with the biological half-life of the antibodies are needed to construct the radiopharmaceuticals (*2*). For example, ^{64}Cu and ^{89}Zr have been extensively used to radiolabel antibodies for PET imaging while ^{225}Ac and ^{177}Lu were chosen for radionuclide therapy (*3-5*). Although this combination may lead to high dose of activity accumulated in targeting tissue, the long circulation time and radioactive half-life can also result in high and unnecessary radiation exposure to healthy tissues such as bone marrow (*6*).

To address such concerns, one potential method is to modify the antibodies to smaller size while maintaining the specificity and binding affinity to the target. The modified antibodies should show more rapid pharmacokinetic thus radioisotopes with shorter physical half-life can be used and the resulting pharmaceuticals will have favorable dosimetry. A common modification strategy is using the truncated antibodies such as F(ab’)$_2$, F(ab’) and scFv fragments (*7*).

However, these antibody fragments either suffer from poor specificity or lose some of the binding affinity, which lead to decreased uptake in targeted region and higher background signal.

Recently, an alternative strategy gained much attention to solve the discrepancy between the slow pharmacokinetic of intact antibody and the desire of reducing the radiation exposure. This strategy, named pretargeting, generally involves four steps. Initially, the nonradioactive antibody is modified with a specific tag and is systematically administered. The tagged antibody is allowed to circulate in the blood and accumulate in the targeting region while slowly clears from the bloodstream. Then a small molecular radio tracer that could specifically binds to the tag on the antibody is intravenously injected. Finally, the PET image is acquired after a short period of time during which the radiotracer binds to the tagged antibody and the excess of unbonded tracer rapidly clears from the body. The conflict between slow pharmacokinetic of intact antibody and minimizing the radiation to nontargeted tissues is avoided by individually injection of targeting antibody and the imaging radiotracer moiety. An ideal pretargeting system has many requirements ranging from the biological end to the chemistry end. For example, the target should be easy to access (on the cell surface other than inside the cell) and should have clear expression level difference between target region and background. The ligand is required to have reasonable binding affinity after certain modification and its pharmacokinetic property would allow sufficient time period to have it accumulate in the targeted region while the unbound ones clear from the bloodstream. Additionally, the ligand should not get internalized after binding to the target and should remain accessible. On the chemistry part, the tag on the ligand and the small molecular radio tracer should be stable and reactive enough in biological environment and at low concentrations. This reaction needs to be bioorthogonal as well. The radio tracer requires a favorable pharmacokinetic to clear out fast.

The core of this pretargeting method is the in vivo conjugation between these two individually injected motifs. Currently, three approaches have been developed to fulfill the in vivo conjugation requirement, including streptavidin-biotin reaction, bispecific antibody that could bind both to the target and radioligand, oligonucleotide reaction with its complementary sequences (*8-10*). However, the wide application of these approaches is denied by some intrinsic limitations such as the immunogenicity of the streptavidin modified antibodies and the lack of modularity of bispecific antibody construction.

As discussed in the previous sections, the TTCO ligation has extremely high reaction kinetic which is one the most important factor for in vivo reaction. Additionally, it is a selective, robust and bioorthogonal reaction which makes it an excellent candidate for pretargeting strategy. Previously, several studies reported the feasibility of using TTCO ligation in pretargeting of antibodies and have proven successful (*11-14*). However, most of them used ^{64}Cu as the radioisotope. **In this chapter, we explore the possibility of using ^{18}F labeled TTCO ligation in pretargeting strategy since it has shorter half-life and can exploit the dosimetric advantage of pretargeting further.**

5.2 Results and Discussion

5.2.1 Pretargeting with ^{18}F *Trans*-cyclooctene and Tetrazine-peptide

Since we have demonstrated the targeting efficiency of RGDyK derivatives in U87MG tumor model and the short biological half-life of peptide allowed us to finish the pretargeting in one day efficiently, we started the exploration of pretargeting with the DiPhTz-RGD-sTCO system. As shown in Figure 5.1, we intravenously injected the DiPhTz-RGDyK 1h before the administration of ^{18}F-sTCO and acquired the PET images at 1 and 4h post injection of ^{18}F-sTCO. Although a tumor uptake of 3.3 ± 0.0 %ID/g at 1h post injection was observed, it is not significantly different from the control group in which only ^{18}F-sTCO was administrated without pretargeted DiPhTz-RGDyK. The overall biodistribution of two groups were similar at both time points indicating the radio signal was mainly coming from the ^{18}F-sTCO other than ligated ^{18}F-DiPhTz-RGDyK-sTCO. This result suggested that either the ^{18}F-sTCO did not ligate with the DiPhTz-RGDyK in vivo or we failed catch the time window during which the DiPhTz-RGDyK was accumulated in the tumor with low concentration in the background. Additionally, although the ^{18}F-sTCO showed relatively fast clearance rate from the body, it was not stable in vivo as a significant bone uptake was observed at 4h post injection of ^{18}F-sTCO indicating the defluorination. Due to the short time window available for peptide to achieve good target to background contrast and the instability of ^{18}F-sTCO, the DiPhTz-RGDyK-sTCO system was not a suitable combination for pretargeting strategy.

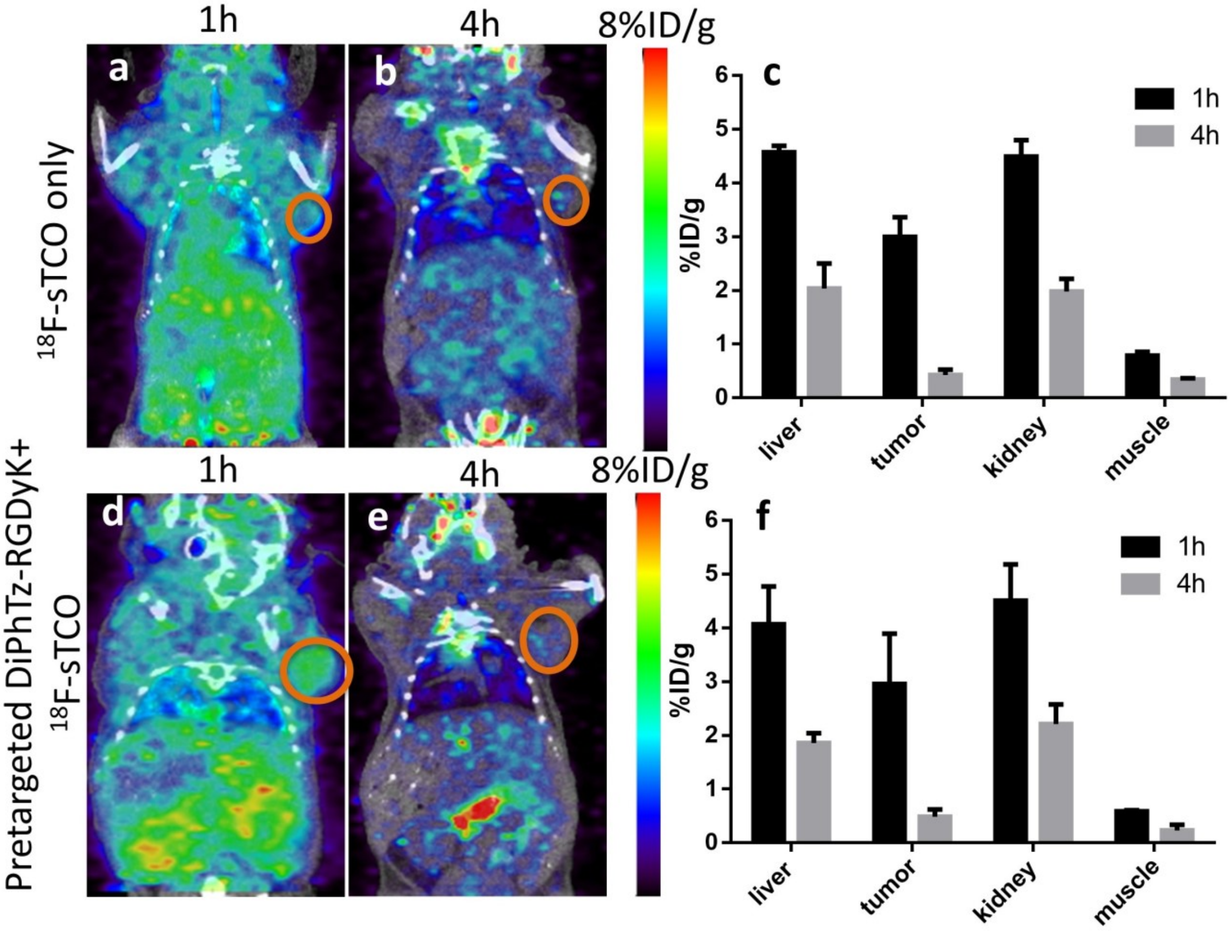

Figure 5.1 Representative PET/CT images of U87MG tumor bearing mice at a) 1h and b) 4h post injection of ^{18}F-sTCO. c) Quantitative uptake of the major organs determined from the PET images. Representative PET/CT images of U87MG tumor bearing mice injected with ^{18}F-sTCO 1h after pretargeting of DiPhTz-RGDyK. Images were acquired at d) 1h and e) 4h post injection of ^{18}F-sTCO. f) Quantitative uptake of the major organs determined from the PET images. Tumor regions are highlighted in orange circle

5.2.2 Pretargeting with ^{64}Cu Tetrazine and TCO-antibody

Since ^{18}F-*trans*-cyclooctenes was not stable in vivo and failed to serve as the radiolabeled small molecule moiety in pretargeting method, we turned to radiolabel the tetrazine and modify the biomolecule targeting vector with TCO tags. In the second experiment we chose the antibody 15D3 as the targeting moiety, which was an anti-P-glycoprotein antibody and can be used to select patients with multidrug resistant cancer to certain P-glycoprotein derived therapies. As shown in Figure 5.2, the TCO-15D3 was allowed to circulate in the bloodstream for 24h before injection of ^{64}Cu-Tz-PEG-NOTA. Unfortunately, low tumor uptake (1.3%ID/g) was observed in the pretargeting group (Fig 5.2d, 5.2e and 5.2f) and the tumor uptake was similar to that in the ^{64}Cu-Tz-PEG-NOTA only group (1.1 %ID/g). However, one thing needs to be mentioned was that the liver uptake was significantly higher in the pretaregeting group. More importantly, distinct radio signal could be observed in the blood pool of the pretargeting group whereas little was observed in the ^{64}Cu-Tz-PEG-NOTA group. The difference in the biodistribution indicated the TTCO ligation occurrence in vivo. The low tumor uptake and distinct blood pool signal suggested that the majority of 15D3-TCO was still circulating in the blood at the time of injection of ^{64}Cu-Tz-PEG-NOTA.

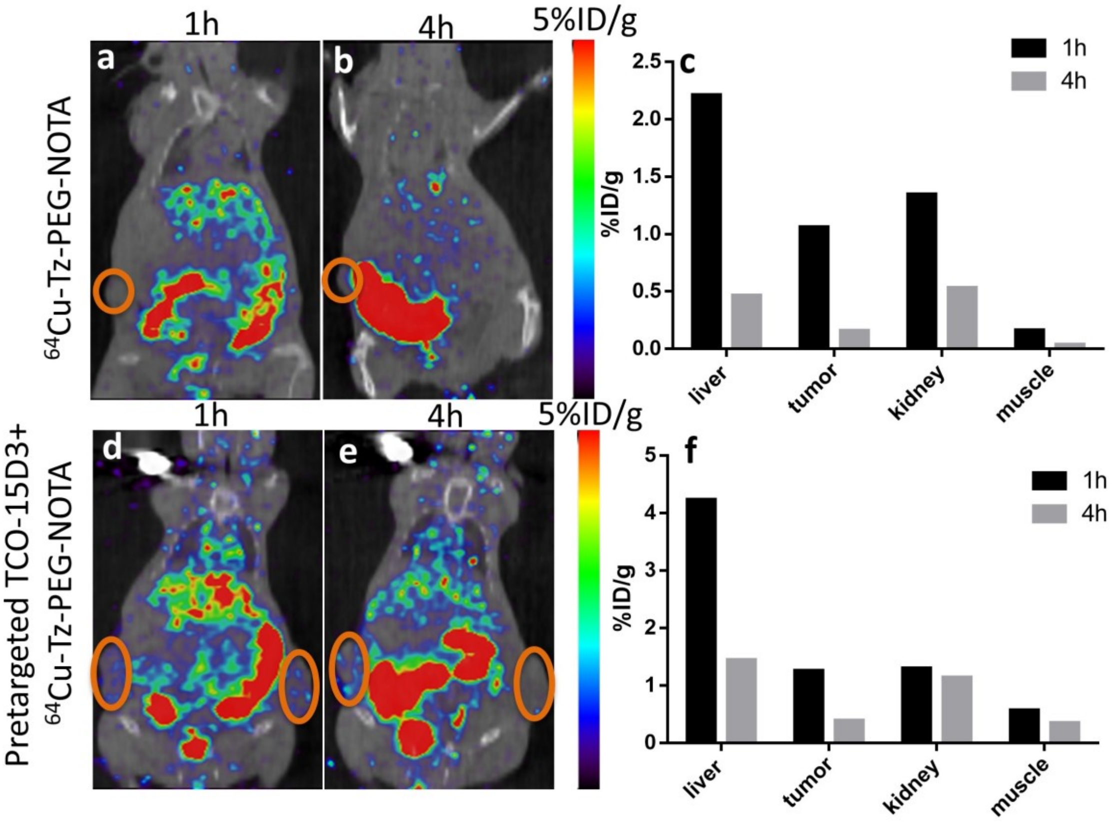

Figure 5.2 Representative PET/CT images of Fadu tumor bearing mice at a) 1h and b) 4h post injection of ^{64}Cu-Tz-PEG-NOTA. c) Quantitative uptake of the major organs determined from the PET images. Representative PET/CT images of Fadu tumor bearing mice injected with ^{64}Cu-Tz-PEG-NOTA 24h after pretargeting of TCO-15D3. Images were acquired at d) 1h and e) 4h post injection of ^{64}Cu-Tz-PEG-NOTA. f) Quantitative uptake of the major organs determined from the PET images. Tumor regions are highlighted in orange circle

5.2.3 Pretargeting with ^{18}F TCO-8Tetrazine and TCO-antibody

The above experiment demonstrated that the TTCO ligation could happen in vivo. The unfavorable tumor uptake in the pretaregting group was mainly due to the misestimation of the pharmacokinetic of the 15D3-TCO. Although there were some encouraging results, the use of ^{64}Cu labeled small molecule did not match with the ultimate goal of pretargeting. In the following experiments, we switched back to ^{18}F labeled small molecule while kept using tetrazine functional group in the small molecule and TCO tags on the antibody. We engineered 8 tetrazines on a polymer core to form an 8-armed tetrazine multimer and served as a linker to conjugate the ^{18}F-TCO and 15D3-TCO. As shown in Figure 5.3, ^{18}F-TCO-8Tz conjugate was mainly localized in liver and kidney with uptakes of 4.0 %ID/g ± 0.9 %ID/g and 4.6 ± 0.5 %ID/g at 1h post injection. The tumor uptake was 2.1 ± 0.2 %ID/g at 1h and 1.4 ± 0.4 %ID/g at 4h post injection. On the contrary, the ^{18}F-TCO-8Tz-TCO-15D3 prepared in vitro showed significantly higher liver and kidney uptake (8.5 %ID/g and 8.3 %ID/g at 1h post injection). The biodistribution difference between the antibody conjugates and small molecule suggested that the engineered 8-armed tetrazine could successfully link the ^{18}F-TCO and 15D3-TCO.

After confirmed the reactivity of 8-armed tetrazine, we proceeded to the pretargeting method using 15D3-TCO and ^{18}F-TCO-8Tz. As we can see in Figure 5.4, the tumor uptake in the pretargeting group was 2.1 ± 0.7 %ID/g and 1.9 ± 0.3 %ID/g at 1 and 4h post injection, respectively. There was no significant difference between the pretargeting group and ^{18}F-TCO-8Tz only group (Fig 5.3a and 5.4) even when the pretargeting time period has been extended to 48h. As we have demonstrated the feasibility of TTCO ligation occurrence in vivo, the failed pretargeting experiment could still be due to the misestimation of the pharmacokinetic of the 15D3-TCO or the binding of such antibody to the tumor model we used.

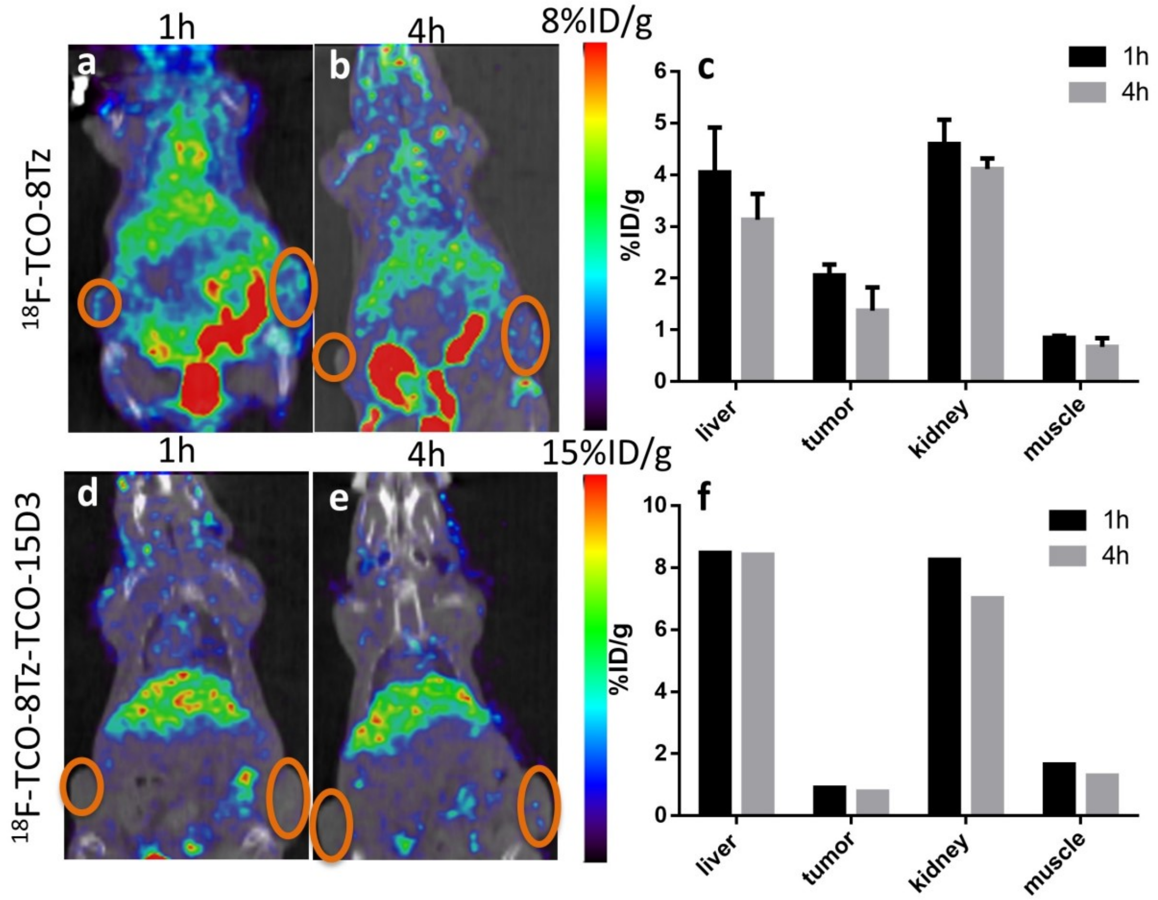

Figure 5.3 Representative PET/CT images of Fadu tumor bearing mice at a) 1h and b) 4h post injection of ^{18}F-TCO-8Tz. c) Quantitative uptake of the major organs determined from the PET images. Representative PET/CT images of Fadu tumor bearing mice at a) 1h and b) 4h post injection of ^{18}F-TCO-8Tz-TCO-15D3. c) Quantitative uptake of the major organs determined from the PET images. Tumor regions are highlighted in orange circle

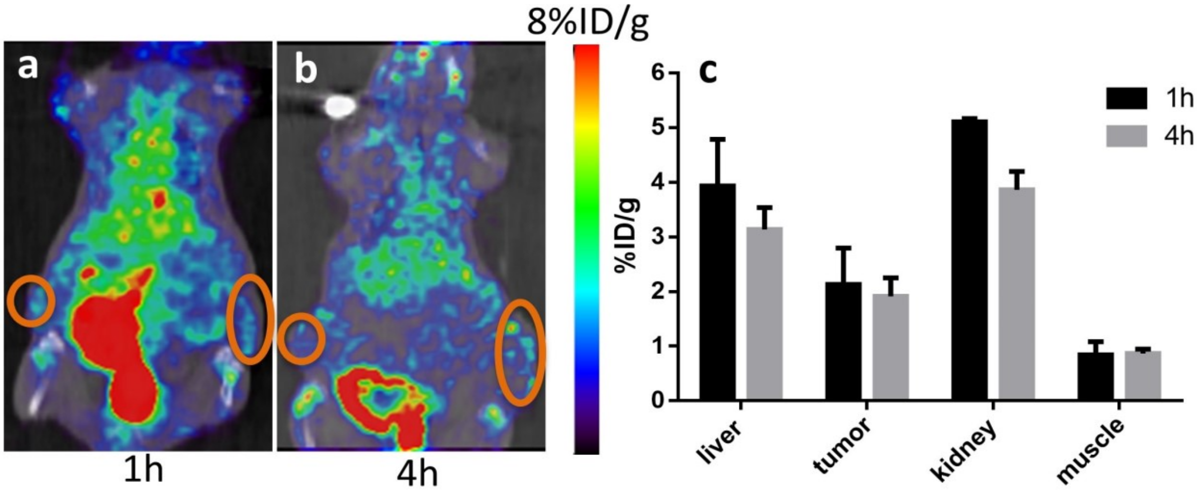

Figure 5.4 Representative PET/CT images of Fadu tumor bearing mice injected with ^{18}F-TCO-8Tz 48h after pretargeting of TCO-15D3. Images were acquired at a) 1h and b) 4h post injection of ^{18}F-TCO-8Tz. c) Quantitative uptake of the major organs determined from the PET images. Tumor regions are highlighted in orange circle

To address this problem, we intratumorally injected the 15D3-TCO in the right tumor 10min before systematically administration of ^{18}F-TCO-8Tz. As shown in Figure 5.5, the right tumor was clearly visualized at both time points after injection of ^{18}F-TCO-8Tz while the unpretargeted left tumor showed little tracer accumulation. Although the uptake in the right tumor (4.5 ± 0.5 %ID/g and 3.4 ± 0.3 %ID/g at 1h and 4h post injection, respectively) was lower than the typical uptake of antibodies, it was significantly higher than that of left tumor (1.2 ± 0.4 %ID/g and 0.9 ± 0.2 %ID/g at 1h and 4h post injection, respectively) at both time points ($P<0.05$). This result suggested that the TTCO ligation could be applied in pretargeting strategy as long as the radiolabeled small molecule was injected at the right time when the antibodies were accumulated in the tumor and cleared out from the background. We would like to point out that the ^{18}F-TCO-8Tz showed relatively long circulation time in blood and low clearance rate (Fig 5.3a). Thus, an ^{18}F labeled tetrazine with faster clearance rate and reasonable stability would be needed for further optimization.

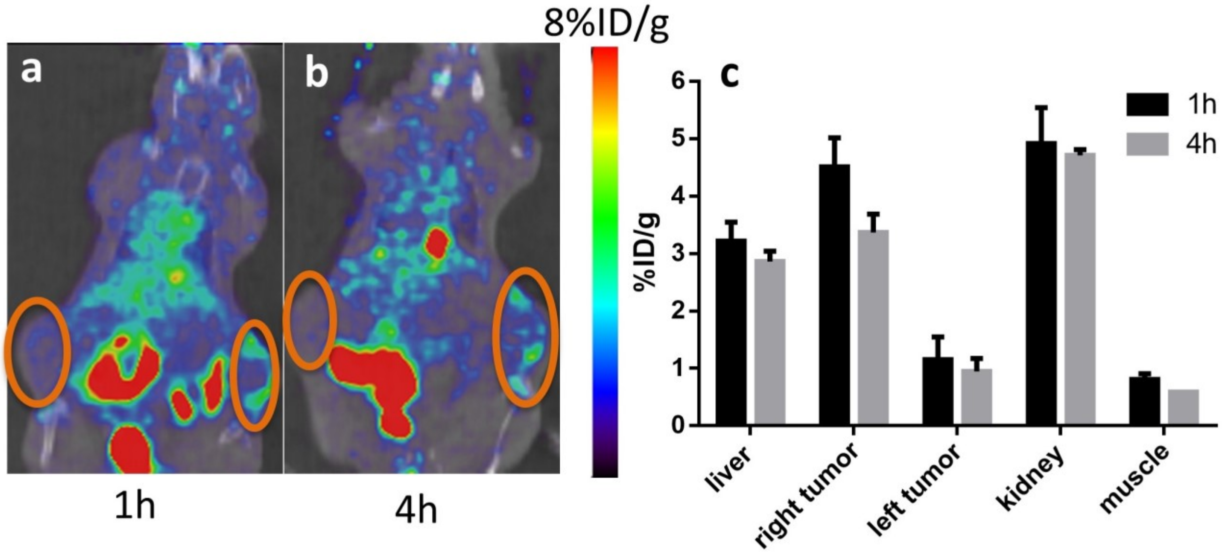

Figure 5.5 Representative PET/CT images of Fadu tumor bearing mice injected with ^{18}*F-TCO-8Tz 10min after intratumorally administration of TCO-15D3 (right tumor). Images were acquired at a) 1h and b) 4h post injection of* ^{18}*F-TCO-8Tz. c) Quantitative uptake of the major organs determined from the PET images. Tumor regions are highlighted in orange circle*

5.3 Conclusion

In this chapter we demonstrated the feasibility of TTCO ligation in vivo and constructed the ^{18}**F-TCO-8Tz-TCO-antibody system for pretargeting**. An intratumor "pretargeting" strategy was applied and the tumor could be successfully visualized if locally injected with TCO-antibody. However, the experiment was still unsuccessful when the TCO-15D3 was systematically injected. Further works would be needed to construct a stable and fast cleared ^{18}F labeled tetrazine, explore a suitable antibody and tumor model combination and gathering more information on the pharmacokinetic of the TCO tagged antibody.

5.4 Materials and Methods

5.4.1 General

All commercially available chemicals were purchased and used without further purification. All *trans*-cyclooctene and tetrazine-NHS ester derivatives were kindly provided by

Dr. Joseph M. Fox from University of Delaware. Antibody 15D3 and 8Tz were provided by Dr. Xin Ming from School of Medicine at Wake Forest University.

5.4.2 Chemistry and Radiochemistry

DiPhTz-RGDyK, ^{18}F-sTCO, ^{18}F-TCO and ^{64}Cu-Tz-PEG-NOTA were synthesized as described in the previous chapters. TCO-15D3 was prepared using the similar protocol as MePhTz-Her2. Briefly, 15D3 antibody (1mg ~ 5.9nmol) was prepared in 1x PBS and the pH was adjusted to 8.5 using borate buffer. TCO-NHS (20 eq) was dissolved in 50 μL Milli-Q water and added to the 15D3 antibody solution. After overnight incubation at 4^{o}C, the mixture was purified by size-exclusive PD-10 column and the elution fraction containing 15D3-TCO was collected in PBS. ^{18}F-8Tz-TCO was prepared by mixing ^{18}F-TCO with 8Tz at a molar ratio of 4:1 and incubated at room temperature for 10min. ^{18}F-TCO-8Tz-TCO-15D3 was prepared by mixing ^{18}F-TCO-8Tz with 20 μg of 15D3-TCO and incubated at room temperature for 10min before PD-10 purification.

5.4.3 Pretargeted Small Animal PET Imaging

All animal procedures were performed according to protocol approved by the UNC Institutional Animal Care and Use Committee. For peptide based pretargeting experiment, 2 groups of U87MG tumor bearing mice were included. The first group of mice were intravenously injected with 50 μg of DiPhTz-RGDyK. 2h post injection of DiPhTz-RGDyK, 3.7 MBq of ^{18}F-sTCO was injected into both groups of animals via tail vein. At 1 and 4h post injection of ^{18}F-sTCO, both groups of animals were subjected to 10min static emission PET scans. For antibody based pretargeting experiment, 6 groups of Fadu tumor bearing mice were included. Group 1 received 300 μg 15D3-TCO intravenously 24h before intravenous injection of 3.7 MBq of ^{64}Cu-Tz-PEG-NOTA. Group 2 received intravenous injection of 3.7 MBq of ^{64}Cu-

Tz-PEG-NOTA only. Group 3 and group 4 were injected with 3.7 MBq of ^{18}F-TCO-8Tz and ^{18}F-TCO-8Tz-TCO-15D3, respectively. Group 5 received 300 μg 15D3-TCO intravenously 48h before intravenous injection of 3.7 MBq of ^{18}F-TCO-8Tz while group 6 was intratumorally injected with 50 μg of 15D3-TCO 10min before intravenous injection of 3.7 MBq of ^{18}F-TCO-8Tz. All groups of animals were subjected to 10min static scans at 1 and 4h post injection of the radio tracer. The regions of interest (ROIs) were manually drawn and converted to %ID/g based on the assumption of 1g/mL tissue density.

5.4.4 Statistical Analysis

Analyzed data were presented as mean ± standard deviation (SD). The comparison of mean values was performed with Student's *t* test and the P value <0.05 was considered to be statistically significant.

REFERENCES

1. Wu AM. Antibodies and Antimatter: The Resurgence of Immuno-PET. *Journal of Nuclear Medicine.* 2009;50:2-5.

2. Zeglis BM, Lewis JS. A practical guide to the construction of radiometallated bioconjugates for positron emission tomography. *Dalton Transactions.* 2011;40:6168-6195.

3. Deri MA, Zeglis BM, Francesconi LC, Lewis JS. PET imaging with ^{89}Zr: From radiochemistry to the clinic. *Nuclear Medicine and Biology.* 2013;40:3-14.

4. van Dongen GAMS, Visser GWM, Lub-de Hooge MN, de Vries EG, Perk LR. Immuno-PET: A Navigator in Monoclonal Antibody Development and Applications. *The Oncologist.* 2007;12:1379-1389.

5. Vugts DJ, van Dongen GAMS. ^{89}Zr-labeled compounds for PET imaging guided personalized therapy. *Drug Discovery Today: Technologies.* 2011;8:e53-e61.

6. Ugur O, Kostakoglu L, Hui ET, et al. Comparison of the targeting characteristics of various radioimmunoconjugates for radioimmunotherapy of neuroblastoma: Dosimetry calculations incorporating cross-organ beta doses. *Nuclear Medicine and Biology.* 1996;23:1-8.

7. Wu AM. Engineered antibodies for molecular imaging of cancer. *Methods.* 2014;65:139-147.

8. Boerman OC, van Schaijk FG, Oyen WJG, Corstens FHM. Pretargeted Radioimmunotherapy of Cancer: Progress Step by Step. *Journal of Nuclear Medicine.* 2003;44:400-411.

9. Goldenberg DM, Rossi EA, Sharkey RM, McBride WJ, Chang C-H. Multifunctional Antibodies by the Dock-and-Lock Method for Improved Cancer Imaging and Therapy by Pretargeting. *Journal of Nuclear Medicine.* 2008;49:158-163.

10. Lewis MR, Wang M, Axworthy DB, et al. In Vivo Evaluation of Pretargeted ^{64}Cu for Tumor Imaging and Therapy. *Journal of Nuclear Medicine.* 2003;44:1284-1292.

11. Houghton JL, Membreno R, Abdel-Atti D, et al. Establishment of the *In Vivo* Efficacy of Pretargeted Radioimmunotherapy Utilizing Inverse Electron Demand Diels-Alder Click Chemistry. *Molecular Cancer Therapeutics.* 2017;16:124.

12. Meyer J-P, Kozlowski P, Jackson J, et al. Exploring Structural Parameters for Pretargeting Radioligand Optimization. *Journal of Medicinal Chemistry.* 2017;60:8201-8217.

13. Zeglis BM, Brand C, Abdel-Atti D, et al. Optimization of a Pretargeted Strategy for the PET Imaging of Colorectal Carcinoma via the Modulation of Radioligand Pharmacokinetics. *Molecular Pharmaceutics.* 2015;12:3575-3587.

14. Zeglis BM, Sevak KK, Reiner T, et al. A Pretargeted PET Imaging Strategy Based on Bioorthogonal Diels–Alder Click Chemistry. *Journal of Nuclear Medicine.* 2013;54:1389-1396.

Chapter 6 OTHER PET PROBES CONSTRUCTION PROJECTS

Despite of the application of TTCO ligation in biomolecule based PET probes construction, I also conducted some other PET probe synthesis projects. These projects are summarized in this chapter.

6.1 ^{18}F-NHC-BF$_3$ Adducts as Water Stable Radio-Prosthetic Groups for PET Imaging

6.1.1 Introduction

Due to the intrinsic decay property of ^{18}F, the ^{18}F labeling strategy requires fast and effective reactions and preferably to be carried out in the late stages of the synthesis of the final tracer. Previously Dr. Perrin etc established a method to rapidly incorporate fluoride ions to arylboronic acids or esters and form aryltrifluoroborates with great in vivo stability (*1-4*). Our group was inspired by the remarkable stability of N-hetercyclic carbene (NHC) boron fluoride adducts and investigated the possibility of radiofluorination of it and usage as prosthetic groups for PET imaging.

6.1.2 Results and Discussion

The radiofluorination of the NHC boron trifluoride adducts was carried out through ^{18}F-^{19}F isotopic exchange reaction promoted by Lewis acid SnCl$_4$. The ^{18}F labeled compound showed unusually high ressitance to hydrolytic fluoride release. The stability was ascribed to its zwitterionic nature, with the cationic charge of the imidazolium unit acting as an electrostatic anchor for the boron-bound fluoride anions. Modification of the NHC backbone with a maleimide functionality provided access to a model peptide conjugates (H-Cys-Phe-OH), which showed no evidence of defluorination when being imaged in vivo.

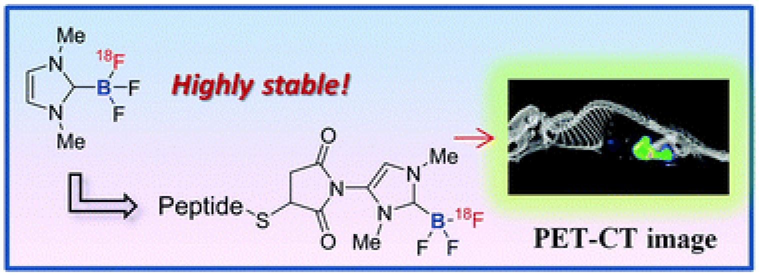

Figure 6.1 Graphical abstract of ^{18}F labeling of NHC-BF_3 adduct and PET images of the constructed PET tracer. Sources: Adapted from Mengzhe et al (5). Reproduced by permission of The Royal Society of Chemistry

6.2 Preparation of ^{18}F-NHC-BF_3 Conjugates and Their Applications in PET Imaging

6.2.1 Introduction

Fluorine-18 is preferably to be incorporated into molecular tracers at the last step of the overall synthesis process due to its short half- life (110 minutes). Several examples demonstrated the feasibility of attaching biomolecules to BF_3 or BF_2 unit and radiofluorinate the conjugates at the final step (*4,6,7*). Previously we synthesized the ^{18}F-NHC-BF_3 prosthetic group and successfully radiolabeled a short peptide with great in vivo stability. Here we validated the direct labeling of NHC-BF_3 pre-functionalized bioactive molecule and tested the in vivo behavior via PET imaging.

6.2.2 Results and Discussion

The NHC-BF_3-maleimide was conjugated to three biomolecules and was successfully radiofluorinated via $SnCl_4$ promoted ^{18}F-^{19}F isotope exchange reaction. The resulting PET probes showed excellent in vitro and in vivo stability due to the zwitterionic nature of the NHC-BF_3 moiety. As shown in Fig 6.2, the probe demonstrated prominent tumor uptake with good tumor to background contrast. This approach allows the ^{18}F to be introduced at late stage of the synthesis and provides broad applications for the radiolabelling of thiol-containing bioactive molecules.

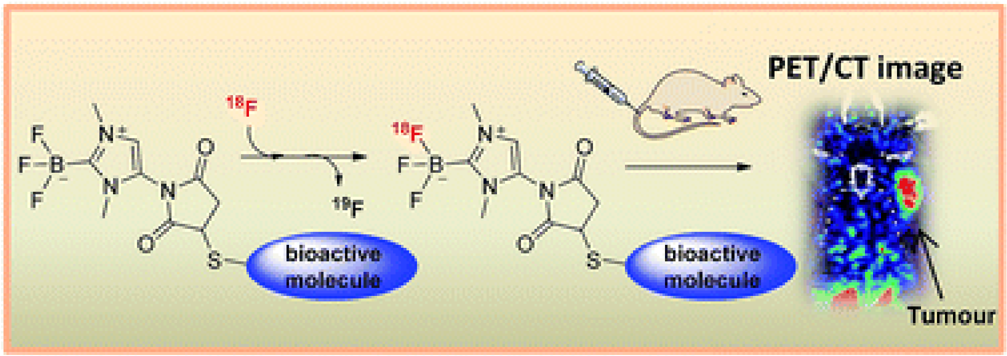

Figure 6.2 Graphical abstract of the synthesis of ^{18}*F-NHC-BF*$_3$*-biomolecule and PET images of the constructed PET tracer. Sources: Adapted from Mengzhe et al (8). Published by The Royal Society of Chemistry*

6.3 Synthesis and *In vivo* Stability Studies of ^{18}F-Zwitterionic Phosphonium Aryltrifluoroborate/Indomethacin Conjugates

6.3.1 Introduction

Inspired by earlier contributions on the use of aryltrifluoroborate prosthetic groups by the group of Perrin (*1,9,10*), we showed that zwitterionic structures which combine the trifluoroborate unit with a proximal cationic group possess superior stability which lessens deactivation of the probe by fluoride anion release (*11*). Previously we described the synthesis and radiolabeling of phosphonium-trifluoroborates (*12*). In this study, we investigated their conjugation with organic derivatives as a mean to generate disease specific radiotracers.

6.3.2 Results and Discussion

Zwitterionic phosphonium arytrifluoroborate complexes were synthesized with two different captor structures. These compounds were conjugated with indomethacin, a nonsteroidal anti-inflammatory drug that selectively binds to the cyclooxygenase 2 (COX-2) enzymes (*13,14*). The resulting conjugates were amendable to late stage radiofluorination via simple ^{18}F-^{19}F isotope exchange in aqueous solution. This approach afforded PET probes which have been tested in vivo in a murine model. One of the key findings of these animal studies was the influence of the captor structure, which largely governed the biodistribution and the stability of the probe.

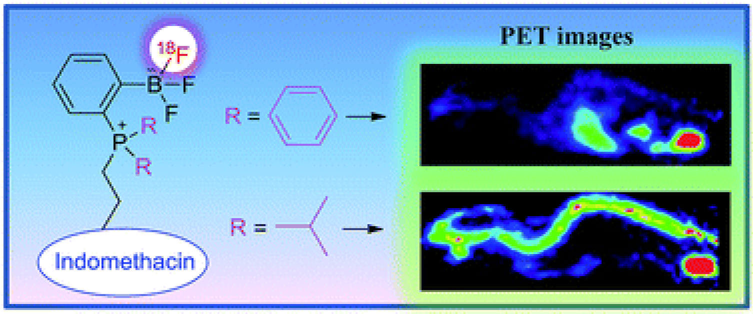

Figure 6.3 Graphical abstract of ^{18}*F labeling of zwitterionic phosphonium arytrifluoroborate-Indomethacin and PET images of the constructed PET tracer. Sources: Adapted from Mengzhe et al (15). Reproduced by permission of The Royal Society of Chemistry*

6.4 The efficiency of ^{18}F labelling of a prostate specific membrane antigen ligand via strain-promoted azide-alkyne reaction: reaction speed versus hydrophilicity

6.4.1 Introduction

In the past few decades, bioorthogonal reactions have become a unique tool in diverse fields including nuclear medicine (*16,17*). In particular, azide based metal-free click reactions were found to be rapid and clean which has been successfully adapted for ^{18}F radiolabeling. Previously our collaborator Dr. Popik's group reported the synthesis of oxa-dibenzocyclooctynes (ODIBOs), which was one the most reactive cyclooctynes for strain promoted azide cycloaddition (*18*). In this study, we performed a side by side comparison between ^{18}F-ODIBO and ^{18}F-bicyclo[6.1.0]nonyne (^{18}F-BCN) for PET probe construction. Both the reaction rate and probe hydrophilicity were explored for ^{18}F labelling of PSMA ligands. The obtained information may provide guidance in selecting appropriate labelling methods for PET probe construction.

6.4.2 Results and Discussion

Both ODIBO and BCN were readily radiolabeled with reasonable yield and conjugated with PSMA ligand yielding PET probes. Although both probes demonstrated comparable target binding affinity in vitro, ^{18}F-ODIBO-PSMA failed to provide a reasonable tumor to background contrast potentially due to the hydrophobicity of the ODIBO motif. The more hydrophilic BCN derived tracer showed much higher tumor uptake and a much higher tumor to background ratio. The information obtained here suggested that both reaction speed and hydrophilicity should be considered when selecting appropriate labeling methods for PET probe construction. ^{18}F-ODIBO might be more suitable for protein labeling which requires a fast reaction rate but may be less affected by hydrophobicity of the labeling motif due to the large molecular weight. Nonetheless, other factors including the position of modification, the degree of modifica- tion, and the charge change could all affect the distribution of the final agents.

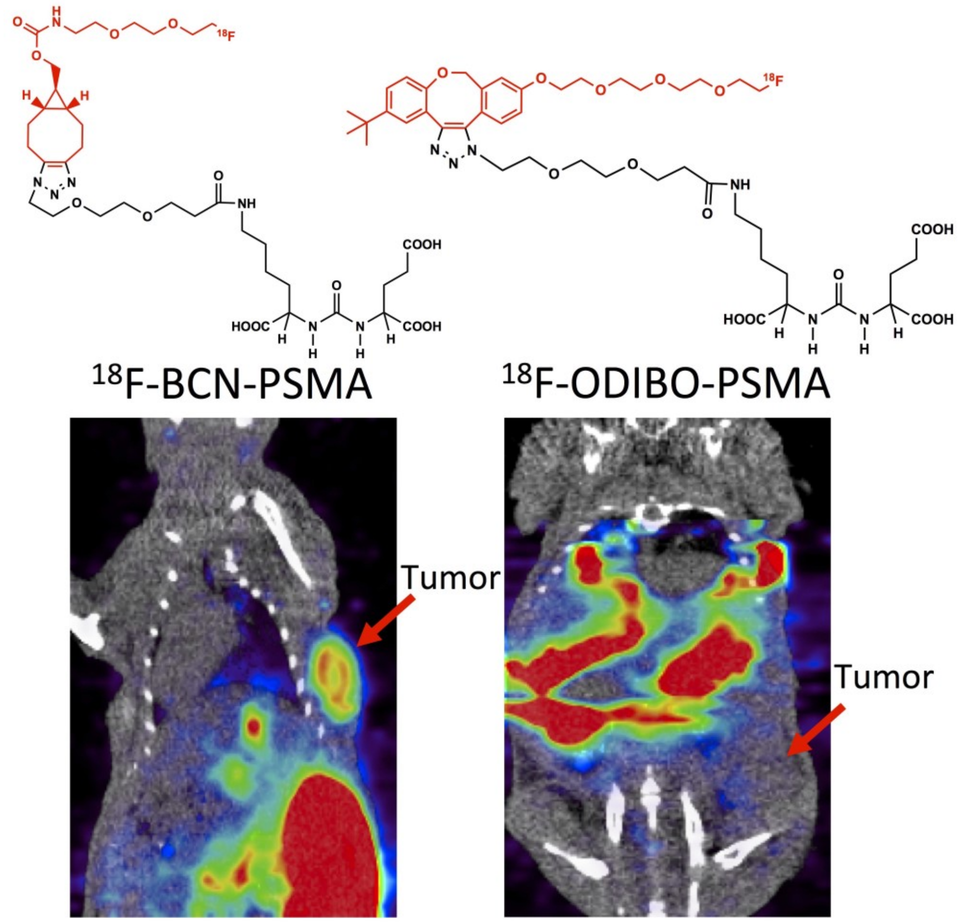

Figure 6.4 Graphical abstract of ^{18}*F-BCN-PSMA,* ^{18}*F-ODIBO-PSMA and corresponding PET images of the constructed PET tracer. Sources: Adapted from Mengzhe et al (19). Reproduced by permission of The Royal Society of Chemistry*

6.5 Molecular Imaging of P-glycoprotein in Chemoresistant Tumors Using a Dual-Modality PET/Fluorescence Probe

6.5.1 Introduction

Drug resistance remains a formidable challenge to cancer therapy. ATP-binding cassette (ABC) transporters, notably P- glycoprotein (Pgp), reduce cytotoxic effects of anticancer drugs by mediating their efflux from cancer cells, and thus become a majorcause of multidrug resistance (MDR) of human cancers (*20-22*). However, clinical translation of Pgp targeted therapeutics has been hindered by lack of patient preselection based on the Pgp presence in tumors. Thus, the success of any Pgp targeted therapeutics depends on a companion diagnostic test that can detect tumoral Pgp expression in a patient and determine if favorable outcome will come from the specific treatments. In this study, we aimed to construct a dual PET/fluorescence probe with an anti-Pgp monoclonal antibody to image tumoral Pgp.

6.5.2 Results and Discussion

A Pgp monoclonal antibody 15D3 was chemically modified with IRDye800 (IR800) and DOTA chelator. The specificity of the antibody conjugates DOTA-Pab-IR800 was verified in Pgp-expressing 3T3-MDR1 and control 3T3 cells. After radiolabeling with ^{64}Cu, the probe was applied in small animal PET imaging of Pgp in a mouse xenograft model of NCI/ADR-Res cells and showed reasonable tumor uptake and tumor to background ratio. Fluorescence imaging was performed following PET experiments, and it demonstrated excellent tumor accumulation of this dual-modality probe in the NCI/ADR-Res tumors. Further, an image-guided surgery was successfully performed using the fluorescence modality of the probe, demonstrating potential utility of this probe in image-guided surgical removal of Pgp-positive drug resistant tumors in the patients. This study clearly demonstrated that the Pgp-targeted antibody probe, ^{64}Cu-DOTA-Pab-IR800, could provide a promising diagnosis tool for detection of Pgp-expressing tumors in vivo.

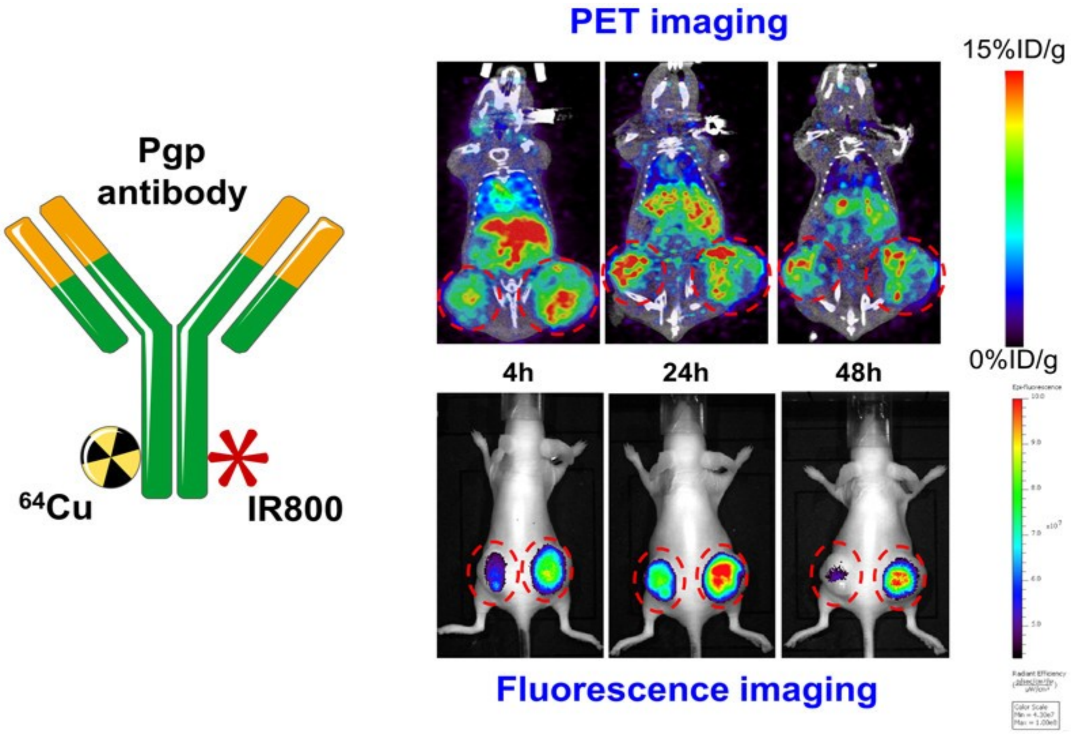

Figure 6.5 Graphical abstract of ^{64}*Cu-DOTA-Pab-IR800 and corresponding PET images. Sources: Adapted from Mengzhe et al (23). Reprinted with permission from Mol. pharmaceutics 2017, 14, 10, 3391-3398. Copyright 2017 American Chemical Society*

6.6 Development of ^{18}F-AlF-NOTA-NT as PET Agents of Neurotensin Receptor-1 Positive Pancreatic Cancer

6.6.1 Introduction

The extremely low 5-year survival rate of pancreatic cancer makes it the fourth deadliest human cancer in the USA and Europe (*24*). Several studies have suggested that neurotensin receptors (NTSRs) and neurotensin (NT) greatly affect the growth and survival of pancreatic ductal adenocarcinoma (PDAC) (*25-27*). Developing NTSR-targeted PET probes could therefore be important for the management of a pancreatic cancer patient by providing key information on the NTSR expression profile noninvasively. Despite the initial success on the synthesis of ^{18}F-labeled NT PET probes, the labeling procedure generally requires lengthy steps including azeotropic drying of ^{18}F. Recently, a straightforward ^{18}F labeling approach was developed according to the fact that the chelator 1,4,7- triazacyclononane-1,4,7-triacetic acid (NOTA) could form stable chelation complex with aluminum fluoride under certain conditions (*28*). In this study, we reported the development of NTSR1 PET probe using AlF chelating method and evaluated in NTSR1 positive tumor models

6.6.2 Results and Discussion

The PET probe could be simply prepared starting from aqueous ^{18}F and purified with HPLC. The cell binding test demonstrated that ^{19}F-AlF-NOTA-NT maintained high receptor-binding affinity to NTSR1. This probe was then further evaluated in NTR1 positive pancreatic tumor models (AsPC-1 and PANC-1). Small animal PET studies showed a high contrast between tumor and background in both models at 1 and 4 h time points. A blocking experiment was performed to demonstrate the receptor specificity. The greatly simplified labeling procedure and good imaging property will allow investigators monitoring NTSR1 expression in vivo using NTSR PET for either diagnosis application or NTSR1-targeted treatment (theranostic).

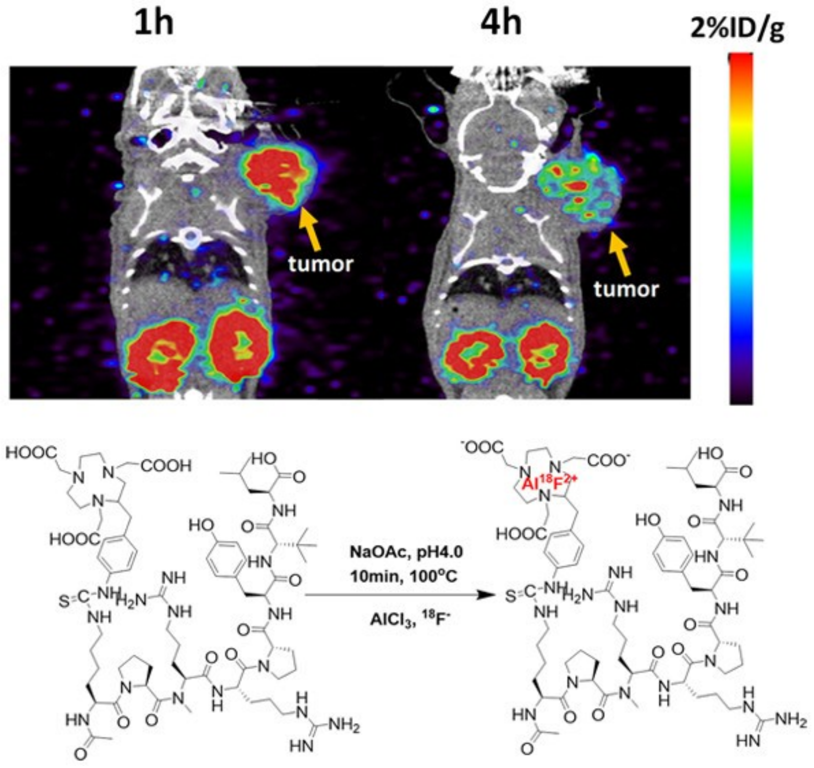

Figure 6.6 Graphical abstract of ^{18}*F-AlF-NOTA-NT synthesis and corresponding PET images. Sources: Adapted from Mengzhe et al (29). Reprinted with permission from Mol. Pharmaceutics 2018, 15, 8, 3093-3100. Copyright 2018 American Chemical Society*

REFERENCES

1. auf dem Keller U, Bellac CL, Li Y, et al. Novel Matrix Metalloproteinase Inhibitor [^{18}F]Marimastat-Aryltrifluoroborate as a Probe for *In vivo* Positron Emission Tomography Imaging in Cancer. *Cancer Research.* 2010;70:7562.

2. Liu Z, Li Y, Lozada J, et al. Stoichiometric Leverage: Rapid ^{18}F-Aryltrifluoroborate Radiosynthesis at High Specific Activity for Click Conjugation. *Angewandte Chemie International Edition.* 2013;52:2303-2307.

3. Liu Z, Pourghiasian M, Radtke MA, et al. An Organotrifluoroborate for Broadly Applicable One-Step ^{18}F-Labeling. *Angewandte Chemie International Edition.* 2014;53:11876-11880.

4. Liu Z, Radtke MA, Wong MQ, Lin K-S, Yapp DT, Perrin DM. Dual Mode Fluorescent ^{18}F-PET Tracers: Efficient Modular Synthesis of Rhodamine-[cRGD]2-[^{18}F]-Organotrifluoroborate, Rapid, and High Yielding One-Step ^{18}F-Labeling at High Specific Activity, and Correlated in Vivo PET Imaging and ex Vivo Fluorescence. *Bioconjugate Chemistry.* 2014;25:1951-1962.

5. Chansaenpak K, Wang M, Wu Z, Zaman R, Li Z, Gabbaï FP. [^{18}F]–NHC–BF3 adducts as water stable radio-prosthetic groups for PET imaging. *Chemical Communications.* 2015;51:12439-12442.

6. Liu Z, Pourghiasian M, Bénard F, Pan J, Lin K-S, Perrin DM. Preclinical Evaluation of a High-Affinity ^{18}F-Trifluoroborate Octreotate Derivative for Somatostatin Receptor Imaging. *Journal of Nuclear Medicine.* 2014;55:1499-1505.

7. Liu Z, Amouroux G, Zhang Z, et al. ^{18}F-Trifluoroborate Derivatives of [Des-Arg^{10}]Kallidin for Imaging Bradykinin B1 Receptor Expression with Positron Emission Tomography. *Molecular Pharmaceutics.* 2015;12:974-982.

8. Chansaenpak K, Wang M, Wang H, et al. Preparation of [^{18}F]-NHC-BF3 conjugates and their applications in PET imaging. *RSC Advances.* 2017;7:17748-17751.

9. Ting R, Adam MJ, Ruth TJ, Perrin DM. Arylfluoroborates and Alkylfluorosilicates as Potential PET Imaging Agents: High-Yielding Aqueous Biomolecular ^{18}F-Labeling. *Journal of the American Chemical Society.* 2005;127:13094-13095.

10. Ting R, Harwig C, auf dem Keller U, et al. Toward [^{18}F]-Labeled Aryltrifluoroborate Radiotracers: In Vivo Positron Emission Tomography Imaging of Stable Aryltrifluoroborate Clearance in Mice. *Journal of the American Chemical Society.* 2008;130:12045-12055.

11. Wade CR, Zhao H, Gabbaï FP. Stabilization of zwitterionic aryltrifluoroborates against hydrolysis. *Chemical Communications.* 2010;46:6380-6381.

12. Li Z, Chansaenpak K, Liu S, Wade CR, Conti PS, Gabbaï FP. Harvesting ^{18}F-fluoride ions in water via direct ^{18}F–^{19}F isotopic exchange: radiofluorination of zwitterionic aryltrifluoroborates and in vivo stability studies. *MedChemComm.* 2012;3:1305-1308.

13. Kalgutkar AS, Marnett AB, Crews BC, Remmel RP, Marnett LJ. Ester and Amide Derivatives of the Nonsteroidal Antiinflammatory Drug, Indomethacin, as Selective Cyclooxygenase-2 Inhibitors. *Journal of Medicinal Chemistry.* 2000;43:2860-2870.

14. Rome LH, Lands WE. Structural requirements for time-dependent inhibition of prostaglandin biosynthesis by anti-inflammatory drugs. *Proceedings of the National Academy of Sciences of the United States of America.* 1975;72:4863-4865.

15. Chansaenpak K, Wang M, Liu S, et al. Synthesis and in vivo stability studies of [^{18}F]-zwitterionic phosphonium aryltrifluoroborate/indomethacin conjugates. *RSC Advances.* 2016;6:23126-23133.

16. Lang K, Chin JW. Bioorthogonal Reactions for Labeling Proteins. *ACS Chemical Biology.* 2014;9:16-20.

17. Meyer J-P, Adumeau P, Lewis JS, Zeglis BM. Click Chemistry and Radiochemistry: The First 10 Years. *Bioconjugate Chemistry.* 2016;27:2791-2807.

18. McNitt CD, Popik VV. Photochemical generation of oxa-dibenzocyclooctyne (ODIBO) for metal-free click ligations. *Organic & Biomolecular Chemistry.* 2012;10:8200-8202.

19. Wang M, McNitt CD, Wang H, et al. The efficiency of ^{18}F labelling of a prostate specific membrane antigen ligand via strain-promoted azide–alkyne reaction: reaction speed versus hydrophilicity. *Chemical Communications.* 2018;54:7810-7813.

20. Fletcher JI, Haber M, Henderson MJ, Norris MD. ABC transporters in cancer: more than just drug efflux pumps. *Nature Reviews Cancer.* 2010;10:147.

21. Gottesman MM, Lavi O, Hall MD, Gillet J-P. Toward a Better Understanding of the Complexity of Cancer Drug Resistance. *Annual Review of Pharmacology and Toxicology.* 2016;56:85-102.

22. Holohan C, Van Schaeybroeck S, Longley DB, Johnston PG. Cancer drug resistance: an evolving paradigm. *Nature Reviews Cancer.* 2013;13:714.

23. Wang M, Mao C, Wang H, et al. Molecular Imaging of P-glycoprotein in Chemoresistant Tumors Using a Dual-Modality PET/Fluorescence Probe. *Molecular Pharmaceutics.* 2017;14:3391-3398.

24. Rahib L, Smith BD, Aizenberg R, Rosenzweig AB, Fleshman JM, Matrisian LM. Projecting Cancer Incidence and Deaths to 2030: The Unexpected Burden of Thyroid, Liver, and Pancreas Cancers in the United States. *Cancer Research.* 2014;74:2913.

25. Mijatovic T, Gailly P, Mathieu V, et al. Neurotensin is a versatile modulator of in vitro human pancreatic ductal adenocarcinoma cell (PDAC) migration. *Cellular oncology : the official journal of the International Society for Cellular Oncology.* 2007;29:315-326.

26. Reubi JC, Waser B, Friess H, Büchler M, Laissue J. Neurotensin receptors: a new marker for human ductal pancreatic adenocarcinoma. *Gut.* 1998;42:546.

27. Shulkes A, Read D, Hardy KJ, Kapuscinski M. Expression of Neurotensin in Endocrine Tumors. *The Journal of Clinical Endocrinology & Metabolism.* 1990;70:100-106.

28. McBride WJ, Sharkey RM, Karacay H, et al. A Novel Method of ^{18}F Radiolabeling for PET. *Journal of Nuclear Medicine.* 2009;50:991-998.

29. Wang M, Zhang H, Wang H, et al. Development of [^{18}F]AlF-NOTA-NT as PET Agents of Neurotensin Receptor-1 Positive Pancreatic Cancer. *Molecular Pharmaceutics.* 2018;15:3093-3100.

Chapter 7 SUMMARY

7.1 Summary of Current Work

In this work, we developed a TTCO ligation method that enabled fast and efficient incorporation of ^{18}F into complex biomolecules, leading to novel PET probes with high specific activity. Due to the modest nucleophilicity of fluoride and the low concentration of both ^{18}F and biomolecule, a labeling method with high reaction rate is needed. We utilize the TTCO ligation with extremely fast reaction kinetic to conjugate ^{18}F labeled prosthetic group with modified biomolecules. **This strategy provides a platform to radiolabel both small and large biomolecules with high specific activity and the pharmacokinetic of the constructed PET tracer can be controlled by choosing different tetrazine-*trans*-cyclooctene combinations**.

For radiolabeled prosthetic groups, we have demonstrated that several types of *trans*-cyclooctenes (TCO, sTCO, dTCO and oTCO) can be effectively ^{18}F fluorinated with reasonable yield and remain their reactivity towards tetrazine. Additionally, these *trans*-cyclooctenes and some tetrazine derivatives can be modified with chelators and subjected to radiometal labeling. The radiometal labeled compounds also retain the reactivity for TTCO ligation.

For the radiolabeling of biomolecules, we radiolabeled both small molecular weighted peptide and relatively large proteins with TTCO ligation. All the PET probes were constructed in acceptable yield with reasonable tumor targeting property and showed comparable binding affinity with parent biomolecules. The pharmacokinetic of the PET probes varied along with the hydrophilicity of the TTCO system.

In the PET imaging studies, we found that the DiPhTz-sTCO system led to an enhanced blood circulation time of the PET tracer. This resulted in the longer retention of tracer in the targeted region but also higher background signal. Switching the DiPhTz to more hydrophilic tetrazines weakened this effect and the constructed PET tracer showed decreased tumor uptake but increased tumor to background ratio. The PET tracer with best imaging contrast was obtained when a combination of both hydrophilic tetrazine and hydrophilic *trans*-cyclooctene was used.

Additionally, we also demonstrated the feasibility of in vivo TTCO ligation. The ^{64}Cu labeled Tz-PEG-NOTA was shown to be conjugated with the pre-injected TCO-15D3 antibody in the blood stream. Similarly, ^{18}F-TCO-8Tz also reacted with the intratumorally injected TCO-15D3 antibody and accumulated in the tumor. Unfortunately, the pretargeting experiment in which both TCO engineered antibody and ^{18}F labeled prosthetic group were systematically injected was not successful. This might be due to the misestimation of the pharmacokinetic of the TCO modified antibody. Nevertheless, the proposed TTCO ligation can be a potential tool for pretargeted imaging and therapy application.

In order to develop and optimize a fully integrated imaging, monitoring and therapy system for image-guided interventions, novel and effective prognostic and therapeutic options are essential. Despite the great potential of using ^{18}F labeled protein or antibodies for both diagnoses and therapy monitoring purposes, their application has been limited due to the challenges to synthesize ^{18}F labeled large biomolecules in adequate yield with high specific activity. Our work develops efficient method to overcome this limitation and the success of our approach will have significant impact on both imaging and therapy areas.

At imaging level, the scope of the our ^{18}F labeling method and pretargeting approach will be broad, and will be used widely to construct a series of molecular probes for imaging while maintaining high specific activity for the radioactive label. In this dissertation, this major advancement in ^{18}F labeling methodology will lead to the discovery of critical imaging probes for diagnosis and treatment monitoring in both basic and clinical research. For therapeutic applications, current radioimmunotherapy uses large biomolecules as carriers of radionuclides that emit cell-killing radiation. Based on the TTCO ligation, the pretargeted approach developed in this dissertation will deliver therapeutic radionuclides with limited radiation exposure towards normal organs and can be used in both basic and translational research.

7.2 Innovation of Current Studies

These studies describe significant innovations in the following aspects: 1) The development of a novel ^{18}F labeling method based on tetrazine and TCO ligation. Guided by calculation and enabled by novel synthetic methodology, it has been possible to achieve extremely fast rates (k_2>250,000 $M^{-1}s^{-1}$ at room temperature). This application overcomes the existing limitations of introducing ^{18}F labels to biomolecules with high specific activity. 2) Fast generation of batches of radiolabeled biomolecules. Biomolecules can be modified with tetrazine and preserved as fast labeling kit and ready for radiolabeled TCO ligation to generate batches of PET agents. 3) The feasibility to develop novel pre-targeted method based on the TTCO ligation. The pretargeted method developed in here can introduce a novel approach to deliver radionuclides of imaging/therapy with limited radiation exposure towards normal organs.

7.3 Future Work

As discussed above, the pharmacokinetic of the TCO modified pretargeted antibody needs to be further explored to gain better pretargeting efficiency. Additionally, a more stable and fast clearing ^{18}F labeled prosthetic group needs to be developed for pretargeting study as the current candidates either suffered from defluorination (^{18}F-sTCO) or showed relatively long blood circulation time (^{18}F-TCO-8Tz). As the DiPhTz-sTCO system showed enhanced bloodstream retention and even increased target region uptake overtime, it could be served as a potential platform for therapeutic radiopharmaceuticals construction. Another interesting optimization can be developing module assisted synthesis of PET probes using the TTCO ligation. Since the tetrazine modified biomolecules can be preserved as labeling kit while the radiolabeling of prosthetic group and TTCO ligation process are quite generous, we can integrate these to the automated module to produce PET agents readily. Furthermore, investigations such as toxicity, stability and dosimetry need to be performed before translating to more clinical related studies.

Overall, PET is a developing technique and holds great interest in future clinical use. I expect that will be much evolution for the next generation of PET. On the hardware part, PET may be fused to other imaging modalities, not only CT but fluorescent or MRI as well. PET probes will also be expanded and enable personalized medicine through precision diagnostics. Additionally, the application of PET may not limit to oncology but also cardiology and neurology etc. These exciting potentials drive me to devote more works to this technique.